Alma Mater Studiorum – Università di Bologna
in cotutela con Università Tecnica di Eindhoven

DOTTORATO DI RICERCA IN

Ingegneria Civile, Chimica, Ambientale e dei Materiali

Ciclo XXIX

Settore Concorsuale: 08/B2 Scienza delle costruzioni

Settore Scientifico Disciplinare: ICAR/08 Scienza delle costruzioni

LARGE EDDY SIMULATIONS APPLIED TO WIND LOADING AND POLLTUANT DISPERSION

Presentata da: Mattia Ricci

Coordinatore Dottorato

Prof. L. Vittuari

Supervisori

Prof. S. de Miranda
Prof. B. Blocken

Esame finale anno 2018

Large Eddy Simulations applied to wind loading and pollutant dispersion

PROEFSCHRIFT

ter verkrijging van de graad van doctor aan de Technische Universiteit Eindhoven, op gezag van de rector magnificus prof.dr.ir. F.P.T. Baaijens, voor een commissie aangewezen door het College voor Promoties, in het openbaar te verdedigen op dinsdag 20 februari 2018 om 13:30 uur

door

Mattia Ricci

geboren te Forlimpopoli, Italië

Dit proefschrift is goedgekeurd door de promotoren en de samenstelling van de promotiecommissie is als volgt:

voorzitter:	prof.ir. E.S.M. Nelissen
1e promotor:	prof.dr.ir. B.J.E. Blocken
copromotor(en):	dr.ir. T.A.J. van Hooff
	dr.ir. S. de Miranda
	(University of Bologna)
independent members:	prof.dr.ir. C. Baniotopoulos
	(University of Birmingham)
	prof.dr.ir. F. Toschi
	prof.ir. H.H. Snijder
advisor(s):	dr.ir. Luca Patruno
	(University of Bologna)

Het onderzoek of ontwerp dat in dit proefschrift wordt beschreven is uitgevoerd in overeenstemming met de TU/e Gedragscode Wetenschapsbeoefening.

LARGE EDDY SIMULATIONS APPLIED TO WIND LOADING AND POLLUTANT DISPERSION

MATTIA RICCI

ALMA MATER STUDIORUM
UNIVERSITÀ DI BOLOGNA
DIPARTIMENTO DI INGEGNERIA CIVILE,
CHIMICA, AMBIENTALE E DEI MATERIALI

The research work presented in this thesis is the result of the collaboration between the Department of Civil, Chemical, Environmental and Materials Engineering (DICAM) of the University of Bologna (Bologna, Italy) and the unit of Building Physics and Services (BPS) at the Department of Built Environment of the Eindhoven University of Technology (Eindhoven, the Netherlands), in the framework of a double-degree agreement between both universities.

A catalogue record is available from the Eindhoven University of Technology Library.

ISBN: 978-90-386-4427-1
Bouwstenen: 235
NUR: 955

Cover designed by Mattia Ricci (adapted from Google Earth ®).

Printed by TU/e print service - DMX print, Eindhoven (the Netherlands).

To my father, Elmo, my mother, Ivana, my uncle, Ellero, and my grandmother, Cesarina.

It is not knowledge, but the act of learning,
not possession, but the act of getting there,
which grants the greatest enjoyment.

— Carl Friedrich Gauss

ACKNOWLEDGEMENTS

A long trip is difficult to be described in a few words. This thesis is the result of the collaboration between two universities: the University of Bologna and the Eindhoven University of Technology. More than research, this thesis represented to me a trip towards my personal boundaries, full of challenges that deeply strengthened me as a person and as a researcher.

First of all, I would like to thank my supervisors, prof. Bert Blocken and prof. Stefano de Miranda, for giving me the possibility to conduct my Ph.D. research and for having supported me during all my work. Without their precious suggestions and their support the present research work would not have been possible. I feel honoured to be part of their research groups and to be the first candidate involved in the dual-degree agreement between the University of Bologna and the Eindhoven University of Technology. I am very grateful to them for that.

I would like to express my gratitude to my co-supervisors, dr. Ivo Kalkman, dr. Twan va Hooff and dr. Luca Patruno, for their teachings and every-day support. I also would like to thank all the members of the committee, prof. E.S.M. Nelissen, prof. C. Baniotopoulos, prof. F. Toschi and prof. H.H. Snijder for their valuable suggestions on the thesis.

I want to express my gratitude to the whole unit of Building Physics and Services (BPS) for having welcome me in their group and to the whole Laboratory of Computational Mechanics of the University of Bologna.

Finally, I want to give a very special thank to my family. This work would not have been possible without their constant support. They represent to me one of the few fixed thoughts I have in my mind, a safe harbour towards which I always come back.

Ho sempre avuto pochissime idee, ma in compenso, fisse.

— Fabrizio de André

SUMMARY

In the past decades, the growing urbanization rate together with the increasing demand for high, slender and complex structures has led to significant scientific developments in the discipline of wind engineering, which is best defined as the rational treatment of the interactions between wind in the atmospheric boundary layer and humans and their works on the surface of earth. In particular, aiming at conceiving healthier, safer and more sustainable buildings and cities, the study of wind flow in the urban environment has become a very active research topic. Recently, due to the continuous increase in computational power, the numerical simulation of wind flow by means of Computational Fluid Dynamics (CFD) techniques is becoming an attractive complementary tool to traditional experimental campaigns for the investigation of problems such as wind loading on structures and pollutant dispersion. In particular, the Reynolds-Averaged Navier-Stokes (RANS) approach has been intensively investigated in the past and successfully applied to several wind engineering problems. Unfortunately, despite their diffusion, the predictive capability of RANS models is limited to the mean flow properties, while the ability to accurately predict turbulent fluctuations is of fundamental importance when dealing with wind loading and pollutant dispersion. This fact has led researchers to move towards scale-resolving turbulence models such as Large Eddy Simulations (LES) which nowadays represent a very promising tool for analysing a wide range of problems in wind engineering.

Although numerical techniques are characterised by several well-known advantages when compared to the traditional experimental approach based on wind tunnel testing, LES results often show to be quite scattered, even for simple geometries. In fact, turbulent flows around bluff bodies, of primary interest in wind engineering, are inherently unsteady, three-dimensional and multi-scale and many parameters can affect LES results, such as the subgrid-scale model adopted, the time and space discretisation schemes, the computational grid and the boundary conditions. It is currently insufficiently known to what extent these parameters can affect the numerical results. Scientists and engineers are confronted with a severe lack of best practice guidelines for LES, while such guidelines for RANS have become well-established in the international community already in the past 17 years.

Within this framework, this thesis focuses on the assessment of the capability of LES when applied to wind loading and pollutant dispersion with the aim to contribute to the development of international best practice guidelines for the application of LES for these topics. To this end, first the adopted numerical setup is validated through an in-depth study of the wind flow predicted around a 5:1 rectangular cylinder, which is the main subject of the BARC (Benchmark on the Aerodynamics of the Rectangular Cylinder 5:1) international benchmark and is considered to be well representative of bluff bodies of interest for civil engineering applications. The effects of different subgrid-scale models as well as the effects of different inflow turbulence intensities and length scales are investigated. Then, the most accurate and cost effective numerical setup is adopted to assess the LES capability in accurately predicting wind loads on a low-rise and a high-rise building. For all the considered cases, the turbulent part of the ABL is generated by means of synthetic methods in order to correctly represent the von Kàrmàn spectrum and to limit as much as possible the computational cost. All the obtained numerical results are systematically compared to available experimental measurements. As an additional element of novelty, the LES results are compared with the experimental data not only in terms of pressure distributions, but also in terms of internal forces on the structural members. Finally, LES are performed aiming at predicting pollutant concentrations from an isolated stack and in the wake of an isolated building.

The analyses on the 5:1 rectangular cylinder show that, when the standard Smagorinsky-Lilly subgrid-scale model is adopted, taking into account even small levels of the incoming flow turbulence intensity is of primary importance in order to obtain accurate results, since the subgrid-scale model is not able to accurately predict the natural laminar to turbulent transition, which strongly affects the pressure distribution on the rectangular cylinder. When the inflow turbulence is introduced in the computational domain, a satisfactory agreement between LES results and experimental measurements is observed in terms of pressure statistics for the different inflow conditions analysed, even considering the need for large domains when the inflow turbulence length scale increases. The obtained results represent at this stage the only contribution in the framework of the international BARC project regarding the effects of the incoming turbulence when LES are adopted.

Regarding the wind load assessment, it is found that the accuracy of LES in reproducing the fluctuating pressure field is not necessarily maintained when internal forces are taken into account. Nevertheless,

the design values predicted by LES can be considered as satisfactory when the envelope of different angles of attack is considered.

Regarding the pollutant dispersion, in order to obtain accurate results the adoption of LES is recommended, in particular when dispersion around obstacles is analysed. In this case, a good agreement between numerical results and experimental measurements is achieved in terms of average concentrations, without the need for calibrating any case-dependent model parameter.

In conclusion, the LES results presented in this thesis appear very promising although a strong sensitivity of the obtained results on the adopted boundary conditions and numerical setup is noted. The proposed research work is expected to provide clear guidance towards the drafting of best practice guidelines for the application of LES to wind loading and pollutant dispersion.

CONTENTS

INTRODUCTION

1 INTRODUCTION

1.1 PROBLEM STATEMENT

Due to the growing urbanization rate, the disciplines of Urban Physics and Wind Engineering are rapidly expanding. They encompass several branches of Science and Engineering, such as Physics, Mathematics, Chemistry, Civil Engineering and Environmental Engineering [1]. These disciplines deal with a wide range of problems, such as pollutant dispersion, pedestrian-level wind conditions for pedestrian comfort and safety [2], wind loads on structures [3–5], outdoor and indoor thermal environment [6] and many others, so they are closely connected to the grand societal challenges of climate change, energy, health and security. The study of wind flows in the urban environment has become an extremely active research area in the last decades, aiming at conceiving healthier, safer and more sustainable cities.

The research in the field of Urban Physics and Wind Engineering is traditionally based on experimental campaigns conducted either on site (field experiments) or in wind tunnels using reduced-scale geometrical models. Different from wind tunnel facilities designed for mechanical and aeronautical studies, when wind flows in the urban environment are analysed, wind tunnel tests have to accurately reproduce the natural turbulent characteristics of the Atmospheric Boundary Layer (ABL). In fact, for a given geographical site, the wind climate is strongly affected by the terrain roughness and the surroundings obstacles. This is reflected into modifications in mean velocity, turbulence intensity and turbulence length scales, which are known to strongly influence the results for a wide range of applications. Before 1950, most of the wind tunnel facilities were aeronautical tunnels with short test sections, but after the publication of Jensen's law, which allowed to scale natural wind properties, the wind tunnel practice changed fundamentally. The need for an artificial reproduction of the ABL in wind tunnels led engineers to design ABL wind tunnels with long working sections where the long length was needed for the reproduction of the ABL characteristics. One of the first large ABL Wind Tunnels (ABLWT) was built by Prof. A. G. Davenport in 1965. Today, ABLWTs

are widespread in most parts of the world. Usually, in a typical ABLWT setup, the incoming flow turbulence is generated by spires, responsible for the generation of the large-scale eddies, and other roughness elements, such as rough carpets and blocks organised in different patterns. This part of the wind tunnel is set upwind with respect to the test model that is usually placed on a turning table to simulate different wind angles of attack. A pattern of blocks is used to generate the desired vertical mean wind speed profile together with the target turbulence intensity profile and turbulence spectra. The approaching flow generated in this way should be representative of the roughness of the upstream obstructions present in reality that however, are not explicitly included in the wind tunnel model, or rather the terrain effect. A view of a typical arrangement of obstacles adopted to reproduce the ABL is shown in Fig. 1.1 (a), while Fig. 1.1 (b) shows an example of a geometrical model of a structure placed on a turning table in the wind tunnel, also with upstream roughness elements.

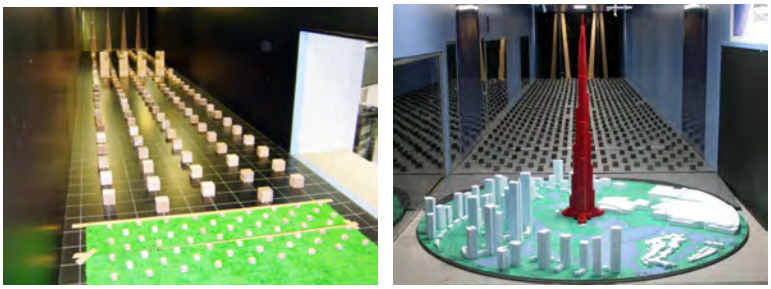

(a) (b)

Figure 1.1: (a) view of a typical arrangement of spires and roughness blocks in an atmospheric boundary layer wind tunnel [7] and (b) view of the geometrical model of the Burj Khalifa also with upstream spires and roughness blocks [8].

In the last decades, thanks to the continuous growth in computer power, numerical techniques based on Computational Fluid Dynamics (CFD) have become very attractive and have gained interest in the scientific community in Urban Physics and Wind Engineering [9]. Although numerical techniques show several advantages when compared to the traditional experimental approach based on wind tunnel testing, CFD results often show to be very sensitive to the numerical setups adopted even when simple geometries are considered [10–12]. In fact, turbulent flows around bluff bodies, which are of primary interest for Civil Engineering applications, are inherently unsteady, three-dimensional and multi-scale so that their numerical simulation

often presents a challenging engineering problem. Notwithstanding the fact that the direct numerical integration of the Navier-Stokes equations is theoretically possible, the high temporal and spatial resolutions needed to accurately resolve all the turbulent scales render its applicability very limited or even impossible for a wide range of Engineering applications [13]. In order to overcome this problem, researchers introduced simplified forms of the governing equations. These simplified forms add additional unknowns to the governing equations, for which turbulence models are needed to provide closure [1, 13, 14]. The simplified forms in combination with turbulence models were introduced with the aim of finding a satisfactory trade-off between accuracy and computational cost. In particular, the Reynolds-Averaged Navier-Stokes (RANS) equations and the associated turbulence models have been intensively investigated in the past and successfully applied to several Urban Physics and Wind Engineering problems [9]. Unfortunately, the predictive capabilities of the RANS approach are limited to the mean flow properties, while the ability to accurately predict turbulent fluctuations is of fundamental importance when dealing with wind loading [4, 15–19] and pollutant dispersion problems [20–25]. This fact led researchers to move towards scale-resolving turbulence approaches such as Large Eddy Simulation (LES), which nowadays represent a very promising tool for analysing urban physics and wind engineering problems. Despite their well-recognised potential, their use is still mainly limited to research due to their considerable computational cost and a careful validation work is still necessary in order to accurately assess their accuracy and reliability.

Besides the adopted turbulence approach, a key aspect for the numerical simulation of ABL wind flows are the boundary conditions. Indeed, an accurate simulation of the natural characteristics of the ABL is of utmost importance in order to obtain accurate results. In principle, the vertical mean wind speed profile as well as the turbulent intensity profile can be applied as an inlet boundary, without loss of time in designing any configuration of blocks and obstacles upwind of the model as required in an ABLWT experiment. However, if the wind flow is not in equilibrium with the aerodynamic roughness of the bottom boundary, the wind profile tends to evolve in the computational domain towards a given equilibrium configuration [26]. As a result, in such cases the ABL is not horizontally homogeneous and it might be difficult to accurately control the wind flow and its turbulence characteristics in the CFD simulation. Furthermore, it should be noted that the treatment of boundary conditions is very different between RANS and LES. Indeed, while RANS can take into account the

incoming turbulence through variables transported by the flow itself, LES requires that turbulent fluctuations are explicitly introduced in the computational domain [27]. In this regard, it should be pointed out that introducing velocity fluctuations at the inlet boundary is not straightforward [28]. In fact such fluctuations should be generated in order to match predefined time and space spectra, correlations and coherences to represent a realistic wind flow and they should not cause unrealistic large pressure fluctuations when introduced in the computational domain (a problem that might appear especially when an incompressible solver is adopted [28]). Among the wide variety of methodologies proposed in the relevant literature, synthetic methods to generate turbulent fluctuations seem to be very promising [29–31]. Indeed, they allow to generate turbulent fluctuation fields in accordance with predefined time power spectral densities, while maintaining the field divergence null and with a limited computational cost. Nevertheless, the synthetic generation of inflow turbulence still appears to be an open research topic as a completely satisfactory approach is still unavailable [32].

The scientific community is nowadays confronted with a severe lack of best practice guidelines for LES, in particular when applied to Urban Physics and Wind Engineering problems. Within this framework, the present thesis aims at assessing LES capabilities when applied to wind loading and pollutant dispersion. For this purpose, three main applications of LES, namely the numerical simulation of bluff body aerodynamics, the numerical simulation of wind loads on buildings and the numerical simulation of pollutant dispersion, are investigated in this thesis.

In the framework of bluff-body aerodynamics, the first part of the present thesis represents a new contribution to the BARC (Benchmark on the Aerodynamics of the Rectangular Cylinder 5:1) international benchmark. To the author's knowledge, this study represents the first one in the framework of the BARC project that deals with LES simulations taking into account inflow turbulence intensities up to 13.5%, which are of interest for Engineering applications. Moreover, as additional elements of novelty, the effects of the LES subgrid-scale model as well as the interaction between the along-wind turbulence length scale characterising the inflow and the domain spanwise dimension are analysed.

Regarding the assessment of wind loads on buildings, the common practice to validate numerical results consists of comparing numerical predictions of pressure statistics with experimental data. As an element of novelty, in the present work LES results are compared to experimental data not only in terms of pressure distributions, but also in terms

of internal forces on the structural members in order to assess LES capabilities to be used as a complementary design tool alongside wind tunnel tests.

Considering pollutant dispersion, the present thesis aims to assess the capabilities of LES to predict it in a turbulent atmospheric boundary layer, in particular when obstacles are taken into account. As an element of novelty, in the present thesis the average concentration field is analysed also far downwind the source and results are compared to the configuration with an isolated stack. In addition to the comparison with experimental data, a comparison with well-known theoretical, empirical and semi-empirical models is provided.

1.2 AIM, OBJECTIVES AND METHODOLOGIES

This thesis focuses on the assessment of LES capabilities when applied to wind loading and pollutant dispersion problems. The aim of the present thesis is to contribute to the development of international best practice guidelines for the application of LES in Urban Physics and Wind Engineering. To this end, this thesis is organised in three parts, which main objective are: (I) the assessment of LES capabilities to reproduce the wind flow around bluff bodies; (II) the assessment of LES capabilities to reproduce the internal forces in the structural members of buildings and (III) the assessment of LES capabilities to accurately reproduce pollutant dispersion.

For all the considered cases, the turbulence characterising the approach flow is generated by means of synthetic methods in order to correctly represent the von Kármán spectrum and to limit as much as possible the computational cost. The obtained numerical results are validated through a systematic comparison with experimental data and solution verification is performed to reduce and assess the numerical errors in each study.

The objectives of the three parts aforementioned are detailed in the following subsections.

1.2.1 *Part I: LES applications to bluff body aerodynamics*

The first objective of the thesis is to validate the adopted LES subgrid-scale model. In order to do that, an in-depth study of the flow around the 5:1 rectangular cylinder, which is the main subject of the BARC international benchmark, is performed. Despite its geometrical simplicity, the flow around the 5:1 rectangular cylinder is regarded as complex,

being characterised by flow reattachment/detachments mechanisms, turbulent shear layers and vortex shedding, therefore it is considered to be well representative of bluff bodies of interest for Civil Engineering applications.

First, the effects of different subgrid-scale models are analysed as well as the effects of small levels of inflow turbulence, in order to assess the sensitivity of the adopted subgrid-scale models to small incoming disturbances. Then, the sensitivity of the results to higher levels of turbulence intensities and length scales are investigated in order to assess LES capabilities in predicting the flow properties in radically different conditions. Furthermore, the interaction between the inflow turbulent length scale and the spanwise domain dimension is analysed. The results of the numerical simulations are analysed in terms of statistics of the pressure coefficient distributions, flow bulk parameters and flow topology.

1.2.2 *Part II: LES applications for assessment of wind loads on buildings*

The second objective of the thesis is to assess LES capabilities in accurately predicting wind loads on buildings.

Using the numerical setup validated in the first part of the thesis, LES simulations are performed in order to assess wind loads on a low-rise building. Then, the wind flow around a high-rise building is analysed as well. The LES results are compared to experimental data in terms of pressure distributions and in terms of internal forces on the structural members. For that purpose, linear structural dynamic analyses are performed starting from the pressure field obtained from the simulations and from the experiments. Then, aimed at assessing LES capabilities to be adopted as a complementary design tool alongside wind tunnel tests, a comparison between numerical and experimental predictions of the internal forces is provided for different wind angles of attack.

1.2.3 *Part III: LES applications to pollution dispersion problems*

The third objective of the thesis is to assess LES capabilities in accurately predicting pollutant dispersion in the urban environment.

First, LES simulations of pollutant dispersion from an isolated stack are performed, aiming at validating the numerical model employed. The results of different computational grids as well as different subgrid-scale models are analysed. LES results are compared to experimental data as well as to results from theoretical, empirical and semi-empirical

formulae in terms of statistics of the concentration field and their along-wind evolution. Subsequently, LES simulations are performed aimed at predicting pollutant concentrations in the wake of an isolated building.

1.3 STRUCTURE OF THE THESIS

This thesis is organised as follows .After the introductory part presented in Chapter 1, Chapter 2 describes the theoretical background of the numerical models adopted as well as their governing equations. Then, the core of the thesis is organised in three parts composed by self-contained chapters, most of which have been published or submitted as papers to international journals with peer review:

- Part I is composed of Chapters 3 and 4 and focusses on LES applications to bluff body aerodynamics. In particular, the flow field around the rectangular cylinder 5:1 is analysed. In Chapter 3, the effects of different subgrid-scale models as well as the effects of small incoming turbulence are analysed, while Chapter 4 studies the effects on the flow field of higher turbulence intensities and length scales and their interaction with the spanwise domain dimension.

- Part II is composed of Chapters 5 and 6 and focusses on LES applications for the assessment of wind loads on buildings. LES capabilities in reproducing wind loads in terms of internal forces on the structural members are assessed for a low-rise and a high-rise building in Chapters 5 and 6, respectively.

- Part III is composed of Chapter 7 and focusses on LES applications to pollutant dispersion problems in the urban environment. Simulations are performed in order to assess the pollutant concentrations for an isolated stack as well as in the presence of obstacles.

Finally, in Chapter 8 conclusions are drawn, summarising the results presented in the previous chapters.

The core of this thesis is composed by articles that have been published or submitted to international peer-reviewed journals. For this reason, the text as well as figures, tables and equations are reported without any change, although this might lead to some repetitions or a slightly different notation among the chapters. In the heading of each chapter, the full reference is reported, referring to the corresponding journal paper.

2 THEORETICAL BACKGROUND

In this chapter, the theoretical background of the numerical approaches and models adopted in the present thesis as well as their governing equations are briefly described. Since a considerable amount of literature exists on these topics, the present chapter is not intended to be exhaustive, but rather aims at providing the basic elements needed in order to understand the main features of the numerical models through which results presented herein are obtained. For a more detailed overview of the physical mechanisms which characterise turbulent flows, the reader is referred to [13, 33, 34], while for an in-depth understanding of the main numerical techniques adopted in CFD, the reader is referred to [14, 35].

2.1 GOVERNING EQUATIONS

In this section, the equations governing the motion of viscous fluids are reported. These equations represent the mathematical formulation of the following physical conservation principles:

- the mass of the fluid is conserved (mass conservation);
- the sum of the forces acting on a fluid particle equals the rate of change of its momentum (Newton's second law).

First, the mass and momentum conservation laws are obtained from simple equilibrium considerations. Then, the constitutive law for Newtonian fluids is described and introduced in the momentum conservation law to derive the Navier-Stokes equations. Einstein's notation is adopted for all equations reported in the present chapter.

2.1.1 *Mass conservation*

In the following, the fluid is considered as a continuum. By means of this approach, the infinitesimal fluid particle is then the smallest element of fluid, the macroscopic properties of which (i.e. density and velocity) are not influenced by the molecular structure of the fluid itself.

Considering the infinitesimal cubical element of fluid with dimensions ∂x_1, ∂x_2 and ∂x_3 reported in Fig. 2.1, it is thus possible to calculate the mass flow rate through its surface.

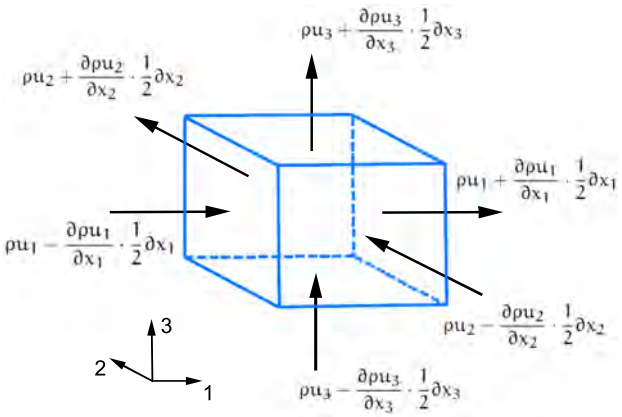

Figure 2.1: Mass conservation for the infinitesimal volume of fluid.

In particular, by approximating the velocity field in the corresponding center of mass of the infinitesimal volume of fluid using the first two terms of its Taylor expansion, the following equation can be easily obtained:

$$\frac{\partial \rho}{\partial t} + \frac{\partial \rho u_i}{\partial x_i} = 0 \,, \tag{2.1}$$

where ρ is the fluid density, u_i is the velocity component in the $i-th$ direction. Eq. 2.1 is the continuity equation for a compressible fluid.

2.1.2 *Momentum conservation*

According to the Newton's second law, the sum of the forces acting on a fluid particle equals the rate of change of its momentum. It is possible to distinguish two types of forces acting on the fluid particles:

- surface forces;
- body forces.

The surface forces can be subdivided into pressure forces and viscous forces, while the body forces can be of different nature, for example gravity force, centrifugal force, Coriolis force and electromagnetic force. In the following, only surface forces are considered. In such a

context, the state of stress of a fluid particle is fully described by the pressure p and the viscous stresses, referred as τ_{ij}, where τ is the viscous force acting on the surface with normal i in the j direction. Fig. 2.2 shows the surface forces components acting in the direction $j = 1$, approximated by considering the first two terms of their Taylor expansion.

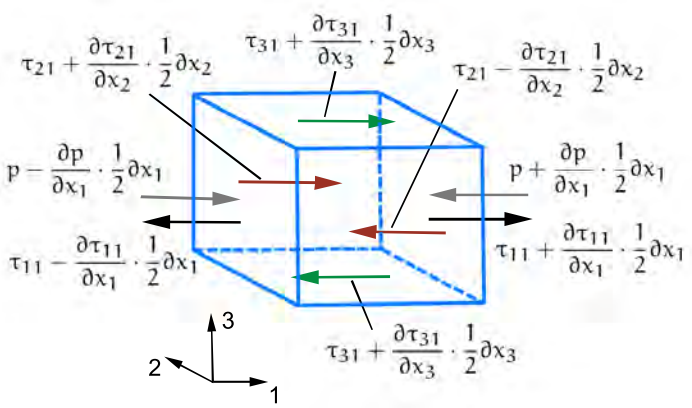

Figure 2.2: Momentum conservation for the infinitesimal volume of fluid in the $i = 1$ direction.

By equalling the net force in each direction with the rate of change of the momentum, it is straightforward to deduce the following equations:

$$\frac{\partial \rho u_i}{\partial t} + \frac{\partial \rho u_i u_j}{\partial x_j} = -\frac{\partial p}{\partial x_i} + \frac{\partial \tau_{ij}}{\partial x_j}, \quad i = 1, 2, 3. \tag{2.2}$$

2.1.3 *Navier-Stokes equations for a Newtonian incompressible fluid*

Many liquids and gases at low speed behave as incompressible fluids. The fluid flows of interest for Urban Physics and Wind Engineering applications fall in this category. In this case, the fluid density is constant in both time and space, consequently the governing equations can be rewritten as:

$$\frac{\partial u_i}{\partial x_i} = 0\,, \tag{2.3}$$

$$\frac{\partial u_i}{\partial t} + \frac{\partial u_i u_j}{\partial x_j} = -\frac{1}{\rho}\frac{\partial p}{\partial x_i} + \frac{1}{\rho}\frac{\partial \tau_{ij}}{\partial x_j}, \quad i = 1, 2, 3. \tag{2.4}$$

Eq. 2.3 and 2.4 are a set of 4 scalar independent equations containing the unknowns p, u_1, u_2, u_3, plus the nine components of the stress matrix, τ_{ij}. In order to close the problem, a constitutive law for the viscous stresses is needed in order to express the stress matrix τ_{ij} as a function of the unknowns p, u_1, u_2, u_3. For incompressible air flow, usually the hypothesis of an isotropic Newtonian fluid is assumed. In this case, the viscous stresses are proportional to the rate of strain matrix s_{ij}:

$$s_{ij} = \frac{1}{2}\left(\frac{\partial u_i}{\partial x_j} + \frac{\partial u_j}{\partial x_i}\right), \tag{2.5}$$

according to the following constitutive law:

$$\tau_{ij} = 2\mu\left[s_{ij} - \frac{1}{3}\delta_{ij}s_{kk}\right], \tag{2.6}$$

where μ is the dynamic fluid viscosity and δ_{ij} is the Kronecker delta.

If Eq. 2.6 is introduced in Eq. 2.3 and 2.4, the Navier-Stokes equations are obtained:

$$\frac{\partial u_i}{\partial x_i} = 0\,, \tag{2.7}$$

$$\frac{\partial u_i}{\partial t} + \frac{\partial u_i u_j}{\partial x_j} = -\frac{1}{\rho}\frac{\partial p}{\partial x_i} + \frac{1}{\rho}\frac{\partial}{\partial x_j}\left(\mu\frac{\partial u_j}{\partial x_i}\right)\,. \tag{2.8}$$

2.2 TURBULENCE MODELLING

In principle, the Navier-Stokes equations can be directly solved numerically. This approach is known as Direct Numerical Simulation (DNS). Despite the fact that DNS is recognised to be the most accurate numerical approach, it is not applicable for many Engineering problems. Indeed, the simulation of turbulent flows at high Reynolds numbers typically encountered in Engineering applications implies that high spatial and temporal resolutions are adopted to accurately reproduce all the flow features, ranging from the largest vortices to the small high-frequency vortices dissipated by viscosity. The computational cost of DNS becomes thus unaffordable and the need for a different approach arises. In order to overcome this problem, several approaches to model turbulent flows have been developed, two of which will be addressed here: the Reynolds-Averaged Navier-Stokes (RANS) approach and the Large Eddy Simulation (LES) approach.

RANS turbulence models simplify the Navier-Stokes equations by introducing a time averaging operator, separating both the velocity and

the pressure fields in a time-averaged and a fluctuating component. Indeed, for most Engineering purposes it is not necessary to simulate the unsteady turbulent fluctuations, but only the time-averaged fields. The averaging procedure introduces additional unknowns to the governing equations, for which turbulence models are needed to provide closure. These unknowns represent the effects of the turbulent fluctuations on the time-averaged field and depending on how they are modelled, different RANS turbulence model classes can be distinguished:

- first-order closure models;
- second-order closure models.

First-order closure models are based on the Boussinesq eddy-viscosity hypothesis [36], while second-order closure models are based on Reynolds stress modelling (RSM) [1]. Boussinesq eddy-viscosity models introduce a turbulent viscosity to model the effects of the turbulent fluctuations on the time-averaged fields. This artificial viscosity might affect the laminar to turbulent transition, which is very important to correctly simulate the free shear layer instabilities and thus the aerodynamic behaviour of many bluff bodies of interest for Civil Engineering applications [37]. Furthermore, RANS turbulence models only resolve the time-averaged field, so all the scales characterising the turbulent fields are modelled (i.e. approximated).

Differently from RANS, LES directly resolves the largest anisotropic turbulent structures of the flow and models only the turbulent structures whose scales are smaller than (or comparable to) a filter that is often taken equal to the local grid size. These subgrid-scales are modelled (i.e. approximated) in the assumption that the smallest scales of the turbulent motion are almost isotropic and problem independent, while the largest scales are directly resolved since they are considered to be deeply affected by the specific geometry of the problem under consideration [14]. In order to correctly reproduce the turbulent features of the resolved flow, LES requires both high grid and time resolutions and thus the computational cost is typically much higher than that required by RANS. However, thanks to the increase in the available computer power, LES simulations are becoming more commonly used to study turbulent flows, although their use still remains mainly limited to research.

In the next sections, more details regarding the turbulence models adopted in the present thesis are presented. In particular, Section 2.3 is focussed on the RANS approach, while Section 2.4 focusses on the LES approach.

2.3 REYNOLDS-AVERAGED NAVIER-STOKES

According to the RANS approach, the unknowns in the Navier-Stokes equations 2.7 and 2.8 are separated in a time-averaged term and in a fluctuating term:

$$u_i = U_i + u_i', \tag{2.9}$$

$$p = P + p', \tag{2.10}$$

where the capital letters denote the averaging operator reported below:

$$\overline{(\cdot)} = \frac{1}{2T}\int_{-T}^{T}(\cdot)dt, \tag{2.11}$$

where 2T is the averaging period. If Eq. 2.9 and Eq. 2.10 are introduced in Navier-Stokes equations 2.7 and 2.8 and then the averaging operator is applied to all the terms, the following set of equations is obtained:

$$\frac{\partial U_i}{\partial x_i} = 0\,, \tag{2.12}$$

$$\frac{\partial U_i}{\partial t} + \frac{\partial U_i U_j}{\partial x_j} = -\frac{1}{\rho}\frac{\partial P}{\partial x_i} + \frac{1}{\rho}\frac{\partial T_{ij}}{\partial x_j} - \frac{1}{\rho}\frac{\partial R_{ij}}{\partial x_j}\,, \tag{2.13}$$

where T_{ij} is the time-averaged tensor of viscous stresses, related to S_{ij} through the assumption of a Newtonian fluid:

$$T_{ij} = 2\mu\left[S_{ij} - \frac{1}{3}\delta_{ij}S_{kk}\right], \tag{2.14}$$

where S_{ij} represents the time-averaged rate of strain tensor reported below:

$$S_{ij} = \frac{1}{2}\left(\frac{\partial U_i}{\partial x_j} + \frac{\partial U_j}{\partial x_i}\right). \tag{2.15}$$

It should be noted that the averaging operator introduces additional unknowns collected in the terms:

$$R_{ij} = -\rho\overline{u_i' u_j'}. \tag{2.16}$$

These terms act as stresses on the fluid flow and are called Reynolds stresses. In order to close the problem, additional equations are needed

to model the Reynolds stresses. The most commonly used approach to deal with this problem is represented by the Boussinesq approximation, which is a first-order closure method and assumes that the Reynolds stresses are proportional to the local mean rate of strain:

$$R_{ij} = -2\mu_t \left(S_{ij} - \frac{1}{3}\delta_{ij} S_{kk} \right) + \frac{2}{3}\rho\delta_{ij} k \,, \tag{2.17}$$

where μ_t is the dynamic turbulent viscosity and k is the turbulent kinetic energy:

$$k = \frac{1}{2}\overline{u_i' u_i'}. \tag{2.18}$$

It should be noted that the turbulent viscosity μ_t is a property of the flow and not of the fluid, so it can vary significantly from point to point and between different fluid flows. The closure of the problem adopted by the SST k-ω model, also adopted in the present thesis in Chapter 7, is reported in the subsequent section.

2.3.1 *SST k-ω model*

The SST k-ω model is a blending between the standard k-ϵ [13] and the standard k-ω [13] model. Indeed, k-ϵ models are generally more accurate in shear type flows, while the standard k-ω model shows better performance in the near wall region [13, 38]. Following the formulation of the SST k-ω model, the specific dissipation rate ω is defined as:

$$\omega = \frac{\epsilon}{C_\mu k} \tag{2.19}$$

where C_μ is a model constant and ϵ is the turbulence dissipation rate:

$$\epsilon = \nu \overline{\frac{\partial u_i'}{\partial x_j} \frac{\partial u_i'}{\partial x_j}}. \tag{2.20}$$

Two transport equations for k and ω are then introduced to complete the mathematical formulation of the problem [39]:

$$\frac{\partial k}{\partial t} + U_i \frac{\partial k}{\partial x_i} = \frac{\partial}{\partial x_i}\left[(\nu + \sigma_k \nu_t) \frac{\partial k}{\partial x_i} \right] + P_k - C_\mu \omega k, \tag{2.21}$$

$$P_k = 2\nu_t S_{ij} S_{ij} - \frac{2}{3}\frac{\partial U_i}{\partial x_j}\delta_{ij} k, \tag{2.22}$$

$$\frac{\partial \omega}{\partial t} + U_i \frac{\partial \omega}{\partial x_i} = \frac{\partial}{\partial x_i}\left[(\nu + \sigma_\omega \nu_t)\frac{\partial \omega}{\partial x_i}\right] + \gamma \frac{\omega}{k} P_k - \beta \omega^2 + \tag{2.23}$$

$$+ (1 - F_1)\frac{2\sigma_\omega}{\omega}\frac{\partial k}{\partial x_i}\frac{\partial \omega}{\partial x_i}, \tag{2.24}$$

where P_k is the kinetic energy production term, while σ_k, σ_ω, γ, β and C_μ are model coefficients. F_1 is a blending function defined as:

$$F_1 = \tanh\left\{\min\left[\max\left(\frac{\sqrt{k}}{C_\mu \omega y}, \frac{500\nu}{y^2\omega}\right), \frac{4\rho\sigma_{\omega 2} k}{CD_{k\omega} y^2}\right]\right\}, \tag{2.25}$$

where y is the normal distance to the wall, $\sigma_{\omega 2}$ is a model coefficient and $CD_{k\omega}$ is:

$$CD_{k\omega} = \max\left(2\rho\sigma_{\omega 2}\frac{1}{\omega}\frac{\partial k}{\partial x_i}\frac{\partial \omega}{\partial x_i}, 10^{-20}\right). \tag{2.26}$$

The model coefficients σ_k, σ_ω, γ and β are computed with the general form:

$$\phi = F_1 \phi_1 + (1 - F_1)\phi_2, \tag{2.27}$$

where ϕ_1 corresponds to coefficients from the $k - \omega$ model and ϕ_2 corresponds to coefficients from the $k - \varepsilon$ model.
The turbulent kinematic viscosity ν_t is calculated from:

$$\nu_t = \frac{a_1 k}{\max\left(\max(a_1\omega, \Omega F_2)\right)}, \tag{2.28}$$

where a_1 is a model coefficient, Ω is the magnitude of the vorticity vector and

$$F_2 = \tanh\left\{\left[\max\left(\frac{2\sqrt[2]{k}}{C_\mu \omega}, \frac{500\nu}{y^2\omega}\right)\right]^2\right\}. \tag{2.29}$$

2.4 LARGE EDDY SIMULATION

Analogously to what was described before in the RANS framework, but applying a filtering operation with respect to space instead of performing a time-averaging operation, the unknowns in the Navier-Stokes equations 2.7 and 2.8 are separated in a resolved term and in a subgrid term:

$$u_i = \widetilde{u}_i + u_i', \tag{2.30}$$
$$p = \widetilde{p} + p', \tag{2.31}$$

where in this case the apexes indicate the subgrid terms and the symbol $\widetilde{(\cdot)}$ represents the spatial filtering operator:

$$\widetilde{(\cdot)}(x) = \int_{-\infty}^{\infty} G(x-\xi)(\cdot)d\xi, \tag{2.32}$$

where G is the filter function. If Eq. 2.30 and Eq. 2.31 are introduced in the Navier-Stokes equations 2.7 and 2.8 and when the spatial filtering operation is performed on all the terms, the following set of equations is obtained:

$$\frac{\partial \widetilde{u}_i}{\partial x_i} = 0\,, \tag{2.33}$$
$$\frac{\partial \widetilde{u}_i}{\partial t} + \frac{\partial \widetilde{u}_i \widetilde{u}_j}{\partial x_j} = -\frac{1}{\rho}\frac{\partial \widetilde{p}}{\partial x_i} + \frac{1}{\rho}\frac{\partial \widetilde{\tau}_{ij}}{\partial x_j} - \frac{1}{\rho}\frac{\partial \widetilde{\tau}_{ij}^{sgs}}{\partial x_j}\,, \tag{2.34}$$

where the symbol $\widetilde{(\cdot)}$ denotes the spatially filtered quantities, $\widetilde{\tau}_{ij}$ is the resolved viscous stress tensor and $\widetilde{\tau}_{ij}^{sgs}$ is the subgrid stress tensor, that needs to be modelled in order to close the problem. The resolved viscous stress tensor $\widetilde{\tau}_{ij}$ can be written as:

$$\widetilde{\tau}_{ij} = 2\mu\left[\widetilde{S}_{ij} - \frac{1}{3}\delta_{ij}\widetilde{S}_{kk}\right]\,, \tag{2.35}$$

where $\widetilde{S}_{ij}$ represents the resolved rate of strain tensor, whose expression is:

$$\widetilde{S}_{ij} = \frac{1}{2}\left(\frac{\partial \widetilde{u}_i}{\partial x_j} + \frac{\partial \widetilde{u}_j}{\partial x_i}\right). \tag{2.36}$$

Adopting the Boussinesq hypothesis, the subgrid stress tensor $\widetilde{\tau}_{ij}^{sgs}$ can be written as:

$$\widetilde{\tau}_{ij}^{sgs} = \rho(\widetilde{u_i' u_j'} - \widetilde{u'}_i\,\widetilde{u_j'}) = -2\rho\nu_t\left(\widetilde{S}_{ij} - \frac{1}{3}\delta_{ij}\widetilde{S}_{kk}\right) + \frac{2}{3}\rho\delta_{ij}k^{sgs} \tag{2.37}$$

where k^{sgs} is the subgrid kinetic energy:

$$k^{sgs} = \frac{1}{2}\left(\widetilde{u_i' u_i'} - \widetilde{u'}_i\,\widetilde{u'}_i\right), \tag{2.38}$$

and $\nu_t = \mu_t/\rho$ is the kinematic turbulent viscosity.

2.4.1 *Smagorinsky-Lilly subgrid-scale model*

The subgrid stress tensor $\widetilde{\tau}_{ij}^{sgs}$ and consequently the turbulent viscosity ν_t need to be modelled to complete the mathematical formulation of the problem. Depending on how the turbulent viscosity is computed, different subgrid-scale models have been proposed in the literature [40–43]. One of the first LES subgrid-scale models is the Smagorinsky-Lilly model [44]. Following its formulation, ν_t is expressed as:

$$\nu_t = (C_s \Delta)^2 \sqrt{2\widetilde{S}_{ij}\,\widetilde{S}_{ij}} \tag{2.39}$$

where C_s is the Smagorinsky constant, set equal to 0.12, while Δ is the local grid spacing [44].

Despite its wide adoption in Science and Engineering, in many cases the Smagorinsky-Lilly subgrid-scale model has shown to be too dissipative and to fail to accurately predict the laminar to turbulent transition [37, 45]. Different subgrid-scale models have been suggested to overcome this issue, among others, the Kinetic Energy Transport (KET) subgrid-scale model, used in the present thesis and described in the subsequent subsection.

2.4.2 *Kinetic Energy Transport subgrid-scale model*

The KET subgrid-scale model introduces, in addition to Eq. (2.33) and (2.34), a transport equation for the subgrid kinetic energy:

$$\frac{\partial}{\partial t}(\rho k^{sgs}) + \frac{\partial}{\partial x_i}(\rho k^{sgs}\widetilde{u}_i) = \frac{\partial}{\partial x_i}\left(\rho \nu_t \frac{\partial k^{sgs}}{\partial x_i}\right) - \widetilde{\tau}_{ij}^{sgs}\frac{\partial \widetilde{u}_j}{\partial x_i} - \rho c_\epsilon \frac{(k^{sgs})^{\frac{3}{2}}}{\Delta}. \tag{2.40}$$

Then the turbulent viscosity ν_t is calculated as:

$$\nu_t = c_\nu \sqrt{k^{sgs}}\Delta, \tag{2.41}$$

where c_ϵ and c_ν are model constants set equal respectively to 1.05 and 0.094. Due to the fact that the subgrid kinetic energy is computed according to a transport equation, the turbulent viscosity evolves consequently and can be null in the regions where the flow is expected to be laminar. Thanks to this feature, the KET model showed to predict the laminar to turbulent transition more accurately than the Smagorinsky-Lilly model [45].

2.5 DISPERSION MODELLING

Pollutant dispersion in the urban environment is often treated as a problem of diffusion and advection of a passive scalar in the turbulent velocity field. According to such assumption, the transport equation for the pollutant concentration c can be expressed as:

$$\frac{\partial c}{\partial t} + \frac{\partial c u_j}{\partial x_j} = \frac{\partial}{\partial x_j}\left(D\frac{\partial c}{\partial x_j}\right), \tag{2.42}$$

where D is the molecular diffusivity of the passive scalar in the fluid. Depending on the adopted turbulence modelling approach, Eq. 2.42 takes different forms. In particular, Section 2.5.1 describes the equation for the pollutant dispersion when the RANS approach is adopted, while Section 2.5.2 focuses on its form in the LES framework.

2.5.1 *Passive scalar transport equation in RANS*

If the averaging operator described in Section 2.3 is applied to Eq. 2.42, the following transport equation is obtained:

$$\frac{\partial C}{\partial t} + \frac{\partial C\, U_j}{\partial x_j} = \frac{\partial}{\partial x_j}\left(D\frac{\partial C}{\partial x_j}\right) - \frac{\partial}{\partial x_j} Q_j, \tag{2.43}$$

where Q_j is an additional unknown introduced with the time-averaging operation and represents the flux in the j direction of the passive scalar due to turbulent fluctuations not explicitly computed by the RANS approach. Depending on how Q_j is modelled, different turbulent scalar flux models have been proposed in the literature [46].]. One of the simplest ways to complete the mathematical formulation of the problem is by adopting the standard gradient-diffusion hypothesis (SGDH). The SGDH model is developed in analogy with molecular diffusion and assumes that the turbulent scalar flux is proportional to the gradient of the time-averaged pollutant concentration:

$$Q_j = -D_t \frac{\partial C}{\partial x_j}, \tag{2.44}$$

$$D_t = \frac{\nu_t}{Sc_t}, \tag{2.45}$$

where D_t is the time-averaged turbulent diffusivity, ν_t is the (kinematic) turbulent viscosity introduced by the RANS approach and Sc_t is a non-dimensional parameter defined as the turbulent Schmidt number [47].

2.5.2 *Passive scalar transport equation in LES*

Analogously to what is described for RANS in the previous section, but applying a filtering operation in space instead of applying a time-averaging operation, the following transport equation for the pollutant concentration can be obtained:

$$\frac{\partial \widetilde{c}}{\partial t} + \frac{\partial \widetilde{c}\,\widetilde{u}_j}{\partial x_j} = \frac{\partial}{\partial x_j}\left(D\frac{\partial \widetilde{c}}{\partial x_j}\right) - \frac{\partial}{\partial x_j}\widetilde{q}_j \,, \tag{2.46}$$

where $\widetilde{q}_j$ is the flux of the passive scalar due to the subgrid turbulent motion in the j direction. If the SGDH model is adopted, then $\widetilde{q}_j$ can be expressed as:

$$\widetilde{q}_j = -\widetilde{D}_t \frac{\partial \widetilde{c}}{\partial x_j} \,, \tag{2.47}$$

$$\widetilde{D}_t = \frac{\nu_t}{Sc_t}, \tag{2.48}$$

where $\widetilde{D}_t$ is the space-filtered turbulent diffusivity, ν_t is the turbulent viscosity introduced by the LES subgrid-scale model and Sc_t is the turbulent Schmidt number.

2.5.3 *Some remarks on the standard gradient diffusion hypothesis*

Due to its inherent simplicity, the SGDH model for the turbulent scalar flux is one of the most commonly used and easy to implement models. Nevertheless, it exhibits many limitations. First, the SGDH model assumes that the turbulent scalar flux vector is aligned with the gradient of the concentration field, which is not verified for many flows [46]. Furthermore, a universal value for the turbulent Schmidt number does not exist, since it is more a local property of the flow rather than of the fluid [25, 48]. Moreover, the SGDH model assumes that the turbulent viscosity is isotropic and does not link the turbulent scalar flux to the strain rate. This fact leads to a poor accuracy in predicting pollutant dispersion in complex flows [49].

Despite the limitations of the SGDH model, in many flows of interest for Civil Engineering applications the dominant transport mechanism is convection, therefore in the framework of LES where large eddies are directly resolved, the effects of the turbulent Schmidt number are limited when the grid resolution is high [25], since $\widetilde{q}_j \to 0$ when the local grid spacing $\Delta \to 0$. The same observation does not hold in the

framework of RANS turbulence models, where the turbulent fluctuations are not resolved but modelled (i.e. approximated). As a consequence, RANS results are significantly affected by the adopted turbulent Schmidt number and a calibration of this parameter is needed.

Part I

LES APPLICATIONS TO BLUFF BODY AERODYNAMICS

The accurate reproduction of turbulent flows around bluff bodies represents a very demanding task for a numerical model even when simple geometries are considered. Indeed, the flow dynamics around bluff bodies is characterised by complex phenomena, as intermittent flow detachments and reattachments, vortex shedding and shear layer instabilities. This part aims at assessing the accuracy and reliability of Large Eddy Simulations when a simple rectangular cylinder with sharp edges and smooth surfaces is considered. Despite its simplicity, this shape is considered to be representative of the aerodynamic characteristics of a wide range of bluff bodies and it is the object of an international benchmark that collects a large amount of both numerical and experimental data. First, the effects of different subgrid-scale models are analysed as well as the effects of small levels of inflow turbulence. Then, higher level of turbulence intensities and length scales are investigated in order to assess LES capabilities in predicting the flow properties in radically different conditions. Furthermore, the interaction between the inflow turbulent length scale and the domain spanwise dimensions is analysed.

3

EFFECTS OF LOW INCOMING TURBULENCE ON THE FLOW AROUND A 5:1 RECTANGULAR CYLINDER AT NON-NULL ATTACK ANGLE

This chapter has been published as:

Ricci, M., Patruno, L., de Miranda, S., Ubertini, F., *Effects of low incoming turbulence on the flow around a 5:1 rectangular cylinder at non-null attack angle*, Mathematical Problems in Engineering, 2016.
http://dx.doi.org/10.1155/2016/2302340

The incompressible high Reynolds number flow around the rectangular cylinder with aspect ratio 5:1 has been extensively studied in the recent literature and became a standard benchmark in the field of bluff bodies aerodynamics. The majority of the proposed contributions focus on the simulation of the flow when a smooth inlet condition is adopted. Nevertheless, even when nominally smooth conditions are reproduced in wind tunnel tests, a low turbulence intensity is present together with environmental disturbances and model imperfections. Additionally, many turbulence models are known to be excessively dissipative in laminar to turbulent transition zones, generally leading to overestimation of the reattachment length. In this paper, Large Eddy Simulations are performed on a 5:1 rectangular cylinder at non-null attack angle aiming at studying the sensitivity of such flow to a low level of incoming disturbances. To this purpose, the performances of a standard Smagorinsky-Lilly and a Kinetic Energy Transport turbulence models are considered with perfectly smooth and low turbulence inlet conditions. Results are compared with experimental data in terms of both flow bulk parameters and statistics of the pressure distributions and show that, when the incoming flow turbulence is considered, both the models are quite accurate. In particular, predictions obtained by means of the standard Smagorinsky-Lilly model are found to be significantly affected by even low levels of incoming turbulence intensity, while the Kinetic Energy Transport model shows to be less sensitive to small incoming disturbances.

3.1 INTRODUCTION

Thanks to the increase in the computer power, the research in the field of Wind Engineering is more and more making use of Computational Fluid Dynamics techniques in order to assess the effects of wind loading on structures.

In fact, a number of flows usually encountered around structures relevant to Civil Engineering applications, like bridge decks and buildings, are characterized by multiple detachments and reattachments which render their prediction by means of CFD an extremely challenging task.

Due to their special geometric simplicity, prismatic shapes have been deeply investigated in the literature and have been often adopted as a prototype of fully detached and reattached flows. A number of experimental studies identified the main mechanisms involved in the definition of the flow field around such simple, nominally two-dimensional, shapes and highlighted the fundamental role played by the stability conditions of the shear layers detached from the leading edges, especially for shapes whose aspect ratio is higher than three, which approximately correspond to the threshold separating fully detached and reattached flows [50–53]. In particular, Nakamura et al. focused on the effects of incoming turbulence, showing that the reattachment point migrates upstream with increasing turbulence levels [50]. Subsequently, it was clarified that Kelvin-Helmholtz instabilities appear in the detached shear layers due to incoming disturbances, destabilizing them and, thus, causing the reattachment point upstream migration. This result was also highlighted by Hillier et al. [54] and Kiya et al. [55], which investigated the effects of free-stream turbulence on the topology of separation bubbles. Their experiments showed that the incoming flow turbulence deeply influences pressure distributions in terms of both mean and standard deviation. Due to these considerations, it appears that the incoming flow turbulence should be accurately taken into account when dealing with wind loading problems, for both experimental and numerical investigations.

For what it concerns numerical studies, several research works have been proposed aiming at reproducing the flow field around bluff bodies. Among them, Yu et al. performed Large Eddies Simulations (LES) around rectangular cylinders with varying aspect ratio at null-attack angle in a two and three-dimensional framework [56]. Sohankar et al. [57] proposed simulations of rectangular cylinders at non-null attack angle focusing on very low Reynolds numbers, for which the flow is expected to be mainly laminar. Such simulations showed good re-

sults in terms of bulk parameters and highlighted that, when using the standard deviation of the lift coefficient as an indicator, the simulation shows to be very sensitive to the adopted numerical setups. Shimada proposed a detailed validation of a two-layers $k-\varepsilon$ model with a modification on the turbulent kinetic energy production term by analysing the flow field around a wide selection of rectangular cylinders at null-attack angle [58] while Noda et al. proposed LES including the effect of incoming turbulence (a turbulence intensity equal to 5% was considered) showing that the standard Smagosinsky model is suitable for reproducing the effects induced by incoming turbulence for engineering purposes [53]. Moreover, a wide number of experimental and computational studies have been also proposed in order to study the aeroelastic behaviour of such bodies in smooth [59] and turbulent conditions [60]. In particular, Daniels et al. [61] performed LES on an elastically mounted rectangular cylinder in smooth and turbulent inflow conditions, showing that increasing the turbulence intensity can diminish significantly the amplitude of oscillations.

Summarising, it appears that, while all computational models are able to approximately reproduce some characteristics of the flow field, their accuracy strongly depends on the adopted numerical setups, and on the quantities taken into consideration. Indeed, if on one hand the mean flow characteristics are generally reproduced by numerical simulations in a satisfactory way, on the other hand the standard deviation of velocity and pressure fields are often predicted with much less accuracy [62]. It also emerged that, due to the large number of parameters which might affect the flow topology, a detailed mapping of the prisms aerodynamic behaviour has not been yet achieved.

Recently, the BARC project focused on the simulation of the turbulent flow around a 5:1 rectangular cylinder and became a standard benchmark for comparison between experimental data and numerical simulations [63]. The overview of the first four years of activity of the BARC project [64] highlighted that even experimental results extracted by various research groups show a remarkable variability whose causes are currently not completely clear. When numerical simulations are considered, Bruno et al. [64] observed that results are even more dispersed showing great sensitivity to the adopted numerical schemes, turbulence model and mesh size while their relative importance is difficult to be evaluated at the current stage. In this context, uncertainty studies can play a fundamental role. In particular, Witteveen et al. [65] showed that the flow field around the 5:1 rectangular cylinder is very sensible to set-up parameters as small variations of the angle of

attack, the incoming turbulence intensity and the incoming turbulence length scales.

It is also noticed that, while disturbances are always present in experimental conditions, when numerical simulations are performed, a fictitious environment is produced where imperfections are introduced only by the differential problem discretization and by the numerical solution itself. Beside the absence of incoming disturbances, many turbulence models are known to be excessively dissipative in laminar to turbulent transition zones [66]. Thus, numerical simulations can be considered as a limit case, expected to produce excessively stable shear layers and, thus, generally overestimating the reattachment length.

In this paper, the performances of the standard Smagorinsky-Lilly [40, 41] model and the Kinetik Energy Transport [67] model are tested when the incoming flow is characterized by a very low turbulence intensity. To this purpose, the flow around a fixed 5:1 rectangular cylinder is considered at 4° attack angle. In fact, the mismatch between experimental and numerical results has been found to increase with the attack angle when perfectly smooth inlet conditions are adopted together with a standard SM turbulence model [68].

The paper is organized as follows. In Section 7.3 the experimental setup adopted in the wind tunnel tests is briefly described, while in Section 4.4 the numerical features of the computational model are discussed. Numerical results obtained from simulations are presented in Section 5.3 and compared with the experimental data. Finally, in Section 7.7 some conclusions are drawn.

3.2 EXPERIMENTAL SETUP

In this section, the setup used to extract the experimental results used for comparison with numerical simulations is described. The experimental study was performed in the open-circuit boundary layer wind tunnel of CRIACIV laboratory, located in Prato, Italy [69].

An aluminium model characterized by width, B, equal to 300 mm, depth, D, equal to 60 mm and length, L, equal to 2380 mm was employed in the experimental tests and equipped with 62 pressure taps monitored by two 32-channels PSI miniaturized piezoelectric scanners at a sampling rate of 500 Hz [70]. The wind tunnel test section is 2.42 m large and 1.60 m high, so that the resulting blockage ratio was 3.75%. The Reynolds number based on D was varied from 2.2×10^4 to 1.12×10^5, while incoming turbulence intensity was varied from 0.7% to 13.6%.

In the present study, the experimental configuration with nose-up angle equal to 4° at Reynolds number based on D equal to 5.5×10^4 has been used as a reference for the numerical simulations.

3.3 COMPUTATIONAL MODEL

In this section, the characteristics of the computational model are reported and compared with other studies, together with the description of the adopted boundary conditions and numerical setups.

According to the aim of this study, the lowest turbulence intensity recorded in the available wind tunnel tests, representing the experimental approximation of the smooth flow condition, is adopted, so that the incoming turbulence intensity is set equal to 0.7%. The inflow turbulent field is synthetically generated by using the Modified Discretizing and Synthesizing Random Flow Generator method proposed by Castro et al. [29, 71], which guarantees the divergence-free condition and is able to satisfy prescribed turbulence spectrum and spatial correlations. It is worth noting that, if the fluctuation field is introduced at the inlet boundary, large pressure fluctuations are generated due to the violation of the Navier-Stokes equations. In order to avoid this phenomenon, fluctuations are introduced in the computational domain by modifying the velocity-pressure coupling algorithm following the procedure reported by Kim at al. [28].

The computational domain size and the grid resolution have been defined according to the guidelines provided by Bruno et al. [64] and the BARC main setup [63]. As showed in Fig. 7.4, the domain dimensions are such that $D_x = 40B$ and $D_y = 30B$, while $D_z = 2.0B$. The resultant blockage ratio is 0.67%, therefore blockage ratio effects can be neglected. In order to avoid boundary effects on the solution, the distance of the front face from the inlet is set equal to $\Lambda_x = 16B$.

As shown in Fig. 4.2 (a), a structured mesh is adopted in the boundary layer close to the wall, with along wind dimension $\delta_x/B = 2.5 \times 10^{-3}$ and cross wind dimension $\delta_y/B = 1.5 \times 10^{-3}$. The maximum y^+ recorded during all simulations is found to be equal to 6.61, while the mean one equals 2.02. Outside the boundary layer, the mesh is unstructured quad dominated and its size is slowly coarsened up to approximately $\delta_x/B = \delta_y/B = 1.8 \times 10^{-2}$ in the wake (see Fig. 4.2 (b)), where the cells aspect ratio is approximately one. In order to limit the numerical dissipation and to propagate the fluctuation field minimizing the energy loss, the mesh sizing in front of the rectangular cylinder has dimensions $\delta_x/B = \delta_y/B = 5 \times 10^{-2}$ and is maintained almost constant and structured until the inlet boundary is reached.

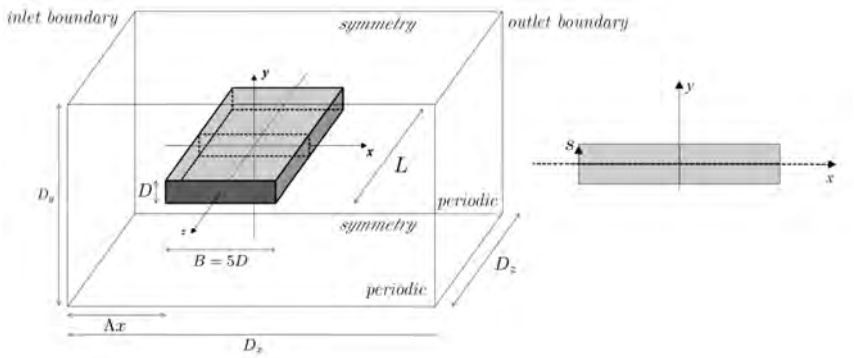

Figure 3.1: Model and computational domain geometries [63].

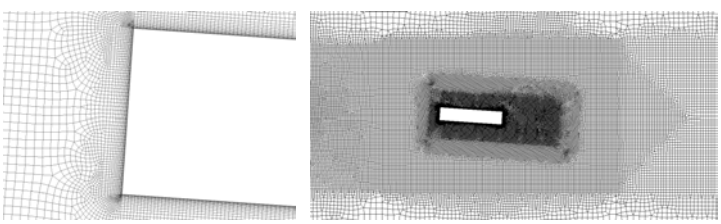

(a) (b)

Figure 3.2: Mesh adopted for the LES simulation: detail of the mesh close to the solid boundary (a) and mesh in proximity of the body and wake (b).

In the z direction, the cell dimension is $\delta_z/B = 0.02$. The final resultant mesh counts about 16.0M finite volumes. A comparison between the domain size and the mesh resolution adopted in the present study and similar ones is reported in Tab. 4.2 and Tab. 4.3.

Source	D_x/B	D_y/B	D_z/B	Λ_x/B
Present simulation	40	30	2	16
Bruno et al. [10, 72]	41	30.2	1, 2, 4	15
Grozescu et al. [73]	41	30.2	1	15
Mannini [74]	200	200	1, 2	100

Table 3.1: Parameters of the computational domain as reported by Bruno et al. [64].

With respect to turbulence modeling, two sub-grid scales models have been considered, namely the standard Smagorisnky-Lilly (SM) model and the Kinetic Energy Transport (KET) model. The fluid flow governing equations are reported in Eq. (3.1) :

Source	n_w/B	δ_x/B	δ_z/B
Present simulation	5.0×10^{-4}	2.5×10^{-3}	0.02
Bruno et al. [10, 72]	5.0×10^{-4}	2.0×10^{-3}	$0.042 - 0.01$
Grozescu et al. [73]	$5 \times 10^{-4}, 2.5 \times 10^{-4}$	$1.0 \times 10^{-2}, 5 \times 10^{-3}$	0.042, 0.01
Mannini [74]	5.0×10^{-5}	1.4×10^{-2}	0.0156

Table 3.2: Grid resolution in the boundary layer: comparison with meshes adopted by other authors as reported by Bruno et al. [64].

$$\begin{cases} \frac{\partial \overline{u_i}}{\partial x_i} = 0 \,, \\ \frac{\partial \rho \overline{u_i}}{\partial t} + \frac{\partial \rho \overline{u_i}\ \overline{u_j}}{\partial x_j} = -\frac{\partial \overline{p}}{\partial x_i} + \frac{\partial \overline{\tau_{ij}}}{\partial x_j} - \frac{\partial \overline{\tau_{ij}^{sgs}}}{\partial x_j} \,, \end{cases} \tag{3.1}$$

where the overbar denotes the spatially filtered quantities and u_i represents the velocity in the $i-th$ direction, while p is the pressure, $\overline{\tau_{ij}}$ is the resolved viscous stress tensor and $\overline{\tau_{ij}^{sgs}}$ is the sub-grid stress tensor. The resolved viscous stress tensor $\overline{\tau_{ij}}$ can be written as:

$$\overline{\tau_{ij}} = 2\mu \left[\overline{S_{ij}} - \frac{1}{3}\delta_{ij}\overline{S_{kk}} \right] \,, \tag{3.2}$$

where $\overline{S_{ij}}$ represents the resolved strain rate tensor, whose expression is below reported:

$$\overline{S_{ij}} = \frac{1}{2}\left(\frac{\partial \overline{u_i}}{\partial x_j} + \frac{\partial \overline{u_j}}{\partial x_i} \right). \tag{3.3}$$

Assuming the Boussinesq's hypothesis, the sub-grid stress tensor $\overline{\tau_{ij}^{sgs}}$ can be written as:

$$\overline{\tau_{ij}^{sgs}} = \rho(\overline{u_i u_j} - \overline{u_i}\ \overline{u_j}) = -2\rho\nu_t \left(\overline{S_{ij}} - \frac{1}{3}\delta_{ij}\overline{S_{kk}} \right) + \frac{2}{3}\rho\delta_{ij}k^{sgs} \tag{3.4}$$

where k^{sgs} is the sub-grid kinetic energy:

$$k^{sgs} = \frac{1}{2}\left(\overline{u_i u_i} - \overline{u_i}\ \overline{u_i}\right), \tag{3.5}$$

and ν_t is the turbulent eddy viscosity. When the SM model is adopted, ν_t is expressed as:

$$\nu_t = (C_s\Delta)^2\sqrt{2\overline{S_{ij}}\ \overline{S_{ij}}} \tag{3.6}$$

where C_s is the Smagorinsky constant, set equal to 0.12, while Δ is the local grid spacing. Conversely, if the KET model is adopted, the transport equation for the sub-grid kinetic energy is considered in addition to equations reported in Eq. (3.1):

$$\frac{\partial}{\partial t}\left(\rho k^{sgs}\right)+\frac{\partial}{\partial x_i}\left(\rho k^{sgs}\overline{u_i}\right)=\frac{\partial}{\partial x_i}\left(\rho\nu_t\frac{\partial k^{sgs}}{\partial x_i}\right)-\overline{\tau_{ij}^{sgs}}\frac{\partial\overline{u_j}}{\partial x_i}-\rho c_\epsilon\frac{(k^{sgs})^{\frac{3}{2}}}{\Delta} \tag{3.7}$$

and the turbulent eddy viscosity ν_t is calculated as:

$$\nu_t = c_\nu\sqrt{k^{sgs}}\Delta, \tag{3.8}$$

where c_ϵ and c_ν are model constants set equal respectively to 1.05 and 0.094.

With respect to the numerical scheme, a centered second-order accurate scheme is adopted to discretize the spatial derivatives, exception made for the non-linear convective term. For this therm, the Linear Upwind Stabilized Transport scheme is used, which was proved to be particularly successful for LES in complex geometries [75].

Time integration is performed by using the two-step second order Backward Differentiation Formulae, in accordance with Bruno et al. [11]. The solution at each time step is obtained by means of the well known Pressure Implicit with Splitting of Operator algorithm. The adopted non-dimensional time step (based on D) is $\Delta t^* = 5.0\times10^{-3}$, leading to a maximum Courant number in all the simulations equal to 3.9.

Symmetry boundary conditions are imposed at the top and bottom surfaces, while periodic conditions are adopted on the faces normal to the span wise direction (see Fig. 7.4). At the outlet boundary, zero pressure is imposed, while at the inlet, the null normal gradient of pressure is prescribed.

The generated fluctuation field is introduced to the computational domain in a plane shifted with respect to the inlet boundary of approximately $5.0\times10^{-1}B$, while the mean velocity is prescribed at the inlet. The power spectral density of the velocity components along x, y and z directions, indicated respectively as u, v and w, are reported in Fig. 7.9 for two different points located near the inlet boundary at $(-15B, 0, 0)$ and just upstream the rectangular cylinder at $(-1.5B, 0, 0)$. As it can be seen, the high frequency content of the spectra appears to be slightly damped proceeding from the inlet towards the rectangular cylinder. With respect to the along-wind turbulent length scale L_u, it is found to be equal to B for both the aforementioned locations.

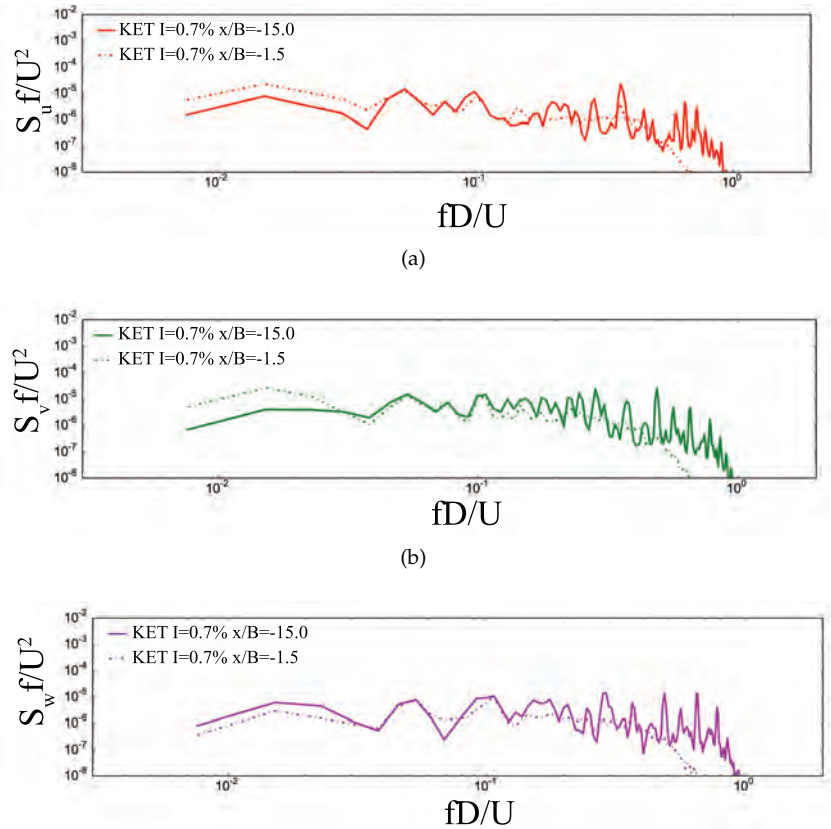

Figure 3.3: Spectra of the velocity time series obtained from the KET simulation with incoming flow turbulence at different locations.

The prism has been equipped with 2500 pressure monitors and data are acquired at each time step, leading to 200 samples for one non-dimensional time unit. All simulations have been run by using the open source Finite Volume software OpenFOAM on 160 CPUs at CINECA on the Galileo cluster (516 nodes, 2-eight cores Intel Haswell 2.40 GHz processors with 128 GB RAM per node).

3.4 NUMERICAL RESULTS

In this section, numerical results obtained for each turbulence model with smooth and turbulent inflow condition are reported and systematically compared with experimental data. In particular, the flow bulk

parameters obtained from each simulation together with a discussion of the resulting flow topology are reported in Section 4.5.2. The pressure coefficient statistics on the central section are showed in Section 4.5.3, while Section 3.4.3 focuses on the spanwise-averaged pressure distributions. Then, in Section 4.5.4, correlations in the span wise direction are discussed.

Numerical results have been obtained by considering a simulation time of $t^* = 1000$, being t^* the non-dimensional time unit. The post-processing of data has been carried out considering only the last 700 non-dimensional time units in order to avoid flow initialization effects [10].

In order to check the convergence of the recorded statistics, the time-history of the lift coefficient has been subdivided in ten segments and first and second order statistics extracted by incrementally extending the part of the signal considered in the post-processing. Despite the relatively long simulation time (longer than the minimum requirements [10]), in the worst case, a plateau has been reached for second-order statistics only when 90% of the total time-history has been used.

3.4.1 *Flow topology and bulk parameters*

In order to have a qualitative view of the turbulent structures obtained from the numerical analyses, the flow topology in terms of isosurfaces of the invariant λ_2 [76] coloured with pressure is reported in Fig. 5.9 for the two investigated turbulence models, in smooth and turbulent inflow conditions. The instantaneous iso-surfaces are plotted to correspond with maximum lift. As it can be seen, when the inflow turbulence is considered, the topology showed by the SM model appears to be quite in accordance with that obtained by means of the KET model. Furthermore, both of them comply well with the topology showed by the KET model in smooth inflow conditions, while in this case the topology obtained by using the SM model shows a narrower wake.

The different behavior of the two turbulence models is also reflected in Tab. 4.4, that shows that the reattachment point at the bottom surface moves from $x_r = 1.16$ to $x_r = 0.01$ when turbulence is introduced and the SM model considered, while no significant differences between turbulent and smooth inlet are observed if the KET model is analyzed.

The effect of incoming turbulence can be also appreciated by observing the streamlines of the time averaged flow fields reported in Fig. 4.9. In particular, the SM model appears to be significantly affected by the presence of incoming turbulence while the KET models appears to be rather stable. It is also noticed that all considered models, apart from

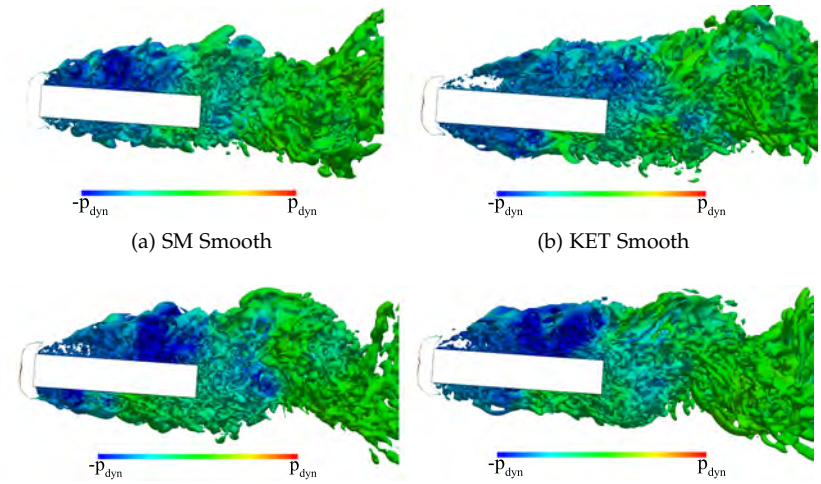

(a) SM Smooth (b) KET Smooth

(c) SM I=0.7% (d) KET I=0.7%

Figure 3.4: Isosurfaces of λ_2 coloured with pressure for the two analysed turbulence models.

the SM in smooth flow, predict the creation of a small elongated vortex at the leading edge, in correspondence to the top side, whose core is located at approximately $x_c = -1.5$.

The statistics of the flow bulk parameters are reported in Tab. 6.1 (results are made non-dimensional with respect to D) and referred to the global reference system. In particular, C_D and C_L are the drag and the lift coefficients, respectively, while their root mean square values are indicated as C'_D and C'_L, respectively. Again, the results obtained by the two turbulence models are in good agreement when a low level of incoming turbulence is considered while remarkable differences are observed in perfectly smooth flow. Furthermore, it should be noticed that the C_D and C_L, together with the Strouhal number St, obtained by taking into account the incoming turbulence agree quite well with experimental measurements. In order to provide a clearer picture of the obtained results, in the following, pressure field statistics distributions are analysed.

3.4.2 *Central section statistics*

In this section, the pressure coefficient statistics on the prism central section are analysed. Data are presented by adopting the curvilinear abscissa s as reported in Fig. 7.4. The upwind face of the prism is

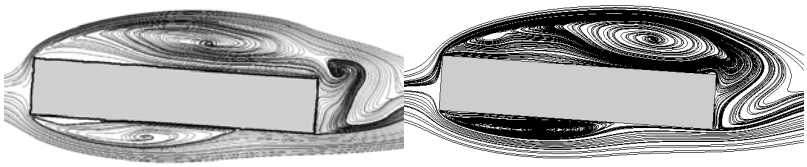

(a) SM Smooth (b) KET Smooth

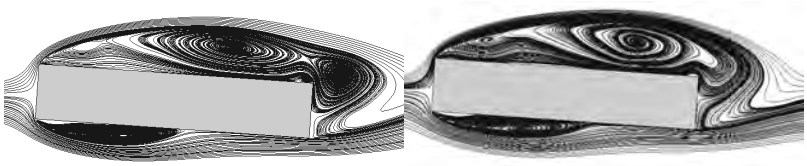

(c) SM I=0.7% (d) KET I=0.7%

Figure 3.5: Time-averaged streamlines for the two analysed turbulence models.

Source	x_r Down	x_c Up	x_c Down	y_c Up	y_c Down
SM (smooth)	1.16	0.54	-0.49	0.96	-0.78
SM I=0.7%	0.01	0.91	-0.81	0.91	-0.63
KET (smooth)	0.05	1.09	-0.65	1.01	-0.54
KET I=0.7%	0.04	1.10	-0.63	1.00	-0.51

Table 3.3: Reattachment point and main vortex core position.

Source	C_D	C'_D	C_L	C'_L	St
SM (smooth)	1.26	0.056	1.44	0.57	0.116
SM I=0.7%	1.28	0.064	1.56	0.61	0.115
KET (smooth)	1.37	0.079	2.27	0.76	0.117
KET I=0.7%	1.3	0.080	2.26	0.81	0.115
Mannini et al. [69] (Exp.)	1.63	-	2.02	-	0.126
Schewe2013 (Exp.)	1.38	-	2.52	-	0.115

Table 3.4: Statistics of the flow bulk parameters.

identified by $0.0 \leqslant s/D \leqslant 0.5$, the along-wind surfaces by $0.5 \leqslant s/D \leqslant 5.0$ while the downwind face by $5.5 \leqslant s/D \leqslant 6.0$.

Figure 3.6 shows the distribution of the pressure statistics obtained by means of the present simulations and comparison with experimental results. As it can be noticed, if the top surface is considered, the time-averaged pressure coefficient, $\overline{C}_p$, distribution predicted by the KET model is almost in perfect accordance with the experimental data for both smooth and turbulent inflow conditions. Contrarily, the SM

model approaches experimental results only when turbulent inlet conditions are adopted. Observing C_p' on the same surface, the KET model always complies with experimental measurements with good accuracy being the peak position and the experimental trend also well reproduced. Generally, the SM model appears to be unable to correctly reproduce the shape of the pressure recovery not catching the change of steepness that occurs at about $s/D = 3$, in correspondence to the separation between the vortex shedding and the vortex coalescing zones as individuated in [10].

When the $\overline{C}_p$ distribution on the bottom surface is analyzed, the SM model appears to be very sensitive to small turbulence intensities in the incoming flow. In fact, the distribution obtained in smooth flow conditions clearly changes when the inflow turbulence is considered: the reattachment point migrates upstream and the distribution shifts, approaching the experimental data. The KET model instead, shows again a lower sensitivity to the incoming turbulence, being results obtained in both configurations approximately the same. The SM model is very accurate when turbulence is taken into account and shows better performances if compared with the KET model, that slightly overestimates the reattachment length and underestimates suctions at the leeward edge. The improvement of the SM model with turbulent inlet observed for mean values can be noticed also by considering the C_p' distribution on the bottom surface. In this case the model correctly predicts the peak position and the trend observed experimentally, even if the peak value is clearly overestimated. The KET model correctly predicts the peak position and the trend in particular at the trailing edge, where an increment in rms is experimentally observed.

The improvement of performance showed by the SM model when the incoming turbulence is taken into account can be due to the fact that the SM model is too dissipative in laminar and transitional regions [66]. Indeed, the SM model predicts a nonvanishing eddy viscosity when the flow is laminar and this results in more stable shear layers when the incoming flow is smooth. Conversely, the KET model is able to adjust the eddy viscosity based on the subgrid kinetic energy, leading to an overall less dissipative behavior. When the incoming flow turbulence is considered, the SM model performs better. In fact, the laminar to turbulent transition is driven by disturbances introduced by the explicitly simulated incoming flow turbulence. This different behaviour in perfectly smooth and low turbulence inflow conditions is not observed when the KET model is considered. Indeed, the less dissipative behavior of the KET model with respect to the SM model

allows to correctly predict the destabilization of the shear layers even without triggering it explicitly by introducing disturbances.

Top Surface

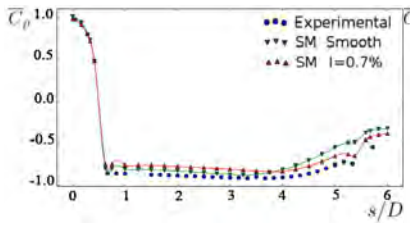

(a) SM

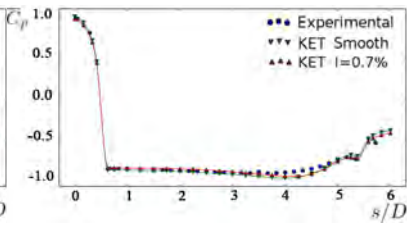

(b) KET

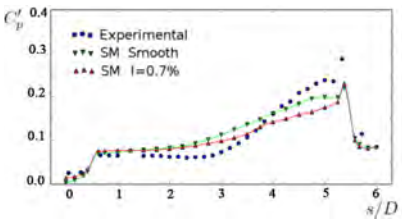

(c) SM

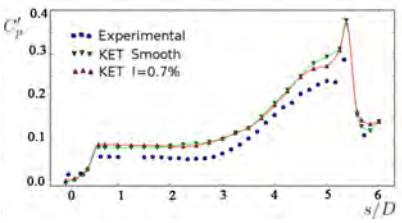

(d) KET

Bottom Surface

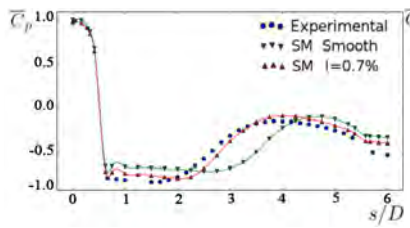

(e) SM

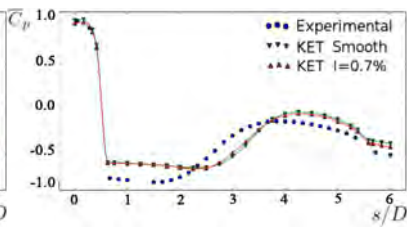

(f) KET

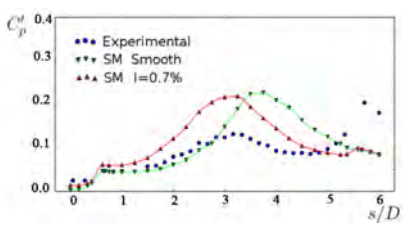

(g) SM

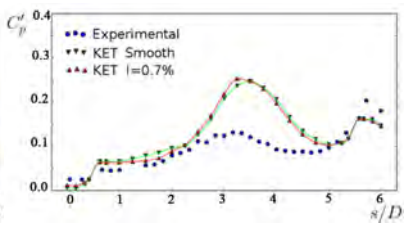

(h) KET

Figure 3.6: Distribution of C_p statistics on the central alignment.

3.4.3 *Spanwise averaged quantities*

The $z-avg$ distributions of C'_p, denoted as $C_p(z-avg)'$, are reported in Fig. 3.7 for each case. Data concerning the central section statistics (see Fig. 3.6) are repeated in this figure in order to better highlight differences with respect to the corresponding $z-avg$ values. Focusing on the top surface, the SM model shows that the gap between C'_p and $C_p(z-avg)'$ increases proceeding from the leading edge to the trailing one, where the peak value of $C_p(z-avg)'$ is radically decreased with respect to the central alignment for both smooth and turbulent inlet condition. The flow two-dimensionality is dominant close the leading edge, where $z-avg$ statistics are identical to the central section one, while the flow three-dimensional mechanisms prevail downwind. This trend is confirmed by the KET model, even if in this case the gap between C'_p and $C_p(z-avg)'$ is reduced if compared with the SM model, suggesting that the predicted flow is more correlated in the span wise direction.

Considering results of the SM model on the bottom surface, the reduction between $z-avg$ and central section statistics is higher when the inflow turbulence is considered. In fact, while for the smooth inlet condition the $z-avg$ peak value is roughly 66% of the central section one, when turbulence is taken into account, the peak of $C_p(z-avg)'$ is only the 44% of the corresponding C'_p value. Therefore, the SM model shows that the inflow turbulence contributes to decrease the flow correlation in the span wise direction to a great extent, much further the direct uncorrelating effects of incoming turbulence.

In agreement with previously reported results, the KET model does not show such an high sensitivity, being differences between $C_p(z-avg)'$ and C'_p in smooth and turbulent condition almost identical. Qualitatively, by observing the rms distributions in terms of both peak amplitude and position, results obtained by using the KET model appear to be intermediate between the ones obtained in smooth and turbulent flow by using the SM model.

3.4.4 *Correlations*

This section reports the C_p correlations along the span wise direction for three different sections, located at $s/D = 1.75,\ 3.00$ and 4.25. Data acquired on probes close to the edges in the span wise direction can be affected by the prescribed boundary conditions, therefore results are presented disregarding a part of the rectangular cylinder near to the boundary, being z/D ranging from -2.5 to 2.5. Fig. 3.8 shows the

Top surface

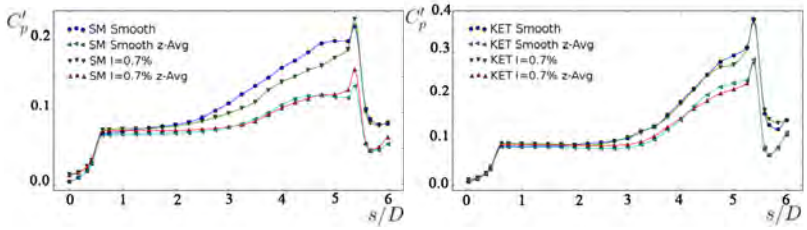

(a) SM (b) KET

Bottom surface

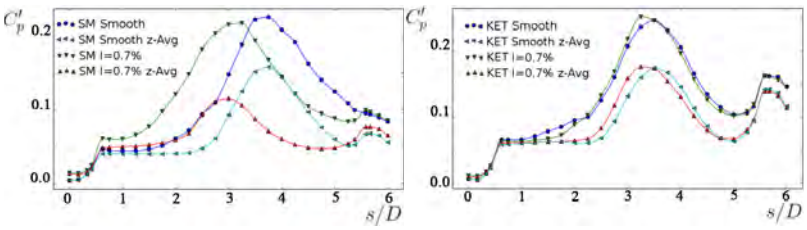

(c) SM (d) KET

Figure 3.7: Comparison between z-averaged and central section statistics for the SM and KET turbulence models.

correlation of C_p, indicated as R_{C_p}, obtained for the SM model on top and bottom surfaces for smooth and turbulent inlet, while results obtained by using the KET model are reported in Fig. 3.9.

Interestingly, in this case the correlation appears to be higher when a small incoming turbulence level is considered. The authors conjecture that this behaviour might be related to the fact that, when perfectly smooth conditions are considered, the flow impinges on the trailing edge as it can be deduced from time-averaged streamlines reported in Fig. 4.9. Contrarily, when incoming turbulence is considered, a higher level of entrapment of the separation bubble is observed, probably leading to higher along-span correlations. Regarding the bottom surface and focusing on results obtained by means of the SM model, an opposite behavior is recorded. This fact might be due to the development of span wise vortical structures that decrease the flow correlation (see for example Sasaki and Kiya [77]).

Also in this case, results predicted by using the KET model are qualitatively intermediate between the ones obtained by using the SM

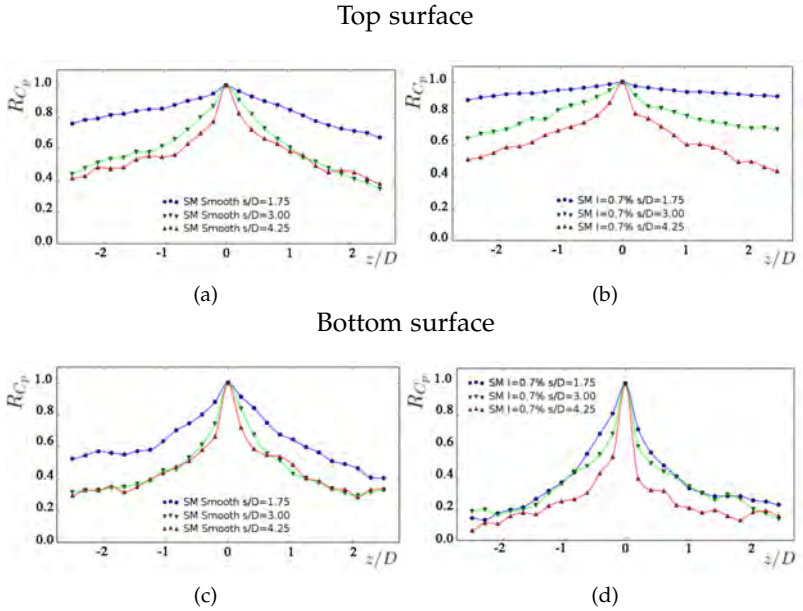

Figure 3.8: Correlation functions for the SM model in smooth and turbulent inflow condition.

model in smooth and turbulent conditions and a good stability with respect to the incoming turbulence level is observed.

3.5 CONCLUSIONS

In this paper, Large Eddy Simulations have been performed aiming at studying the unsteady flow field around a rectangular cylinder with aspect ratio 5:1 at 4° attack angle, when a small level of incoming turbulence is taken into account. Two different turbulence models have been considered, namely the classical Smagorinsky-Lilly model and the Kinetic Energy Transport model. Both of them have been studied by adopting perfectly smooth and turbulent inlet conditions, with turbulence intensity set equal to 0.7%. The inflow turbulence has been synthetically generated with the MDSRFG method and introduced in the computational domain by modifying the velocity-pressure coupling algorithm. Results in terms of flow bulk parameters, time-average and rms of the pressure coefficient distributions in correspondence of the prism central section have been compared to available experimental data. It appears that, when the Smagorinsky-Lilly model is adopted, the modeling of a realistic turbulent inflow is important in order to ob-

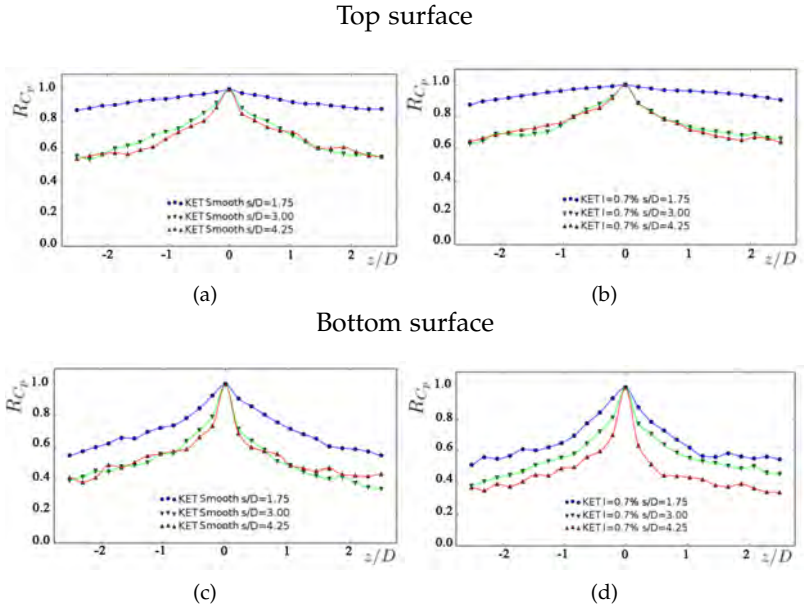

Figure 3.9: Correlation functions for the KET model in smooth and turbulent inflow condition.

tain accurate results, since, even small values of the incoming flow turbulence intensity, can deeply affect results. The Kinetic Energy Transport model proved to be less sensitive to the low inflow turbulence and provided results qualitatively intermediate between the Smagorinsky-Lilly model adopted with perfectly smooth and turbulent inflow conditions. The different behavior of the two considered models can be due to the fact that the Smagorinsky-Lilly model is not able to make the turbulent eddy viscosity null, showing to be too dissipative and failing in accurately predicting the laminar to turbulent transition. On the contrary, the Kinetic Energy Transport model can adjust the turbulent eddy viscosity depending on the subgrid kinetic energy, showing satisfactory results for both smooth and turbulent inlet conditions. Indeed, the less dissipative behavior of the Kinetic Energy Transport model with respect to the Smagorinsky-Lilly model allow the shear layer instabilities to develop even without directly triggering them with incoming disturbances. In all, when incoming turbulence is considered, a good agreement between numerical results and experimental data is observed, in particular in terms of time-average pressure distributions. Moreover, the differences between the flow fields obtained by the two considered models significantly reduce.

ACKNOWLEDGEMENTS

The authors are thankful to CRIACIV for providing the experimental results and CINECA for providing the HPC facilities need to accomplish the present research work. In particular, we would like to thank Ivan Spisso for his invaluable constant support.

4

FLOW FIELD AROUND A 5:1 RECTANGULAR CYLINDER USING LES: INFLUENCE OF INFLOW TURBULENCE CONDITIONS, SPANWISE DOMAIN SIZE AND THEIR INTERACTION

This chapter has been published as:

Ricci, M., Patruno, L., de Miranda, S., Ubertini, F., *Flow field around a 5:1 rectangular cylinder using LES: influence of inflow turbulence conditions, spanwise domain size and their interaction*, Computers and Fluids, 149:181-193, 2017.
https://doi.org/10.1016/j.compfluid.2017.03.010

The flow field around the rectangular cylinder with aspect ratio 5:1 has been widely investigated in recent literature as a prototype of reattached flow around elongated bluff bodies like bridge decks and high rise buildings. Due to the technical importance of such flows, many research works have been proposed aiming at studying the accuracy of available simulation techniques in reproducing the flow organization. When Large Eddy Simulations (LES) are considered, to the authors' knowledge, the proposed contributions focused on perfectly smooth inlet conditions which, indeed, represent more an exception than a rule in Computational Wind Engineering. In the present paper, LES are performed aiming at reproducing the modifications occurring in the flow when turbulent inflow conditions are adopted. In order to synthetically produce the unsteady inlet condition, a divergence-free and spatially correlated fluctuations field is generated by means of the Modified Discretizing and Synthesizing Random Flow Generator technique. The obtained synthetic fluctuations are imposed in the computational domain by modifying the velocity-pressure coupling algorithm in order to avoid nonphysical pressure fluctuations. Two configurations, corresponding to mild and strong incoming turbulence levels, are investigated highlighting the role played by the spanwise domain size. Results are compared to experimental data showing good agreement between experiments and numerical simulations.

4.1 INTRODUCTION

The prediction of the aerodynamic behavior of bluff bodies at high Reynolds numbers is of fundamental importance in the field of Wind Engineering and has been widely investigated in the literature. Recently, thanks to the increase in the computer power, Computational Fluid Dynamics is becoming an attractive tool, complementary to wind tunnel tests, for the study of the structure aerodynamic behavior in the early stage of the design process. Nevertheless, due to the complexity of the turbulent flows usually encountered around bluff bodies, the prediction of pressure distributions still represents a demanding engineering challenge.

Several numerical studies analysed the complex flow organization around bluff bodies in order to characterize both their aerodynamic and aeroelastic behavior [58–60, 64, 78–85] in some cases presenting also the sensitivity of these analyses to the body geometrical details [86] and to the inflow turbulence characteristics as the turbulence intensity and the turbulence length scale [61, 87]. Recently, the flow around the 5:1 rectangular cylinder received increasing attention and became a standard benchmark in the Computational Wind Engineering (CWE) community thanks to the BARC project [63]. In fact, despite its geometric simplicity, such rectangular cylinder represents a very interesting case from the aerodynamic point of view: the flow field is characterized by strong detachments at the leading edge which lead to the formation of shear layers, unsteady recirculation bubbles and vortex shedding. The reattachment point location, responsible for the global flow organization, is strongly related to the stability conditions of the shear layers detached from the leading edges, rendering the numerical simulation of such flow an extremely challenging task [62]. Without surprise, the first four years of activity of the BARC project highlighted a remarkable variability of the results obtained by different research groups, even for what concerns time-averaged flow fields at null attack angle [64]. Furthermore, the dispersion observed in the experimental data presented within the BARC project highlighted the sensitivity of the flow to the adopted experimental setup and, indeed, further stressed the remarkable difficulties that can be expected in the numerical simulation of such instability-driven phenomena.

As regards numerical simulations, a remarkable research work has been done in the framework of Reynolds-averaged Navier-Stokes (RANS) turbulence models. In particular, the sensitivity of results based on RANS models has been deeply investigated by Mariotti et al. [88], which performed uncertainty quantification analyses aiming at study-

ing the effects of the angle of attack, the incoming turbulence intensity and the incoming turbulence length scale. Among other results, it is shown that the inflow turbulence intensity not only affects the fluctuating pressure field on the prism surface, but, in accordance with experimental results, also its average distribution, in particular close to the leading edge. When Large Eddy Simulations (LES) turbulence models are considered, to the authors' knowledge, the analyses presented in the literature focused exclusively on perfectly smooth inlet conditions [64] which represent an extreme case of limited practical relevance for Computational Wind Engineering applications. From this perspective, assessing the capability of commonly adopted LES models in reproducing the flow modifications occurring in the presence of incoming turbulence for reattached flows represents a matter of utmost importance in the field of CWE [53]. On this regard, it must be noticed that the commonly adopted smooth inlet condition might contribute to the observed scatter in the numerical results. In fact, in the absence of incoming disturbances, the position of the reattachment point is controlled by the natural insurgence of Bloor-Gerrard vortices in the detached shear layers. On the contrary, the presence of incoming turbulence facilitates the destabilization of the shear layers whose behaviour, thus, is expected to become less dependent on the amount of viscosity introduced by the turbulence model. A study on the role played by low levels of incoming turbulence when LES is adopted in nominally smooth inlet conditions has been recently presented in [37].

In this paper, aiming at assessing the performance of LES in reproducing reattached flows when a turbulent inflow is adopted, the flow around a 5:1 fixed rectangular cylinder is studied at null attack angle. Two inlet conditions, characterized by varying turbulence intensity and length scales are considered and the corresponding modifications in the flow organization are analysed. The fluctuating velocity field imposed at the inlet is synthetically generated by using the Modified Discretizing and Synthesizing Random Flow Generator (MDSRFG) method which guarantees the divergence-free condition and satisfies prescribed spatial correlation and turbulence spectrum [71]. In order to avoid nonphysical pressure fluctuations at the inlet, the obtained fluctuating velocity field is imposed directly within the computational domain by modifying the PISO (Pressure-Implicit with Splitting of Operator) pressure-velocity coupling algorithm [28]. Additionally, due to the remarkable computational cost of such simulations, the role played by the spanwise domain size is also analysed highlighting that, when turbulent inflow conditions are adopted, its choice must be carefully considered. Results are compared to experimental data obtained at the

CRIACIV wind tunnel in terms of flow bulk parameters and pressure distributions [69, 70].

The paper is organized as follows. In Section 4.2, currently available turbulence generation methods are reviewed and the one adopted in the present work is briefly described. The experimental setup adopted in the wind tunnel tests used for comparison is described in Section 7.3, while Section 4.4 presents the main features of the adopted numerical model. Results obtained by means of numerical simulations are compared to experimental ones in Section 5.3. Finally, in Section 7.7 some conclusions are drawn.

4.2 TURBULENT INFLOW CONDITIONS

The generation of realistic unsteady inflow conditions is one of the main difficulties encountered in LES simulations of turbulent flows. In this section, a brief review of the most common methodologies adopted to tackle the problem is reported and the method chosen in the present paper is presented.

The generation of incoming turbulence can be performed by using two main approches [89]. The first one is based on the recycling/rescaling of recorded velocity and pressure fluctuations memorized in a database which can be obtained by means of either a precursor simulation or wind tunnel tests [90]. As the turbulent fluctuations are extracted from a simulated or a real flow, they fulfill the Navier-Stokes equations and are characterized by realistic spectra and integral scales. The drawback of such an approach is represented by the fact that a large amount of data needs to be stored, that the characteristics of the obtained turbulence might be difficult to be imposed *a priori* and that, if a precursor simulation is adopted, the computational effort might be remarkably increased.

The second approach is based on the synthetic generation of the incoming turbulence by using random sequences and can be itself subdivided into three main methodologies. The first one consists in building a trigonometric series based on the FFT of the velocity fluctuations [91]. Following such an approach, the power spectral density of the resulting field can be imposed but, generally, the obtained fluctuating field does not respect the divergence-free condition, causing nonphysical large pressure fluctuations at the inlet boundary. Additionally, the fluctuating field can not be assembled independently at every point, so rendering the procedure not ideal for parallel computations. It must be remarked that an extension of such techniques aimed at correctly imposing the divergence free condition has been also proposed [92].

The second methodology is mainly based on the vortex method and its variants [93, 94]. In this case, discrete coherent vortical structures are introduced in the computational domain and such methods, especially in their more recent versions, appear to be promising although they still do not allow full control over the obtained spectra. The third method, mainly steams from the work by Kraichnan [95]. In particular, in the Smirnov's Random Flow Generation technique (RFG), an inhomogeneous and anisotropic velocity field can be obtained starting from an isotropic field, generated by using Kraichnan's procedure, by applying a scaling transformation in accordance with a prescribed velocity correlation tensor [29]. Unfortunately, these methods can generate only fields whose spectral density follows the Gaussian model which is known to contain less energy in the inertial subrange if compared to realistic turbulence spectra, where instead scales represented by LES can be significative [30]. In fact, it is well known that atmospheric turbulence mainly follows the von Kármán spectrum and that the spectrum choice is of great significance for the evaluation of loads on buildings [96, 97]. A review of such kind of turbulence generation procedures, together with new developments focused on the generation of homogeneous anisotropic turbulence, has been recently proposed in [32].

In this paper, velocity fluctuations are generated by adopting the Modified Discretizing and Synthesizing Random Flow Generation (MDSRFG), which belongs to the third category of previously described synthesis approches. The MDSRFG has several advantages if compared to other synthesis methods [30, 71]. In particular, the fluctuating velocity field is generated in accordance with a generic target power spectral density that can be independently controlled in each space direction. Furthermore, the generated field is divergence-free and space correlations can be easily controlled. Moreover, the fluctuations time-histories can be generated independently in each point of interest, so that the method is suitable for parallel computations. Following the MDSRFG method, a homogeneous and anisotropic velocity field can be computed as:

$$u_i(\mathbf{x},t) = \sum_{m=1}^{M}\sum_{n=1}^{N}\Big[p_i^{m,n}\cos\left(k_j^{m,n}\frac{x_j}{L_s}+\omega^{m,n}\frac{t}{\tau_0}\right)+ \tag{4.1}$$

$$q_i^{m,n}\sin\left(k_j^{m,n}\frac{x_j}{L_s}+\omega^{m,n}\frac{t}{\tau_0}\right)\Big], \tag{4.2}$$

with:

$$p_i^{m,n} = \mathrm{sign}(r_i^{m,n}) \sqrt{\frac{2}{N} S_i(f^m) \Delta f \frac{(r_i^{m,n})^2}{1 + (r_i^{m,n})^2}}, \tag{4.3}$$

$$q_i^{m,n} = \mathrm{sign}(r_i^{m,n}) \sqrt{\frac{2}{N} S_i(f^m) \Delta f \frac{1}{1 + (r_i^{m,n})^2}}, \tag{4.4}$$

$$\begin{cases} \mathbf{k}^{m,n} \cdot \mathbf{p}^{m,n} &= 0, \\ \mathbf{k}^{m,n} \cdot \mathbf{q}^{m,n} &= 0, \\ |\mathbf{k}^{m,n}| &= f^m / \bar{U}, \end{cases} \tag{4.5}$$

$$u_{rms,i}^2 = \int_0^\infty S_i(f) \, df, \tag{4.6}$$

where $i = 1, 2, 3$ while N and M are the number of considered random extractions and the number of frequencies, respectively. The $m-th$ frequency adopted for sampling the target spectrum is indicated as f^m, $\omega^{m,n}$ is a random number extracted from a Gaussian distribution $\mathcal{N}(f_m, 2\pi\Delta f)$, Δf is the spectrum sampling step, $\bar{U}$ is the time averaged velocity, L_s is a factor calibrated *a posteriori* related to the turbulent length scale, τ_0 is a dimensionless parameter that allows to control the time correlation of the series and set equal to one in the present work. Parameters $r_i^{m,n}$ are random numbers extracted from a Gaussian distribution $\mathcal{N}(0, 1)$, while $S_i(k)$ is the target spectrum for the $i-th$ velocity component whose total variance is equal to $u_{rms,i}^2$.

In this paper, isotropic turbulence is assumed and the well known von Kármán spectrum reported below is adopted:

$$S(f) = \frac{4(I\bar{U})^2 (L/\bar{U})}{\left[1 + 70.8(fL/\bar{U})^2\right]^{5/6}}, \tag{4.7}$$

where I is the turbulence intensity and L is the turbulence length scale. It should be noticed that in Eq. (4.7) the subscript i has been omitted since the spectrum is assumed to be identical for the three velocity components.

It is worth noticing that, despite the fact that the generated flow field is divergence-free, if it is applied directly at the inlet boundary where a null pressure gradient is imposed, it causes large nonphysical pressure fluctuations. In order to overcome this issue, the MDSRFG method has been adopted aiming at producing a good quality, realistic turbulent field but the velocity fluctuations have been imposed inside the computational domain rather than been adopted as a boundary condition. In particular, the PISO algorithm has been modified introducing velocity fluctuations at the centre of internal cells after the PISO predictor

step [28]. In such a way, velocities and pressures are corrected by the pressure-velocity coupling algorithm itself, avoiding nonphysical large pressure fluctuations and without any additional computational cost. The effect of such procedure on the solution accuracy was analysed in detail in [28], showing that the numerical errors introduced by the procedure are small and in accordance with the levels suggested by Issa [98].

4.3 EXPERIMENTAL SETUP

In this section, the setup used to obtain the experimental data which are compared with numerical results is described. The experimental data were obtained in the open-circuit boundary layer wind tunnel of CRIACIV laboratory, located in Prato, Italy [69]. The model employed in the experimental investigations was made of aluminium and was characterized by width, B, equal to 300 mm, depth, D, equal to 60 mm and length, D_z, equal to 2380 mm and had sharp edges and smooth surfaces. The wind tunnel test section was 2.42 m wide and 1.60 m high, so that the resulting blockage ratio in the vertical direction was 3.75%. The model locking system was conceived in order to avoid screws and keep lateral surfaces smooth so minimizing disturbances to the flow. The prism was equipped with 62 pressure taps monitored by two 32-channels PSI miniaturized piezoelectric scanners at a sampling rate of 500 Hz [70].

Experimental Setup #2 and Setup #6, corresponding to mild and high turbulence at null attack angle, are used to compare results of the numerical simulations [69]. The turbulence intensity and the turbulence length scale in the along wind direction for each setup are reported in Tab. 4.1. Measurements refer to the location of the model in the wind tunnel facility, but in its absence.

The inflow turbulence was generated by placing upstream the model two grids characterized by a mesh of 100 mm × 100 mm with 25 mm thick slats (grid 1) and of 550 mm × 550 mm with 140 mm thick slats (grid 2). The grid type and the grid position for each setup are listed in Tab. 4.1, where d indicates the distance of the grid from the longitudinal axis of the model.

Setups	Grid	d [m]	I[%]	L/D
#2	1	4.95	2.9	1.3
#6	2	4.95	13.6	3.9

Table 4.1: Experimental setups simulated in the present work [69].

In order to correct wind tunnel flow asymmetries, the exact position of the null attack angle is obtained comparing the mean pressure distributions on the top and bottom surfaces of the prism and rotating the model of 0.45° nose-up with respect to the horizontal plane when symmetry is achieved. The Re number, based on D, is in the range between 2.2×10^4 and 1.12×10^5.

4.4 NUMERICAL MODEL

In this section, the characteristics of the numerical model in terms of domain dimensions and grid features are reported and compared with other studies, together with the description of the adopted boundary conditions and the adopted numerical setups. In this study, Setup #2 and Setup #6 as listed in Tab. 4.1 and a Re number based on D equal to 5.5×10^4 have been considered. The incoming turbulence is generated by using the MDSRFG method as previously discussed. The considered values of the inflow turbulence intensity are close to the ones suggested in the additional sensitivity analyses proposed within the BARC project.

The computational domain size and the grid resolution are in overall agreement with the guidelines provided by Bruno [64] and the BARC main setup [63]. As showed in Fig. 7.4, the computational domain is such that $D_x = 40B$ and $D_y = 30B$ leading to a blockage ratio equal to 0.67%, while the distance of the front face of the prism from the inlet, Λ_x, is set equal to 16B. As showed by Mariotti et al. [88], when the blockage ratio varies from 0.7% to 3.75.%, negligible effects have been observed on the solution. Therefore, both blockage ratio effects and boundary effects on the solution can be neglected.

A structured mesh with along wind dimension $\delta_x/B = 2.5 \times 10^{-3}$ and cross wind dimension $\delta_y/B = 1.5 \times 10^{-3}$ is adopted close to the wall (see Fig. 4.2 (a)) , leading to an average y^+ equal to 1.9. The mesh stretching ratio close to the wall is set equal to 1.1. Outside the boundary layer, the mesh is unstructured quad dominated and its size is slowly coarsened up to approximately $\delta_x/B = \delta_y/B = 1.8 \times 10^{-2}$ in the wake (see Fig. 4.2 (b)). The mesh sizing in front of the rectangular cylinder is grown up to $\delta_x/B = \delta_y/B = 5 \times 10^{-2}$ and then maintained almost constant and structured until the inlet boundary is reached, in order to limit the numerical dissipation of the introduced fluctuations field. Finally, the mesh is further coarsened in the far field where an unstructured mesh is adopted.

The mesh extrusion along the z direction is performed for a total length of $D_z/B = 1$ when Setup #2 is considered while for Setup #6,

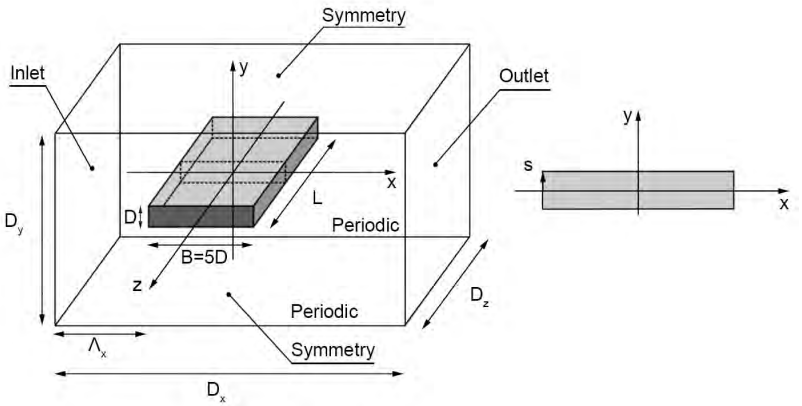

Figure 4.1: Model and domain geometry adopted for computational studies [63].

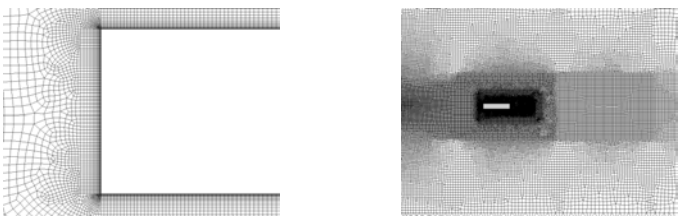

(a) (b)

Figure 4.2: Mesh adopted for the LES simulation: detail of the mesh close to the solid boundary (a) and mesh in proximity of the body and wake (b).

which is characterized by a higher turbulence length scale (see Tab. 4.1), D_z/B is set equal to 3. Such choice is aimed at minimizing the effect of the periodic condition as will be later discussed, but additional simulations, performed by using a domain identical to the one adopted for Setup #2, are also presented. The cell dimension in the extrusion direction is set equal to $\delta_z/B = 0.02$ in both cases. The grid resolution in the extrusion direction is higher than the minimum requirements given by Tamura [99]. The mesh characterized by $D_z/B = 1$ counts approximately 8.0M, while for $D_z/B = 3$ the cell number rises up to about 24.0M and, in both cases, the finite volume aspect ratio is close to one in the body proximity and in the wake. A comparison between the domain size and the grid resolution adopted in the present simulation and other similar ones are reported in Tab. 4.2 and Tab. 4.3, respectively.

Source	D_x/B	D_y/B	D_z/B	Λ_x/B
Present simulation (Setup $D_z/B = 1$)	40	30	1	16
Present simulation (Setup $D_z/B = 3$)	40	30	3	16
Bruno et al. [10, 72]	41	30.2	1, 2, 4	15
Grozescu et al. [73]	41	30.2	1	15
Mannini et al. [74]	200	200	1, 2	100

Table 4.2: Parameters of the computational domain as reported by Bruno [64].

Source	n_w/B	δ_x/B	δ_z/B
Present simulation (Setup $D_z/B = 1, 3$)	5.0×10^{-4}	2.5×10^{-3}	0.02
Bruno et al. [10, 72]	5.0×10^{-4}	2.0×10^{-3}	$0.042 - 0.01$
Grozescu et al. [73]	$5 \times 10^{-4}, 2.5 \times 10^{-4}$	$1.0 \times 10^{-2}, 5 \times 10^{-3}$	0.042, 0.01
Mannini et al. [74]	5.0×10^{-5}	1.4×10^{-2}	0.0156

Table 4.3: Grid resolution in the boundary layer: comparison with meshes adopted by other authors as reported by Bruno [64].

As regards the turbulence model, the Smagorinsky-Lilly turbulence model [40, 41] is adopted aiming at testing a simple and well known approach which provides good results with the adopted numerical setup. The wall treatment is performed with van Driest damping law.

The pressure-velocity coupling is obtained for all analyses by using the well known PISO algorithm with two correctors, modified in order to introduce the incoming turbulence as discussed in Section 4.2 [28]. The time advancement is performed by using the implicit two-step second order Backward Differentiation Formulae [11].

For what it concerns the spatial discretization, a centered second-order differentiation scheme is adopted for the diffusive terms, while, for non-linear advective terms, the LUST scheme, which proved to be particularly successful for LES in complex geometries [75], is used. The LUST scheme is a fixed blend between linear upwind and centered linear schemes. As recommended by Weller [75], the blending factor is set equal to 0.25, in order to find the better trade off between low dissipative behaviour and numerical stability. The characteristic of the LUST scheme to be less dissipative if compared with the well known monotonic van Leer scheme makes it suitable for Large Eddy Simulations. The adopted non-dimensional time step (based on D) is $\Delta t^* = 5.0 \times 10^{-3}$, leading to approximately 1500 steps for a shedding cycle. The maximum Courant number obtained in all the simulations is equal to 3.1.

The mean velocity field is prescribed at the inlet boundary, while Neumann conditions on the normal component of the stress tensor are imposed at the outlet boundary. Fluctuations are introduced in a plane shifted from the inlet one of about $5.0 \times 10^{-1} B$. Symmetry boundary conditions are imposed at the top and bottom surfaces, while periodic conditions are adopted on the faces normal to the extrusion direction (see Fig. 7.4).

The prism has been equipped with 1288 and 3864 pressure monitors for $D_z/B = 1$ and $D_z/B = 3$, respectively, and data are acquired at each time step, leading to 200 samples for one non-dimensional time unit. All simulations have been run by using the open source Finite Volume software OpenFOAM version 2.3.0 on 96 CPUs at CINECA on the Galileo cluster (516 nodes, 2-eight cores Intel Haswell 2.40 GHz processors with 128 GB RAM per node).

4.5 NUMERICAL RESULTS

In this section, the numerical results obtained for each setup are reported and systematically compared with experimental data. Firstly, in Section 4.5.1 a characterization of the incoming flow is provided. Then, in Section 4.5.2 results in terms of flow topology and bulk parameters are reported and compared with those obtained in experimental tests and other numerical studies. Section 4.5.3 focuses on the analysis of the pressure coefficient statistics on the central section. Then, in Section 4.5.4 and Section 4.5.5, the span wise correlations and the Covariance Proper Transformation (CPT) of the obtained pressure distributions are discussed.

Considering that the introduced turbulence impinges the body after $80t^*$, being $t^* = tU/D$ the non-dimensional time unit, simulations are run over a total time of $880t^*$ while, in order to avoid the effects of the flow initialization, only the last $500t^*$ are considered in the post-processing. In order to check the convergence of the inflow statistics, velocities have been sampled in a point located at $(-15B, 0, 0)$. Figure 4.3 (a) reports the inflow statistics in terms of time-average along-wind velocity, $\overline{U}$, and its standard deviation, u_{rms}. As it can be seen, after $500t^*$ both first and second order statistics reach a plateau, indicating that a good convergence is achieved.

Focusing on the pressure distribution, a qualitative evidence of the statistical convergence can be appreciated by focusing on Fig. 4.3 (b), which reports the distribution of the root mean square of the pressure coefficient, indicated as C_p', for the Setup #6. As expected, the distribu-

tion appears smooth and two-dimensional with very good approximation, so indicating that a good convergence has been reached.

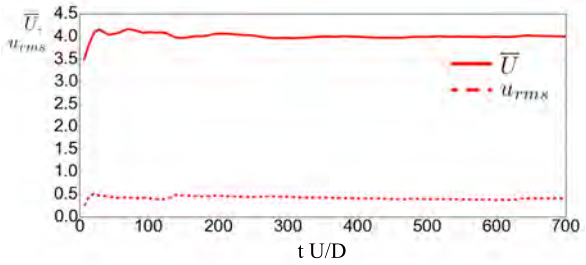

(a)

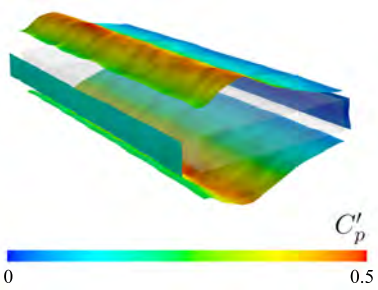

(b)

Figure 4.3: Incremental average velocity and standard deviation at the inlet boundary (a) and three-dimensional C'_p distribution for the Setup #6.

Finally, in order to check if the adopted sampling window of $500t^*$ can be considered sufficiently extended to reach the convergence of the first and second order statistics of integral forces, the statistics of the lift coefficient, C_L, and of the drag coefficient, C_D, made non-dimensional with respect to D, have been analysed. Following the procedure adopted by Bruno et al. [10], the time histories of C_D and C_L have been subdivided in sampling windows of extent T_n, where $T_{n+1} = T_n + 50t^*$ and $T_0 = 0t^*$. Then, for the $n-th$ sampling window, the percentage residual ϕ_{res} relative to the considered statistic has been calculated as $\phi^n_{res} = \frac{\phi_n - \phi_{n-1}}{\phi_n} \cdot 100$. The time histories of C_L and C_D for the Setup #2 are reported in Fig. 4.4 (a), while the trend of the percentage residual ϕ_{res} on the considered statistic is shown in Fig. 4.4 (b). The first $180t^*$ have been disregarded in order to exclude the initialization effects. As it can be seen from Fig. 4.4 (b), after $500t^*$ the percentage residual on the rms of C_D is less than 2%, while it results lower than 1% when the average C_D and the rms of C_L are consid-

ered (referred respectively as $\overline{C}_D$ and C'_L). Therefore, in the following the sampling windows of $500t^*$, corresponding to about 55 shedding cycles, has been retained for the calculation of the signal statistics.

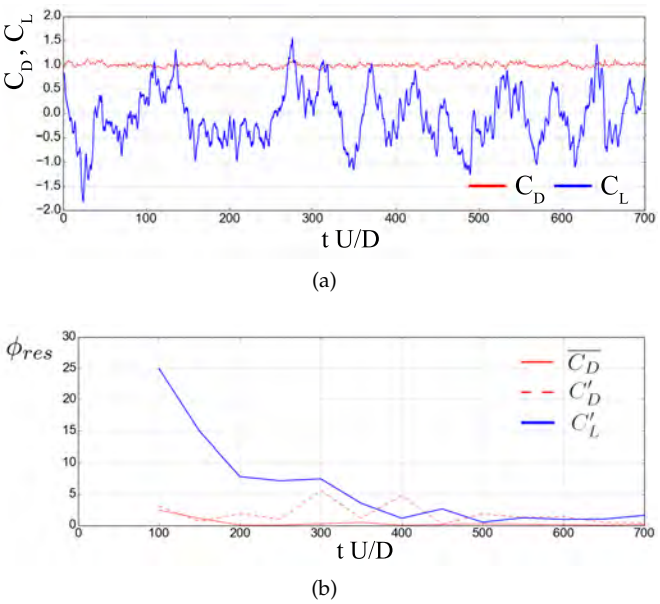

Figure 4.4: Time histories of the drag and lift coefficients (a) and convergence of their statistics (b).

4.5.1 *Turbulent inflow characterization*

In this section, the main features of the incoming flow are analysed in order to check the agreement between the statistics of the synthetic fluctuation field imposed at the inlet and the ones observed in the computational domain. To this purpose, 1680 velocity monitors have been placed in the domain and velocities sampled at each time step. With reference to Fig. 7.4, the monitors have been organized in a grid with $-8.0 \leqslant x/B \leqslant -1.5$, $-1.25 \leqslant y/B \leqslant 1.25$ and $-0.25 \leqslant z/B \leqslant 0.25$ and with 14 alignments along x, 12 along y and 10 along z. The profiles of the time-averaged velocity together with those of turbulence intensity and turbulence length scale are plotted in Fig. 7.8 (a), (b) and (c) respectively at $z/B = 0$ and for two different along-wind positions, $x/B = -15$ and $x/B = -1.5$. It can be noticed that a good agreement is achieved for the mean velocity component in the stream direction while the turbulence intensity, I_u, is slightly underestimated with re-

spect to the target one for both $x/B = -15$ and $x/B = -1.5$. The profile of the turbulent integral length scale reported in Fig. 7.8 (c) is obtained by fitting the recorded along wind velocity fluctuations spectrum with the von Kármán one. Also in this case, a reasonable agreement between the profile obtained from the LES and the target one is reached.

The obtained spectra of the velocity components are reported in Fig. 7.9. In order to check if the fluctuation field is correctly propagated starting from the inlet boundary and proceeding towards the body, the spectra are plotted in the correspondence of two different locations, near the inlet boundary at $(-15B, 0, 0)$ and near the prism at $(-1.5B, 0, 0)$. Up to frequencies of about $1/20$ of the shedding cycle the target von Kármán spectrum can be considered reproduced with good accuracy in both the considered locations, so highlighting that vortical structures are correctly propagated from the inlet boundary to the immersed body.

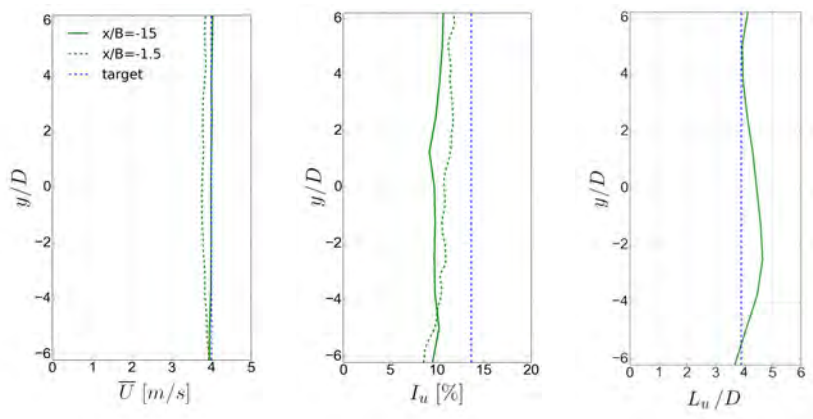

(a) (b) (c)

Figure 4.5: Time-averaged velocity (a), turbulence intensity (b) and turbulence length (c) in along wind direction for the Setup #6 in two different locations. Dotted lines represent the target values.

4.5.2 *Flow topology and bulk parameters*

The flow topology for the analysed setups is reported in Fig. 5.9 by means of isosurfaces of the invariant λ_2 coloured with the sign of the z component of the instantaneous vorticity vector. The λ_2 criterion proved to be successful in reproducing the topology and the geometry of vortex core for a large variety of turbulent flows [76]. The iso-

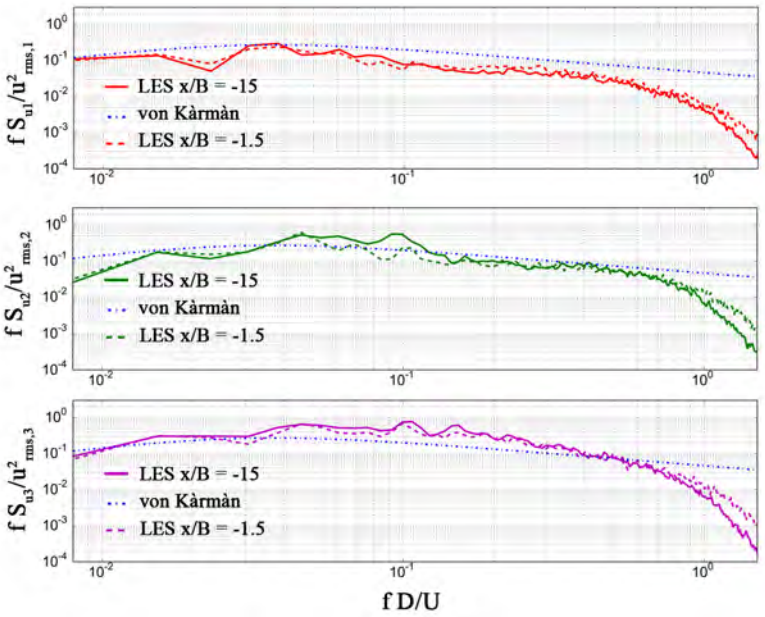

Figure 4.6: Spectra of the velocity time series obtained from LES for the Setup #6.

surfaces are plotted in correspondence to the maximum lift condition, when the main vortex on the top side reaches its maximum extension. It can be observed that the separation of the vortical structures rotating in the clockwise and anti-clockwise direction (coloured with light blue) is sharper in Setup #2 than in Setup #6, so clearly highlighting an increased turbulent mixing in the latter case. In order to better analyze the instantaneous flow dynamics, Fig. 4.8 shows the instantaneous streamlines for the two analysed setups in correspondence to the maximum lift condition. Focusing on the part of the prism near the leading edge, it can be seen that the destabilization of the shear layer occurs upwind when the highest level of the incoming turbulence is considered, leading to a higher shear layer curvature and consequently to a shorter reattachment length. Indeed, considering a region that, starting from the leading edge is 0.5D long, Setup #6 shows the presence of three vortical structures, while Setup #2 does not highlight vortices within the same zone. In this case in fact the distance between the first vortex core and the leading edge is approximately 0.75D.

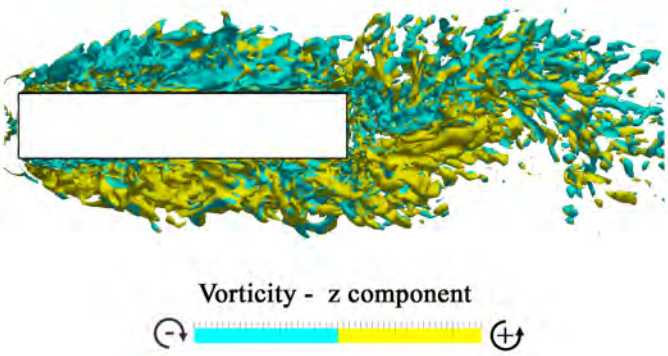

(a) Setup #2

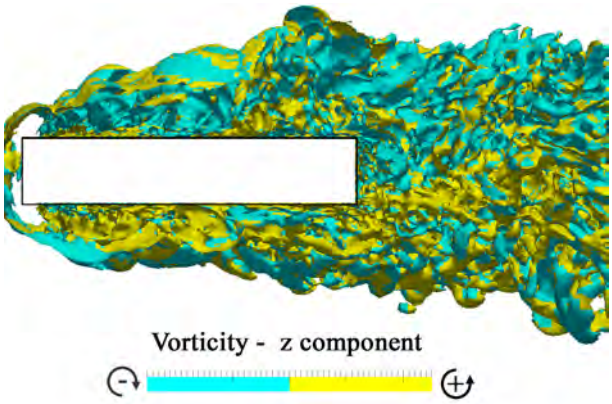

(b) Setup #6

Figure 4.7: Isosurfaces of $\lambda_2\ D^2/U^2 = -0.375$ coloured with the sign of the z component of the instantaneous vorticity vector.

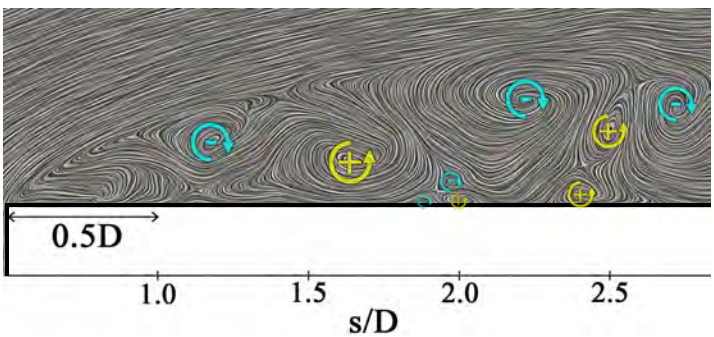

(a) Setup #2

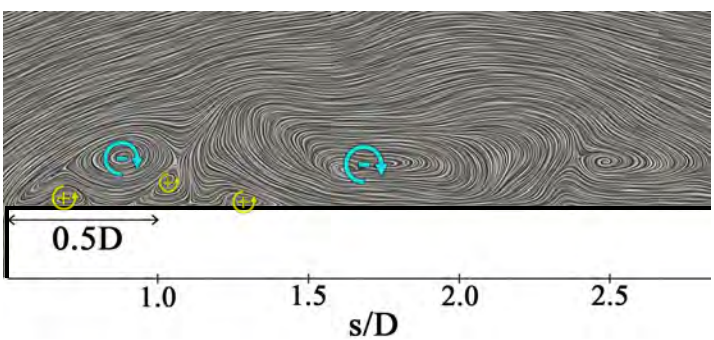

(b) Setup #6

Figure 4.8: Instantaneous streamlines for the two analysed setups and sign of the z component of the instantaneous vorticity vector. Detail of the flow dynamics in correspondence of the leading edge.

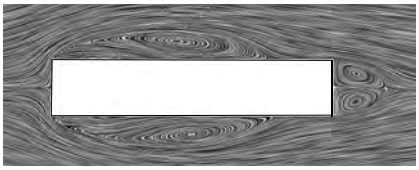

(a) LES-smooth (Patruno et al. [68])

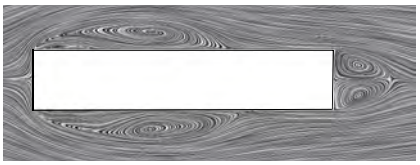

(b) Setup #2

(c) Setup #6

Figure 4.9: Time-averaged streamlines for the three analysed setups.

Looking at time averaged streamlines, other differences between the analysed setups can be recognized. In particular, the streamlines of the time-averaged velocity field reported in Fig. 4.9 clearly show the decrease in size of the time averaged separation bubble and the migration of the vortex core, which reduces its abscissa from $x_c/D = -0.19$ in case of perfectly smooth inflow to $x_c/D = -0.63$ and $x_c/D = -1.35$ for Setups #2 and #6, respectively, as reported in Tab. 4.4. The same trend is also showed by the mean position of the reattachment point, that decreases its abscissa from $x_r/D = 1.76$ in case of smooth inlet to $x_r/D = 0.98$ and $x_r/D = -0.20$ for Setups #2 and #6. The y coordinate of the main vortex core, denoted as y_c, decreases its value in a less significant way so that, with reference to the smooth inflow case, its value is reduced of only 12% for Setup #6. It is worthy noticing that the length of the mean recirculation bubble is deeply affected by the numerical setups as well as by the mesh resolution in the spanwise direction. In particular, when a very low dissipative setup is adopted together with a very fine resolution in the spanwise direction, the reattachment length shortens becoming even smaller than that found in the experiments, at least for the smooth inflow condition [100].

Figure 4.10 reports the distribution of the average friction coefficient $\overline{C_f}$ made non-dimensional with respect to D on the central alignment of the rectangular prism. In order to analyze the obtained results, it is useful to firstly review the organization of the flow around the 5:1 rectangular cylinder. In particular, as described by Bruno [10], the recirculation zone can be subdivided into three main sub-regions, according to the role played in the shedding mechanism. Proceeding from the leading to the trailing edge, the first zone is characterized by the

Inlet	Source	$Re\ [\times 10^4]$	x_r/D	x_c/D	y_c/D
Turb.	Setup #2	5.5	0.98	-0.63	0.81
	Setup #6	5.5	-0.20	-1.35	0.72
Smooth	Bruno et al. [10] (LES)	4.0	2.18	0.04	0.80
	Grozescu et al. [73] (LES)	2.0 to 4.0	1.64	-0.17	0.35 to 0.82
	Mannini et al.[74] (DES)	2.64	1.72 to 2.06	-1.44 to -0.05	0.77 to 0.88
	Patruno et al. [68] (LES)	2.4	1.51	-0.19	0.82

Table 4.4: Reattachment point and main vortex core position.

development of vortices due to the formation of the shear layer instabilities and, in that study, has been named inner-region. A small recirculation region is observed in correspondence of the wall, below the inner-region, which is characterized by opposite vorticity. Downstream with respect to such regions, vortices coalesce forming the main vortex. These regions have been qualitatively recognised in Fig. 4.10. For both the considered setups, a change in sign of $\overline{C_f}$ highlights the presence of the aforementioned recirculation region immediately downwind with respect to the leading edge. This mean vortical structure significantly reduces its along-wind dimension when the inflow turbulence intensity is increased: its length decreases from 0.96D for the Setup #2 to 0.43D when Setup #6 is considered. Also the inner region appears to progressively reduce its size when the inflow turbulence increases, becoming difficult to be identified when the Setup #6 is considered. The main vortex region follows the same trend, reducing its extension from 2.43D in Setup #2 to 2.05D in Setup #6.

Figures 4.11 (a) and (b) show respectively the profiles of the average velocity and of the turbulence intensity on the central section for different along-wind positions, for Setup #2, Setup #6 and for the smooth case [68]. Focusing on Fig. 4.11 (a), the flow topology previously discussed can be recognized, with results obtained from Setup #2 being very close to those relative to the smooth inflow condition. In particular, according to Fig. 4.10, for Setup #2 the main vortex region extends from approximately $1.8 \leqslant s/D \leqslant 4.1$ and downwind this range, Fig. 4.11 (a) shows that velocity profiles do not change sign anymore, indicating that the average flow is reattached. A similar observation holds true when Setup #6 is considered, even if, in this case, the main vortex region extends only from $s/D = 1.1$ to about $s/D = 3.1$. If the profiles reported in Fig. 4.11 (b) are analysed, it can be observed that inside the corresponding main vortex regions, each setup clearly shows a peak of the turbulence intensity, while proceeding downwind, profiles tend to become almost constant. For both analysed setups, the position of this

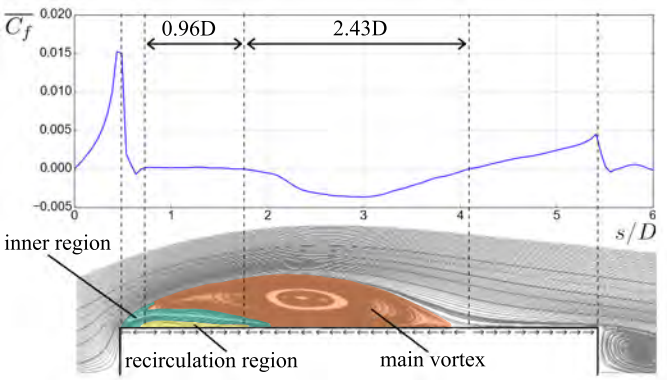

(a) Setup #2

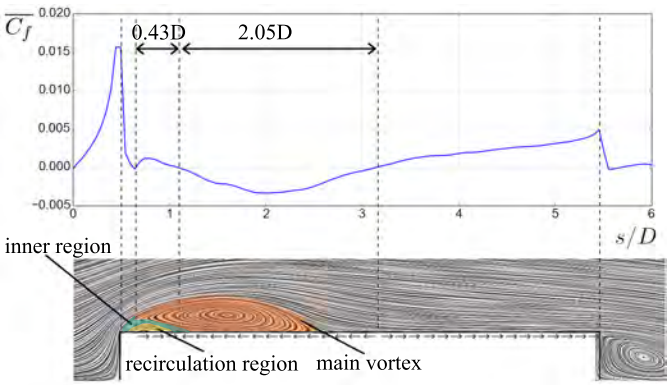

(b) Setup #6

Figure 4.10: Friction coefficient distribution on the central alignment for the two analysed setups and recognized mean structures according to Bruno et al. [10].

peak of turbulence intensity is located above the point where the average velocity changes sign, indicating that the highest turbulent mixing occurs above the main vortex region.

Focusing on the pressure coefficient, C_p, its power spectral density is plotted in Fig. 4.12 for different along-wind positions on the central alignment of the prism top surface. For each position, the spectra have been averaged in the spanwise direction. Regarding Setup #2, Fig. 4.12 shows that for $s/D = 3$ the signal energy is spread in a wide frequency range approximately located between $fD/U = 0.15$ and $fD/U = 0.3$ without showing clear apparent peaks. When Setup #6 is considered, both the spectra at $s/D = 1.75$ and $s/D = 3.0$ show a peak located at approximately $fD/U = 0.11$, that is close to the Strouhal number

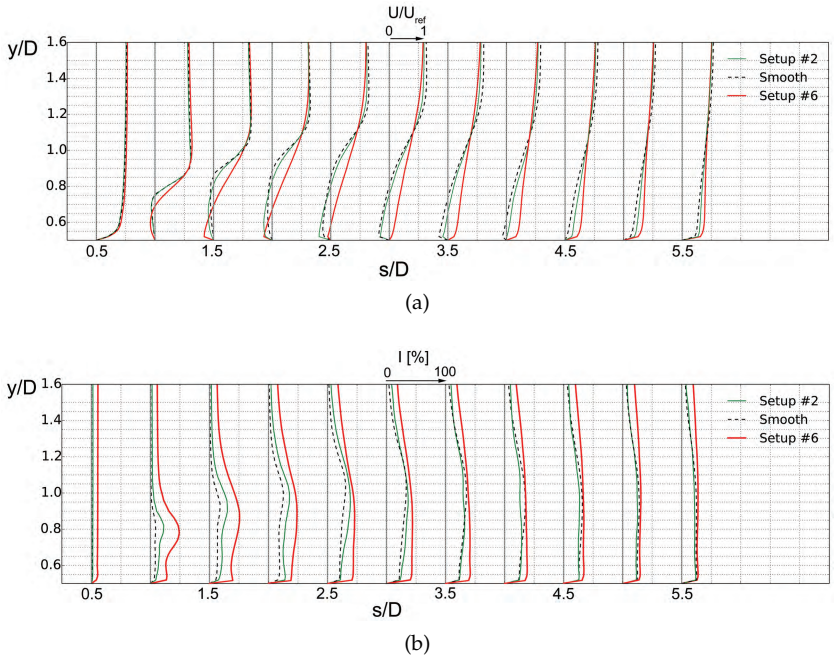

Figure 4.11: Profiles of average velocity (a) and turbulence intensity (b) on the central section in different along-wind positions, for Setup #2, Setup #6 and smooth flow (the simulation setup is described in Patruno et al. [68]).

obtained in smooth flow conditions, and a second peak at lower frequency located at $fD/U = 0.04$ approximately corresponding to the peak of the power spectral density of the incoming velocity field (see Fig. 7.9). In fact, considering the von Kármán spectra $S(f)$ reported in Eq. (4.7), the peak value of the function $S(f)f$ can be computed as $f_{peak}D/U = 0.146(U/L) = 0.037$.

The statistics of the flow bulk parameters, obtained by integrating the pressure field for a spanwise length equal to B and made non-dimensional with respect to D, are reported in Table 6.1. As expected, the rms of the lift coefficient clearly grows with increasing turbulence intensity, while the mean lift coefficient can be considered almost null.

4.5.3 *Central section statistics*

In this section, the pressure coefficients statistics on the central section are analysed. Data are presented by adopting the curvilinear abscissa s as reported in Fig. 7.4. For Setup #2, only the mesh characterized by $D_z/B = 1$ is adopted while, for Setup #6, C_p statistics on the cen-

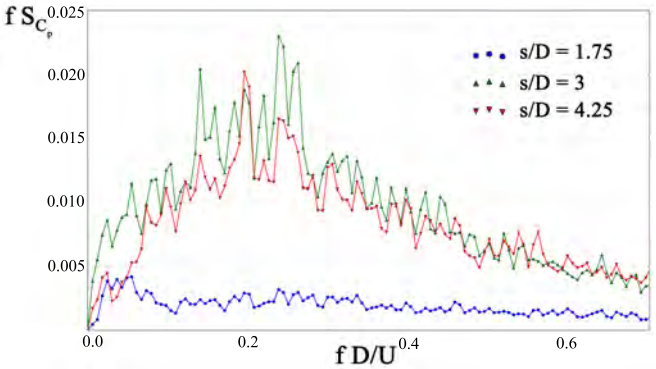

(a) Setup #2

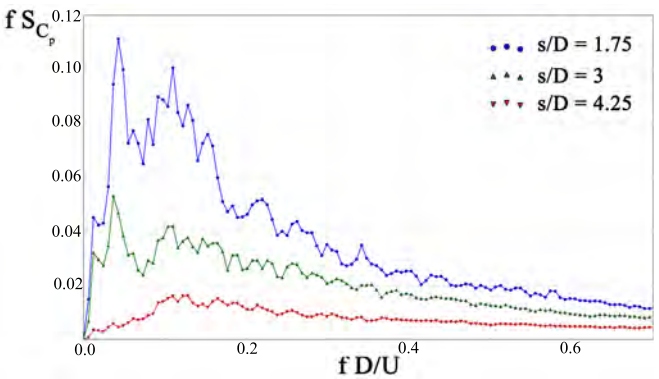

(b) Setup #6

Figure 4.12: Spanwise averaged power spectral density of the pressure coefficient on the central section in different along-wind positions for Setup #2 and Setup #6.

Inlet	Source	C_D	C'_D	C_L	C'_L
Turb.	Setup #2	0.990	0.042	−0.07	0.55
	Setup #6	1.105	0.145	−0.09	1.42
Smooth	Bruno et al. [72] (LES)	0.96 to 1.03	-	-0.315 to -0.0024	0.2 to 0.73
	Grozescu et al. [73] (LES)	0.97 to 0.98	-	-0.097 to 0.0043	0.52 to 0.65
	Mannini et al. [74] (DES)	0.97 to 1.07	-	0.0032 to 0.047	0.42 to 1.07
	Patruno et al. [68] (LES)	1.02	0.02	-0.05	0.19

Table 4.5: Statistics of the flow bulk parameters.

tral section are plotted for two different domain extrusions: $D_z/B = 3$, that represents the main setup as reported in Tab. 4.2 and for an additional shorter domain, identical to the one adopted for Setup #2. The need to increase the domain size for Setup #6 with respect to Setup #2

and other results presented within the BARC project, should be traced in the high value of the turbulence length scales found in the experimental data used for comparison. The choice of $D_z/B = 3$ represents the result of preliminary tests and has been found to be a reasonable compromise between accuracy and computational cost. Nevertheless, due to the remarkable computational effort required to perform such analyses, results obtained by using $D_z/B = 1$ are also reported. Such choice is aimed at providing an evaluation of the inaccuracies that can be introduced by using relatively small computational domains which might be attractive in practical applications in order to contain the computational cost.

Looking at Figs. 4.13 and 4.14 it can be observed that the reattachment point migrates upstream, leading to an upstream shift of the pressure recovery zone when the turbulence intensity is increased in agreement with previous observations. Focusing on Setup #2, a good accordance in terms of time-averaged pressure coefficients between numerical and experimental data is achieved along the whole path. Regarding Setup #6, the dependence of the obtained results on the domain size can be clearly observed: $D_z/B = 3$ appears to be close to the experimental data while a considerable decrease in accuracy is observed for $D_z/B = 1$.

Considering Figs. 4.13 and 4.14, which report the C'_p distributions, it can be also seen that at the frontal stagnation point (i.e. $s/D = 0$) the recorded value is equal to $2I$ with good approximation for all setups, indicating that the energy content of the impinging flow is in good accordance with the experimental one. Additionally, the comparison between the simulation and the experimental results reveals an overestimation of C'_p in the pressure-recovery zone, which has been often observed in LES results presented within BARC.

Moreover, for Setup #2, the peak of C'_p approximately corresponds to the reattachment point position of the time averaged velocity field. Such position falls in the central part of the pressure recovery zone in both numerical and experimental results. When Setup #6 is considered, such observation does not hold as experiments show that the peak is located in a zone characterized by relatively high suctions. Also in this case, the accuracy of the obtained results increases when the larger domain is adopted, although the peak position is slightly shifted downwind also when the larger domain is considered.

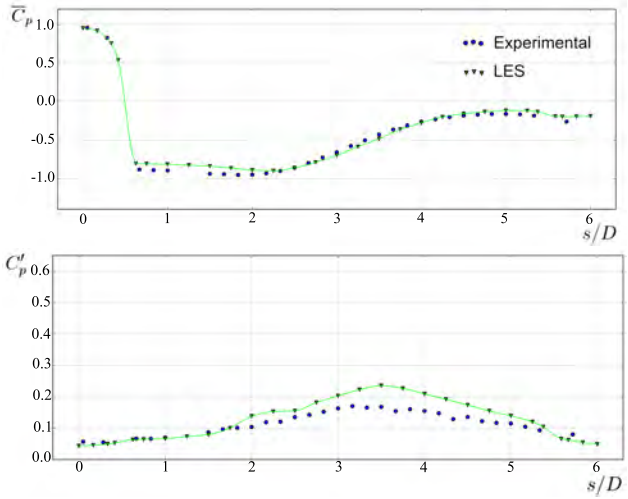

Figure 4.13: Distribution of C_p statistics on the central section for Setup #2 .

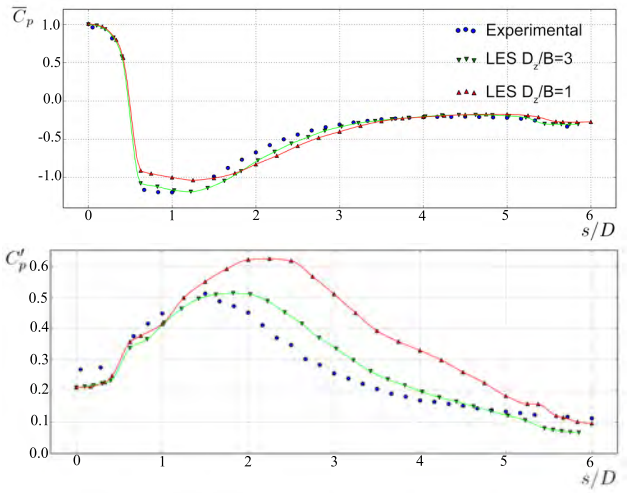

Figure 4.14: Distribution of C_p statistics on the central section for Setup #6 .

4.5.4 *Correlations*

This section aims at analyzing the C_p correlations along the extrusion direction. As a general comment, it should be noticed that spanwise correlations obtained from numerical simulations are deeply affected by the spanwise grid resolution, by the numerical model adopted and by the spanwise dimension of the computational domain [64, 74]. In

particular, the spanwise cell dimension (δ_z/D) shows to deeply influence the R_{C_p} distributions, decreasing correlations when the spanwise cell resolution is increased [11]. Nevertheless, as shown by Bruno et al. [11] the spanwise grid resolution $\delta_z/D = 0.1$ and the spanwise domain dimension $D_z/B = 1$ lead to acceptable results, representing a good trade-off between accuracy and computational cost when smooth inflow conditions are adopted. This is confirmed also by the good results obtained in Sec. 4.5.3 for Setup #2. Note that Setup #6 clearly showed increased accuracy when the mesh characterized by $D_z/B = 3$ has been adopted. In order to highlight the problem, Fig. 4.15 reports correlation functions, denoted as R_{C_p}, for all analysed cases at three points located at $s/D = 1.75,\ 3.00$ and 4.25.

With reference to Fig. 4.15, it is shown that, when Setup #2 is considered, correlations, although they do not reach a null value, fall rapidly to small values in the proximity of 0.30 for $z/D = 1.25$. When Setup #6 is analysed, it can be clearly seen that correlations never go below a minimum value of approximately 0.7 when $D_z/B = 1$ is considered. Such effect, related to the high value of the turbulent length scale, has been well studied by Shirato et al. [101], which experimentally observed an almost linear relation between the spanwise correlation of the lift force (calculated on two-dimensional strips) and the incoming turbulent length scale. In numerical simulations, this high value of R_{C_p} denounces also a relatively high effect of the periodic boundaries on the flow field and it is responsible for the diminished accuracy of the simulations which, thus, should be performed on a wider computational domain. Interestingly this effect not only affects the fluctuating flow field but also appreciably modify the time-averaged pressure distribution on the prism central section. When the domain characterized by $D_z/B = 3$ is considered, correlations decrease more steeply and results appear to be characterized by higher accuracy. Figure 4.16 provides a qualitative comparison of the incoming vortical structures characterizing Setup #2 and Setup #6. In can be observed that, while the Setup #2 does not show the presence of strong incoming vortices, when Setup #6 is considered, the incoming flow vortical structures become apparent and that their scale is comparable to the prism dimensions.

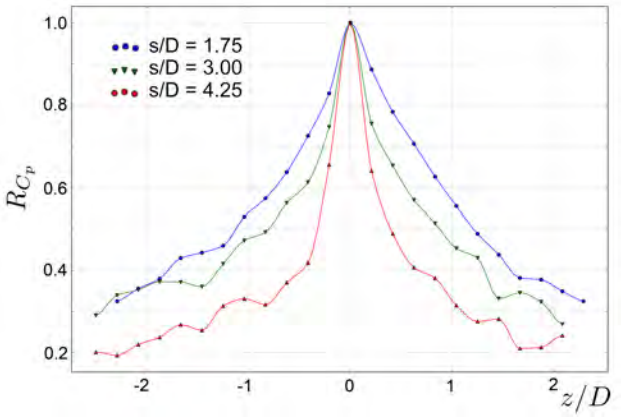

(a) Setup #2

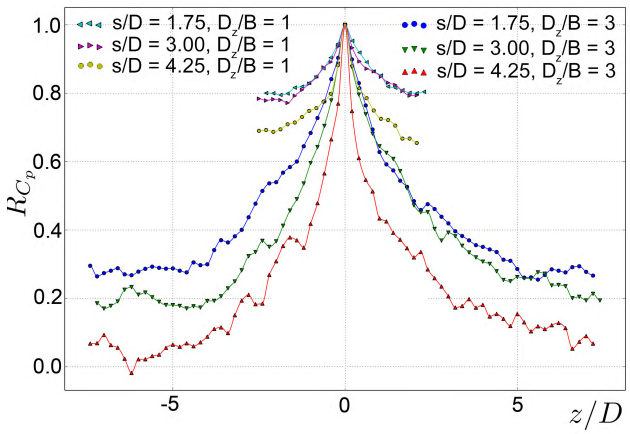

(b) Setup #6

Figure 4.15: Spanwise correlation for the two analysed inflow conditions.

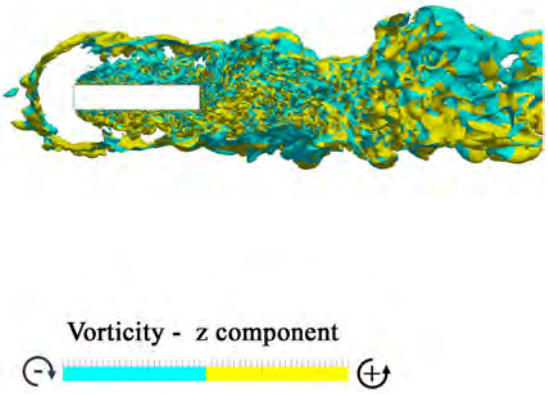

(a) Setup #2

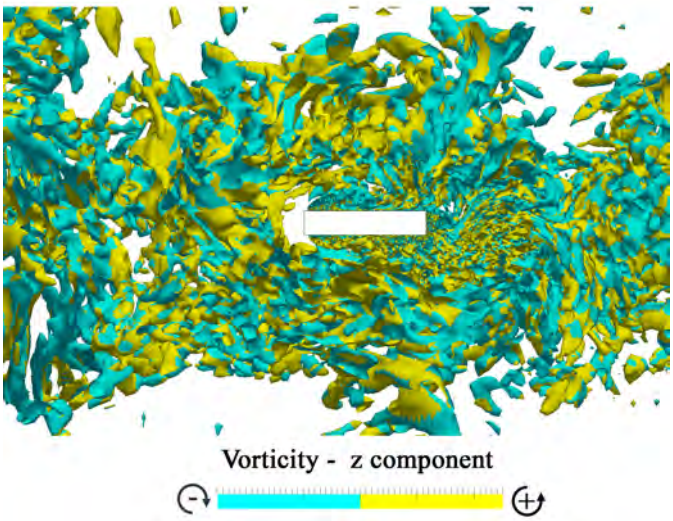

(b) Setup #6

Figure 4.16: Isosurfaces of $\lambda_2\ D^2/U^2 = -0.0125$ coloured with the sign of the z component of the instantaneous vorticity vector: focus on the incoming turbulence.

4.5.5 *Covariance Proper Transformation*

Covariance Proper Transformation (CPT) is here adopted aiming at further characterizing the flow dynamic behaviour and at describing the fluctuating pressure field. According to the CPT methodology [102, 103], starting from pressure time histories measured at each pressure tap the eigenvalues and the eigenvectors of the covariance matrix have been extracted. Each eigenvalue represents the variance associated to the corresponding eigenvector, hereinafter referred as pressure mode. The modes have been calculated up to the 95 % of the total variance. Since the CPT modes are inherently related to the domain dimensions, in order to compare the mode shapes and the associated variances, all the results hereinafter presented are relative to a domain spanwise dimension $D_z/B = 1$. In order to do this, only the central third of the domain used for Setup #6 is here considered, so rendering the two simulations comparable. Then, the CPT technique has been applied as previously described.

The first three pressure modes for each analysed setup are reported in Fig. 4.17. It clearly appears that the first two CPT modes are strongly two-dimensional in all the considered setups. From the qualitative point of view, a good correspondence between the first two modes is preserved despite the radical changes in the flow topology, meaning that the order in which mode shapes appear seems rather stable. Nevertheless, for all modes shapes, the migration of the pressure fluctuation peaks toward the leading edge is clearly observed.

Table 4.6 reports the ratio between the variance associated to each CPT mode, indicated as σ, and the total variance, σ_t, for the analysed cases and the first 8 modes. In particular, in the table, modes which are symmetric with respect to the xy plane are denoted as Sym., the antisymmetric ones as Asym., while the dash indicates modes which do not fall in such categories.

It should be noticed that Mode 1 is the one which strengthen the most, passing from 15% to 26% of the total variance, indicating a strong energy concentration on a mode which is antisymmetric with respect to the xy plane. Mode 2 appears to be antisymmetric in both Setup #2 and #6. As a result, taking into account the first eight modes, it is observed that the total variance associated to antisymmetric modes increases with the incoming turbulence intensity if compared to the one associated to symmetric ones. In fact, the sum of the variance associated to asymmetric modes passes from 25% for Setup #2 to 41% for Setup #6. This is indeed coherent with the fact that the incoming turbulence unsteadily modifies the flow attack angle, providing energy

mainly to antisymmetric modes. Additionally, it should be noticed that Mode 3 of Setup #6 is the only one of the first eight modes that clearly involves the frontal surface and its associated variance is equal to 5% of the total one.

Mode	Setup #2		Setup #6	
	σ/σ_t [%]	Type	σ/σ_t [%]	Type
1	15	Asym.	26	Asym.
2	7	Asym.	10	Asym.
3	3	-	5	Sym.
4	3	Asym.	3	Sym.
5	2	Sym.	3	Asym.
6	2	-	2	Asym.
7	2	-	2	-
8	1	-	2	Sym.

Table 4.6: Comparison of the percentage of the total variance (first 8 modes) between analysed setups.

4.6 CONCLUSIONS

In the present paper, LES simulations of the unsteady flow field around a prism characterized by a rectangular 5:1 cross section in presence of incoming turbulence have been performed. The study has the twofold objective of analysing the main flow features modifications occurring in reattached flows in presence of incoming turbulence and assess LES turbulence models ability in reproducing them.

Two different inflow conditions, corresponding to mild and strong inflow turbulence levels have been analysed. The unsteady inflow conditions have been synthetically generated by adopting the MDRSFG model and imposed in the computational domain by modifying the PISO algorithm in order to avoid non-physical pressure fluctuations. The analysed inflow conditions are characterized by increasing incoming turbulence intensity and turbulence length scale, so allowing to test the numerical model performances in radically different configurations. Results have been compared with available experimental data in terms of both time-average and root mean square of the pressure coefficients in correspondence of the prism central section.

It appears that the changes in the flow topology due to the presence of incoming turbulence can be well reproduced by LES simulations. The shear layer instabilities arise closer to the leading edge when the higher level of inflow turbulence is analysed, leading to higher shear

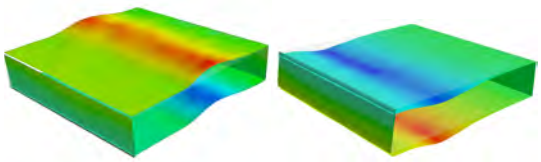

(a) Setup #2 - Mode 1 (b) Setup #6 - Mode 1

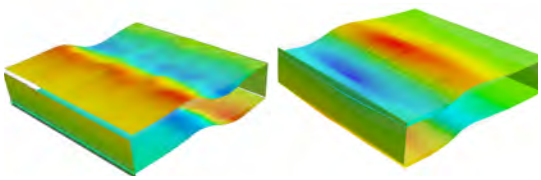

(c) Setup #2 - Mode 2 (d) Setup #6 - Mode 2

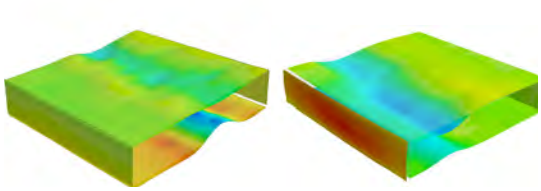

(e) Setup #2 - Mode 3 (f) Setup #6 - Mode 3

Figure 4.17: First three CPT mode shapes for the analysed setups.

layer curvature and consequently to a shorter reattachment length. The statistics of the pressure coefficient along the prism central section are well predicted by LES, even for low levels of incoming turbulence, the maximum C_p' is generally overestimated. When the higher inflow turbulence intensity is considered, results appear to be acceptable in terms of both time-average and root mean square of the pressure coefficient distributions, even if LES predicts the peak of C_p' slightly shifted downwind with respect to experimental data. It should be noticed in this case that the ratio between the inflow turbulence length scale and the domain spanwise extension plays an important role, showing that the accuracy of the obtained results significantly improves as this ratio decreases. Finding an appropriate compromise between accuracy and computational cost appears to be a challenging task in presence of large scale incoming turbulence as, in this cases, large domains should be ideally adopted in order to decrease the effects of the periodic boundary conditions leading to extremely demanding simulations.

Finally, Covariance Proper Transformation has been used in order to further characterize the flow dynamic behaviour. In such case, it has been observed that the presence of incoming turbulence leads to the concentration of the flow energy in antisymmetric CPT modes. In all, the numerical results are in good agreement with the experimental ones and show that the presence of incoming turbulence might represent an advantage in the simulation of reattached flows around bluff bodies.

ACKNOWLEDGEMENTS

The authors are thankful to CRIACIV for providing the experimental results and CINECA for providing the HPC facilities need to accomplish the present research work. In particular, we would like to thank Ivan Spisso for his invaluable constant support.

Part II

LES APPLICATIONS FOR ASSESSMENT OF WIND LOADS ON BUILDINGS

The traditional approach to validate numerical models when dealing with wind loading problems consists in comparing numerical predictions of the statistics of the pressure field to the corresponding experimental measurements. In order to assess LES capabilities to be adopted as a complementary design tool alongside wind tunnel tests, in this part LES results are compared to experiments not only in terms of pressure statistics distributions, but also in terms of internal forces in the structural members. First, LES are performed to assess wind loads on a low-rise building. Then, wind loads on a high-rise building are analysed. In both cases simulations are performed for different angles of attack in order to assess LES performances also when the envelope of different wind directions is considered.

5

WIND LOADS AND STRUCTURAL RESPONSE: BENCHMARKING LES ON A LOW-RISE BUILDING

This chapter has been published as:

Ricci, M., Patruno, L., de Miranda, S., *Wind loads and structural response: benchmarking LES on a low-rise building*, Engineering Structures, 144:26-42, 2017.
https://doi.org/10.1016/j.engstruct.2017.04.027

The correct and safe design of structures subjected to the wind actions requires a realistic estimate of the wind effects on their resisting systems. In this context, the present paper proposes a complete numerical study that, starting from Large Eddy Simulation of the turbulent flow around a low-rise building, arrives to the assessment of the wind loading effects, that is the evaluation of design forces in all structural members. Since it is well known that a realistic representation of the turbulent features found in the lower part of the atmospheric boundary layer is required in order to obtain accurate predictions of the structural response, firstly, the incoming flow turbulence is synthetically generated by means of the Modified Discretizing and Synthesizing Random Flow Generator technique. Then, the obtained synthetic fluctuation field is used as inflow condition for the subsequent Large Eddy Simulations taking into consideration different angles of attack. Results in terms of pressure distributions statistics are analyzed and systematically compared to experimental data. Finally, starting from both simulated and experimental pressure fields, dynamic structural analyses are performed and results directly compared in terms of design forces in the structural elements.

5.1 INTRODUCTION

The evaluation of wind effects often represents a delicate point in the design of light and slender structures relevant for Civil Engineering applications. Currently, standard design practice often involves the use of wind tunnel tests aimed at characterizing the wind action taking into consideration the aerodynamic behavior of the building itself and the expected site conditions in terms of terrain roughness and surrounding obstacles.

More recently, Computational Wind Engineering is receiving increasing attention and, in the next future, it can be foreseen that numerical simulations based on Computational Fluid Dynamics (CFD) will gradually complement and/or substitute the well established experimental practice in a number of Wind Engineering applications [9, 23, 68, 82, 104–107]. In fact, numerical approaches could potentially lead to remarkable savings in terms of time needed to set up the analyses and provide a flexible and powerful tool able to investigate phenomena which might be difficult to be represented when scaled models are adopted. Nevertheless, it should be noticed that, when bluff bodies are analyzed, CFD results often appear to be inaccurate even when simple geometries are considered [64, 108–112]. This is often due to the fact that the local stability criteria of shear layers, usually detached in correspondence of sharp edges, can strongly affect the overall flow arrangement rendering the global flow organization extremely sensitive to local behaviours. Unfortunately, such local effects are well known to be deeply influenced by the incoming flow characteristics, such as turbulence intensity and turbulence length scales [16] but, when computational models are considered, also by the adopted discretization schemes, the mesh sizing and the adopted turbulence model. The relative role of such aspects is nowadays not fully assessed and only a few studies tried to investigate the issue on a statistical base in order to validate CFD as a methodology rather than concentrating on a specific test case solved by adopting a particular setup [64].

In addition to the previously presented difficulties, exactly as in wind tunnel tests, another crucial aspect is represented by the generation of appropriate inflow conditions. In fact, an accurate evaluation of wind loads can not leave aside a realistic representation of the turbulent structures found in the lower part of the atmospheric boundary layer (ABL). In wind tunnel practice, the need for an artificial reproduction of the ABL led engineers to design boundary-layer wind tunnels with long working sections. In particular, Tieleman et al. [113] investigated the distributions of mean, standard deviation and

peak pressures on the roof of a low-rise building immersed in a turbulent boundary layer considering different roughness configurations. He concluded that much attention should be paid to the correct representation of the horizontal incoming turbulence intensity, in particular at the roof height. A review of available experimental techniques which might prove useful also in numerical simulations, together with new considerations useful to improve the quality of wind tunnel tests, have been proposed by Tieleman [114].

Regarding the wind flow around low-rise buildings, a large number of studies have been proposed in the literature aiming at comparing numerical results to wind tunnel and full scale measurements [115]. In particular, Richards et al. [116, 117] focused on the Silsoe Structures Building and compared wind tunnel measurements to numerical and full scale measurements, showing that a satisfactory agreement between the different data is obtained in terms of mean pressure coefficient, while differences increase when the fluctuating pressure coefficient and turbulent kinetic energy fields are analyzed. More recently, Ozmen at al. [118] investigated the wind flow around low-rise buildings with gabled roofs having different pitch angles, showing that in the recirculation regions and mixing layer results obtained by means of numerical simulations deviate with respect to experimental measurements, in particular in terms of turbulent kinetic energy.

From all previous considerations it is clear that, aiming at assessing the reliability of numerical simulations as a design tool, a careful validation of the accuracy of the results obtained by means of numerical models is mandatory before extensive application in practical cases. Such validation, should take into consideration all the aforementioned aspects and investigate their relative importance with respect to the evaluation of design values which are, indeed, the main quantity of interest. On such regard, it is observed that currently, in the majority of the cases, the accuracy of numerical simulations is assessed by comparing numerical results to experimental data in terms of pressure statistics distributions, usually up to the second order. It should be noted that, although such way of proceeding surely represents the first step of the aforementioned validation process, it can not be considered sufficient in order to fully assess numerical simulations as a design tool with respect to the dimensioning of structural systems. In fact, the characteristics of the pressure field, which contribute to the definition of the design loads, inevitably include also the pressure field spatial coherence, its spectral content and its higher order moments distributions. Although systematic comparison of all such quantities would be

theoretically possible, the resulting picture would probably not be of straightforward interpretation.

In the present paper, in order to overcome such difficulties, a synthetic approach is adopted. In particular, a low-rise building, for which wind tunnel tests results are publicly available, is considered. Firstly, Large Eddy Simulations (LES) are performed leading to the numerical evaluation of unsteady pressure distributions for all the building surfaces exposed to the wind action. The inflow conditions for such simulations are synthetically generated by means of the Modified Discretizing and Synthesizing Random Flow Generator technique (MD-SRFG) which allows to obtain a solenoidal fluctuating velocity field allowing to control its temporal and spatial correlations. According to standard practice, results are firstly analyzed in terms of integral forces and pressure statistics distributions on the building. Then, starting from both experimental and numerical results, dynamic structural analysis are performed for each considered attack angle leading to the definition of design envelopes which contains peak values of the design forces for each considered structural member. The comparison between such design envelopes, obtained by considering experimental and simulated pressure fields, allows to obtain direct indications regarding the accuracy of numerical models in terms of design forces. Adopting such a way of proceeding, all elements contributing to the definition of the structural response are naturally taken into account, so providing a synthetic comparison of the predictions of the adopted numerical model with respect to experimental evidences.

The paper is organized as follows. Section 7.3 describes the setup used to obtain experimental data while Section 5.3 describes the computational model adopted for the proposed simulations and discusses the obtained numerical results in terms of pressure statistics distributions by comparing them with available experimental data. Then, Section 6.5 analyses wind loads effects on the structure directly in terms of internal forces. Finally, in Section 7.7 some conclusions are drawn.

5.2 WIND TUNNEL SETUP

In this section, the experimental setup adopted to obtain pressure data used in the following for comparison with numerical results is described. Experiments were carried out at the Boundary Layer Wind tunnel of the Tokyo Polytechnic University (TPU) and are publicly available for download [7]. The database of the Tokyo Polytechnic University provides pressure measurements for a wide range of low-rise and high-rise buildings at different angles of attack and for different

terrain roughness conditions. In the present work the attention is focused on a low-rise building with gabled roof without eaves. The considered geometry is characterized by a height (H_0) to breadth (B) ratio equal to 2 : 4, a depth (D) to breadth (B) ratio equal to 3 : 2 and a roof pith angle (β) equal to 9.4° (see Fig. 5.2 (a)). In experiments the length scale was set at 1/100, leading to a model with $B = 160$ mm, $D = 240$ mm and $H_0 = 80$ mm. The wind tunnel section was 2.2 m wide and 1.8 m high, leading to a blockage ratio lower than 1%. The wind field profile reproduced in the wind tunnel corresponded to that of terrain category III according to the Architectural Institute of Japan (AIJ) standards [119]:

$$U(z) = 1.7\left(\frac{z}{Z_G}\right)^{\alpha} U_{ref}, \qquad Z_b < z \leqslant Z_G, \tag{5.1}$$

$$U(z) = 1.7\left(\frac{Z_b}{Z_G}\right)^{\alpha} U_{ref}, \qquad z \leqslant Z_b, \tag{5.2}$$

where the exponent α is equal to 0.2, Z_G is a reference height of the ABL equal to 450 m, Z_b represents the characteristic dimension of the surface roughness element and it is equal to 10 m while U_{ref} is the reference wind velocity measured at a height of 10 m (previously introduced quantities should be intended to be in full scale). In the wind tunnel tests here adopted for reference U_{ref} is equal to 7.4 m/s and it is measured at a height equal to z_{ref}=0.1 m from the wind tunnel floor.

In wind tunnel tests, also the turbulence intensity profile as prescribed by AIJ, has been reproduced. This profile is reported in Eqs. (6.3) and (6.4) for the terrain category III:

$$I(z) = 0.1\left(\frac{z}{Z_G}\right)^{-\alpha-0.05}, \qquad Z_b < z \leqslant Z_G, \tag{5.3}$$

$$I(z) = 0.1\left(\frac{Z_b}{Z_G}\right)^{-\alpha-0.05}, \qquad z \leqslant Z_b. \tag{5.4}$$

As in standard wind tunnel practice, the correct wind velocity profiles have been obtained by means of turbulence-generating spires and square blocks as roughness elements placed upstream the model.

It is noticed that, according to the experimental setup, the blocks distribution adopted in the preliminary simulation is uniform over the bottom of the wind tunnel, so an empirical estimation of the roughness

length can be also obtained by using the equation proposed by Lettau [120]:

$$z_0 = 0.5h\frac{A_r}{A_t}, \tag{5.5}$$

where z_0 is the roughness length as defined by EN1991-1-42005 [121], A_r is the area of the element normal to the wind direction and A_t is the ground area per roughness element, as reported in Fig. 5.1. The

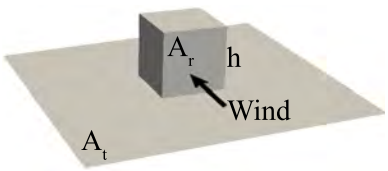

Figure 5.1: Roughness block geometry.

resultant roughness length is about 0.22 m in full scale, showing a good agreement with the roughness of the considered terrain category when compared to the analogous one reported in EN1991-1-42005 [121].

Experiments were conducted for seven wind directions, starting from $\theta = 0°$ to $\theta = 90°$ with a step of 15°. The wind angle of attack θ is defined so that $\theta = 0°$ corresponds to the direction parallel to the roof ridge, as reported in Fig 5.2 (b). The model was equipped with 192 pressure taps that acquired synchronously at a sampling frequency of 500 Hz for a duration of 18 seconds.

5.3 LARGE EDDY SIMULATIONS OF THE TURBULENT FLOW AROUND A LOW-RISE BUILDING

In this section, the characteristics of the adopted numerical model are described together with the obtained numerical results. Firstly, Section 5.3.1 describes the geometry of the computational domain, together with the numerical schemes and the adopted turbulence model. Then, in Section 5.3.2, a discussion of the turbulent inflow condition adopted for LES is provided. Finally, in Section 5.3.3, the LES results in terms of pressure statistics distributions are presented.

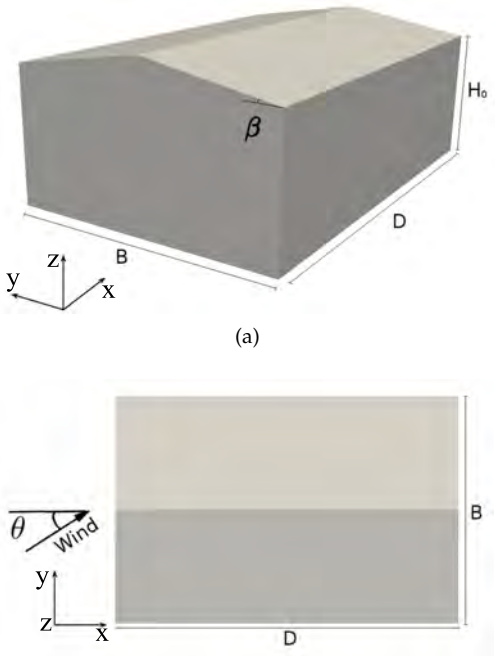

Figure 5.2: Geometry of the low-rise building: three-dimensional (a) and top (b) views.

5.3.1 *Numerical setups*

The computational domain dimensions together with the adopted reference system are reported in Fig. 7.4. The reference system origin is located in correspondence to the center of the building windward facade. The across-stream section is $27.5H_0$ wide and $22.5H_0$ high in accordance to the actual measures of the wind tunnel facility, while the distance of the building from the inlet boundary is set equal to $25H_0$ in order to avoid boundary conditions effects on the solution. The outflow boundary is placed at a distance equal to $37.5H_0$ from the building so that the overall domain dimensions result to be higher than the minimum requirements provided by Tominaga et al. [122]. Three rows of square blocks with edge length equal to $1.25H_0$ are placed upstream the model and arranged in agreement with the wind tunnel tests so that the minimum distance of the roughness blocks to the building model is equal to $12.5H_0$. The role played by such rows of blocks will be further discussed in Section 5.3.2.

The mean velocity profile is prescribed at the inlet boundary, while Neumann conditions on the stress tensor are imposed at the outlet. The fluctuating part of the velocity field is generated by means of the MDSRFG method and, then, introduced by modifying the pressure-velocity coupling algorithm as reported by Kim et al. [28]. Symmetry conditions are prescribed on top and lateral surfaces, while bottom and building surfaces are modeled as walls.

Grid independency of the solution, not here reported for brevity, has been checked by means of meshes with a refinement ratio equal to two in all directions in the proximity of the building. When negligible differences have been observed between subsequent refinements, the obtained mesh has been used for all subsequent analyses. In the resulting grid, a structured mesh is adopted close to the wall, where cell dimensions in x, y and z directions are respectively $\delta_x/H_0 = \delta_y/H_0 = 1.5 \times 10^{-3}$ and $\delta_z/H_0 = 1.3 \times 10^{-4}$, leading to a resolution higher than that suggested by Tominaga et al. [122]. In front of the building, the mesh sizing is slowly coarsened up to $\delta_x/H_0 = \delta_y/H_0 = \delta_z/H_0 = 2.5 \times 10^{-2}$ and then maintained constant until the inlet boundary is reached. No further coarsening has been adopted in order to minimize the numerical dissipation caused by the grid and, so, to correctly propagate incoming turbulent fluctuations. A frontal and a lateral view of the mesh in the proximity of the model are shown in Fig. 6.5.

As regards the sub-grid scales model, the Smagorinsky-Lilly turbulence model [123] with, in addition, the transport equation of the sub-grid turbulent kinetic energy is adopted. The near wall treatment is performed by adopting the van Driest damping function for the turbulent eddy viscosity.

The pressure-velocity coupling is obtained by means of the well known PISO algorithm, modified in order to introduce the incoming turbulence in the inflow region [28]. The time advancement scheme is the implicit two-step second order Backward Differentiation Formula [11]. The adopted dimensionless time step is $\Delta t^* = 8.75 \times 10^{-3}$, being $t^* = tU_{ref}/H_0$ the dimensionless time, leading to a maximum Courant number in all simulations equal to 3.1 and a mean one equal to 0.05. The mean dimensionless wall distance y^+ is equal to 2.3.

As regards the spatial discretisation, a centered second-order differentiation scheme is adopted for the diffusive terms, while, for non-linear advective terms, the LUST scheme with a blending factor equal to 0.25 is used. The LUST scheme is second order accurate and proved to be particularly successful for LES in complex geometries [124], offering a good trade-off between low dissipative behavior and numerical stability.

The building has been equipped with 1288 pressure monitors and data acquired at each time step. Simulations have been run by using the open source Finite Volume software OpenFOAM ® and, after performing some scalability tests, analyses have been performed by using 80 CPUs at CINECA on the Galileo cluster (516 nodes, 2-eight cores Intel®Xeon®2.40 GHz processors with 128 GB RAM per node). Each simulation required about 2.5×10^4 CPU hours.

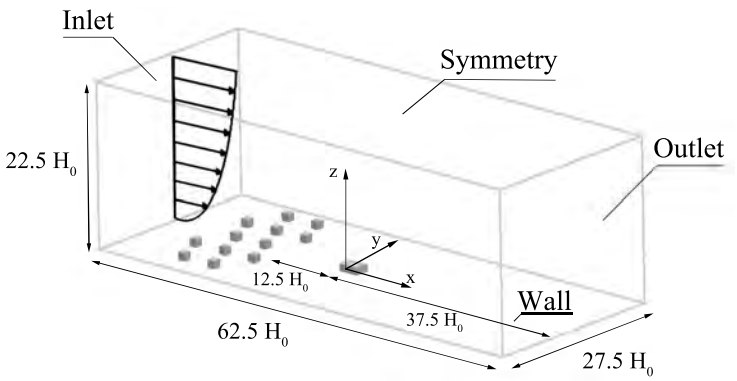

Figure 5.3: Computational domain adopted for the numerical study.

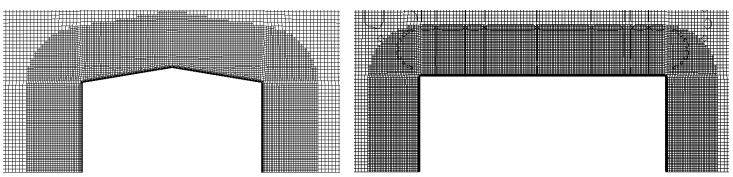

(a) (b)

Figure 5.4: Mesh adopted for LES near the building: frontal (a) and lateral (b) views.

5.3.2 *Inflow generation for LES*

In the following, details regarding the inflow generation adopted in the present simulation are reported. Firstly, a preliminary LES of the wind tunnel, including the complete upstream arrangements of roughness blocks, is performed in order to fully characterize the experimental conditions. Then, the obtained results are used in order to synthetically generate the inflow turbulence of the main simulation.

5.3.2.1 *Preliminary analysis*

Since the experimental measures of the turbulence length scales L are not explicitly reported in the aerodynamic database for low-rise buildings of TPU [7], a preliminary simulation is used in order to evaluate such quantity. The numerical setups and the turbulence sub-grid model adopted for this analysis are the same as those described in Section 5.3.1. A uniform and constant velocity profile is imposed at the inlet boundary and its value is set in order to have the same mass flow of the power-law profile recorded in experimental tests. Velocities are sampled at each time step in a grid of monitors arranged in a plane orthogonal to the flow and located where the model is placed during testing. The analysis is run as long as the wind tunnel tests and the post-processing has been done discarding the first $900t^*$, where t^* is the dimensionless time based on the height of the roughness blocks (indicated as h in Fig. 5.1) and U_{ref}.

Figure 5.5 (a) shows the geometry of the computational domain and the layout of obstacles, while Fig. 5.5 (b) shows the resulting topology of the flow by means of three-dimensional iso-contours of the second invariant of the velocity gradient tensor, hereinafter referred as Q, coloured by instantaneous pressure. As it can be seen from Fig. 5.5 (a), the reference system adopted in this case is the same as that reported in Fig. 7.4, so its origin corresponds to the section where the model will be placed afterwards.

The along-wind turbulence integral length scale is calculated from such simulation by applying Taylor's hypothesis and using the velocity time-histories measured at $(0,0,1.25H_0)$, that is at the reference height. The along-wind turbulence length estimated in such a way is equal to 0.35 m and it is found to be very close to the value of 0.4 m reported in Kim and Tamura [125], who describe an experimental setup which is very similar to that considered in the present study and relative to the same wind tunnel facility.

5.3.2.2 *Synthetic inflow conditions*

Once an estimate of the target integral turbulence length scale has been obtained by using the preliminary simulation, a synthetic inflow condition can be generated. In the present work, velocity fluctuations are synthetically generated by means of the MDSRFG method according to the anisotropic von Kármán spectra reported below:

$$S_u(f) = \frac{4(I_u U_{ref})^2 (L_u/U_{ref})}{[1 + 70.8(fL_u/U_{ref})^2]^{5/6}}, \tag{5.6}$$

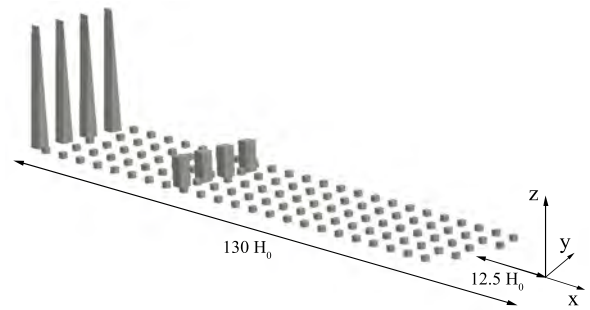

(a)

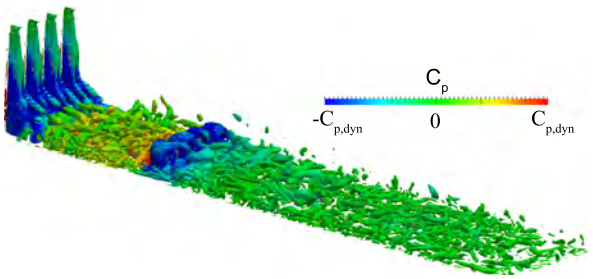

(b)

Figure 5.5: LES of the fetch as reported by the wind tunnel setup: three-dimensional view of the wind tunnel (a) and iso-contour of Q coloured by instantaneous pressure (b).

$$S_v(f) = \frac{4(I_v U_{ref})^2 (L_v/U_{ref})[1 + 188.4(2fL_v/U_{ref})^2]}{[1 + 70.8(fL_v/U_{ref})^2]^{11/6}}, \tag{5.7}$$

$$S_w(f) = \frac{4(I_w U_{ref})^2 (L_w/U_{ref})[1 + 188.4(2fL_w/U_{ref})^2]}{[1 + 70.8(fL_w/U_{ref})^2]^{11/6}}, \tag{5.8}$$

where I is the turbulence intensity, U_{ref} is the average wind velocity at the reference height as previously defined, L is the turbulence length scale and u, v, w subscripts indicate the components of the velocity vector in x, y and z directions, respectively. According to experimental measurements, the along-wind turbulence intensity is set as $I_u = 0.26$ at 10 m height in full scale, while, according to the literature, $I_v = 0.75 I_u = 0.195$ and $I_w = 0.5 I_u = 0.13$ [126].

Then, the upstream arrangement of obstacles has been removed, exception made for the first three alignments, and the domain shortened (see Fig. 7.4). The synthetic fluctuations field, generated by means of

the MDSRFG, is thus applied as inlet condition and introduced in a plane parallel to the inlet and shifted downwind with respect to it of 2.5×10^{-2} H_0, following the procedure proposed by Kim et al. [28].

Unfortunately, the MDSRFG method does not take as input the target value of the turbulence length scale but, rather, a length scale parameter [32]. Therefore, an iterative process is necessary in order to obtain a fluctuating velocity field characterized by the desired value of the turbulence length in correspondence to the section where the model is placed.

Then, several LES of the empty wind tunnel have been performed and velocities monitored. Simulations are iterated until the length scale parameter adopted for the inflow generation is able to reproduce the target turbulence characteristics in the testing section. Figure 7.8 reports the profiles on the central alignment of the average velocity, of the turbulence intensity and of the turbulence integral length measured along the vertical alignment at $x/H_0 = y/H_0 = 0$ (see Fig. 7.4 and Fig. 5.5 (a)). Aiming at comparing experimental and numerical results, these profiles are plotted by analyzing data obtained by using LES of the wind tunnel, LES of the testing section with the synthetic inlet condition and from experimental measurements. Furthermore, a comparison with the AIJ standard is provided.

Focusing on the average wind velocity profile shown by Fig. 7.8 (a), a very good agreement between experimental measurements and data obtained by means of LES with the synthetic inlet is observed. Indeed, experimental and numerical profiles appear to be very close to each other, in particular in the lower part of the simulated ABL, which is of major interest for low-rise buildings. As regards the along-wind turbulence intensity, Fig. 7.8 (b) shows that the profile obtained by using the synthetic inlet condition is in good agreement with that obtained by simulating the wind tunnel, even if both of them slightly underestimate the turbulence intensity when $z/z_{ref} < 1$. It should be noticed that, this part of the ABL represents the roughness sub-layer in which turbulence and mean profiles are deeply affected by the geometry of the roughness elements. In order to reproduce the constant turbulence intensity shown by experimental data in this region, three rows of roughness blocks are explicitly considered in simulations, even when the synthetic inlet is adopted. It should be pointed out that this methodology is not usually adopted in this kind of simulations, in fact in most of cases, when a synthetic inlet is adopted, no rows of roughness elements are introduced. Nevertheless, these rows of blocks are of fundamental importance for obtaining accurate profiles in the roughness sub-layer, that is of major interest when dealing with low-rise

buildings. In fact, when such elements are not adopted, the incoming velocity profile accelerates due to the reduced roughness of the building surroundings, introducing inaccuracies that are particularly strong in the lower part of the profile. Regarding the turbulent length reported in Fig. 7.8 (b), a reasonable agreement can be considered achieved between the LES of the wind tunnel and that with the synthetic inlet condition.

The spectra of the three velocity components, respectively S_u, S_v and S_w measured at $y/H_0 = 0$, $z/H_0 = 1.25$ and at two different along-wind positions corresponding to $x/H_0 = -12.5$ and $x/H_0 = 0.0$ are reported in a dimensionless form in Fig. 7.9. As it can be seen, the target von Kármán spectra at $x/H_0 = 0$ can be considered well reproduced, even if, as expected, some numerical dissipation is observed with respect to the last alignment of roughness blocks (at $x/H_0 = -12.5$) in particular in the high frequency range.

In all, the synthetic inlet condition performances are considered to be satisfactory, leading to profiles that are in good agreement with experimental measurements. Therefore, the synthetically generated fluctuation field is adopted as inlet condition for all the subsequent simulations.

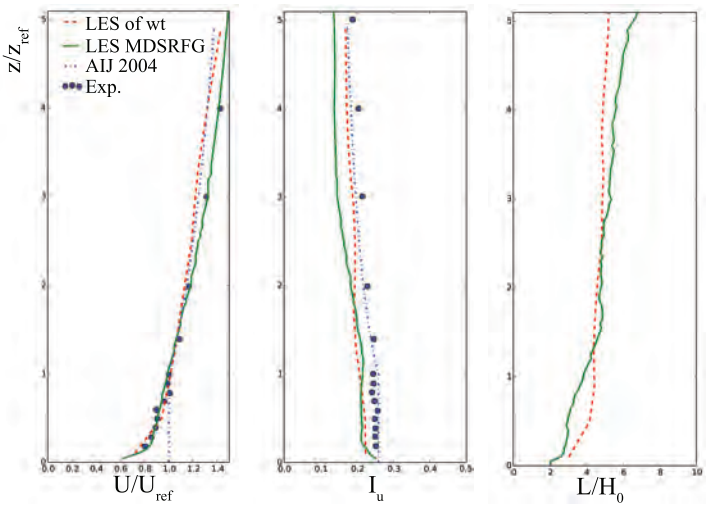

Figure 5.6: Wind velocity profiles measured in the wind tunnel along the vertical alignment at $x/H_0 = y/H_0 = 0$: average (a), turbulence intensity (b) and turbulence length (c) profiles.

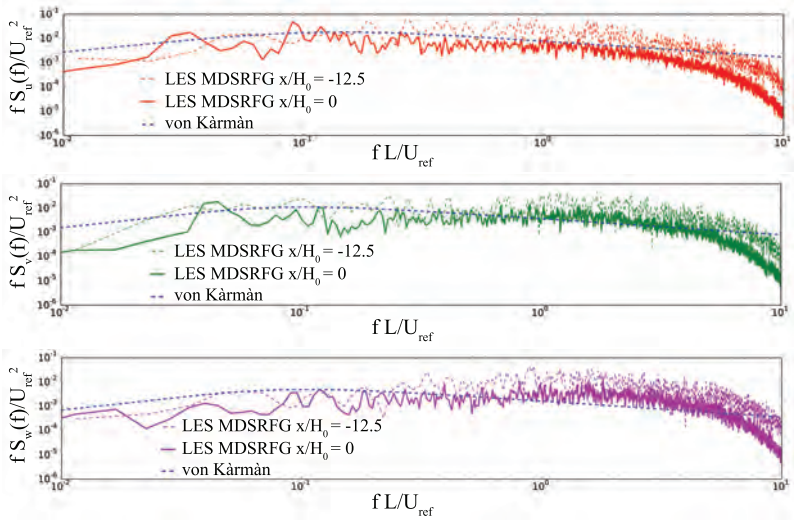

Figure 5.7: Spectra of the velocity time series obtained from LES at $y/H_0 = 0$, $z/H_0 = 1.25$ and at different along-wind positions.

5.3.3 *Large Eddy Simulations results*

In this section, the numerical results obtained for three angles of attack, respectively 0°, 45° and 90°, are reported and systematically compared to experimental data. Each simulation is run for a total time of $t^* = 1900$ being t^* the dimensionless time as defined in Section 5.3.1. In order to avoid flow initialization effects, the first 300 dimensionless time units are disregarded in the post-processing of the data, so that the duration of each analysis is the same of wind tunnel tests. Pressures are recorded at each time step in correspondence of the probe positions reported by the experimental setup and showed in Fig. 5.8 (a). Then, data are coarsened in order to match the sampling frequency of 500 Hz adopted in the wind tunnel tests.

A view of the flow topology obtained by LES can be appreciated in Fig. 5.9 for the angles of attack of 0° and 45°. In particular, three-dimensional instantaneous iso-contours of Q coloured by instantaneous pressure are reported.

The statistics of the flow bulk parameters are reported in Table 6.1, where C_D and C'_D represent respectively the mean and the standard deviation of the drag coefficient made dimensionless with respect to H_0, while C_L and C'_L represent the same quantities for the lift coefficient. It can be observed that a satisfactory agreement between experimental measurements and data obtained from LES can is achieved for

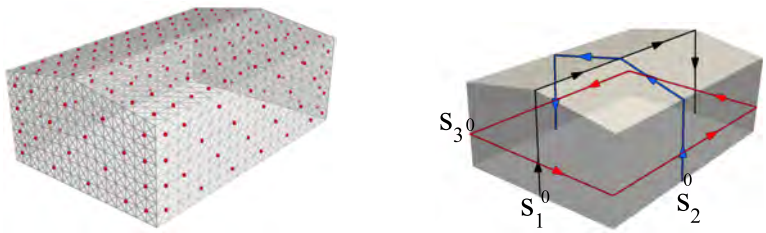

(a) (b)

Figure 5.8: Position of pressure probes according to the experimental setup (a) and view of curvilinear abscissae adopted for plotting the pressure coefficient statistics (b).

all the angles of attack, being the relative difference lower than 10% in most cases, exception made for the lift coefficient at 90°, that appears to be underestimated by the simulation of about 16%.

Angle	Source	C_D	C'_D	C_L	C'_L
0°	LES MDSRFG	1.842	0.595	2.664	1.066
	Exp.	1.950	0.730	2.895	0.976
45°	LES MDSRFG	1.478	0.490	3.848	1.200
	Exp.	1.655	0.623	4.251	1.125
90°	LES MDSRFG	-0.07	0.451	4.001	1.255
	Exp.	-0.027	0.447	4.795	1.240

Table 5.1: Statistics of the flow bulk parameters.

As regards the statistics of the pressure coefficient C_p, they are analyzed in terms of average, hereinafter referred as $\overline{C_p}$, and standard deviation, denoted as C'_p. These quantities are plotted for each angle of attack along three different curvilinear abscissae as reported by Fig. 5.8 (b). In order to compare numerical and experimental results along these paths, the experimental measurements are interpolated starting from the probes positions showed in Fig. 5.8 (a).

5.3.3.1 *Angle of attack:* 0°

The distributions of the pressure coefficient statistics are reported for the angle of attack of 0° in Figs. 5.10, 5.11 and 5.12 for paths S_1, S_2 and S_3, respectively (Fig. 5.8 (b)). Focusing on the mean pressure coefficient $\overline{C_p}$, it can be noticed that a very good agreement is obtained between numerical and experimental data, being the two curves almost overlapping for all the considered paths. In particular, mean suctions on the roof are well predicted by LES (see Fig. 5.10 (a)), and

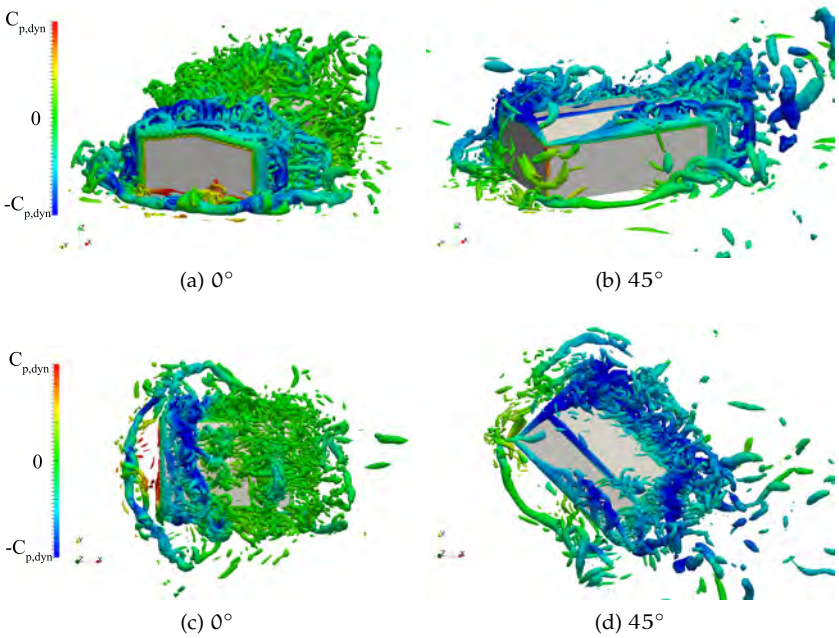

(a) 0° (b) 45°

(c) 0° (d) 45°

Figure 5.9: Flow topology at different angles of attack: the three-dimensional views of LES are presented as Q isosurfaces (5.0×10^4) coloured by instantaneous pressure.

this is reflected also in a satisfactory prediction of the mean lift coefficient, as reported in Table 6.1. Regarding the standard deviation of the pressure coefficient C'_p, LES and experimental data show to be in satisfactory agreement, even if discrepancies are slightly higher than those observed for mean values distributions. Nevertheless, it should be noticed that the maximum difference between experimental and numerical data is equal to about 28% and it is recorded in correspondence of the close proximity of the leading edge of the roof, as it can be observed in Fig. 5.10 (b) at $S_1/H_0 \leqslant 1.2$. As expected, the prediction of the suction peaks in the proximity of these points represents a very demanding request for numerical simulation.

Due to the problem geometry and boundary conditions, numerical and experimental results are expected to be symmetric and distributions show to reflect this property in a satisfactory way, for both $\overline{C_p}$ and C'_p. In fact, by observing Fig. 5.11, data show to be symmetric with respect to the axis $S_2/H_0 = 2$, and looking at Fig. 5.12, results

for $2 \leqslant S_2/H_0 \leqslant 6$ appear to be mirrored with respect to those for $6 \leqslant S_2/H_0 \leqslant 10$.

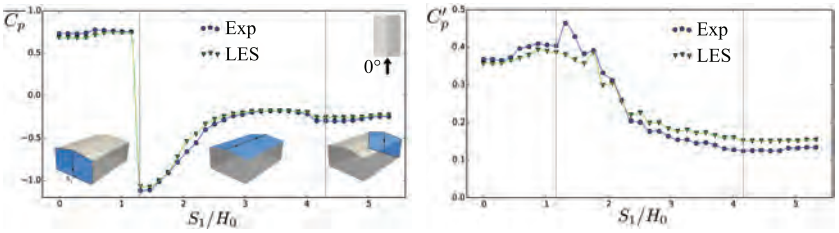

(a) (b)

Figure 5.10: Pressure coefficient along the curvilinear abscissa S_1 for 0°: average (a) and standard deviation (b).

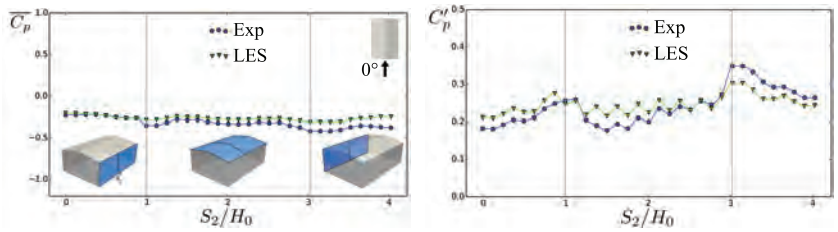

(a) (b)

Figure 5.11: Pressure coefficient along the curvilinear abscissa S_2 for 0°: average (a) and standard deviation (b).

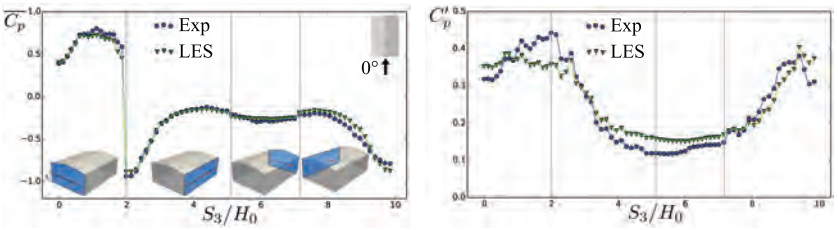

(a) (b)

Figure 5.12: Pressure coefficient along the curvilinear abscissa S_3 for 0°: average (a) and standard deviation (b).

5.3.3.2 *Angle of attack:* 45°

Focusing on the angle of attack of 45°, as already observed for 0°, a very good agreement between numerical and experimental data in terms of $\overline{C_p}$ is achieved for all considered paths, as it can be seen in Figs. 5.13 (a), 5.14 (a) and 5.15 (a). Also in this case, the maximum suction on the roof edge is slightly underestimated by LES. Looking at distributions in terms of C'_p, LES correctly predicts peaks positions for all the considered paths and fits very well to the experimental curves, being the two distributions very close to each other on all sides of the building. The maximum deviations from experimental results is observed for path S_1 (Fig. 5.13 (b)), where differences with respect to wind tunnel measurements are of about 30%.

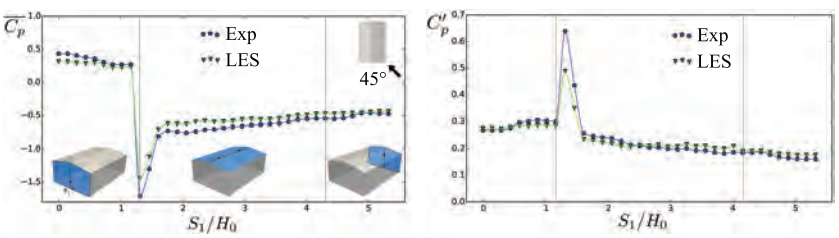

(a) (b)

Figure 5.13: Pressure coefficient along the curvilinear abscissa S_1 for 45°: average (a) and standard deviation (b).

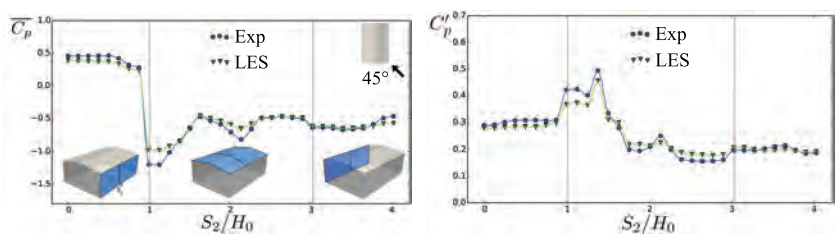

(a) (b)

Figure 5.14: Pressure coefficient along the curvilinear abscissa S_2 for 45°: average (a) and standard deviation (b).

5.3.3.3 *Angle of attack:* 90°

For what it concerns the angle of attack 90°, Figs. 5.16 (a), 5.17 (a) and 5.18 (a) show that experimental and numerical prediction of $\overline{C_p}$

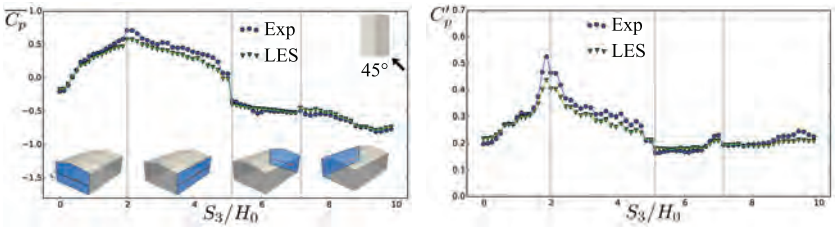

(a) (b)

Figure 5.15: Pressure coefficient along the curvilinear abscissa S_3 for 45°: average (a) and standard deviation (b).

are in good accordance, even if, again, the maximum suction on the roof is slightly underestimated by LES (Fig. 90° at $S_2/H_0 \approxeq 1$). The simulation predicts in a satisfactory way the characteristics of the distributions of C'_p, being this close to experimental data for all alignments with good accuracy. Again, as expected, Figs. 5.16 (a) and (b) show to be symmetric with respect to the axis $S_1/H_0 = 2.67$, while in Figures 5.18 (a) and (b) data for $0 \leqslant S_3/H_0 \leqslant 3.5$ are symmetric with respect to those for $3.5 \leqslant S_3/H_0 \leqslant 7.0$.

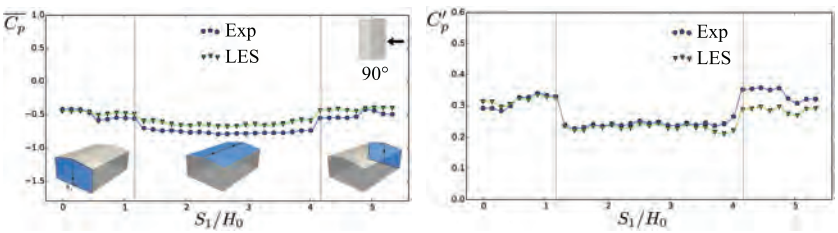

(a) (b)

Figure 5.16: Pressure coefficient along the curvilinear abscissa S_1 for 90°: average (a) and standard deviation (b).

5.3.3.4 *Some remarks*

In this section, aiming at providing a synthetic picture of the obtained results, statistics of the pressure coefficient are analyzed by comparing experimental measurements and numerical data for each pressure probe by representing them in the form of correlation plots, reporting in abscissa the experimental data and in ordinate the corresponding values obtained by means of LES. Figure 6.14 shows the correlation plots obtained for the angle of attack of 0°, while Fig. 6.26 and Fig.

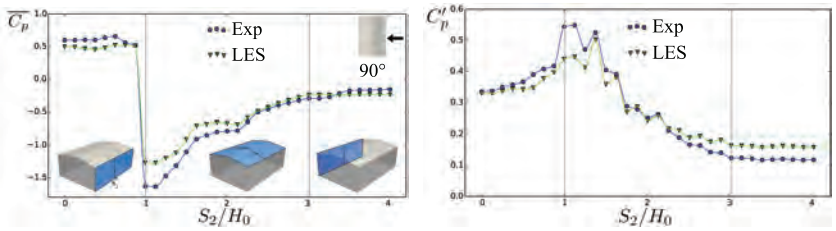

(a) (b)

Figure 5.17: Pressure coefficient along the curvilinear abscissa S_2 for 90°: average (a) and standard deviation (b).

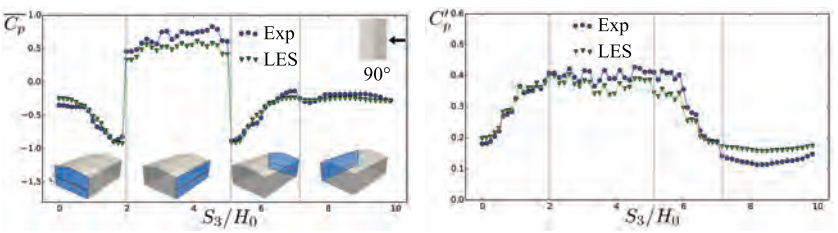

(a) (b)

Figure 5.18: Pressure coefficient along the curvilinear abscissa S_3 for 90°: average (a) and standard deviation (b).

6.27 report the same plots for 45° and 90°, respectively. For all the three angles, the mean pressure coefficient $\overline{C_p}$ results to be well predicted by simulations for all probes. As expected, results are concentrated in the proximity of the bisector and Table 5.2 shows that for 0°, 98% of them falls in the range of tolerance of 30%, while for 45° and 90° the percentage of points in the same range is equal to 91.8% and 89.4%, respectively. Regarding the standard deviation of the pressure coefficient, the correlation plots show a slightly wider dispersion around the bisector if compared to those concerning $\overline{C_p}$. Nevertheless, as reported in Table 5.2, also results regarding C'_p can be considered satisfactory considering that 92.7% and 97.9% of points is in the range of tolerance of 30% for 0° and 45°, respectively. When 90° angle of attack is considered, the percentage of points in the same tolerance is equal to 89.6%.

In all, the statistics of the pressure distributions obtained by LES can be considered in good accordance with experimental data over the whole building surface. In order to investigate how differences in terms of pressure distributions are reflected when internal forces on

the structural elements are analyzed, in the next section the pressure field obtained by LES together with that recorded in wind tunnel tests are used as inputs for dynamic structural analyses.

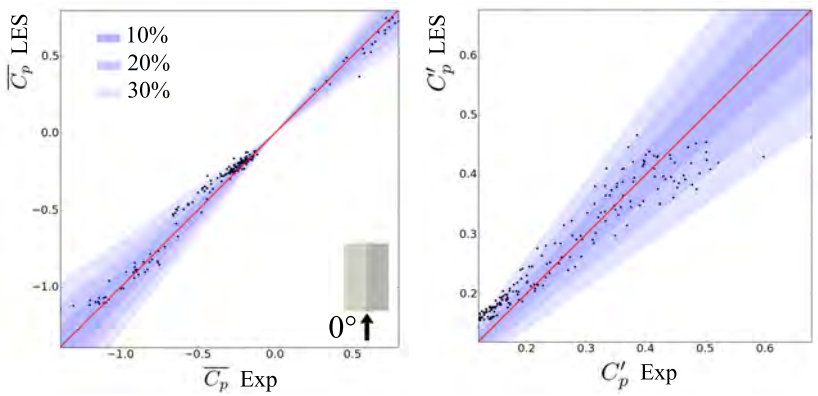

(a) (b)

Figure 5.19: Correlation graphs of the pressure coefficient over the whole building for 0°: average (a) and standard deviation (b).

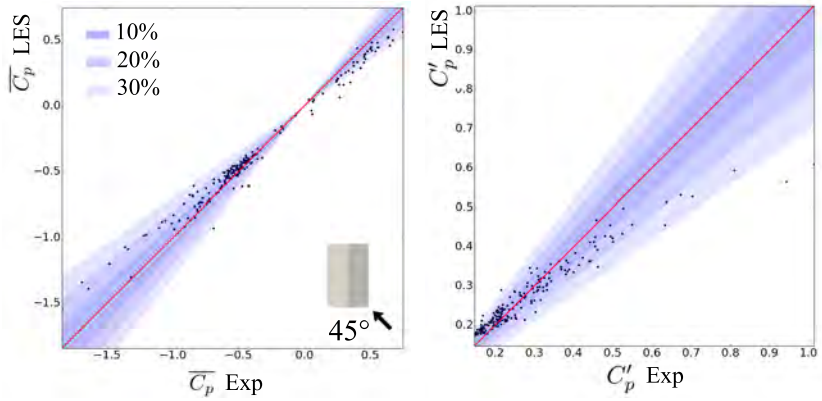

(a) (b)

Figure 5.20: Correlation graphs of the pressure coefficient over the whole building for 45°: average (a) and standard deviation (b).

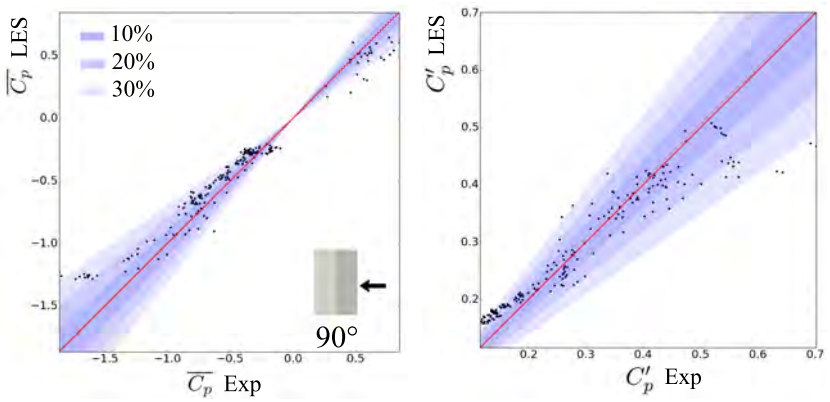

(a) (b)

Figure 5.21: Correlation graphs of the pressure coefficient over the whole building for 90°: average (a) and standard deviation (b).

Tolerance	0°		45°		90°	
	$\overline{C_p}$	C'_p	$\overline{C_p}$	C'_p	$\overline{C_p}$	C'_p
10%	53.1 %	38.5 %	50.52 %	51.6 %	20.3 %	46.9 %
20%	87.5 %	70.3 %	84.4 %	90.6 %	63.5 %	73.4 %
30%	97.4 %	92.7 %	92.7 %	97.9 %	85.4 %	89.6 %

Table 5.2: Pressure coefficient: comparison between experimental and numerical data.

5.4 ASSESSMENT OF WIND LOADING EFFECTS

In this section, starting from both recorded and simulated pressure fields, linear dynamic structural analyses are performed for each considered angle of attack, aiming at investigating wind effects in terms of internal forces on structural elements. In order to do this, a structural model of the low-rise building is considered.

The structure of the building is reported in Fig. 5.22 and it is 24 m long and 16 m wide, while the height of the columns is 8 m. The roof is composed of six trussed beams positioned every 4.8 m and purling with spacing 2.0 m in plan view. The structural properties of the adopted elements are reported in Tab. 5.3, where E is the elastic modulus, A is the cross-section area and I_{11} and I_{22} are the principal moments of inertia, that are not reported for the wind bracing elements, since they are modeled as trusses. The columns are clamped at their

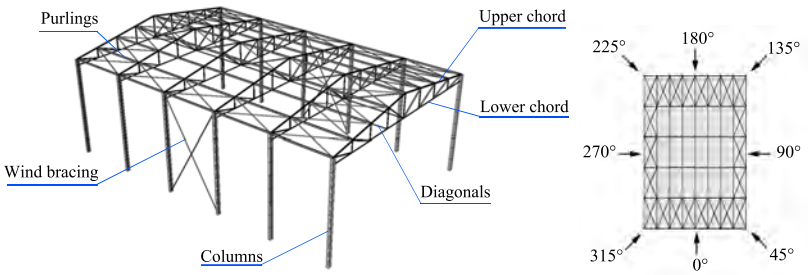

Figure 5.22: Structure of the building: (a) prospective view, (b) plan view (adapted from Patruno et al. [127]).

base sections. The building is considered to be completely closed on the sides by elements which are not considered in the structural analysis. The first three structural modes of the building are reported in Fig. 5.23.

Element	Section type	E [Pa] [$\times 10^{11}$]	A [m^2]	I_{11} [m^4]	I_{22} [m^4]
Columns	HE 220 B	2.06	9.1×10^{-3}	8.09×10^{-5}	2.84×10^{-5}
Purlings	IPE 120	2.06	1.32×10^{-3}	3.18×10^{-6}	2.77×10^{-7}
Upper chord	C-channels x2	2.06	1.42×10^{-3}	5.35×10^{-7}	8.71×10^{-7}
Lower chord	L-section x2	2.06	7.50×10^{-4}	1.89×10^{-7}	1.69×10^{-7}
Diagonals	L-section x2	2.06	9.50×10^{-4}	5.80×10^{-7}	2.25×10^{-7}
Wind bracing	Round	2.06	4.75×10^{-4}	-	-

Table 5.3: Structural properties of the elements constituting the building.

Results are presented in terms of axial forces in 585 monitored sections. Due to the symmetry of the structure, the pressure field is mirrored in order to reproduce wind effects also for 135°, 180°, 225°, 270° and 315°. In particular, structural dynamic analyses are performed by calculating time-histories of the structural response following the procedure proposed in [127]. In particular, this procedure calculates the structural response my means of modal superposition and introduces quasi-static corrections in order to take into account the effect of high frequency modes. In such a way, all three components of the structural response to wind excitation are correctly taken into account (namely static, quasi-static and resonant contributions). The design wind speed is set to 25 m/s while the structural damping is provided by means of the Rayleigh method imposing its value to be 3.0% for the first and third structural modes.

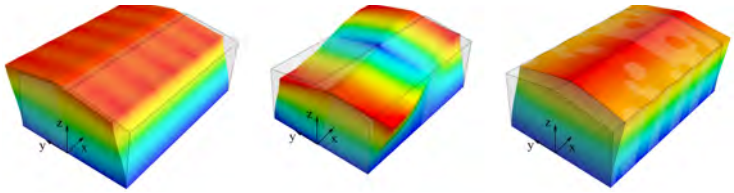

(a) 1.66 Hz (b) 2.47 Hz (c) 2.99 Hz

Figure 5.23: Structural modes of the building: first three modes (adapted from Patruno et al. [127]).

Figure 5.24 (a), (b) and (c), show the correlation plot of the standard deviation of axial forces, indicated as N', for 0°, 45° and 90°, respectively, while Figure 5.24 (d) reports the envelope obtained by considering all possible attack angles. As it can be seen, results in terms of N' given by LES are in good agreement with those obtained by using experimental measurements for the structural analyses. Nevertheless, it should be noticed that, in this case, LES tend to overestimate the fluctuating load for all the considered cases, although the incoming flow turbulence is slightly underestimated in the simulations, as reported in Fig. 7.8. Table 5.4 reports, for each case of Fig. 5.24, the percentage of points that show a difference between experimental and numerical values lower than 10%, 20% and 30%, here indicated as ranges of tolerance. Comparing data showed in this table to those reported in Table 5.2 (which concerns the statistics of the pressure coefficient) it can be seen that when C_p' is considered, for all the considered cases, the percentage of points in the range of tolerance of 30% is always higher than 85% while, regarding axial forces, this value decreases down to 53.6%, 58.7% and 57.9% for 0°, 45° and 90°, respectively. Therefore, as expected, it appears that the accuracy showed by LES regarding the standard deviation of the pressure fields does not lead automatically to the same precision when the standard deviation of internal forces is considered. Nevertheless, when the total envelope is observed, Table 5.4 shows that the percentage of points in the range of 30% of tolerance grows up to 88.3%.

Aiming at providing a synthetic comparison between LES and experimental results also in terms of yielded design values, Figure 5.25 (a), (b) and (c), show the correlation plot of the peak of axial forces, indicated as N_{peak}, for 0°, 45° and 90°, respectively. The peak axial force is here simply defined as the mean value plus (and minus) 3.5 times the standard deviation. Finally, Fig. 5.25 (d) reports the envelope obtained by considering all possible attack angles. Although the agreement be-

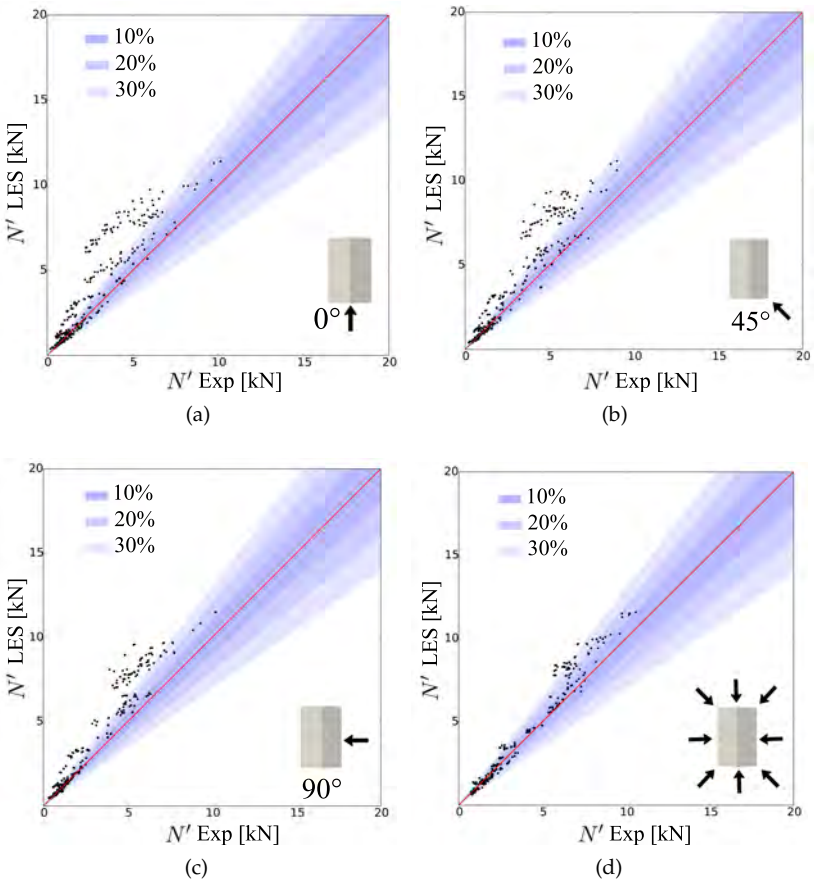

Figure 5.24: Correlation graphs of the standard deviation of axial forces: angle of attack of 0° (a), 45° (b), 90° (c) and total envelope considering also 135°, 180°, 225°, 270° and 315° (d).

Tolerance	0°	45°	90°	Total envelope
10%	28.4 %	29.6 %	32.0 %	48.0 %
20%	45.1 %	48.3 %	43.0 %	77.4 %
30%	53.6 %	58.7 %	57.9 %	88.3 %

Table 5.4: Standard deviation of the axial force N′: comparison between experimental and numerical data.

tween numerical and experimental results is satisfactory, also in this case LES tend to overestimate the peak load. Indeed, Table 5.5 shows that if the data outside the 30% of tolerance are analyzed, LES predic-

tions are higher than the experimental ones for the 97.2%, 96.6% and 99.7% when 0°, 45° and 90° are considered, respectively. Interestingly, in this case, when the total envelope is analyzed, 100% of axial forces predicted by LES outside the largest range of tolerance are overestimated. It should be anyway noticed that the effects on highly stressed members are usually correctly reproduced in the overall envelope.

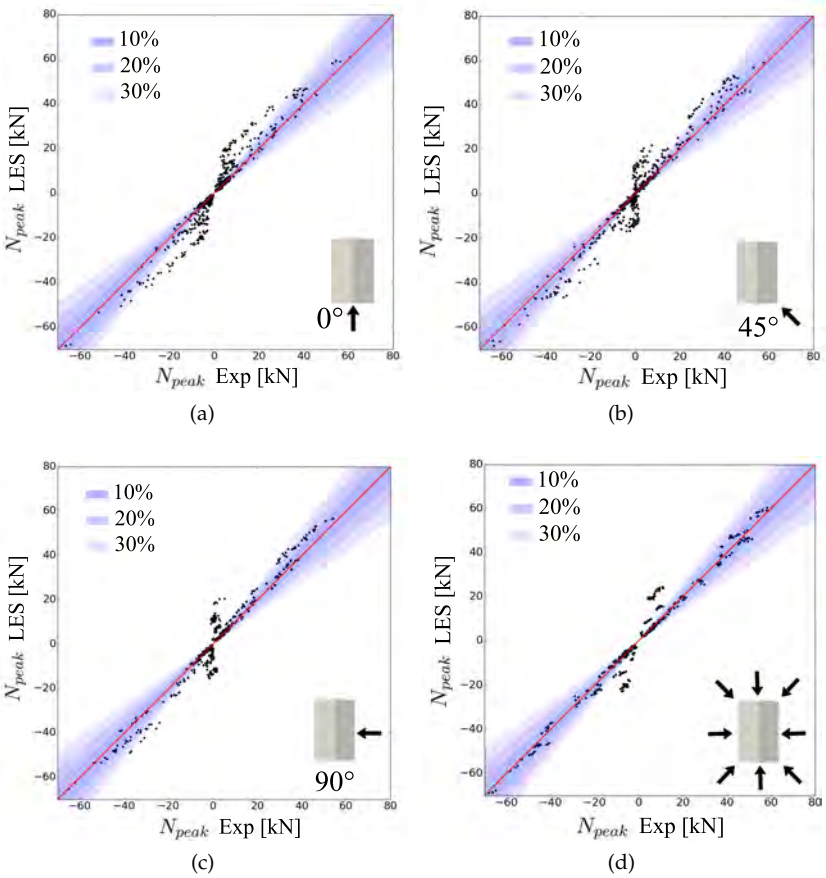

Figure 5.25: Correlation graphs of peak of axial forces: angle of attack of 0° (a), 45° (b), 90° (c) and total envelope considering also 135°, 180°, 225°, 270° and 315° (d).

Tolerance	0°	45°	90°	Total envelope
10%	25.9 %	35.5 %	36.4 %	50.3 %
20%	48.1 %	53.2 %	55.0 %	72.1 %
30%	57.1 %	62.0 %	63.6 %	76.0 %
Data outside 30% of tolerance overestimated by LES	97.2 %	96.6 %	99.7 %	100 %

Table 5.5: Peak axial forces N_{peak}: comparison between experimental and numerical data.

5.5 CONCLUSIONS

In the present paper, the accuracy of LES as a design tool in the prediction of wind loads on structures has been investigated. To this purpose, LES of the turbulent flow around a low-rise building were performed and, then, the simulated pressures were used to evaluate the design forces in all structural members.

As regards LES, firstly a simulation of the wind tunnel facility was carried out, including the upstream arrangement of roughness blocks as reported by the experimental setup, in order to fully characterize the turbulent profile adopted in the wind tunnel tests. Then, the MDSRFG method was used in order to synthetically reproduce such turbulent inflow conditions. In addition to the synthetically generated turbulence, three rows of blocks (placed according to the experimental setup) were explicitly included in the simulations. These rows of blocks are of fundamental importance in order to obtain accurate profiles of turbulence characteristics in the roughness sub-layer, that is of major interest when dealing with low-rise buildings. Simulations of the empty wind tunnel testing section highlighted a good agreement between experiments and numerical simulations in terms of the incoming wind profile. Finally, once the inflow condition was properly reproduced, a LES of the flow around a gable roof low-rise building was performed taking into consideration different angles of attack. It appears that, the mean pressure coefficient field is well predicted by simulations, while its standard deviation is predicted by the numerical model in a less accurate way. Nevertheless, also for second order statistics of the pressure coefficient a good accuracy can be considered achieved, considering that about 90% of monitored points show a difference between experimental data and numerical predictions lower than 30%. It should be noticed that, as expected, these discrepancies are mainly observed in correspondence to the building edges.

As regards the evaluation of design forces in the structural members, once pressure distributions have been obtained, starting from both measured and simulated unsteady pressure fields, linear dynamic structural analyses were performed aiming at comparing results in terms of axial forces in each element of the structure.

It is found that internal forces predicted by LES are in good agreement with those obtained starting from experimental data, even if, with respect to pressure distributions, results are less accurate. Nevertheless, it should be noticed that inaccuracies of the numerical model in terms of axial forces are mainly due to overestimation. Even more interestingly, it is found that when a single angle of attack is considered, LES predictions show some inaccuracies, especially for mildly stressed members. On the other side, when the envelope is built by taking into consideration all wind directions, this effect is greatly reduced. This fact might be due to difficulties in accurately simulating secondary flow mechanisms when a single angle of attack is considered. When all wind directions are taken into consideration simultaneously, it is reasonable to assume that each structural member will be involved in the structural response triggered by a global flow mechanism which will lead to the maximum value in the considered element. Following such a conjecture, it is expected that the reproduction of the extreme values of the structural response obtained by considering all possible attack angles will be generally more accurate than a partial analysis in which only one wind direction is considered. The obtained results, at the current stage, appear to confirm such a hypothesis.

Summarizing, it can be stated that the present study indicates that, aiming at assessing the potential of LES as a design tool, on one side, the simple comparison of pressure distributions statistics should not be considered sufficient: this is due to the fact that, besides the first two statistical moments of the pressure distribution, many parameters can deeply influence the structural response to the wind action. On the other side, it is found that considering a single attack angle might be excessively restrictive as inaccuracies in the prediction of secondary flow mechanisms might be responsible for biases which, when all attack angles are considered, be proved to be of limited significance. Although further research is surely needed on the topic and cases involving structure nonlinearity and/or aeroelasticity should be taken into account, the presented results appear to be extremely encouraging in the assessment of LES as a design tool in Civil Engineering applications.

ACKNOWLEDGEMENTS

The authors are thankful to CINECA for providing the HPC facilities needed to accomplish the present research work.

6

TOWARDS LES AS A DESIGN TOOL:WIND LOADS ASSESSMENT ON A HIGH-RISE BUILDING

This chapter has been submitted as:

Ricci, M., Patruno, L., de Miranda, S., *Towards LES as a design tool:wind loads assessment on a high-rise building.*, Journal of Wind Engineering and Industrial Aerodynamics.

The accurate evaluation of wind loads on high-rise buildings represents a key point in their design process. The traditional approach followed for their wind load assessment is represented by wind tunnel tests. Recently, thanks to the increase in computers power, Computational Fluid Dynamics (CFD) techniques gained interest among the scientific community as a complementary tool to experimental campaigns. Unfortunately, the wind flow around bluff bodies, typical in Civil Engineering applications, often appears to be very complex and a strong research effort is still needed in order to assess the accuracy and reliability of CFD results. In this paper, Large Eddy Simulations are performed aiming at assessing the wind loads on an isolated high-rise building. In particular, an unsteady inflow condition, representative of the turbulence encountered in the atmospheric boundary layer, is synthetically generated by means of the Modified Discretizing and Synthesizing Random Flow Generator technique. Firstly, the obtained numerical results are compared to experimental measurements in terms of pressure distribution statistics. Then, in order to evaluate the structural response, transient structural analyses are performed taking into consideration both numerical and experimental unsteady pressure distributions. It is found that the accuracy of LES in reproducing the fluctuating pressure field is not necessarily maintained when internal forces are taken into account. Nevertheless, the design values predicted by LES can be still considered satisfactory, in particular when global envelopes are considered.

6.1 INTRODUCTION

The new generation of high-rise buildings is leading to taller and more slender structures with respect to the past while their shape appears to be increasingly complex and often unconventional. Due to these characteristics, particular attention has to be paid to the design of these structures that have to face increasing environmental loads while still remaining as light as possible. In particular, wind loads on tall buildings may play a fundamental role in the design process and have to be accurately assessed with respect to both structural integrity and serviceability [128].

In particular, the turbulence naturally present in the Atmospheric Boundary Layer (ABL), together with aerodynamic phenomena typical of bluff bodies, like vortex-shedding and detachments/reattachment of the shear layers, causes the structure to experience dynamic forces, thus leading to along wind and across wind vibrations.

The traditional approach for the assessment of wind loads on high-rise buildings strongly relies on wind tunnel practice. The most commonly adopted experimental techniques can be ideally subdivided into three main methodologies. In particular, the High-Frequency Force Balance (HFFB) method, initially developed by Tschanz et al. [129], represents one of the first approaches proposed in order to address the problem. The HFFB method satisfied the need for a relatively simple technique able to evaluate the structural response in a reduced time, without employing expensive aeroelastic models and, at the same time, without introducing simplifications typical in analytical approaches and not of general applicability [130–132]. The main characteristic of this method is that the structural response can be reconstructed by measuring only forces and moments at the building base. According to this experimental approach, a rigid model of the building is mounted on a balance characterized by high stiffness and high sensitivity, which records time-histories of shear forces, torque and bending moments. Then, the structural response can be evaluated by post-processing results in the frequency domain or in the time domain. Historically, the frequency domain approach prevailed over the time domain one due its reduced computational cost. Adopting a stochastic framework, the power spectral densities of the generalized forces acting on the building are assumed to be proportional to the power spectral densities of the measured integral forces according to factors defined as mode shape corrections [133]. Alternatively to this approach, Xie et al. [134] avoided the use of mode shape corrections by post-processing data directly in the time domain. In this case, the generalized forces are

reconstructed by assuming a linear pressure variation over the building height. The slope of such distribution is calculated at each time by equilibrium considerations starting from the balance measurements. It should be noted that methodologies based on the use of HFFB always imply the introduction of assumptions with respect to the structural behaviour and/or the pressure distributions. Due to this considerations, the HFFB method can perform well only for the fundamental modes of the structure [5], while high frequency modes effects can not be satisfactorily predicted and structures characterized by unconventional geometries cannot be easily studied. Furthermore, in order to avoid effects of inertial forces, the model should be as stiff as possible, and this requirements might not be well respected, in particular when dealing with very slender tall buildings.

The second experimental methodology commonly adopted to assess wind loads on tall buildings is represented by the High-Frequency Pressure Integration (HFPI) method. Early developed by Irwin et al. [135], this approach consists in equipping the exposed surfaces of the building model with a number of pressure taps, closely spaced in order to accurately sample the fluctuating pressure field acting on it at each sampling time. Differently from the HFFB method, no assumptions on the modal shapes or on the spatial distribution of the pressure field are necessary, so that wind effects on structures with irregular distribution of stiffness and mass and complex modal shapes can be analyzed. Indeed, modal forces can be reconstructed directly from pressure measurements and the structural response can be consequently assessed. Furthermore, differently from the HFFB method, the pressure measurements are not affected by inertial forces caused by the model itself. On the other hand, buildings with complex geometrical shapes would require a very large number of pressure taps acquiring simultaneously and, sometimes, the limited number of available taps might lead to an inaccurate sampling of the pressure field.

The third experimental methodology for wind loading assessment on high-rise structures involves the use of aeroelastic models. In this case, the model is intended to reproduce the stiffness and the damping properties of the real scale structure, approaching its modal shapes up to a certain natural frequency as precisely as possible. The adoption of aeroelastic models allows for the measurement of the full response of the structure, taking into account aeroelastic effects like the aerodynamic damping. Adopting such an approach, complex fluid-structure interactions can be experimentally investigated. Nevertheless, due to its high costs, this technique is usually limited to the study of structures for which aeroelastic effects are expected to be of primary im-

portance and, in may cases, the HFPI method still represents a good alternative and a satisfactory trade-off between accuracy and complexity of the experimental tests.

In the last decades, thanks to a significant growth of the computer power, numerical approaches based on Computational Fluid Dynamics (CFD) become more and more adopted as a complementary tool to investigate the wind flow around buildings [9]. Numerical methods show several advantages if compared to wind tunnel tests. In particular, their costs are reduced with respect to experiments and each quantity of interest can be measured everywhere in the computational domain rather than just sampled at a few points. Due to these characteristics, numerical simulations allow to study phenomena which might be difficult to be analyzed in wind tunnel tests.

In particular, CFD simulations based on Reynolds-Averaged Navier-Stokes (RANS) models have been thoroughly investigated in the past. However, such models are often found to be inaccurate when bluff bodies are considered and their predictive capability is limited to the mean flow properties, while the ability to accurately predict turbulent fluctuations is recognized to be of fundamental importance for the assessment of the dynamic response of structures [30]. The need for correctly taking into account the flow dynamics led researchers to move towards scale-resolving turbulence models, such as Large Eddy Simulations (LES), that represent nowadays a promising tool for the numerical prediction of wind loads on buildings. Although such models are commonly considered to be well suited for the analysis of flows around bluff bodies, it has been often observed that CFD results appear to be considerably scattered even when simple geometries are considered [12, 37, 64]. Indeed, the complex, instability driven, phenomena observed in the turbulent flows around bluff bodies, like shear layer detachment/reattachment and vortex shedding/coalescing, make the simulation of this kind of flows an extremely challenging task and results are often found to be dependent on the simulation setup and the adopted turbulence model. Additionally, it should be noted that the generation of realistic unsteady boundary conditions, able to reproduce the main features of the turbulence found in the ABL, is mandatory in order to obtain accurate results in terms of pressure distributions and, thus, forces acting on the structure.

As a result, even if CFD techniques represent nowadays a very attractive tool for the assessment of wind loads on structures, it appears that strong research efforts are still needed in order to evaluate their reliability and accuracy. In particular, the available literature focused mainly on the comparison of pressure distributions and its statistics,

typically up to the second order. Even if such studies are definitely necessary, they do not appear to be sufficient in order to assess the capabilities of the numerical models in the prediction of wind loads. In fact, internal forces on structural members are related to a number of factors which are often not taken into account in such studies as, for example, the spatial coherence of the pressure field and its frequency content, whose relevance and overall effect can be amplified or weakened depending on the mechanical transfer functions characterizing the structural dynamic behaviour itself. A first detailed evaluation of LES capabilities in the simulation of flows around low-rise buildings with specific application to structural design has been recently proposed in [27].

In such context, the present paper represents a first step towards the assessment of LES as a design tool for high-rise buildings. In particular, the turbulent fluctuations which characterize the wind impinging on the structure are generated by means of the Modified Discretizing and Synthesizing Random Flow Generator (MDSRFG), which produces a solenoidal fluctuation field and allows to control its spatial and temporal correlations [71]. Firstly, in accordance with standard procedures, results are analyzed in terms of statistics of pressure distributions on the building and systematically compared with wind tunnel measurements. Then, dynamic structural analyses are carried out for each considered angle of attack starting from both numerically predicted and experimentally obtained pressure data. Results are analyzed in terms of envelopes of internal forces acting on structural elements so allowing to analyze the effectiveness of the adopted numerical strategy in predicting design wind loads on the considered high-rise structure. It should be noticed that by adopting such a framework, all the elements which play an important role in the definition of the structural response are automatically taken into account, providing a synthetic picture of the effectiveness of the proposed numerical strategy compared to the traditional experimental practice.

The paper is organized as follows. In Section 7.3 the experimental setup is described, while Section 7.4 reports the main features of the adopted computational model together with the discussion of the inflow condition adopted for LES. Section 6.4 is devoted to the analysis of pressure distributions for each considered angle of attack. Then, Section 6.5 describes the results obtained from the dynamic structural analyses, focusing on internal forces on structural elements. Finally, in Section 7.7 some conclusions are drawn.

6.2 EXPERIMENTAL SETUP

In this section, the experimental setup adopted to obtain pressure data used for comparison with numerical results is described. Experiments have been carried out at the Boundary Layer Wind tunnel of the Tokyo Polytechnic University (TPU) and results are collected in a public database organized in different sections, depending on the specific analyzed geometry and the considered layout [7]. The present work focuses on an isolated high-rise building characterized by a height (H) to breadth (B) ratio equal to 5 : 2 and a depth (D) to breadth (B) ratio equal to 1 : 2 (see Fig. 6.1 (a)). During wind tunnel tests, the length scale ratio was equal to 1/400, leading to a model with $B = 200$ mm, $D = 100$ mm and $H = 500$ mm. The wind tunnel section was 2.2 m wide and 1.8 m high, so the maximum blockage ratio was less than 2.5%. The wind field profile reproduced in the wind tunnel corresponded to that of terrain category IV according to the Architectural Institute of Japan (AIJ) standards [119]:

$$U(z) = 1.7\left(\frac{z}{Z_G}\right)^{\alpha} U_{ref}, \qquad Z_b < z \leqslant Z_G, \tag{6.1}$$

$$U(z) = 1.7\left(\frac{Z_b}{Z_G}\right)^{\alpha} U_{ref}, \qquad z \leqslant Z_b, \tag{6.2}$$

where the exponent α is equal to 0.25, Z_G is a reference height of the ABL equal to 550 m, Z_b represents the characteristic dimension of the surface roughness element being equal to 20 m. U_{ref} is the reference wind velocity. All the quantities referred to the AIJ standards are relative to the atmospheric boundary layer, so they are intended to be in full scale. In the experiments, the wind velocity at the height of the building was equal to $U_H = 11.11$ m/s, leading to a Reynolds number equal to $Re = \frac{U_H H}{\nu} = 3.8 \cdot 10^5$.

The adopted turbulence intensity profile was in agreement with AIJ standards for the terrain category IV as reported in Eqs. (6.3) and (6.4):

$$I(z) = 0.1\left(\frac{z}{Z_G}\right)^{-\alpha-0.05}, \qquad Z_b < z \leqslant Z_G, \tag{6.3}$$

$$I(z) = 0.1\left(\frac{Z_b}{Z_G}\right)^{-\alpha-0.05}. \qquad z \leqslant Z_b. \tag{6.4}$$

The mean and turbulent profiles were obtained by means of turbulence-generating spires and square blocks as roughness elements placed upstream the model. Experiments were conducted for 21 wind directions,

starting from $\theta = 0°$ to $\theta = 100°$ with a step of 5°. The wind angle of attack θ is defined so that $\theta = 0°$ corresponds to the direction orthogonal to the edge D, as reported in Fig. 6.1 (b). The model was equipped with 510 pressure taps that acquired synchronously at a sampling frequency of 1000 Hz for a duration of 32.8 seconds.

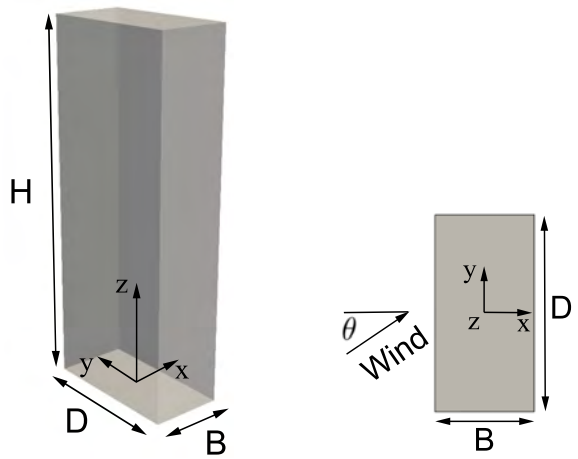

(a) (b)

Figure 6.1: Geometry of the high-rise building: three-dimensional (a) and top (b) views.

6.3 COMPUTATIONAL MODEL

In the present section, the characteristics of the numerical model adopted for LES are described. In particular, Section 7.4.1 describes the main features of the adopted numerical settings, together with the computational domain characteristics. Then, Section 7.4.2.1 focuses on the generation of the turbulent inflow condition for LES.

6.3.1 *Numerical setups*

The computational domain dimensions adopted for the simulations are close to wind tunnel ones and slightly reduced with respect to them in order to adopt symmetry boundary conditions without modeling the effects of lateral and top walls. In particular, a three dimensional view of the adopted computational domain is reported in Fig. 6.2, while Fig. 7.4 (a) and Fig. 7.4 (b) show its lateral and top views, respectively. The across wind section is 4.4H wide and 3.6H, while the distance of

the building from the inlet boundary is set equal to 4H. The resulting blockage ratio at the 0° angle of attack is equal to 2.5%, while at 90° it equals 1.25% and in both cases it is lower than the maximum requirements of 3.0% suggested by COST guidelines [136]. According to Tominaga et al. [122], the distance of the high-rise building from the outlet boundary is set equal to 10H.

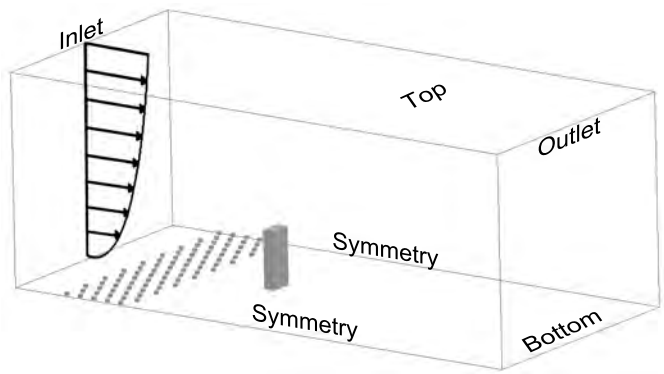

Figure 6.2: Computational domain adopted for the numerical study: three-dimensional view.

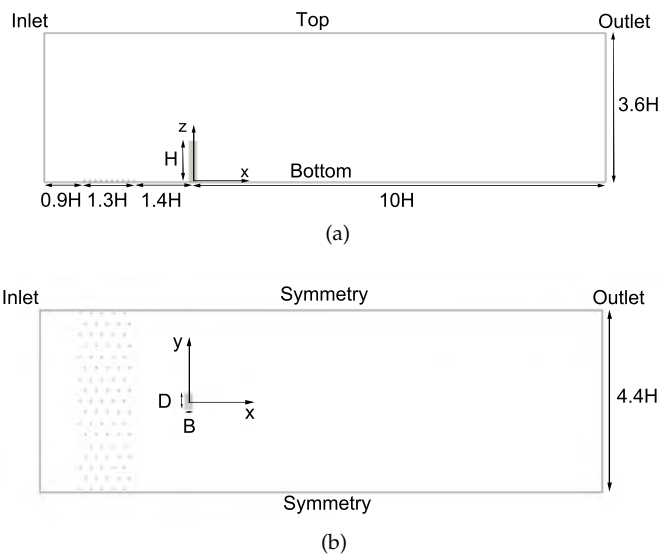

Figure 6.3: Computational domain adopted for the numerical study: lateral (a) and top (b) views.

Aiming at reducing as much as possible the along wind deterioration of profiles imposed at the inlet, five rows of square blocks with edge length equal to 0.06H are placed upstream the model. The blocks distribution is uniform over the bottom surface of the domain, in accordance to the experimental setup. The blocks height is calculated in order to reproduce the aerodynamic roughness characterizing the mean velocity profile imposed at the inlet boundary by means of the equation proposed by Lettau [120] subsequently reported:

$$z_0 = 0.5h\frac{A_r}{A_t}, \tag{6.5}$$

where z_0 is the roughness length as defined by EN1991-1-42005 [121], A_r is the area of the element normal to the wind direction and A_t is the ground area per roughness element, as reported in Fig. 6.4 (a).

The resultant roughness length is about 0.3 m in full scale and it is in good agreement with the roughness of the terrain category reported in EN1991-1-42005 [121] and equivalent to that considered in the present study.

When the roughness fetch ends, a new boundary layer starts developing which might effect results at least in correspondence of the lower part of the high-rise building. In particular, the height of the new boundary layer can be estimated by adopting Eq. (6.6) proposed by Elliot [137]:

$$H_{bl} = z_{0,2}\left[0.75 + 0.03\log\left(\frac{z_{0,1}}{z_{0,2}}\right)\right]\left(\frac{d}{z_{0,2}}\right)^{0.8}, \tag{6.6}$$

where H_{bl} is the height of the new boundary layer, $z_{0,1}$ and $z_{0,2}$ are the aerodynamic roughnesses characterizing two different zones and d is the distance from which the new boundary layer starts developing. The distance of the roughness blocks from the model is set in order to limit the new boundary height up to a height of H/10. According to Eq. 6.6, this requirement leads to a distance of about 1.4H between the building model and the first alignment of blocks (see Fig. 6.4 (b)).

As regards the boundary conditions, the mean velocity profile is prescribed at the inlet boundary, while Neumann conditions on the stress tensor are imposed at the outlet. The turbulent part of the inflow is generated by means of the MDSRFG method and introduced to the computational domain by modifying the pressure-velocity coupling algorithm following the procedure described by Kim et al. [28]. Bottom floor, building and roughness blocks surfaces are modeled as walls, while symmetry boundary conditions are imposed on the other domain boundaries.

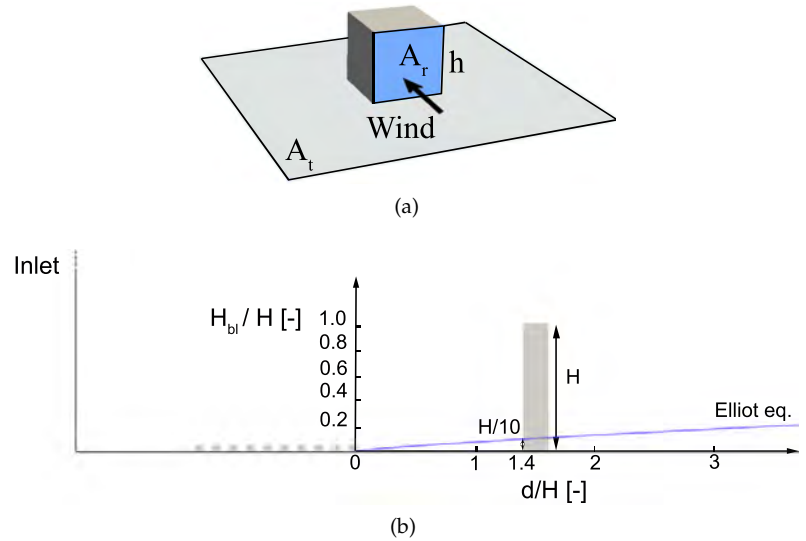

Figure 6.4: Roughness block geometry (a) and view of the boundary layer development according to Elliot's equation [137] (b).

A cubic structured mesh is adopted near the high-rise building surfaces, where cell dimensions in x, y and z directions are respectively $\delta_x/H = \delta_y/H = \delta_z/H = 3.1 \times 10^{-3}$, leading to a resolution higher than that suggested by Tominaga et al. [122]. Immediately close to the wall, a structured mesh is adopted for the boundary layer and the first cell height is set equal to $\delta_z/H = 5.1 \times 10^{-4}$. Proceeding away from the building, the mesh is slowly coarsened up to $\delta_x/H_0 = \delta_y/H_0 = \delta_z/H_0 = 5.0 \times 10^{-2}$. This sizing is kept constant until the inlet boundary is reached in order to correctly propagate inflow fluctuation and to keep as low as possible the numerical dissipation caused by the grid. Two views of the adopted mesh can be observed in Figure 6.5 (a) and (b). The final grid counts about 12×10^6 cells.

The pressure-velocity coupling is performed by means of the well known PISO algorithm, modified as proposed by Kim et al. [28] as previously reported. The time discretization is obtained by adopting the second order accurate Backward Differentiation Formulae [11]. The adopted dimensionless time step, based on H, is $\Delta t^* = 4.4 \times 10^{-3}$. The maximum Courant number in all simulations is 2.9, while it is lower than 1.0 in the 97% of points and its mean value in the whole domain equals 0.06. The maximum dimensionless wall distance y^+ is equal to 9.0, while it is lower than 5.0 on the 94% of the high-rise building surfaces.

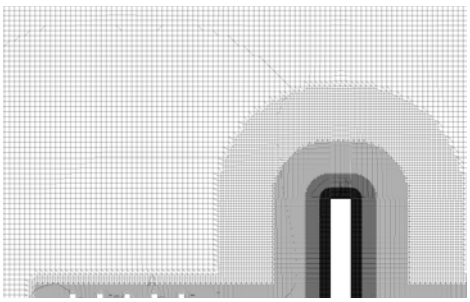

(a)

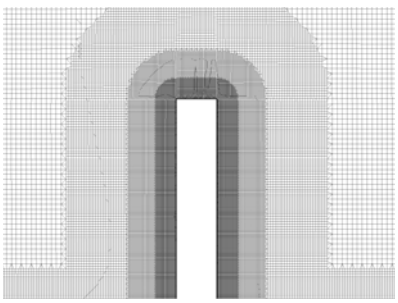

(b)

Figure 6.5: Mesh adopted for LES: lateral (a) and detailed lateral (b) views.

The spatial discretization of the advective terms is performed by means of the LUST scheme, that is second-order accurate and showed to perform well in particular for LES in complex geometries [124], offering a good trade-off between low dissipative behaviour and numerical stability. For all the other terms of the equations, a centered second-order differentiation scheme is adopted.

Regarding the LES subgrid scales model, the Smagorinsky-Lilly model [123] with, in addition, the transport equation of the subgrid turbulent kinetic energy is adopted. This model is able to adjust the turbulent eddy viscosity depending on the subgrid kinetic energy, showing a less dissipative behaviour when compared to the standard Smagorinsky-Lilly model [37].

The high-rise building has been equipped with 2844 pressure monitors and data acquired at each time step. Simulations have been run by using the open source Finite Volume software OpenFOAM ® v. 2.3.0 and analyses have been performed by using 96 CPUs at CINECA on the Galileo cluster (516 nodes, 2-eight cores Intel®Xeon®2.40 GHz processors with 128 GB RAM per node). Each simulation required about 2.5×10^4 CPU hours.

6.3.2 *Turbulent inflow characteristics*

The turbulent part of the simulated atmospheric boundary layer is generated by means of the MDSRFG method. In particular, following the MDSRFG procedure, a homogeneous and anisotropic velocity field can be computed as:

$$u_i(\mathbf{x},t) = \sum_{m=1}^{M}\sum_{n=1}^{N}\Big[p_i^{m,n}\cos\left(k_j^{m,n}\frac{x_j}{L_s}+\omega^{m,n}\frac{t}{\tau_0}\right)+ \tag{6.7}$$

$$q_i^{m,n}\sin\left(k_j^{m,n}\frac{x_j}{L_s}+\omega^{m,n}\frac{t}{\tau_0}\right)\Big], \tag{6.8}$$

with:

$$p_i^{m,n} = \mathrm{sign}(r_i^{m,n})\sqrt{\frac{2}{N}S_i(f^m)\Delta f\frac{(r_i^{m,n})^2}{1+(r_i^{m,n})^2}}, \tag{6.9}$$

$$q_i^{m,n} = \mathrm{sign}(r_i^{m,n})\sqrt{\frac{2}{N}S_i(f^m)\Delta f\frac{1}{1+(r_i^{m,n})^2}}, \tag{6.10}$$

$$\begin{cases} \mathbf{k}^{m,n}\cdot\mathbf{p}^{m,n} &= 0,\\ \mathbf{k}^{m,n}\cdot\mathbf{q}^{m,n} &= 0,\\ |\mathbf{k}^{m,n}| &= f^m/\bar{U}, \end{cases} \tag{6.11}$$

$$u_i'^{\,2} = \int_0^\infty S_i(f)\,df, \tag{6.12}$$

where $i = 1,2,3$ while N is the number of random extractions adopted in correspondence of the M frequencies, f^m, adopted to sample the spectrum while $\omega^{m,n}$ is a random number extracted from a Gaussian distribution $\mathcal{N}(f^m, 2\pi\Delta f)$, Δf is the step adopted in the spectrum sampling, $\bar{U}$ is the time averaged velocity, L_s is a factor calibrated *a posteriori* related to the turbulent length scale and τ_0 is a dimensionless parameter, set equal to one in the present work, that allows to control the time correlation of the series. Parameters $r_i^{m,n}$ are random numbers extracted from a Gaussian distribution $\mathcal{N}(0,1)$, while $S_i(k)$ is the target spectrum characterizing the $i-th$ velocity component whose total variance is equal to $u_i'^{\,2}$. For a detailed review of the characteristics of MDSRFG and other methods used for the generation of synthetic turbulence based on the spectral approach, the reader is referred to Patruno et al. [12].

In this paper, the well known von Kármán spectra reported below are assumed for the velocity components [5]:

$$S_u(f) = \frac{4(I_u U_{ref})^2 (L_u/U_{ref})}{[1+70.8(fL_u/U_{ref})^2]^{5/6}}, \tag{6.13}$$

$$S_v(f) = \frac{4(I_v U_{ref})^2 (L_v/U_{ref})[1+188.4(2fL_v/U_{ref})^2]}{[1+70.8(fL_v/U_{ref})^2]^{11/6}}, \tag{6.14}$$

$$S_w(f) = \frac{4(I_w U_{ref})^2 (L_w/U_{ref})[1+188.4(2fL_w/U_{ref})^2]}{[1+70.8(fL_w/U_{ref})^2]^{11/6}}, \tag{6.15}$$

where I, U_{ref} and L are the turbulence intensity, the average velocity and the turbulence length at the reference height H, respectively, while u, v, w subscripts indicate the components in x, y and z directions. In the present work, I_u is set equal to 11.6% according to experimental measurements, while $I_v = 0.75 I_u = 8.7\%$ and $I_w = 0.5 I_u = 5.8\%$ [126].

The turbulent length scale is not reported in the database for isolated high-rise buildings of TPU [7], therefore two different values have been investigated, respectively $L/H = 0.6$ and $L/H = 0.8$. It should be noticed that the MDSRFG procedure does not allow to prescribe the turbulence length scale *a priori* and, therefore, an iterative procedure becomes necessary to match the target values. The iterative procedure consists in generating the synthetic turbulent field by adjusting the parameter L_s in Eq. (7.21) until the resulting field matches the desired length scale. At the end of this procedure, two synthetic inlet conditions are obtained, hereinafter referred as inflow #1 and inflow #2, that differ only in the turbulent length scale, that are $L/H = 0.6$ and $L/H = 0.8$, respectively. These values were chosen to be close to those reported by Kim and Tamura [125], who analyzed several inflow conditions in the same wind tunnel facility referred in the present work.

In order to check if the turbulence introduced in the proximity of the inlet is correctly propagated downstream, two simulations have been performed by adopting the two aforementioned inflow conditions. In this case, according to the standard wind tunnel practice, LES are performed on a empty wind tunnel, i.e. the computational domain adopted is identical to that showed by Fig. 6.2 but without the building. The numerical setups and the turbulence subgrid model adopted for this analysis are the same as those described in Section 7.4.1. Within the computational domain, 21,560 velocity monitors sampling at each time step are arranged in a regular grid, ranging from $x/H = -2.0$ to $x/H = 5.5$, from $y/H = -1.0$ to $y/H = 1.0$ and from $z/H = 0.0$ to $z/H = 0.7$.

In order to check the convergence of the LES performed in the empty domain, the velocity signal recorded in a point located at the building height H and in the correspondence of the section where the building will be placed afterwards are considered. Figure 6.6 (a) shows the time history of the velocity u in the along-wind direction for the inflow #1. In the spirit of the procedure proposed by Bruno et al. [112], such time histories of the along wind velocity were expressed as a function of the dimensionless time $t^* = tU_H/H$ and subdivided in N partially overlapping sampling window which extend from $t^* = 0$ to nT, where T has been chosen equal to 10 times the signal dimensionless integral time scale (calculated from the autocorrelation function) and $n = 0, .., N$. For each sampling windows, first and second order statistics of the signal are calculated. Then, for each considered statistics the percentage residual ϕ_{res} is computed as $\phi^n_{res} = \frac{\phi_n - \phi_{n-1}}{\phi_n} \cdot 100$. Figure 6.6 (a) reports the trend of ϕ_{res} for both the time average and the root mean square. As it can be observed, after $170t^*$, residuals on both average velocity $\overline{u}$ and its standard deviations u' are lower than 1%, indicating that a satisfactory convergence of inflow statistics can be considered achieved at this time, at least up to the second order statistics.

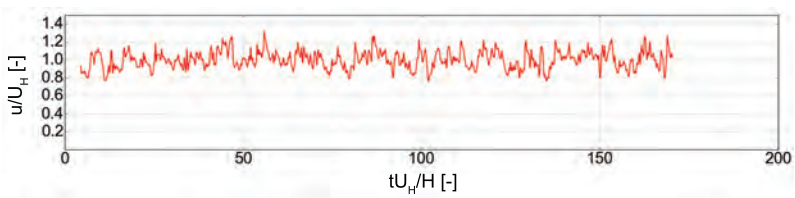

(a)

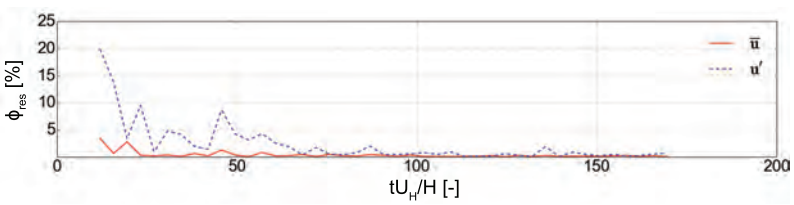

(b)

Figure 6.6: Convergence of inflow velocity statistics: time history of the along wind velocity (a) and incremental residuals on its average and standard deviation (b).

Results in terms of profiles of average velocity, U, along-wind turbulence intensity, I, and turbulence length scale, L, in the correspondence of the section where the building will be placed afterwards are reported in Fig. 7.8 (a), (b) and (c) for the two analyzed inflow condi-

tions, respectively. As it can be noticed, no remarkable differences can be observed in terms of average velocity profiles between inflow #1 and #2, being them almost overlapping and very close to experimental measurements. If the turbulence intensity is analyzed, differences between inflow #1 and #2 slightly increase, remaining anyway lower than 3% (in terms of relative percentage difference) everywhere. Also in this case, a good agreement between LES and experimental measurements can be considered achieved. Regarding the turbulent length scale, this has been computed by using the Wiener-Khinchin theorem together with Taylor hypothesis and the resulting integral turbulence length scale at each height has been averaged in the across wind direction for a length equal to B, that will be the maximum projection on the across-wind section of the building area (occurring at the angle of attack equal to 0°). In terms of turbulent length scale, the differences between inflow #1 and #2 remain almost constant until the height of $z/H = 0.5$ is reached and above $z/H = 0.2$ both the curves appear to be almost constant. In this range, L/H for the inflow #1 is equal to 0.77 while for the inflow #2 it is 0.65, showing a satisfactory agreement with the target parameters. Proceeding with increasing height, the two curves become closer and differences almost vanish at the height of $z/H = 1.0$.

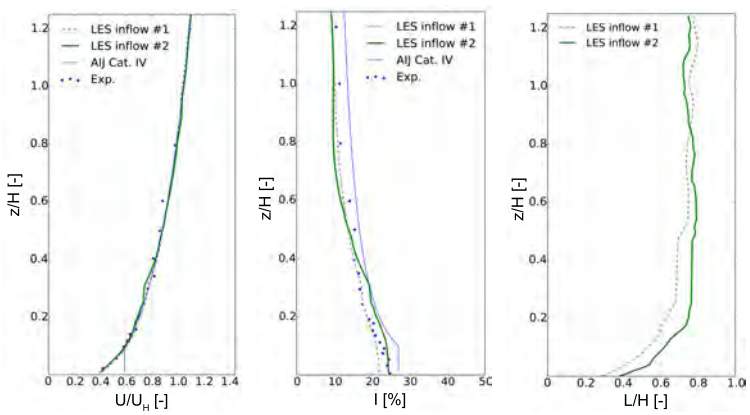

Figure 6.7: Comparison between wind velocity profile obtained from LES and from wind tunnel tests: average (a), along-wind turbulence intensity (b) and turbulence length (c) profiles.

Figure 7.9 shows the power spectral density of the three velocity components, namely S_u, S_v and S_w, in a dimensionless form for the inflow #1. Aiming at analyzing the dissipation of the turbulent fluctuations proceeding in the along wind direction, spectra are plotted for

two different points, located respectively at the end of the roughness blocks fetch at $(-1.4H, 0, H)$ and in the correspondence of the section where the building will be placed at $(0, 0, H)$. As it can be seen, dissipation appears to be very limited, since spectra at the two locations are very similar to each other. Furthermore, the obtained spectra result to be in good agreement with the target von Kármán ones, even if the frequency cut-off due to the grid size becomes evident starting from approximately $fH/U_H = 2$.

In all, both the synthetic inlet conditions comply in a satisfactory way with the target profiles leading to a good agreement with experimental measurements and so they are retained for the subsequent simulations when the high-rise building is introduced in the domain.

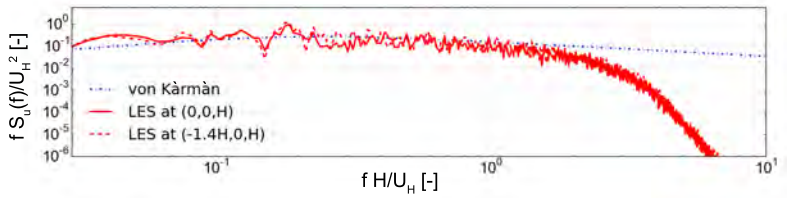

(a)

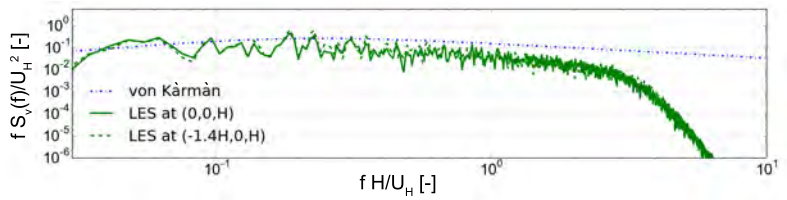

(b)

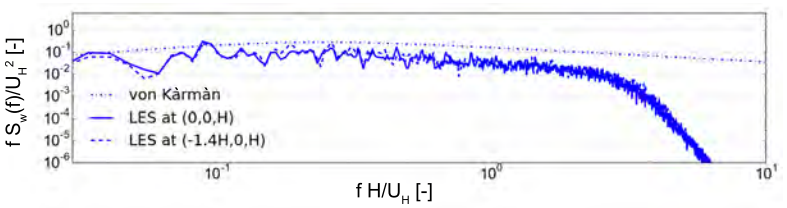

(c)

Figure 6.8: Spectra of the velocity time histories obtained from LES: along wind (a), across wind (b) and vertical (c) components.

6.4 LARGE EDDY SIMULATIONS

In this section, results obtained from LES are systematically compared with experimental data in terms of both pressure distributions and integral forces. Firstly, the analysis of convergence of LES together with the obtained integral forces for each angle of attack are reported in Section 6.4.1. Then, Section 6.4.2 shows some characteristics of the flow topology, while Section 6.4.3 compares results of LES in terms of statistics of the pressure distributions to experimental measurements for each considered angle of attack. Finally, in Section 6.4.4, the correlation plots between experimental and numerical prediction of the statistics of the pressure distribution are shown for all the building surfaces.

For each simulation, pressures are acquired at each time step and then data are coarsened to match the sampling frequency adopted in the wind tunnel tests, that was equal to 1000 Hz. The positions of the pressure probes on the building model are identical to those reported by the experimental setup and showed in Fig. 6.9 (a), while Fig. 6.9 (b) reports the paths s_1, s_2 and s_3 subsequently adopted for plotting pressure statistics.

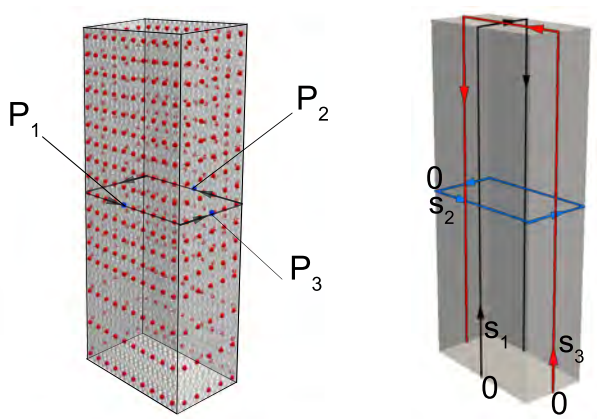

(a) (b)

Figure 6.9: Positions of the pressure probes according to the experimental setup (a) and view of the curvilinear abscissae adopted for plotting the pressure coefficient statistics (b).

6.4.1 *Convergence and integral forces*

The simulations convergence is checked for each angle of attack by analyzing the pressure signals acquired at the three different locations showed in Fig. 6.9 (a), namely $P_1 = (-0.1H, 0, 0.5H)$, $P_2 = (0.1H, 0, 0.5H)$ and $P_3 = (0, -0.2H, 0.5H)$. For the sake of brevity, only results regarding the angle of attack equal to 0° and the inflow #1 are here reported. In particular, Fig. 6.10 (a) shows the time history of the pressure coefficient $C_p = \frac{p}{0.5\rho U_H^2}$ for the location P_1, while Fig. 6.10 (b) shows the incremental residual on its average $\overline{C_p}$ and standard deviation C_p', obtained by following the method previously described in Section 7.4.2.1. Figures 6.11 and 6.12 show the same quantities relative to the locations P_2 and P_3, respectively. At can be observed, after $250t^*$ the residuals in terms of both $\overline{C_p}$ and C_p' are lower than 1% at all the considered locations.

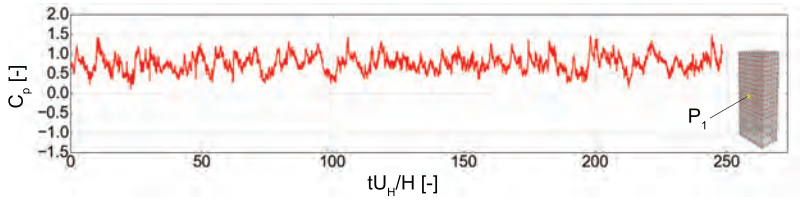

(a)

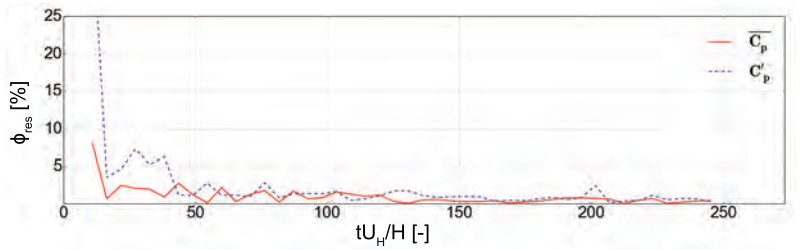

(b)

Figure 6.10: Convergence of pressure signal at location P_1: time history of the pressure coefficient (a) and incremental residual on its average and standard deviation (b).

The convergence is checked not only in terms of punctual pressure measurements, but also in terms of integral forces acting on the high-rise building. In particular, the same procedure adopted for the inlet condition and for pressure measurements is applied to the integral force coefficients in x and y directions, referred respectively as $C_{F_x} = \frac{F_x}{0.5\rho U_H^2 DH}$ and $C_{F_y} = \frac{F_y}{0.5\rho U_H^2 DH}$, where F_x and F_y denote the

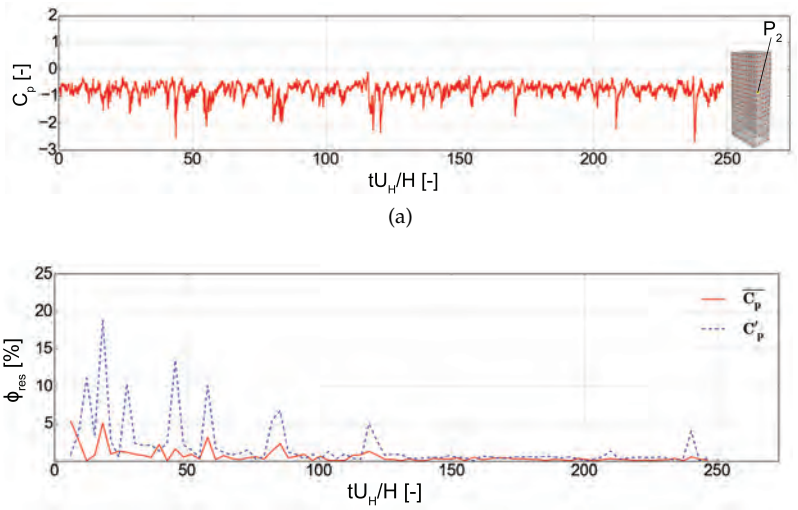

Figure 6.11: Convergence of pressure signal at location P_2: time history of the pressure coefficient (a) and incremental residual on its average and standard deviation (b).

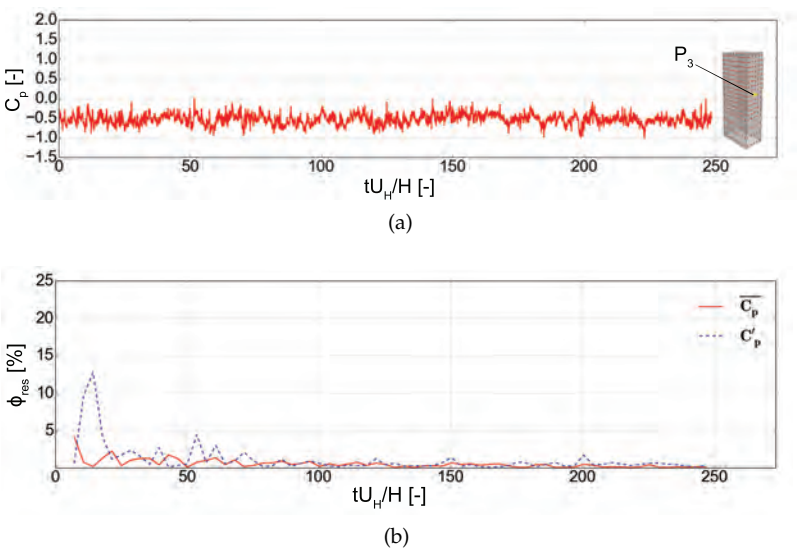

Figure 6.12: Convergence of pressure signal at location P_3: time history of the pressure coefficient (a) and incremental residual on its average and standard deviation (b).

integral forces. Figure 6.13 (a) shows the time history of C_{F_x} and C_{F_y} for the angle of attack equal to 0°, while Fig. 6.13 (b) reports the incremental residual in terms of average C_{F_x}, defined as $\overline{C}_{F_x}$, and in terms of standard deviation of C_{F_x} and C_{F_y}, denoted as C'_{F_x} and C'_{F_y}, respectively. As it can be noticed, also in terms of integral force coefficients after $250t^*$ all the investigated residuals fall below the threshold of 1%. In all, the duration of $250t^*$ is considered to be sufficient in order to reach a satisfactory converge of results at least up to second order statistics, so the simulations at all the investigated angles of attack are run until this duration is reached.

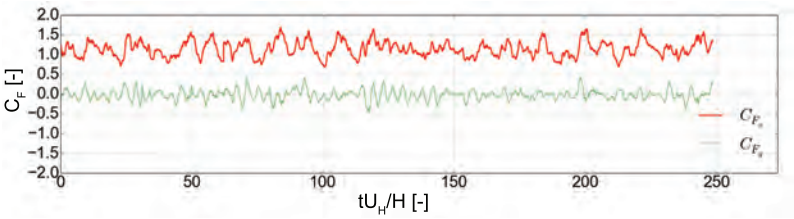

(a)

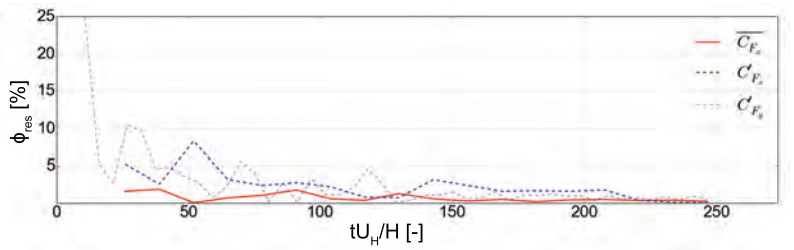

(b)

Figure 6.13: Convergence of integral force coefficients in x and y directions: time histories (a) and incremental residual on their average and standard deviation (b).

In order to study the impact of the different length scales adopted for inflow #1 and #2, the pressure time correlations between each pressure probe and all the others are calculated and the resulting fields are interpolated over the whole building surfaces. In particular, a comparison between inflow #1 and #2 at 0° is provided in Fig. 6.14, that shows the pressure coefficient time correlation $C_{p,corr}$ between the pressure probe P_1 and all the other probes along the path s_1 for the two considered inflows together with the corresponding experimental data. As it can be observed, inflow #2, characterized by the larger turbulent length scale, results in a very good agreement with experimental measurements. Indeed, in the windward surface the two curves

are almost overlapping, while compared to experiments the inflow #1 shows a more rapid decay of correlations proceeding away from the probe P_1. The higher values of correlations showed by inflow #2 compared to inflow #1 is somehow expected, since its incoming flow is characterized by a larger turbulent length. Differences become even more evident when the leeward surface is analyzed. In this part, results from inflow #1 seem to be uncorrelated with the signal recorded in P_1, being $C_{p,corr}$ almost null along the whole path. On the contrary, correlations obtained from inflow #2 appears to be negative and equal to about -0.2 in average, resulting to be quite close to experimental measurements.

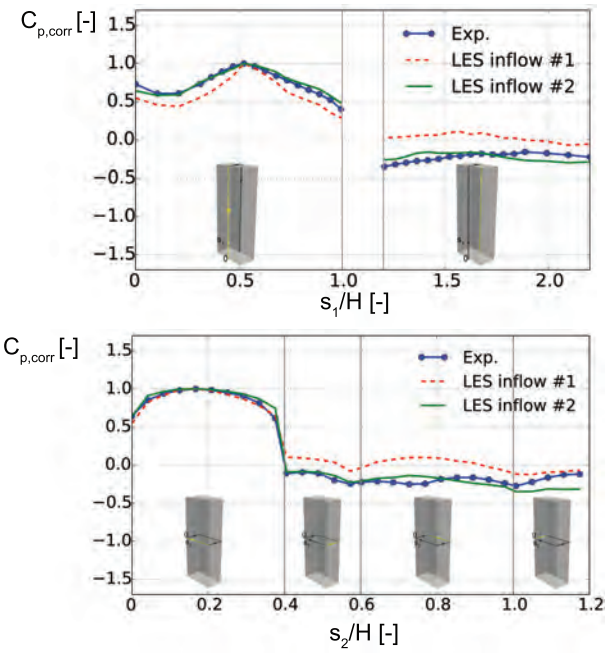

Figure 6.14: Time correlation between the pressure probe P_1 and all the other probes along the paths s_1 (a) and s_2 (b): comparison between inflow #1 and inflow #2 at the angle of attack equal to 0°.

Differences observed in pressure correlations are also reflected on the flow bulk parameters, in particular in terms of the standard deviation of the along wind force coefficient C_{F_x}. Table 6.1 reports the statistics of the force coefficients for all the considered angles of attack. As it can be noted, at 0° the standard deviation of C_{F_x} is equal to 0.153 when the inflow #1 is considered, while it equals 0.196 when the inflow #2 is adopted, resulting very close to the experimental data of

0.195 in this case. The better performances showed by the inflow #2 in terms of both pressure correlations and C'_{F_x} led to consider only this inflow condition for angles of attack equal to 45° and 90°. Also for these wind directions, Table 6.1 shows that a very good agreement is achieved between numerical and experimental measurements both in terms of average and standard deviation of the force coefficients, even if C'_{F_y} appears to be slightly underestimated by LES.

In all, it appears that the integral force coefficients are predicted by LES with a satisfactory accuracy for all the considered angles of attack, in particular in terms of average quantities, being the maximum absolute relative error between numerical and experimental predictions equal to about 8% in this case.

Angle	Source	Inflow	$\overline{C}_{F_x}$	C'_{F_x}	$\overline{C}_{F_y}$	C'_{F_y}
0°	LES	#1	1.13	0.153	-0.01	0.12
	LES	#2	1.14	0.196	-0.01	0.13
	Exp.	—	1.13	0.195	0.002	0.19
45°	LES	#2	0.81	0.15	0.37	0.07
	Exp.	—	0.88	0.17	0.34	0.09
90°	LES	#2	0.42	0.08	0.002	0.18
	Exp.	—	0.43	0.09	0.02	0.19

Table 6.1: Statistics of the integral force coefficients.

6.4.2 *Flow topology*

In this section, the flow topology obtained with LES is described for each considered angle of attack. In particular, a qualitative view of the vortical structures for the angle of attack equal to 0° is reported in Fig. 6.15 by means of isocontour of the invariant λ_2, coloured with pressure. As it can be observed, the boundary layer approaching the high-rise building becomes unstable leading to the development of the well known horseshoe vortex. Indeed, the vertical component of the velocity gradient that characterizes the approaching boundary layer causes pressures to be higher near the top part of the high-rise building, where velocities are higher, and lower near the ground. This pressure gradient drives the flow downward close to the windward surface of the high-rise building and then, as it approaches the ground surface, it is deviated upwind according to a reversal pressure gradient, that is considered to be responsible for the instability of the incoming boundary layer [138] and that consequently controls the position of the horseshoe vortex core.

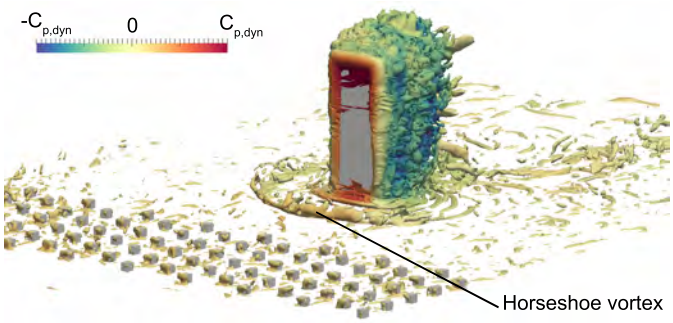

Figure 6.15: Three dimensional view of the flow topology at 0°: isocontours of the invariant λ_2 at the dimensionless value of $\lambda_2 U^2/H^2 = -30.5$.

These flow dynamics can be better appreciated if the average streamlines are observed. In particular, Figures 6.16, 6.17 and 6.18 show the average streamlines obtained with the Line Integral Convolution technique [139] for 0°, 45° and 90°, respectively. The streamlines are plotted for the xz plane passing from $(0, 0, 0)$ and for the xy plane passing from $(0, 0, 0.5H)$. As it can be observed in Fig. 6.16, when 0° angle of attack is considered, the core of the horseshoe vortex is located at approximately $x/D = -1.3$, while it moves closer to the building windward surface as the angle of attack increases, reaching $x/D = -1.0$ at 90° (see Fig. 6.18).

Focusing on the average flow reattachments/detachments, that significantly affect the pressure distribution and consequently the wind load on the building, it can be observed in Fig. 6.16 that, when the angle of attack equal to 0° is considered, the average flow field appears to be detached from both the lateral and the top surfaces. Conversely, the average flow reattaches on the top surface for the 45° angle of attack (at least in the xz plane considered) and on both top and along wind surfaces for 90°, as showed in Figures 6.17 and 6.18, respectively. In particular, in the configuration at 90° showed in Fig. 6.18 (b), in nominally smooth inflow conditions, the flow is known to be detached, since the aspect ratio of the considered rectangular shape is $D/B = 2$, so less than the threshold value of 2.8 reported by Noda et al. [53]. Nevertheless, the incoming turbulence and the enhanced turbulent mixing cause the shear layer instabilities to occur upwind with respect to the smooth inflow condition, leading the mean flow to reattach also for aspect ratio smaller than 2.8 [140]. Furthermore, it is worth noticing that, in the considered case, the flow topology is complicated due to the fact that the model is immersed in a turbulent shear flow, that is the simulated atmospheric boundary layer, so the reattachment length changes pro-

ceeding from the bottom towards the top side of the high-rise building. In particular, Fig. 6.19 (a) shows the change in the along wind position of the reattachment point (indicated as x_r) with the height at the angle of attack equal to 90°. In the same figure, the curve $1/I(z)$, where $I(z)$ is the turbulence intensity profile, appropriately shifted by a calibrated offset. Interestingly, the two curves show a very similar trend, at least up to approximately $z/D = 2.0$, where the reattachment bubble reaches its maximum along wind extension, so suggesting a linear proportionality between the reciprocal of the turbulence intensity and the reattachment length, at least in the considered range. Moreover, it is worth noticing that the height of $z/D = 2.0$, at which the reattachment length reaches its maximum, represents the boundary between the regions where the flow is deviated downwards, as it can be observed in Fig. 6.18 (a). Indeed, above this height the flow is deviated upwards by the high suctions occurring in the top part of the high-rise building and showed in Fig. 6.19 (b), so the along wind position of the reattachment point starts decreasing reducing from a maximum of $x_r/D = 0.34$ to $x_r/D = 0.005$.

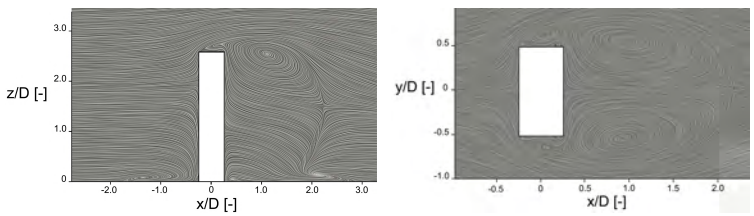

(a) (b)

Figure 6.16: Average streamlines at 0°: view of the xz plane passing from (0,0,0) (a) and of the xy plane passing from $(0, 0, 0.5H)$.

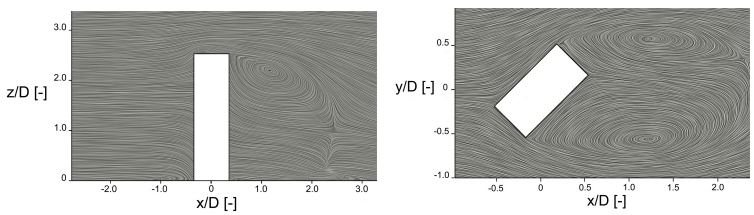

(a) (b)

Figure 6.17: Average streamlines at 45°: view of the xz plane passing from (0,0,0) (a) and of the xy plane passing from $(0, 0, 0.5H)$.

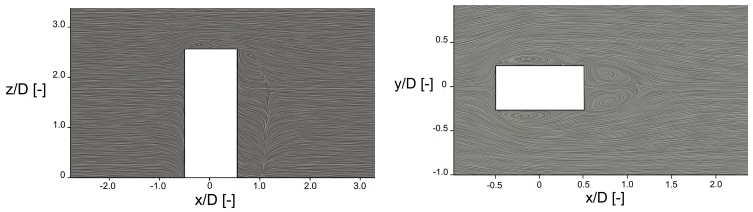

(a) (b)

Figure 6.18: Average streamlines at 90°: view of the xz plane passing from (0,0,0) (a) and of the xy plane passing from $(0, 0, 0.5H)$.

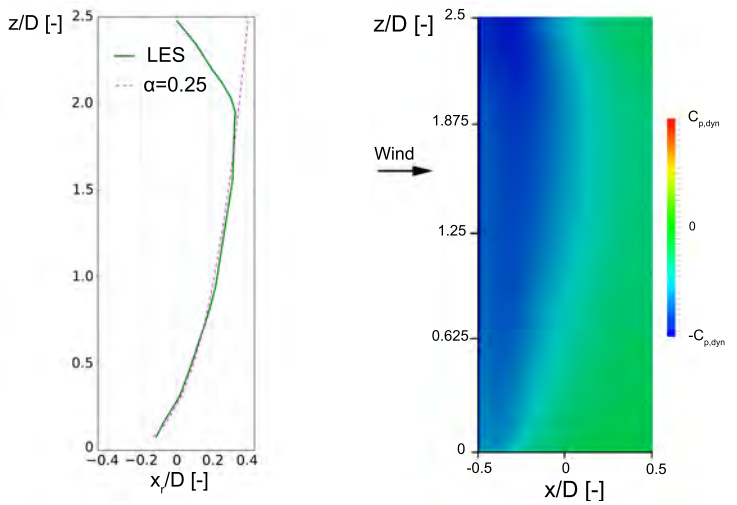

(a) (b)

Figure 6.19: Average position of the reattachment point (a) and average pressure field on the along-wind surface (b) at 90°.

6.4.3 *Pressure distributions*

The distribution of the average pressure coefficient $\overline{C_p}$ and of its standard deviation C'_p along the path s_1 for the 0° angle of attack is reported in Fig. 6.20. As can be observed, a good agreement is reached in terms of $\overline{C_p}$ on both windward and leeward sides. Focusing on the windward surface, both numerical and experimental data show a maximum of $\overline{C_p}$, located approximately at $s_1/H = 0.8$. Since the vertical component of the average pressure gradient changes in sign in correspondence of this maximum, comparing this figure with Fig. 6.16, it

can be observed that this height corresponds to the streamline that separates the flow deviated upwards from that deviated downwards. Regarding the numerical prediction of C_p', it can be observed that while in the windward surface LES tends to slightly overestimate it, in the leeward surface the behavior is opposite, with LES underestimating C_p' in particular near the bottom side, where the average streamlines in Fig. 6.16 (a) show the presence of a vortex structure.

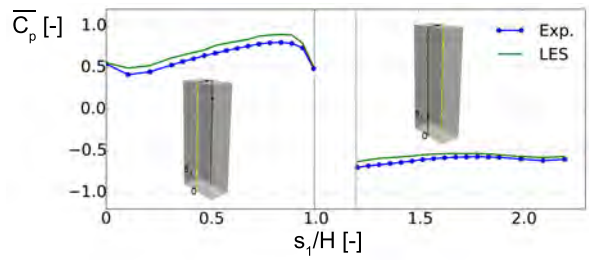

(a)

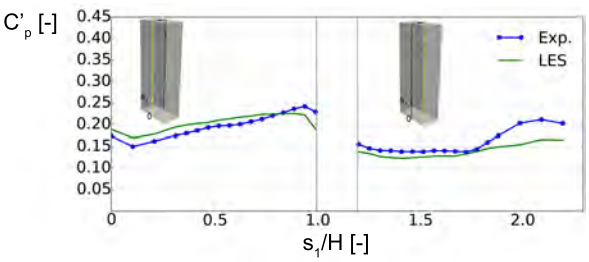

(b)

Figure 6.20: Statistics of the pressure coefficient at 0° along the path s_1: average (a) and standard deviation (b).

When the angle of attack equal to 45° and path s_1 are analyzed, from Fig. 6.21 it appears that the average pressure coefficient predicted with LES almost overlaps the experimental data, while discrepancies previously observed for 0° angle of attack in terms of C_p' become more evident in this case, in particular in the leeward part of the path. Anyway also in this case, C_p' appears to be satisfactory predicted by LES on the windward surface, being the maximum relative difference between numerical and experimental data less than 8%.

The $\overline{C_p}$ and C_p' distributions along the path s_2 for the 90° angle of attack are showed in Fig. 6.22. Looking at the $\overline{C_p}$ distribution, the same observations done for 0° and 45° hold, being the numerical and the experimental data in good accordance, with a maximum relative difference of about 15%, recorded close to the leading edges where high

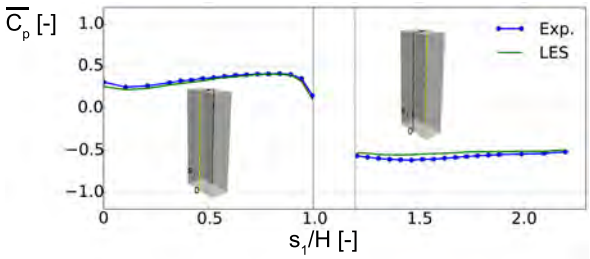

(a)

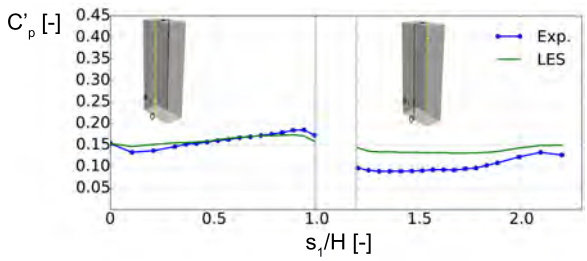

(b)

Figure 6.21: Statistics of the pressure coefficient at 45° along the path s_1: average (a) and standard deviation (b).

suctions due to the flow separation occur. On such regard, it should be noticed that the accurate reproduction of the flow dynamics near such zones represent a very challenging task for numerical simulations, since it would require extremely high spatial and, consequently, time resolutions, rendering LES very time consuming and, indeed, compromising their use for practical applications. Moving away from the locations where the highest suctions are recorded, the pressure recovery starts and the slope of the curve increases as the reattachment point is passed, so before $s_2/H = 0.32$ and after $s_2/H = 0.68$. Looking at the distribution of the standard deviation of the pressure coefficient reported in Fig. 6.22 (b), the numerical results underestimate the peak of C_p', even if the maximum relative difference between numerical and experimental data is below 15%. Conversely, the numerical predictions of C_p' values on the windward part of the path are in good accordance with the experimental measurements, indicating that the energy content in the approaching flow is correctly reproduced. This observation also holds for the previously analyzed angles of attack.

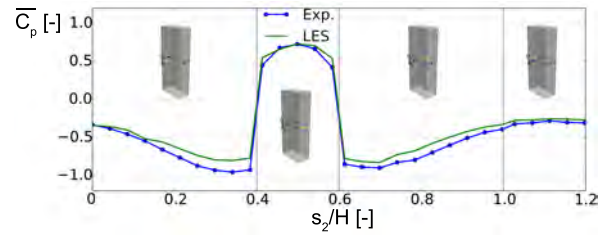

(a)

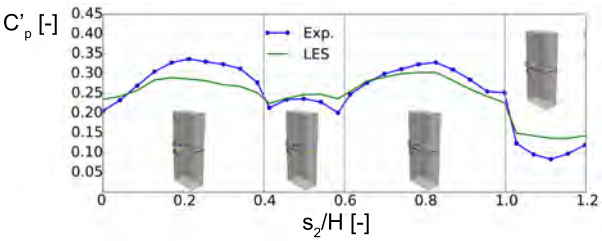

(b)

Figure 6.22: Statistics of the pressure coefficient at 90° along the path s_2: average (a) and standard deviation (b).

6.4.4 *Overall pressure distributions*

In order to analyze the accuracy of the numerical prediction of the pressure coefficient statistics over the whole building surfaces, in this section the correlation plots between the numerical measurements and data obtained with LES for all the pressure probes and all the considered angles of attack are reported. In particular, Fig. 6.23 shows the correlation plot for $\overline{C_p}$ and C_p' at the 0° angle of attack, while the same plots for 45° and 90° are reported in Fig. 6.24 and 6.25, respectively. Furthermore, Table 6.2 reports for each angle of attack and each analyzed statistics the percentage of points whose difference between numerical and experimental predictions is less than 10%, 20% and 30% (hereinafter referred as ranges of tolerance). The same ranges are highlighted in the correlation plots. In addition to these data, Table 6.2 shows for each case also the Mean Normalized Bias (MNB), that is the average relative error between numerical and experimental predictions defined as follows:

$$MNB = \frac{1}{N}\sum_{i=1}^{N}\left(\frac{Q_{i,num} - Q_{i,exp}}{Q_{i,exp}}\right), \tag{6.16}$$

where N is the number of the pressure probes, while $Q_{i,num}$ and $Q_{i,exp}$ are the considered quantities obtained from the numerical model and from the experiments, respectively. The MNB is used as an index able to synthetically characterize the correlation plots subsequently reported.

As previously observed in Section 6.4.3 for paths s_1, s_2 and s_3, when the average pressure coefficient is analyzed the numerical results show to be quite accurate over the whole building surfaces and for all the angles of attack. Indeed, Table 6.2 shows that at 0° the percentage of points in the range of tolerance of 30% is 93.3%, while at 45° and 90° the corresponding percentage is 82.0% and 99.0% respectively. Also the MNB appears to be quite reduced in this case, since it equals 1.5% at 0° and 1.33% at 45°, while at 90° it increases up to −9.47% and it changes in sign, indicating that in this case the average tendency of LES is to underestimate the mean pressure coefficient.

The correlation plots of Figures 6.23 (b), 6.24 (b) and 6.25 (b) show that the standard deviation of the pressure coefficient is predicted with less accuracy than the average one, being the distribution of points slightly deviated with respect to the bisector line for all the considered wind directions. These characteristics are also reflected in Table 6.2, that reports that, while at 0° the 94.5% of point is within the 30% of tolerance, this percentage decreases down to 69.4% and 88.8% for 45° and 90°. Also the MNB values appear to be higher than those observed for the distributions of $\overline{C_p}$, showing a maximum value of 19%, observed for the angle of 45°. Nevertheless, it is worth noticing that, in this case, the overestimation of the numerical data is mainly concentrated in points with relatively small values of C'_p (see Fig. 6.24 (b)).

In all, the maximum absolute MNB observed for the $\overline{C_p}$ distribution is less than 10%, while for the C'_p distributions, the maximum absolute MNB is less than 15%.

Performance metrics	0°		45°		90°	
	$\overline{C_p}$	C'_p	$\overline{C_p}$	C'_p	$\overline{C_p}$	C'_p
10%	45.1 %	27.8 %	59.8 %	31.6 %	30.6 %	52.9 %
20%	89.6 %	53.9 %	76.1 %	49.2 %	90.2 %	80.8 %
30%	93.3 %	94.5 %	82.0 %	69.4 %	99.0 %	88.8 %
MNB	1.15 %	−14.4 %	1.33 %	19.0 %	−9.47 %	4.54 %

Table 6.2: Performance metrics of the pressure coefficient at 0°, 45° and 90°.

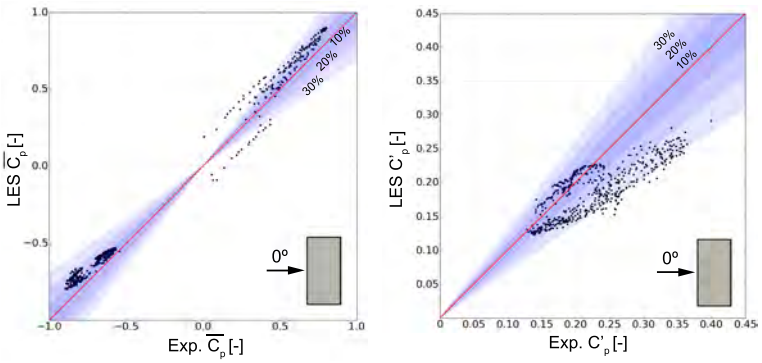

(a) (b)

Figure 6.23: Statistics of the pressure coefficient at 0°: average (a) and standard deviation (b).

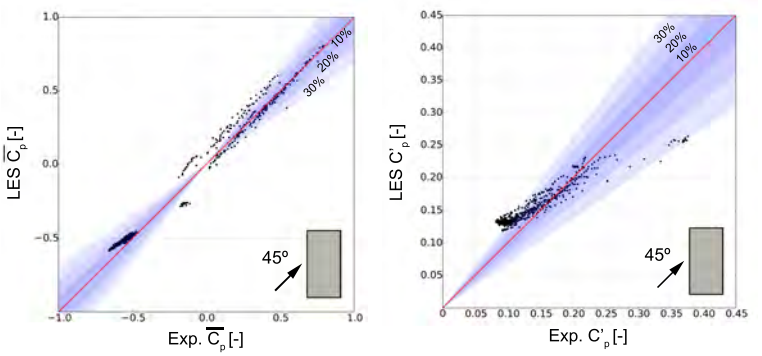

(a) (b)

Figure 6.24: Statistics of the pressure coefficient at 45°: average (a) and standard deviation (b).

6.4.5 *Pressure time correlations*

In order to accurately assess the structural response, not only the punctual statistics of the pressure coefficient should be well predicted, but also the time correlations need to be correctly reproduced. In order to analyze this aspect, for each angle of attack the time correlations between each probe and all the others are calculated. The time correlations of the probe P_1 along the paths s_1 and s_2 for the angle of attack equal to 45° are reported in Fig. 6.26, while Fig. 6.27 shows the time correlation along the paths s_3 and s_2 for the probe P_3 at 90° . For what

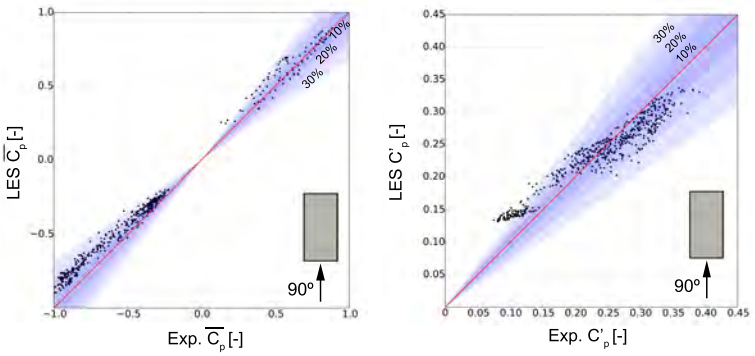

(a) (b)

Figure 6.25: Statistics of the pressure coefficient at 90°: average (a) and standard deviation (b).

concerns the 0° angle of attack, the same plot is reported in Fig. 6.14 and so it is not repeated here for the sake of brevity.

Focusing on the windward part of the paths, a good agreement between experimental and numerical data can be considered achieved for all the considered wind directions. Conversely, despite results at 0° show to be satisfactory also on leeward and along wind surfaces, in these zones, when 45° and 90° are considered, the LES lack in accuracy, showing values of the time correlation opposite in sign with respect to experiments. This fact might be responsible for the underestimation of the force coefficient C'_{F_x} reported in Table 6.1 and observed for the angles of 45° and 90°, while at 0° correlations are better predicted and C'_{F_x} becomes close to the experimental data.

6.5 ASSESSMENT OF WIND LOADS ON STRUCTURAL ELEMENTS

In this section, the results of linear structural dynamic analyses are presented, aiming at assessing the accuracy of LES in reproducing the internal forces on the structural elements. For each angle of attack, structural analyses are performed starting from the time histories of the pressure fields obtained from both experimental data and numerical simulations.

The characteristics of the adopted structural model are reported in Figs. 6.28 and 6.29. The structure is made of a steel-framed tube embedding two cores and it counts 50 floors arranged with regular distribu-

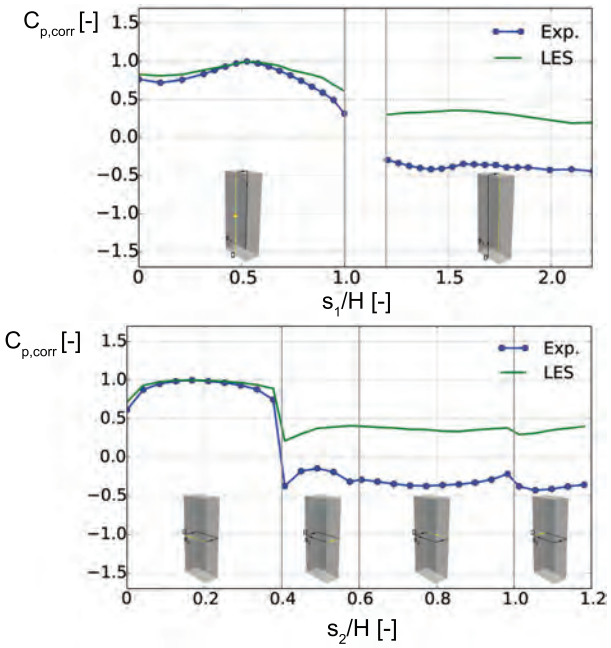

Figure 6.26: Time correlation between the pressure probe P_1 and all the other probes along the paths s_1 (a) and s_2 (b) at the angle of attack equal to 45°.

tion along the height. The steel-framed tube structure represents a very efficient structural solution for high-rise buildings, since it tends to behave as an equivalent hollow tube, leading to a considerable saving of material compared to classical framed buildings [141]. Each floor is composed of a concrete slab with a thickness of 0.45 m. At the ground floor, the end sections of the beams are considered perfectly clamped.

The dimensions of the cross-sections of the structural elements constituting the framed structure and the core are varied with the height every 40 m according to the 5 levels showed in Fig. 6.28 (b). According to the nomenclature introduced in Fig. 6.29 (b), the dimensions of the cross-section for each level are reported in Table 6.3.

The first three natural structural modes are reported in Fig. 6.30, while for the linear dynamic analyses subsequently discussed, 10 structural modes are considered. The first natural frequency is equal to 0.204 Hz and is in good accordance with the empirical value for steel-framed structures that can be calculated as $f_1 = 1.0/(0.1N_f) = 0.2$ Hz [141], where N_f is the total number of floors.

The linear structural dynamic analyses are performed by adopting the procedure described in Patruno et al. [142]. Following this method-

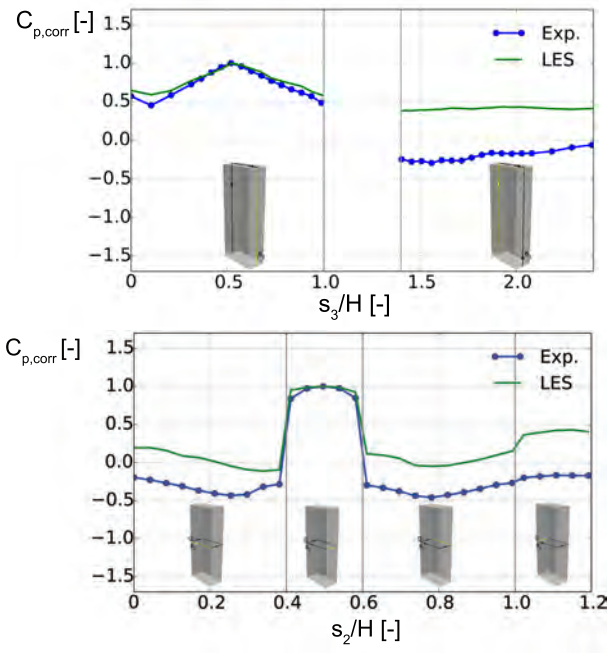

Figure 6.27: Time correlation between the pressure probe P_3 and all the other probes along the paths s_3 (a) and s_2 (b) at the angle of attack equal to 90°.

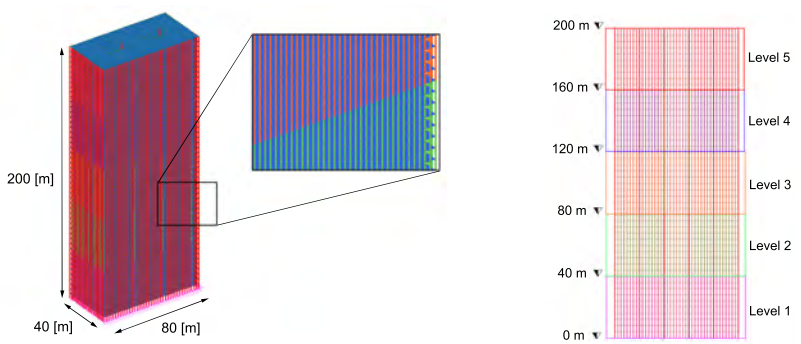

(a) (b)

Figure 6.28: Three dimensional view (a) and frontal view (b) of the structural model.

ology, the structural response is assessed by means of modal superposition while quasi-static corrections are introduced to take into account the effect of high frequency modes. In this way, static, quasi-static and resonant response to the wind loads can be simply and efficiently as-

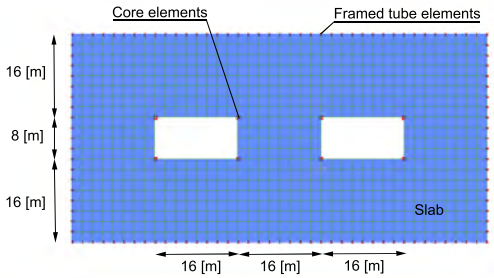

(a)

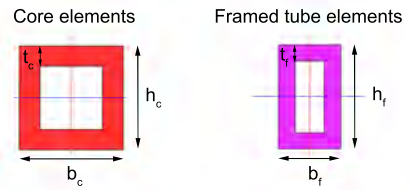

(b)

Figure 6.29: View of the characteristic floor of the structural model (a) and sections dimensions (b) of frame and core elements.

Level	Core elements			Framed tube elements		
	b_c [m]	h_c [m]	t_c [m]	b_f [m]	h_f [m]	t_f [m]
1	0.7	0.7	0.18	0.3	0.5	0.08
2	0.7	0.7	0.14	0.3	0.5	0.05
3	0.7	0.7	0.1	0.3	0.5	0.045
4	0.7	0.7	0.08	0.3	0.5	0.04
5	0.7	0.7	0.04	0.3	0.5	0.04

Table 6.3: Dimension of the sections of the structural members.

sessed. The design wind speed adopted for the analyses is equal to 30 m/s at the building top for all the considered directions.

Results are analyzed in terms of axial forces in 12800 sections. In particular, Figures 6.31 (a), 6.31 (b), and 6.31 (c) show the correlation plots for the standard deviation of the axial force (referred as N′) for the angles of attack of 0°, 45° and 90°, respectively, while Fig. 6.31 (d)

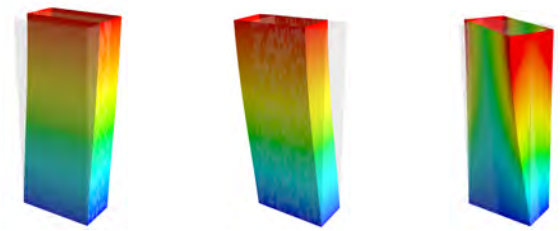

(a) 0.204 Hz (b) 0.209 Hz (c) 0.252 Hz

Figure 6.30: First three structural modes and their natural frequencies (coloured by displacement magnitude).

shows the envelope of these three angles. In order to better analyze the characteristics of the distributions of N', in accordance to what previously done for the standard deviation of the pressure coefficient, Table 6.4 reports for each graph of Fig. 6.31 the percentage of points falling within the three considered ranges of tolerance, together with the MNB. As it can be observed, while for the angle of 0° the 99% of points is within the range of tolerance of 30%, when 45° and 90° are considered the same data fall down to 22.5% and 37.3%, respectively. If these results are compared to those reported in Table 6.2, and relative to C'_p, it is observed that the accuracy shown by LES in predicting the standard deviation of the pressure coefficient is not reflected on the standard deviation of the axial forces. Focusing on the MNB reported in Table 6.4, for all the considered angles a negative value is observed, indicating that LES tend to underestimate the value of N'. This can be noticed also in Fig. 6.31 (a), (b) and (c), where points are concentrated near the lower boundary line relative to the higher considered range of tolerance. The best agreement between the values of N' obtained starting from experimental and numerical pressure fields is observed at 0°, for which the value of MNB is the minimum one (in absolute value) and it equals −14.2%. Anyway, when the envelopes of the three angles of attack are considered, differences decrease, since the 98.2% of points fall below the 30% tolerance and the MNB becomes equal to −23.9%, despite a maximum one of −33.7% observed at 45°. Furthermore, if the higher level of tolerance is increased from 30% up to 38%, the percentage of points included in the new tolerance range increases significantly, reaching 77% for 45° and 99.6% for 90°, so indicating that the distribution of the normalized bias is quite narrow around its mean value.

In all, it is worth noticing that, in order to accurately assess the wind loads effect on structures, the correct reproduction of the punc-

tual statistics of the pressure coefficient on the building surfaces is not sufficient, even if it obviously represents a first necessary step. Indeed, the structural analyses are affected also by the spectral content of the pressure signals as well as its spatial correlations. Bearing in mind this consideration, in the analyzed cases it can be observed that the numerical predictions of N' show the best accuracy for 0° angle of attack, for which also the pressure correlations result in a very good agreement with the experimental data, as shown in Fig. 6.14. Conversely, Fig. 6.26 and Fig. 6.27 show that for 45° and 90° the pressure correlations are predicted with less accuracy, and the correlation plots of N' are less accurate as well. In particular, as previously observed for these wind directions, LES show a positive pressure correlation between the windward surface and the leeward one, despite experimental data report a negative correlation. This fact might be responsible for the observed almost systematic underestimation of N' in these cases. Although it is not so straightforward to identify the cause of the discrepancies observed in the pressure correlations, it is worthy pointing out that the inflow conditions might affect them and that some parameters characterizing the incoming turbulence have been assumed since their values are not reported in the experimental setup, as for example the across wind and vertical turbulence intensities as well as the turbulence integral length scales in the same directions.

Performance metrics	0°	45°	90°	Envelope
10%	23.3 %	0 %	0 %	0.1 %
20%	82.9 %	0.43 %	0.5 %	8.86 %
30%	99.0 %	22.5 %	37.3 %	98.2 %
MNB	−14.2 %	−33.7 %	−30.5 %	−23.9 %

Table 6.4: Performance metrics of the standard deviation of the axial force (N').

In order to provide also quantities of interest for the design of structural members, Figures 6.32 (a), (b) and (c) show the correlations plots of the peaks of the axial forces N_{peak} for 0°, 45° and 90° respectively while Fig. 6.32 (d) shows the envelope of the three considered wind directions. The peaks of axial forces are defined as the mean values plus (and minus) 3.5 times the standard deviation (N'). As it can be seen, a good agreement between experimental and numerical data is achieved, even if some discrepancies are observed for all the angles in particular for lightly loaded elements.

If elements loaded less than 10% of the maximum axial force in the whole structural model are disregarded, data reported in Table 6.5 show that the number of points within the 30% range of toler-

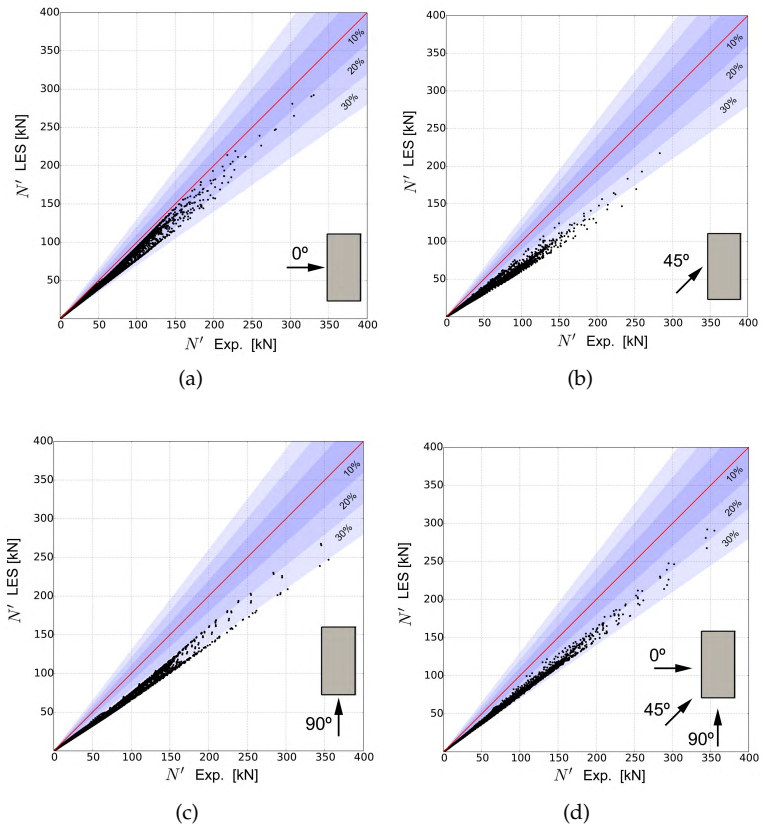

Figure 6.31: Correlation graphs of the standard deviation of the axial force (N′).

ance increases and the absolute values of the MNB decrease for all the considered wind directions. In particular, when the total envelope is considered, the MNB relative to N_{peak} equals -8.28%, that is significantly lower in absolute terms with respect to the value of -23.9% relative to N′. Therefore, it appears that, since the average axial force is predicted more accurately by LES than its standard deviation N′, the accordance between numerical and experimental results improves significantly when overall effects are considered.

6.6 CONCLUSIONS

In the present paper, the capabilities of LES as a tool useful for structural design were investigated. In particular, the turbulent flow around

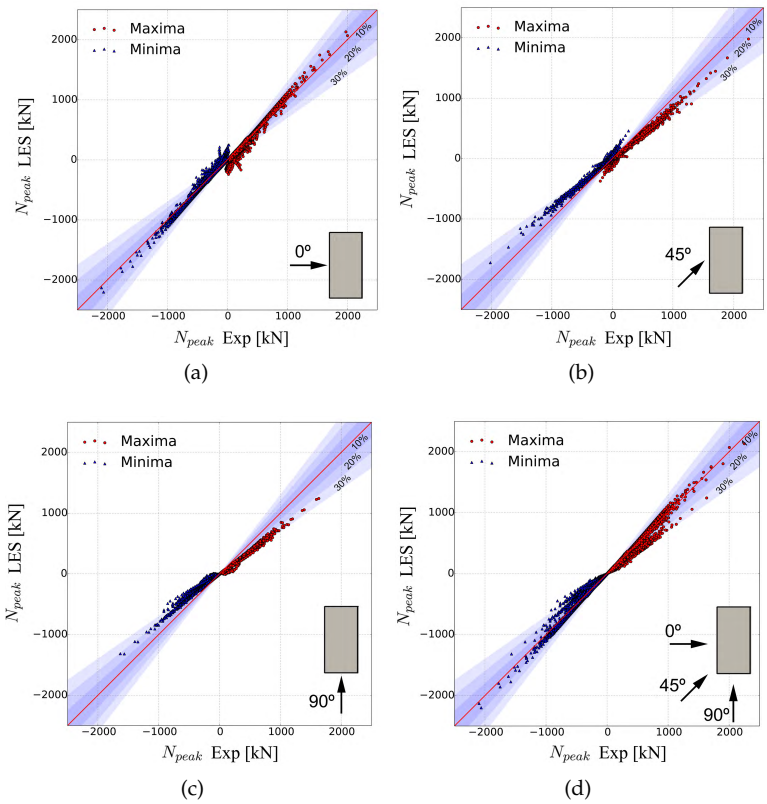

Figure 6.32: Correlation graphs of the peak axial force (N_{peak}).

Performance metrics	0°	45°	90°	Envelope
10%	78.0 %	5.18 %	0 %	54.8 %
20%	89.6 %	47.1 %	5.26 %	66.0 %
30%	99.0 %	96.8 %	70.0 %	90.9 %
MNB	0.283 %	−18.6 %	−27.3 %	−8.28 %

Table 6.5: Performance metrics of the peak axial force (N_{peak}) disregarding members loaded less than 10% the maximum load.

an isolated high-rise building was simulated and the numerically predicted pressure field was compared to the experimental measurements and used to assess the wind loads effects on the structure.

A key point in the simulation process, in particular when dealing with LES, is represented by the inflow boundary conditions. In order to obtain accurate results in terms of pressure distributions, the charac-

teristics of the incoming turbulent flow need to be represented as accurately as possible. In order to do this, two synthetic fluctuation fields matching the target spectra were generated by means of the MDSRFG method and introduced to the computational domain. The so generated fields differed only in the choice of the turbulent length scale and since the MDSRFG procedure does not allow to control it *a priori*, an iterative procedure was performed until the desired turbulent length scale was obtained. Then, according to the experimental practice, LES were performed in an empty domain, representing the wind tunnel in the absence of the high-rise building model. A good agreement between both the inflow profiles and the experimental measurements was obtained in terms of average velocity and turbulence intensity profiles. Then, the high-rise building was introduced in the computational domain and a first LES was performed at 0° angle of attack. Results in terms of statics of the pressure distributions on the high-rise building were systematically compared with experimental measurements and for the best performing inlet condition, simulations at angles of attack equal to 45° and 90° were run.

Firstly, the punctual statistics of the pressure field for the considered angles of attack were analyzed. In terms of $\overline{C_p}$, a good agreement between numerical predictions and experimental measurements was achieved, being the maximum absolute MNB obtained in all cases less than 10%. Regarding the fluctuating part of the pressure field, LES results showed to be slightly less accurate, being the maximum MNB equal to 19%. Nevertheless, in particular for 45° and 90°, it was observed that the larger relative errors are concentrated in points showing relatively small values of C_p'. This fact might suggest that secondary flow mechanisms were not predicted by LES with the same accuracy as global and more energetic flow mechanisms.

Once the characteristics of the pressure field were analyzed, in order to study the effects of the wind loads also in terms of internal forces, a steel-framed tube was considered and linear dynamic structural analyses were performed for each angle of attack starting from both experimental measurements and numerical predictions of the pressure field. It was observed that the accuracy showed by LES in reproducing the C_p' distribution was not reflected when the standard deviation of the axial forces N' was analyzed, being the maximum MNB obtained in all the analyses equal to -33.5%. Furthermore, differently from the distributions of C_p', an almost systematic underestimation was obtained with LES in terms of N'. This fact might be related to the results showed by the analysis of the pressure time correlations fields. Indeed, while at 0° a good agreement in terms of pressure cor-

relations is obtained, at 45° and 90° some discrepancies were observed in particular on the leeward surfaces, where numerical and experimental results were opposite in sign. This different flow dynamics might be responsible for the systematic underestimation of N', that becomes particularly pronounced at 45° and 90°, so when also the accuracy in the prediction of pressure correlations is lower. Nevertheless, when the envelope of the three angles is considered, results significantly improved, since the effects of minor flow mechanisms were partially hidden by the enveloping of the results. In this case, the MNB characterizing the N' distribution was equal to -23.9%.

Regarding the peak axial forces, results showed to be more accurate than those obtained for N' for all the considered angles. This improvement was due to the fact that the mean values of the axial forces were predicted with higher accuracy than their fluctuating parts, so final results appeared to be globally more accurate. When the envelope of the three angles was considered in this case, the relative MNB was equal to -8.28%, indicating that a satisfactory level of accuracy could be considered achieved.

Summarizing, it could be stated that, in the view of using LES as a design tool for the sizing of structural members, a comparison between experimental and numerical results in terms of pressure fields is necessary, but not sufficient. Indeed, the structural response is deeply affected also by the spectral content of the pressure field as well as by its temporal and spatial correlations. These characteristics are directly related to both the body aerodynamics and the turbulent inflow conditions. In the awareness of the complexity of the problem and bearing in mind that a large number of factors contribute to the definition of the structural response, the present study indicates that a satisfactory accuracy can be obtained with LES if the envelope of several angles of attack is considered, in particular in terms of peak forces. In the awareness that wind tunnel tests still represent the most reliable technique to assess the structural response to the wind action, the obtained results are considered to be encouraging for pursuing the research which is still needed in order to assess LES as a reliable tool for structural design.

ACKNOWLEDGEMENTS

The authors are thankful to CINECA for providing the HPC facilities needed to accomplish the present research work.

Part III

LES APPLICATIONS TO POLLUTANT DISPERSION PROBLEMS

Pollutant dispersion is one of the most important current environmental problem since it is strongly connected to air quality and thus to human health. In this part, LES are performed aiming at assessing their capabilities in reproducing the average pollutant concentration field downstream a pollutant source. In particular, first the pollutant dispersion from an isolated stack is analysed and results are compared to experimental data as well as to theoretical, empirical and semi-empirical formulae. Then, pollutant dispersion from a stack placed downwind a building is investigated.

7

NUMERICAL SIMULATION OF POLLUTANT DISPERSION: EFFECTS OF A RECTANGULAR BUILDING UPWIND OF A STACK

The accurate prediction of pollutant dispersion is of large scientific and societal importance. This can be performed by on-site measurements, wind tunnel tests or numerical simulations with Computational Fluid Dynamics (CFD) techniques, where the latter are attractive due to their ability to provide more detailed information on the pollutant concentration distribution. However, the accurate prediction of pollutant dispersion with CFD, especially in the urban environment, is complicated as it is governed by both atmospheric boundary layer (ABL) turbulence and turbulence in the flow patterns generated by bluff bodies such as buildings. This paper consists of two parts: firstly, a discussion regarding theoretical, empirical and semi-empirical models is provided. In the present paper, the results of these approaches are compared to experimental data as well as to numerical results. Then, Reynolds-Averaged Navier-Stokes simulations and Large Eddy Simulations are performed to predict the pollutant dispersion for two different configurations: an isolated stack and a building placed upwind of a stack. The first case is representative of situations in which the dispersion process is mainly governed by the ABL turbulence, while the second case involves both ABL and building-induced turbulence. Numerical results obtained for the two aforementioned cases are systematically compared with experimental data in terms of time-averaged pollutant concentrations allowing to assess the performance of the adopted numerical approaches.

7.1 INTRODUCTION

Nowadays, pollutant dispersion is one of the most important problems in the field of Urban Physics and Wind Engineering since it is strongly connected to air quality and thus, to human health. Indeed, air pollution is associated with a wide range of chronic and acute health diseases [24, 143], which represent a very actual problem in several parts of the world. In this context, the ability to accurately predict pollutant dispersion, especially in the urban environment, is of primary importance in order to improve the air quality and to avoid or limit undesirable effects caused by high pollutant concentrations. In the near future, it can be foreseen that the design of healthier, more comfortable and more sustainable cities will more and more rely on studies concerning pollutant dispersion to accurately predict the air quality in the urban environment.

The traditional approach used to assess pollutant dispersion relies on experimental practice and is based on either wind tunnel tests [144–148] or on-site measurements [149–153]. These techniques can be also adopted in combination with theoretical, empirical and semi-empirical models, which can provide an estimation of the pollutant concentration field in the area of interest based on experimental results [23]. Experimental techniques can provide useful information regarding the pollutant distribution but, unfortunately, the number of monitored points is usually limited by the experimental equipment and, in particular in case of on-site measurements, an accurate control of the boundary conditions is very difficult or even impossible.

Alongside the experimental approach, numerical techniques based on Computational Fluid Dynamics (CFD) are becoming increasingly popular for the study of the pollutant dispersion, as indicated by a fairly large number of review papers on the topic [1, 9, 23, 104, 105, 154–162]. In fact, numerical simulations offer several advantages if compared to wind tunnel tests and on-site measurements: they provide whole-flow field data, i.e. data on the relevant parameters in the entire computational domain and boundary conditions can be accurately controlled.

In the past decades, CFD simulations have been performed in order to investigate the near-field pollutant dispersion around isolated buildings [20, 47, 148, 163–165], idealised street canyons [166, 167], regular building blocks [168–172] and also in actual urban areas [173–176]. Nevertheless, CFD results showed to be very sensitive to the numerical setup adopted and an in-depth research work is still needed in order to further assess their accuracy and reliability.

In particular, several previous studies noted the inadequacy of Reynolds-Averaged Navier-Stokes (RANS) turbulence models for accurately predicting the wind flow patterns and consequently the pollutant concentrations around buildings [21, 47]. These considerations led researchers to move towards transient and scale-resolving approaches as Large Eddy Simulations (LES), which generally showed an improved accuracy when compared to RANS turbulence models [21, 22]. Nevertheless, due to their high computational cost, LES simulations still remain mainly limited to the research arena and further studies are necessary in order to accurately assess their capabilities in predicting the pollutant dispersion.

In this paper, firstly, a brief discussion regarding theoretical, empirical and semi-empirical dispersion models is provided. Then, numerical simulations of pollutant dispersion are performed for two configurations: an isolated stack and a building placed upwind of a stack. In the first case, the plume spread is mainly controlled by the atmospheric boundary layer turbulence while in the second case, also the local building-induced flow pattern and turbulence play a crucial role. Results are analysed in terms of time-averaged pollutant concentrations and systematically compared to corresponding experimental data. In the configuration with the isolated stack, both RANS and LES simulations are performed, in order to compare their results when a relatively simple configuration is analysed. To the best of the authors' knowledge, this contribution is the first to present an in-depth study of LES results for the configuration with the isolated stack. When the configuration with the building placed upwind of a stack is analysed, the time-averaged pollutant concentrations are evaluated not only close to the pollutant source, but also far downwind, aimed at assessing LES capabilities in predicting the pollutant concentrations also in the far wake region.

This paper is organised as follows. In Section 7.2 some of the most commonly adopted theoretical, semi-empirical and empirical dispersion models are briefly recalled. Then, the setup adopted in the wind-tunnel experiments used as reference in this paper is described in Section 7.3. Section 7.4 focusses on the setup adopted for the numerical simulations. The results obtained for the isolated stack configuration are discussed in Section 7.5, while the case of the building with downwind stack is discussed in Section 7.6. Finally, Section 7.7 contains discussion and conclusions.

7.2 THEORETICAL BACKGROUND

In this section, the theoretical background underlying dispersion models subsequently used for a comparison of their results with numerical and experimental data is briefly recalled. In particular, Section 7.2.1 briefly recalls stochastic models for both Markovian and non-Markovian random processes. Then, Section 7.2.2 introduces gradient diffusion models and, finally, Section 7.2.3 focusses on the widely adopted Gaussian plume model.

The classical decomposition of the velocity field, $\mathbf{u}$, and the concentration field, c, in time-averaged and zero-mean fluctuating part is adopted:

$$\mathbf{u} = \mathbf{U} + \tilde{\mathbf{u}}, \tag{7.1}$$

$$c = C + \tilde{c}, \tag{7.2}$$

where instantaneous quantities are indicated in lowercase, time-averaged ones with capital letters while the zero-mean fluctuating parts are denoted as $\tilde{(\cdot)}$. The components of the velocity field along the x, y and z directions are indicated as u, v, w, respectively.

7.2.1 *Stochastic models for convection-diffusion problems*

The microscopic description of diffusion process is usually modelled as a Brownian motion, assuming that the variation of the particle position can be described by a Markovian random process [177, 178]. It must be noted that, in order to accept such an hypothesis, a strong scales separation between the microscopic particle motion and the macroscopic evolution of the studied phenomena is required. Since the integral scales that characterise the velocity field are usually comparable to that of the studied phenomenon, the convection and diffusion within a turbulent wind flow can usually not be modelled as a Markovian process [177].

In particular, adopting a Lagrangian reference system, marked as $\mathcal{L}$ in the following, the time correlation coefficient of w can be computed as:

$$R_{w,\mathcal{L}}(t') = \frac{\overline{\tilde{w}(t)\tilde{w}(t+t')}}{\sigma_w^2}, \tag{7.3}$$

where t is the time, t' is the time lag, $\overline{(\cdot)}$ denotes the time-averaging operator and σ_w^2 is the variance of $\tilde{w}$. Then, starting from the work of Taylor [179], it is possible to demonstrate that:

$$\sigma_z^2 = 2\sigma_w^2 \int_0^t \int_0^{t'} R_{w,\mathcal{L}}(t')\,dt'\,dt, \tag{7.4}$$

where σ_z^2 is the dispersion parameter in the vertical direction, which is equal to the square of the standard deviation of a Gaussian distribution that can be used in order to fit the particle concentration profile along the z direction (for more details the reader is referred to Hanna et al. [177]). If an exponential decay is assumed for $R_{w,\mathcal{L}}(t')$:

$$R_{w,\mathcal{L}}(t') = e^{-\frac{t'}{T_{w,\mathcal{L}}}}, \tag{7.5}$$

where $T_{w,\mathcal{L}}$ denotes the integral time scale of the w fluctuations, by substituting Eq. (7.5) into Eq. (7.4), the following analytical solution for σ_z^2 can be obtained:

$$\sigma_z^2 = 2\sigma_w^2 T_{w,\mathcal{L}}^2 \left[\frac{t}{T_{w,\mathcal{L}}} - 1 + e^{-\frac{t}{T_{w,\mathcal{L}}}}\right]. \tag{7.6}$$

The along-wind distribution of σ_z^2 can be obtained by replacing t with x/U in Eq. (7.6), where U is the time-averaged wind velocity along the x direction.

Furthermore, it is also possible to obtain σ_z^2 as a function of the velocity power spectral density $S_{w,\mathcal{L}}(f)$ instead of the time correlation $R_w(t')$, since these two are related through the Wiener-Khinchin theorem [180]. It can be thus demonstrated that [177]:

$$\sigma_z^2 = \sigma_w^2 t^2 \int_0^\infty S_{w,\mathcal{L}}(f)\hat{\Phi}(f,t)\,df, \tag{7.7}$$

where $S_{w,\mathcal{L}}(f)$ is the power spectral density of $\tilde{w}$ in a Lagrangian reference system, while $\hat{\Phi}(f,t)$ is the function reported below:

$$\hat{\Phi}(f,t) = \frac{\sin^2(\pi f t)}{(\pi f t)^2}. \tag{7.8}$$

Analogous relationships can be obtained for σ_y^2, $R_v(t')$ and σ_v^2. It should be noted that $\hat{\Phi}(f,t)$ acts as a filter function. Indeed, as the time increases, $\hat{\Phi}(f,t)$ moves the frequency cutoff from high to low frequencies, as shown in Fig. 7.1, where $\hat{\Phi}(f,t)$ is plotted in a non-dimensional form for different non-dimensional times $tU/L_{w,\mathcal{L}}$ and compared to the well-known von Kármán spectrum obtained with unitary values of σ_w^2, turbulence length scale $L_{w,\mathcal{L}}$ and along-wind velocity U.

Looking at Eq. (7.4), it is interesting to observe that if $t' \to \infty$, then by definition $\int_0^{t'} R_{w,L}(t')dt' \to T_{w,L}$, where $T_{w,\mathcal{L}}$ is the turbulence time scale defined in a Lagrangian reference system. Consequently, in

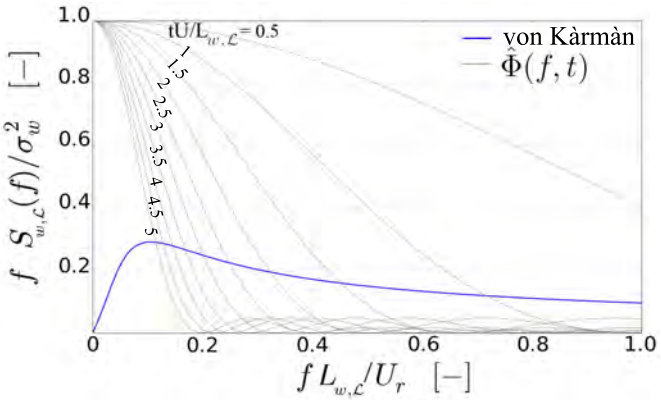

Figure 7.1: Effects of eddies filtering: non-dimensional von Kármán spectrum and filter function $\hat{\Phi}(f,t)$ plotted for $0.5 \leqslant tU/L_{w,\mathcal{L}} \leqslant 5$.

this case if $t, t' \to \infty$ then $\sigma_z^2 \to \sigma_w^2 t T_{w,\mathcal{L}}$ and thus $\sigma_z \propto t^{\frac{1}{2}}$. Therefore, it appears that far from the source Eq. (7.4) is in accordance with the classical Brownian motion theory, which predicts $\sigma_z \propto t^{\frac{1}{2}}$ independently from t. Nevertheless, when the convection-diffusion process near the source is investigated (that corresponds to $t, t' \to 0$), then Eq. (7.4) gives $\sigma_z \propto t$ and so it differs from the Brownian motion theory. This fact is expected: the effects introduced by the non-Markovianity of the process are significant near the source due to the fact that the incoming turbulence integral time scale and the advection time from the source are comparable. Proceeding further downstream their ratio tends to vanish rendering such effects of secondary importance.

7.2.2 *Gradient transport models*

Starting from the stochastic model described in Section 7.2.1, using Kolmogorov equations [181] and adopting an Eulerian reference system, it is possible to obtain the well-known convection-diffusion equation for the pollutant concentration reported below [182]:

$$\frac{\partial c}{\partial t} + \mathbf{u} \cdot \nabla c = D \nabla^2 c, \tag{7.9}$$

where D is the molecular diffusivity coefficient and ∇ and ∇^2 represent the gradient and the Laplace operators, respectively. Models based on Eq. (7.9) are referred as gradient transport models. Applying a time-averaging operator on Eq. (7.9), it is possible to obtain [182]:

$$\frac{\partial C}{\partial t} + \mathbf{U} \cdot \nabla C = D\nabla^2 C - \nabla \cdot \overline{\tilde{\mathbf{u}}\tilde{c}}, \tag{7.10}$$

where the last term needs to be modelled in order to express the problem only in terms of time-averaged quantities. The simplest way is to model the term $\overline{\tilde{\mathbf{u}}\tilde{c}}$ in analogy with molecular diffusion as follows:

$$\overline{\tilde{\mathbf{u}}\tilde{c}} = -D_t \nabla C, \tag{7.11}$$

where D_t is the turbulent diffusion coefficient. Equation (7.11) relates the turbulent transport of the pollutant concentration to the gradient of the time-averaged concentration and represents the well-known Standard Gradient Diffusion Hypothesis (SGDH), which is one of the most widely adopted models for pollutant dispersion studies. Note that the turbulent diffusion coefficient D_t is unknown *a priori* since it is a local property of the flow field and not a fluid property. Apart from the SGDH, many other models based on higher order closure equations can be found in the literature and for a detailed review the reader is referred to Kao [182].

If the SGDH is adopted, the governing balance equation for the pollutant concentration can be obtained by substituting Eq. (7.11) into Eq. (7.10) and is reported below:

$$\frac{\partial C}{\partial t} + \mathbf{U} \cdot \nabla C = D\nabla^2 C + D_t \nabla^2 C. \tag{7.12}$$

7.2.3 *Gaussian plume model*

Using the previously presented models for the description of the convection-diffusion problem, the well-known Gaussian plume model can be obtained.

In particular, the Gaussian plume model finds its origin in the pioneering works of Sutton [183], Pasquill [184] and Gifford [185] and still represents one of the most commonly used approaches to deal with stack gas dispersion or far-field pollutant dispersion in the atmospheric boundary layer [177]. Let us consider a pollutant source located at height H_s above the ground and characterised by a constant mass flow rate Q, placed in a uniform wind flow with time-averaged velocity $\mathbf{U} = (U_r, 0, 0)$ (see Fig. 7.2). Note that the adopted reference velocity should be representative of the time-averaged velocity in the plume. It is generally considered to be equal to the time-averaged wind

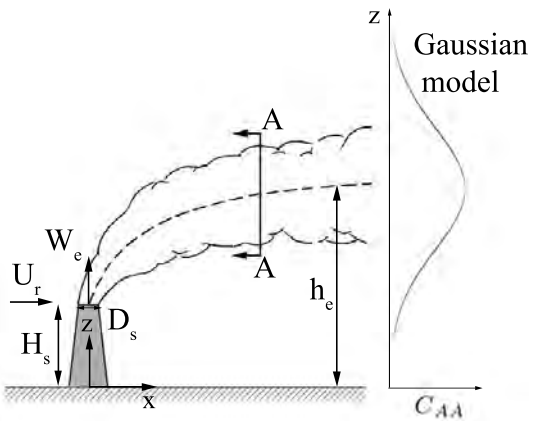

Figure 7.2: Simplified sketch of a typical plume rising from an isolated stack (left side) together with the shape of the time-averaged pollutant concentration that can be obtained with the Gaussian plume model (right side) (adapted from Hanna et al. [177]) .

velocity in the along-wind direction at the plume centerline [177]. The time-averaged pollutant concentration can be estimated as:

$$C = \frac{Q}{2\pi\sigma_y\sigma_z U_r} e^{-\frac{y^2}{2\sigma_y^2}} [e^{-\frac{(z-h_e)^2}{2\sigma_z^2}} + e^{-\frac{(z+h_e)^2}{2\sigma_z^2}}], \tag{7.13}$$

where h_e is the effective plume height, while σ_y and σ_z are the dispersion parameters as defined in Sec. 7.2.1. The effective plume height is the height at which the maximum time-averaged concentration is observed and can be computed by adopting simplified approaches based on empirical formulae, as subsequently described in the present section. Near the ground, the pollutant concentration is subjected to reflection phenomena that are taken into account by means of the last term in Eq. (7.13), which is obtained by assuming a virtual source identical to the considered one but symmetrical with respect to the ground [177].

The dependence of the pollutant concentration C on the distance x is not explicitly visible in Eq. (7.13), but it is implicitly included by the parameters σ_y and σ_z, which are functions of the along-wind distance from the pollutant source. It should be noted that σ_y and σ_z are representative of the turbulence characteristics of the atmospheric boundary layer as well as its stability properties [184].

The Gaussian plume model allows fast and simple calculations and descends from the convection-diffusion equation, reported in Eq. (7.9) [177]. When properly calibrated such model can lead to results in good

agreement with experimental data as well as other more refined models [186–188]. Nevertheless, it has some limitations in particular for near-field dispersion in the presence of obstacles such as buildings.

Moreover, an aspect that is not taken into account by such model is the presence of a vertical gradient in the average wind velocity profile. Such aspect can play a role in the convection-diffusion process and becomes particularly important when the plume widens downstream the source. Furthermore, the parameters σ_y and σ_z as well as the effective height h_e are unknown *a priori*.

Nevertheless, the effective height can be estimated using the formula presented by Briggs [189], who focussed on the study of buoyant plumes and jets in both vertical and bent-over conditions. In the case of a bent-over plume coming from a stack in absence of buoyancy effects, h_e can be calculated as [189]:

$$h_e = H_s + 3D_s M, \tag{7.14}$$

where H_s is the stack height, D_s is the stack internal diameter and M is the ratio between the vertical component of the time-averaged momentum of the gas coming from the stack and the horizontal component of the time-averaged momentum characterising the approaching wind flow (see Fig. 7.2).

For what concerns the estimation of σ_y and σ_z, the most frequently adopted methods are represented by the Stability Class Method and the $\sigma_\theta - \sigma_e$ Method, which are briefly described in the following sections.

7.2.3.1 *Stability Class Method*

If a detailed characterisation of the inflow turbulence is not available, a first estimate of the dispersion parameters can be obtained by means of the Stability Class Method, firstly proposed by Pasquill [184]. In particular, Briggs [190] combined the work of Pasquill [184], Gifford [185] and Smith [191] to produce the well-known formulae reported in Table 7.1, valid for flat terrain with uniform roughness.

The evaluation of the dispersion parameters through such formulae inherently suffers from the main limitations typical of empirical approaches. Indeed, no dependence of σ_y and σ_z on the terrain aerodynamic roughness length has been included in the model due to the limited number of experimental tests performed in the original study in order to investigate the effects of such parameter [177]. Furthermore, the correct classification of the atmospheric stability can be challenging if appropriate data are unavailable. As a result, such way of proceeding

Pasquill type	Description	σ_y [m]	σ_z [m]
A	Extremely unstable	$0.22x(1.0+1e^{-4}x)^{-\frac{1}{2}}$	$0.2x$
B	Moderately unstable	$0.16x(1.0+1e^{-4}x)^{-\frac{1}{2}}$	$0.12x$
C	Slightly unstable	$0.11x(1.0+1e^{-4}x)^{-\frac{1}{2}}$	$0.08x(1.0+2e^{-4}x)^{-\frac{1}{2}}$
D	Neutral	$0.08x(1.0+1e^{-4}x)^{-\frac{1}{2}}$	$0.06x(1.0+1.5e^{-3}x)^{-\frac{1}{2}}$
E	Slightly stable	$0.06x(1.0+1e^{-4}x)^{-\frac{1}{2}}$	$0.03x(1.0+3e^{-4}x)^{-1}$
F	Moderately stable	$0.04x(1.0+1e^{-4}x)^{-\frac{1}{2}}$	$0.016x(1.0+3e^{-4}x)^{-1}$

Table 7.1: Dispersion parameters in the atmospheric boundary layer based on stability classes: formulae proposed by Briggs for flat terrain with uniform roughness and $10^2 < x < 10^4$ [m] [190].

necessarily relies on a layer of empiricism and can provide accurate results only when applied to conditions similar to that used in the experiments adopted to develop the methodology. Unfortunately, this does not include the presence of complex terrains and/or high aerodynamic roughness as in urban environments.

7.2.3.2 $\sigma_\theta - \sigma_e$ *Method*

When measurements are available in order to characterise the incoming turbulence, it is possible to estimate the dispersion parameters from the standard deviation of the wind velocity. Starting from the work of Taylor [179], σ_y and σ_z can be expressed as:

$$\sigma_y(x) = \sigma_\theta x f_y\left(\frac{x}{U_r T_{v,L}}\right), \tag{7.15}$$

$$\sigma_z(x) = \sigma_e x f_z\left(\frac{x}{U_r T_{w,L}}\right), \tag{7.16}$$

where $\sigma_\theta = \sigma_v/U_r$, $\sigma_e = \sigma_w/U_r$ and f_y and f_z are empirical functions. Different forms for f_y and f_z have been proposed in the literature mainly based on experimental data [192–195]. In particular, Draxler [194] proposed the following equations for stable and neutral atmospheric conditions:

$$f_y = f_z = \left[1 + 0.4\left(\frac{x}{U_r T_{v,L}}\right)^{\frac{1}{2}}\right]^{-1}. \tag{7.17}$$

The $\sigma_\theta - \sigma_e$ Method has the appreciable feature to link the turbulence characteristics of the atmospheric boundary layer to the dispersion parameters σ_v and σ_w but, similarly to the Stability Class Method it relies on empirical relations, represented by the functions f_y and f_z. It is interesting to note that, using Eq. (7.6) with Eq. (7.15) and substituting into Eq. (7.17), it is possible to obtain an analytical expression for f_y and f_z. Due to the fact that in the present paper no significant differences are observed when the analytical expression for f_y and f_z are used, in the next sections only Eq. (7.17) is adopted.

7.3 EXPERIMENTAL SETUP

In this section, the experimental setup adopted for the wind tunnel experiments used for validation of the numerical simulations is described. The setups for the two configurations (with and without the building) are identical except for the presence of the building itself. The experiments were conducted in the Meteorological Wind Tunnel of the U.S. Environmental Protection Agency Fluid Modeling Facility and results are presented in Huber et al. [146, 196]. The present work focusses on an isolated rectangular building placed adjacent to a stack. The building is characterised by a vertical square section with dimension H_b and a length of $2H_b$, as shown in Fig. 7.3. The Cartesian coodinate system is defined so that the time-averaged approach flow wind velocity is oriented in the x direction, while z and y represent the vertical and the across-wind directions, respectively. The origin of the coordinate system is placed on the ground in the correspondence of the downwind surface of the building as shown in Fig. 7.3. A stack with a circular cross section is placed adjacent to the building (see Fig. 7.3). The stack height is $H_s = 1.5H_b$ and its internal diameter is $D_s = 4.2 \times 10^{-2} H_b$.

During wind tunnel tests, a length scale equal to $1/200$ was adopted, leading to a reduced-scale model with $H_b = 2.5 \times 10^{-1}\,m$. The section of the wind tunnel was 3.7 m wide and 2.1 m high, so that the resulting blockage ratio was 1.6%.

The time-averaged wind velocity profile reproduced in the wind tunnel showed to fit a $1/6$ power law, which is representative of neutral atmospheric conditions and mildly rough terrain [196, 197]. Therefore, the time-averaged wind velocity profile can be expressed as:

$$U(z) = U_r \left(\frac{z}{H_b} \right)^{1/6}, \tag{7.18}$$

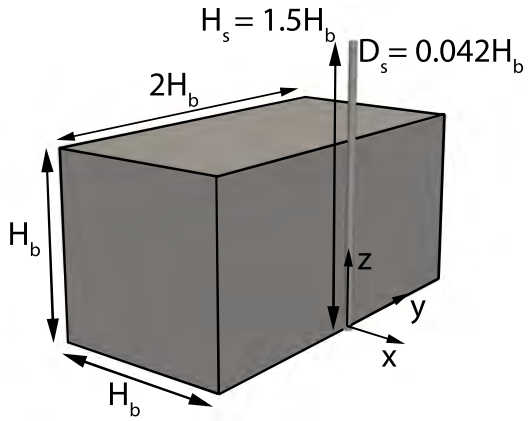

Figure 7.3: Perspective view of the building with downwind stack together with the coordinate system adopted.

where U_r is a reference velocity, which in this case was measured at a height of $1.5H_b$ and it was equal to 2.34 m/s. Such wind velocity leads to a building Reynolds number equal to $Re = \frac{U_r H_b}{\nu} = 4 \times 10^4$, which can ensure the independence of results with respect to Re based on the criteria reported by Snyder [198].

The turbulence intensity in the along-wind direction was equal to 11% at the reference height $z = 1.5H_b$ while it was equal to 25% near the ground surface at $z = 0.06H_b$, again in agreement with neutral atmospheric conditions over moderately rough terrains [199]. The time-averaged mean wind velocity and the turbulence intensity profiles were obtained by means of castellated barriers, elliptic-wedge vortex generators and roughness elements placed upwind of the geometrical model [200] and where measured at the origin of the aforementioned Cartesian system in absence of the stack and the building (see Fig. 7.3).

During the experiments, the pollutant was emitted from the stack with a vertical time-averaged velocity W_e equal to $1.5U_r$. The gas emitted from the stack was composed by air and a mass fraction of methane equal to 1%. The turbulent regime of the emitted gas was ensured by serrated washers placed upwind of the gas exit [146, 196]. In the following, only the experiments for which no buoyancy effects were present are considered.

Concentration measurements were performed by means of a flame ionisation detector and time-averaged concentrations were computed based on a sampling time of one minute, for which stable averages were recorded [146].

7.4 NUMERICAL SETUP

Section 7.4.1 describes the numerical setup, while Section 7.4.2.1 and Section 7.4.2.2 focus on the turbulent inflow condition used for LES and RANS, respectively.

7.4.1 *Numerical setups*

The dimensions of the computational domain are reported in Fig. 7.4 (a) and (b) that show its lateral and top views, respectively. The across-wind section is $9.6H_b$ wide and $7.2H_b$ high (see Fig. 7.4), leading to a blockage ratio equal to 1.5%. The distance of the building from the outlet boundary is set equal to $20H_b$ in order to allow flow development in the wake region [201–203]. The domain dimensions, the distance of the building from the boundaries and the blockage ratio are in agreement with the requirements suggested by the COST guidelines [136] and the AIJ guidelines. [122]. Also the directional blockage ratios are calculated and they are equal to 20.8% and 13.8% in the lateral and vertical direction, respectively [1].

In order to limit the along-wind deterioration of the wind profiles prescribed at the inlet boundary, five rows of square blocks with edge length equal to $h = 0.1H_b$ are placed upwind of the building [27]. The height and distribution of the blocks are calculated by the formula proposed by Lettau [120]:

$$z_0 = 0.5h\frac{A_r}{A_t}, \tag{7.19}$$

where z_0 is the aerodynamic roughness length defined according to EN1991-1-42005 [121], while A_r and A_t are the areas of the block normal to the wind direction and the ground area per roughness block, respectively. The aerodynamics roughness length obtained from Eq. (7.19) is equal to 7×10^{-4} m (reduced-scale value) and it results in good agreement with the aerodynamic roughness length estimated during experiments, which was equal to 6.5×10^{-4} m [146]. In correspondence of the last alignment of roughness blocks, a new boundary layer starts developing. The distance between the upwind surface of the building and the first alignment of roughness blocks is equal to $3H_b$. This distance is calculated by means of the equations proposed by Elliot [137] in order to limit the new boundary layer height below $z = 0.15H_b$.

At the inlet boundary the time-averaged wind velocity profile reported in Eq. (7.18) is prescribed, while at the outlet Neumann con-

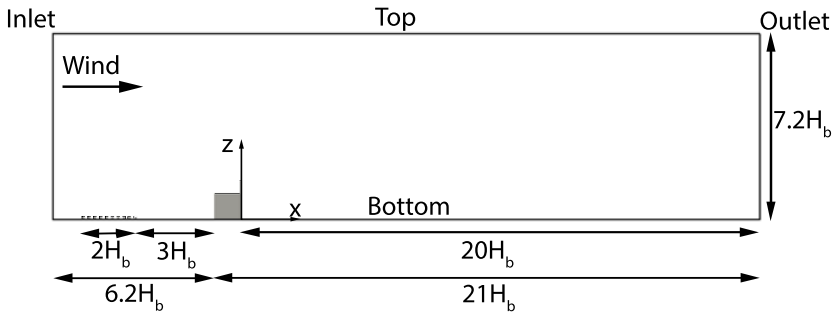

(a)

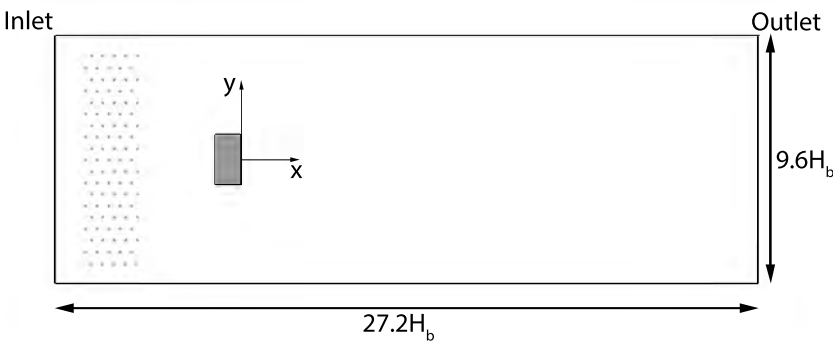

(b)

Figure 7.4: Computational domain: (a) view of the xz plane through $(0, 0, 0)$ and (b) view of the xy plane through $(0, 0, H_b)$.

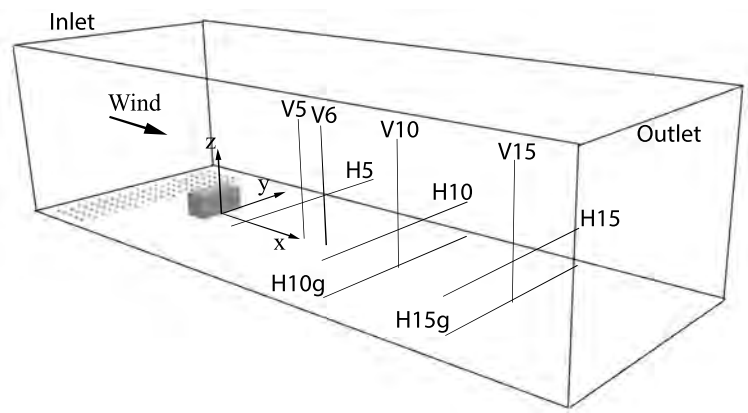

Figure 7.5: Perspective view of the computational domain together with measurement lines.

ditions are imposed. The building, the stack surface and the bottom surface of the domain as well as the roughness blocks are modelled as smooth walls while symmetry conditions are adopted for all the other boundaries. For the walls, the Launder-Spalding wall function on the turbulent viscosity is adopted [204].

Near the building surface a structured grid is adopted, so that the cell dimensions in x, y and z directions are respectively $\delta_x/H_b = \delta_y/H_b = \delta_z/H_b = 7.6 \times 10^{-3}$. Near the stack surface, a structured grid is adopted and cells are refined up to $\delta_x/H_b = \delta_y/H_b = \delta_z/H_b = 1.9 \times 10^{-3}$. Note that the grid resolution adopted is higher than that recommended by Tominaga et al. [122]. Far from the building the cell size is slowly increased up to $\delta_x/H_b = \delta_y/H_b = \delta_z/H_b = 1.2 \times 10^{-1}$. In the wake, at the height of $z = 1.5H_b$ the cell size is kept constant and equal to $\delta_x/H_b = \delta_y/H_b = \delta_z/H_b = 3 \times 10^{-2}$ in order to correctly propagate the incoming turbulence and to limit the numerical dissipation. A lateral view of the computational grid is shown in Fig. 7.6 (a), while Fig. 7.6 (b) shows a perspective view of the grid near the building and the stack. The final grid counts approximately 6.6×10^6 cells.

In order to study the sensitivity of the results on the grid size adopted, three different grids are used to study the case with the isolated stack. In particular, a grid obtained by means of the previously described settings, but without the building, is considered and denoted in the following as M2 (see Fig. 7.7). Starting from the grid M2, a finer one, denoted as M3, and a coarser one, denoted as M1, are obtained using a uniform and isotropic refinement factor equal to $2^{1/3}$. Figures 7.7 (a) and (c) show grids M1 and M3 respectively. The grid refinement led to a number of cells within the stack diameter equal to 16, 20 and 25 for the grids M1, M2 and M3 respectively, as shown in Fig. 7.7 (d-f).

For the spatial discretisation of the advective terms, the Gamma scheme proposed by Jasak et al. [205] is used. This scheme is Total Variation Diminishing and, thus, it does not introduce unphysical fluctuations within the computational domain and it provides a good trade-off between numerical accuracy and numerical stability. All the other terms appearing in the balance equations are discretised in space by means of a centered second-order differentiation scheme.

For LES simulations, the time dicretisation is performed by means of the second-order Backward Differentiation Formulae [11]. The non-dimensional time step adopted, Δt, is fixed and such that $\Delta t^* = \Delta t U_r/H = 1.4 \times 10^{-3}$. In the simulations, the maximum Courant-Friedrichs-Lewy number is equal to 2.7, while its time-averaged value is 1.6×10^{-2}. Regarding the non-dimensional wall distance y^+, its time-averaged

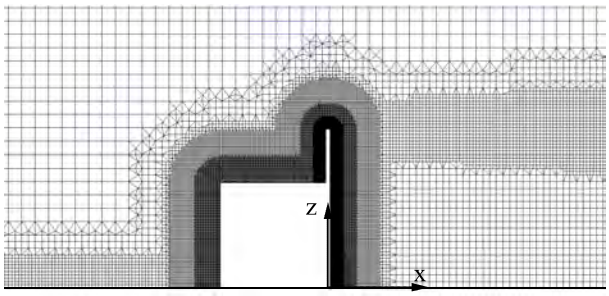

(a)

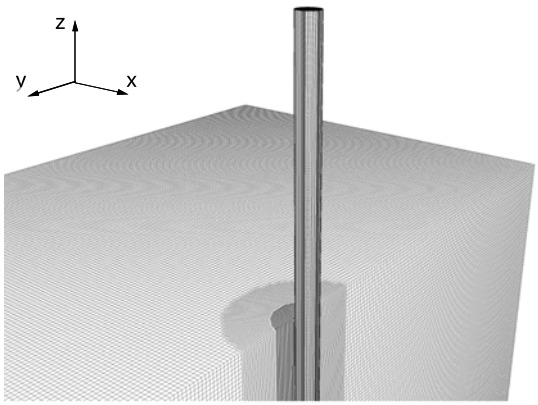

(b)

Figure 7.6: Grid adopted for simulations with the stack and building: (a) view of the xz plane through $(0,0,0)$ and (b) detailed perspective view of the stack and building surfaces.

and space-averaged value equals about 2.4 and 5.4 on the stack and the building surfaces, respectively. The Kinetic Energy Transport (KET) subgrid-scale model is adopted, which consists in the Smagorinsky-Lilly subgrid-scale model [123] with in addition the transport equation of the subgrid turbulent kinetic energy. The KET subgrid-scale model has the capability to adjust the turbulent viscosity based on the subgrid turbulent kinetic energy and it shows to be less dissipative if compared to the standard Smagorinsky-Lilly subgrid-scale model [37]. The KET subgrid-scale model is adopted using $C_e = 1.048$ and $C_k = 0.094$. Additionally, also the subgrid-scale model proposed by Germano et al. [40] is considered in which C_e and C_k are dynamically updated based on the simulation results. In the last case, the subgrid-scale model is referred as dynamic KET.

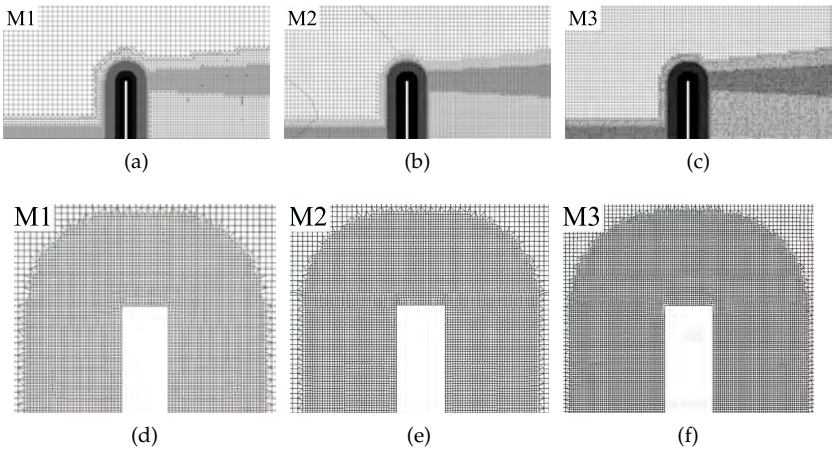

Figure 7.7: Grids adopted for simulations of the isolated stack: view of the xz plane through $(0,0,0)$ of grid (a) M1, (b) M2 and (c) M3 and corresponding detailed views near the top of the stack in (d), (e) and (f) respectively.

The inflow turbulence adopted for LES simulations is generated by means of the Modified Discretising and Synthesising Random Flow Generator (MDSRFG) method [71] and the turbulent fluctuations are introduced in the computational domain following the procedure described by Kim et al. [28].

In addition to LES, the configuration with the isolated stack is studied also by means of steady RANS simulations. In this case, the $k-\omega$ SST turbulence model proposed by Menter [206], which proved to be particularly successful for external aerodynamic problems [207], is adopted. The numerical setups as well as the computational domain adopted for steady RANS are the same as those previously described for LES.

Pollutant dispersion is modelled as the convection and diffusion of a passive and non-reactive scalar. The pollutant is emitted from the top of the stack and is assumed to follow exactly the instantaneous velocity field. The SGDH reported in Eq. (7.11) is adopted, so that the turbulent mass transport vector is assumed to be aligned with the gradient of the average concentration field [24, 47, 163, 208]. The turbulent diffusion coefficient D_t (see Section 7.2.2) is expressed in a non-dimensional form through the turbulent Schmidt number Sc_t, defined as $Sc_t = D_t/\nu_t$, where ν_t is the turbulent viscosity. The pollutant concentration is sampled at each time step and compared to experimental data along the lines shown in Fig. 7.5 and listed in Tab. 7.2.

	Name	x/H_b		Name	y/H_b
Vertical	V5	5	Horizontal	H5	1.5
	V6	6		H10	1.6
	V10	10		H10g	0.1
	V15	15		H15	1.6
				H15g	0.1

Table 7.2: Lines for comparison between experimental and numerical data.

All the numerical simulations are performed using OpenFOAM ® v.1612+ [209] on the CINECA MARCONI cluster. A typical run is performed using 340 cores on 5 computational nodes. Each node is composed by a 68-core Intel® Knights Landing 1.40 GHz and has 93 GB of RAM. By means of such setup, the computational cost of a typical run is about 4×10^4 CPU hours.

7.4.2 *Inflow conditions*

In this section, the turbulent inflow conditions adopted are discussed. In particular, Section 7.4.2.1 describes the generation of the turbulent fluctuation field used in LES simulations, while Section 7.4.2.2 focusses on the inflow boundary conditions adopted for RANS simulations.

7.4.2.1 *Turbulent inflow adopted for LES*

The turbulent fluctuations characterising the atmospheric boundary layer are generated by means of the MDSRFG method [71]. In particular, a homogeneous and anisotropic velocity field can be generated as:

$$\tilde{\mathbf{u}}(\mathbf{x},t) = \sum_{m=1}^{M}\sum_{n=1}^{N}\left[\mathbf{p}^{m,n}\cos\left(k_j^{m,n}\frac{x_j}{L_s}+\omega^{m,n}\frac{t}{\tau_0}\right)+ \right. \tag{7.20}$$

$$\left. \mathbf{q}^{m,n}\sin\left(k_j^{m,n}\frac{x_j}{L_s}+\omega^{m,n}\frac{t}{\tau_0}\right)\right], \tag{7.21}$$

where N is the number of random samples generated for each of the M frequencies f^m, $\omega^{m,n}$ is a random angular frequency extracted from a Gaussian distribution $\mathcal{N}(f^m,\Delta f)$, L_s is a scale factor calibrated *a*

posteriori and related to the turbulence length scale. The dimensionless parameter τ_0 is set equal to one in the present work. Vectors $\mathbf{p} = (p_u, p_v, p_w)$ and $\mathbf{q} = (q_u, q_v, q_w)$ are calculated as:

$$p_i^{m,n} = \text{sign}(r_i^{m,n}) \sqrt{\frac{2}{N} S_i(f^m) \Delta f \frac{(r_i^{m,n})^2}{1 + (r_i^{m,n})^2}}, \tag{7.22}$$

$$q_i^{m,n} = \text{sign}(r_i^{m,n}) \sqrt{\frac{2}{N} S_i(f^m) \Delta f \frac{1}{1 + (r_i^{m,n})^2}}, \tag{7.23}$$

where $i = u, v, w$, Δf is the frequency increment adopted in the sampling of the spectra, $r_i^{m,n}$ are random numbers extracted from a Gaussian distribution $\mathcal{N}(0, 1)$, while $S_i(f)$ is the target spectrum characterising the i velocity component whose total variance is equal to σ_i^2.

Imposing the condition of null divergence to the velocity field in Eq. (7.21) and following the procedure proposed by Castro et al. [71], the system of equations reported below is obtained:

$$\begin{cases} \mathbf{k}^{m,n} \cdot \mathbf{p}^{m,n} &= 0, \\ \mathbf{k}^{m,n} \cdot \mathbf{q}^{m,n} &= 0, \\ |\mathbf{k}^{m,n}| &= f^m / U_r, \end{cases} \tag{7.24}$$

For a detailed review of the characteristics of MDSRFG and other methods used for the generation of synthetic turbulence based on the spectral approach the reader is referred to Patruno et al. [32].

The fluctuations spectra adopted in the present paper are the well-known von Kármán spectra reported below:

$$S_u(f) = \frac{4(I_u U_r)^2 (L_u / U_r)}{[1 + 70.8(f L_u / U_r)^2]^{5/6}}, \tag{7.25}$$

$$S_v(f) = \frac{4(I_v U_r)^2 (L_v / U_r)[1 + 188.4(2f L_v / U_r)^2]}{[1 + 70.8(f L_v / U_r)^2]^{11/6}}, \tag{7.26}$$

$$S_w(f) = \frac{4(I_w U_r)^2 (L_w / U_r)[1 + 188.4(2f L_w / U_r)^2]}{[1 + 70.8(f L_w / U_r)^2]^{11/6}}, \tag{7.27}$$

where I_i is the turbulence intensity and L_i is the turbulence length scale (for i=u, v, w).

The turbulence length scale is not reported in the experimental database [146] and so it is assumed to be equal to $L_u = 1.5 H_b$, based on the experimental data reported by Kim and Tamura [125] who analysed

different inflow conditions in a wind tunnel with dimensions similar to those considered in the present study. As the MDSRFG method allows to control the turbulence length scale through a scaling parameter L_s (see Eq. (7.21)), an iterative procedure is necessary in order to find the value of L_s that leads to the desired turbulence length scale. At the end of this iterative procedure, the obtained synthetic fluctuation field is used as inflow condition.

For the turbulence of the gas coming from the stack, the turbulent fluctuations are generated with the same procedure as adopted for the inflow but, in this case, due to the presence of two serrated washers in the experimental tests, an homogeneous and isotropic turbulence is considered, with $I_u = I_v = I_w = 14\%$ and $L_u/H_b = 0.5D_s$.

In order to check if the turbulent fluctuation field introduced at the inlet boundary is correctly propagated within the computational domain, a preliminary LES in an empty domain containing only the roughness blocks is performed using the numerical settings reported in Sec. 7.4.1.

The convergence of first and second order statistics has been continuously monitored and checked calculating moving residuals following the procedure suggested by Bruno et al. [112]. Following this procedure, the time history of the considered signal is subdivided in N windows, which extents are nT, where T is set equal to 10 times the autocorrelation time and $n = 0, .., N$. For each window, time-averaged and standard deviation values are calculated, then the residual at the step n is defined as $\phi^n_{res} = \frac{\phi_n - \phi_{n-1}}{\phi_n} \cdot 100$. After $155t^*$, being $t^* = tU_r/H_b$ the non-dimensional time, residuals for both first and second order statistics fell under the threshold of 1.5%, indicating that a satisfactory convergence of the inflow velocity field has been achieved.

In order to compare LES results with the reference experimental data, Fig. 7.8 (a), (b) and (c) report in a non-dimensional form the vertical profiles of the time-averaged velocity, the along-wind turbulence intensity and the along-wind turbulence length scale, respectively. The considered vertical line is taken through the origin of the reference system, where the building and the stack will be placed afterwards. No significant differences in terms of time-averaged velocity are present; i.e. LES results and experimental data almost overlap. A good agreement between LES and experiments is also obtained in terms of along-wind turbulence intensity, in particular for $z \geqslant 0.5H_b$. The along-wind turbulence length scale shown in Fig. 7.8 (c) is computed using the Wiener-Khinchin theorem [180] and the Taylor hypothesis, and at the reference height $z = 1.5H_b$ it is in good agreement with the target value of $L_u = 1.5H_b$.

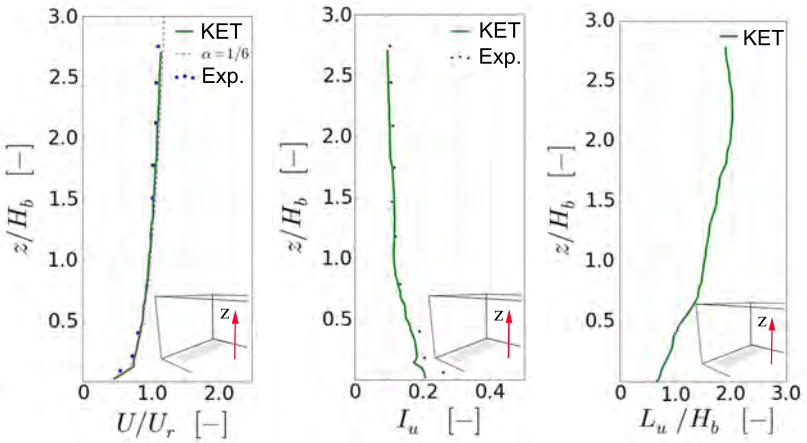

(a) (b) (c)

Figure 7.8: Vertical profiles through $(0, 0, 0)$ of (a) time-averaged velocity, (b) along-wind turbulence intensity and (c) along-wind turbulence length scale obtained from LES and experiments. A comparison with the power law profile with $\alpha = 1/6$ is also provided.

In order to check the spectral content of the inflow turbulence, Fig. 7.9 reports the non-dimensional power spectral density of all velocity components u, v and w for two different locations in the along-wind direction, which are point $(0, -0.4H_b, 1.5H_b)$ and point $(10H_b, -0.4H_b, 1.5H_b)$. The analysis of the frequency content shows that the dissipation is limited, as the spectra at the two locations are very similar to each other. Indeed, the dissipation in terms of percentage over the total variance is equal to 10.9%, 7.9% and 6.9% for u, v and w, respectively. Furthermore, spectra are found to be in good agreement with the target von Kármán ones.

7.4.2.2 *Inflow boundary conditions adopted for RANS*

Different from the LES approach, when the RANS approach is considered the inflow turbulence is taken into account through scalar variables convected and diffused by the flow itself. Starting from the experimental data, the profiles of the turbulent kinetic energy k and the specific dissipation rate ω are computed and imposed as inlet boundary conditions. Also in this case, a preliminary steady RANS simulation is performed in an empty domain identical to that shown in Fig. 7.4 but including only the roughness blocks and adopting grid M2. Figure 7.10 (a) shows the time-averaged along-wind velocity profile obtained from

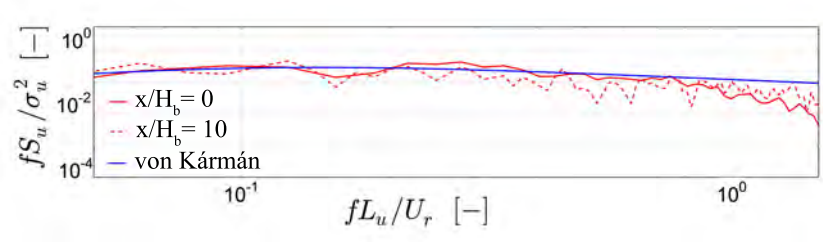

(a)

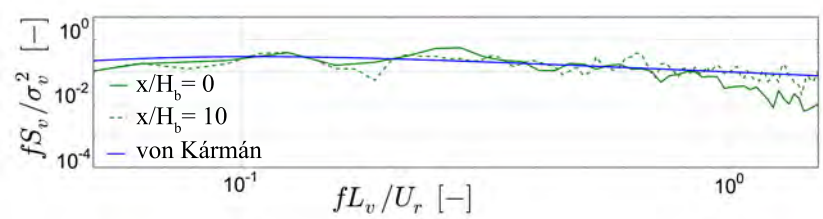

(b)

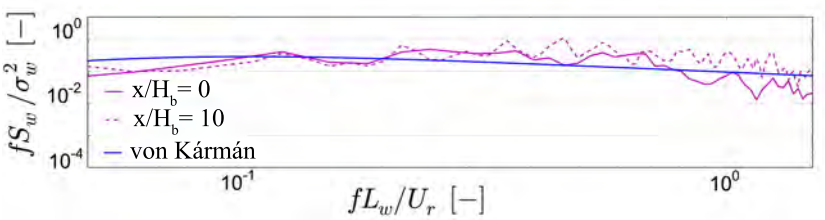

(c)

Figure 7.9: Power spectral densities of velocity components (a) u, (b) v and (c) w at two different along-wind locations, namely $(0, -0.4H_b, 1.5H_b)$ and $(10H_b, -0.4H_b, 1.5H_b)$ and comparison with the von Kármán spectrum.

experiments and RANS simulation and relative to the vertical alignment taken through the origin of the reference system. No significant differences are observed between the numerical and the experimental data.

Regarding the turbulent kinetic energy, it is computed starting from the experimental data of I_u and assuming $I_v = 0.75I_u$ and $I_w = 0.5I_u$, as suggested by Dyrbye et al. [126]. A comparison between the vertical profiles of the turbulent kinetic energy obtained from experiments and RANS is shown in Fig. 7.10 (b). At the reference height $z = 1.5H_b$, the relative difference between RANS and experiments is equal to about 30%.

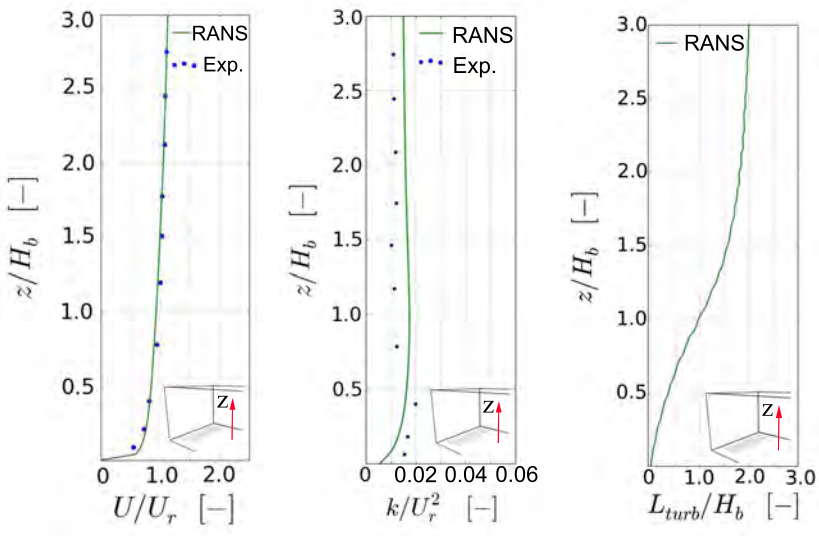

(a) (b) (c)

Figure 7.10: Vertical profiles through $(0, 0, 0)$ of (a) time-averaged velocity, (b) along-wind turbulence intensity and (c) turbulence length scale from RANS and experiments.

The turbulence length scale is computed starting from ω and k as $L_{turb} = \frac{C_\mu^{-0.25}\sqrt{k}}{\omega}$, where $C_\mu = 0.09$ is a constant of the turbulence model adopted [209]. The resulting turbulence length scale is plotted in Fig. 7.10 (c) and at the reference height $z = 1.5H_b$ it results in good agreement with the along-wind turbulence length L_u shown in Fig. 7.8 (c).

7.5 POLLUTANT DISPERSION FROM AN ISOLATED STACK

7.5.1 *RANS results*

In order to analyse the sensitivity of RANS results on the turbulent Schmidt number Sc_t, three different values of Sc_t are investigated, namely $Sc_t = 0.5$, $Sc_t = 0.7$ and $Sc_t = 0.9$ using the grid previously denoted as M2. Such values fall in a range commonly investigated in the scientific literature [20, 21, 24, 47, 208, 210]. The time-averaged pollutant concentrations obtained from RANS along vertical lines V5, V6,

V10 and V15 (see Fig. 7.5) are plotted in Fig. 7.11 (a), (b), (c) and (d), respectively. In the same figure, a comparison with experimental data is also provided.

As expected, a significant dependence of RANS results to the turbulent Schmidt number in terms of time-averaged pollutant concentrations is observed for all vertical lines. As Sc_t decreases, the turbulent diffusivity increases, leading to the underestimation of maximum concentrations and an overestimation of the variances of the vertical distribution. Moreover, if the height of the plume centerline is analysed, it is observed that the RANS simulations systematically underestimate its vertical position, which is found to be equal to $z/H_b = 1.43$ for all the vertical lines when $Sc_t = 0.9$ is considered.

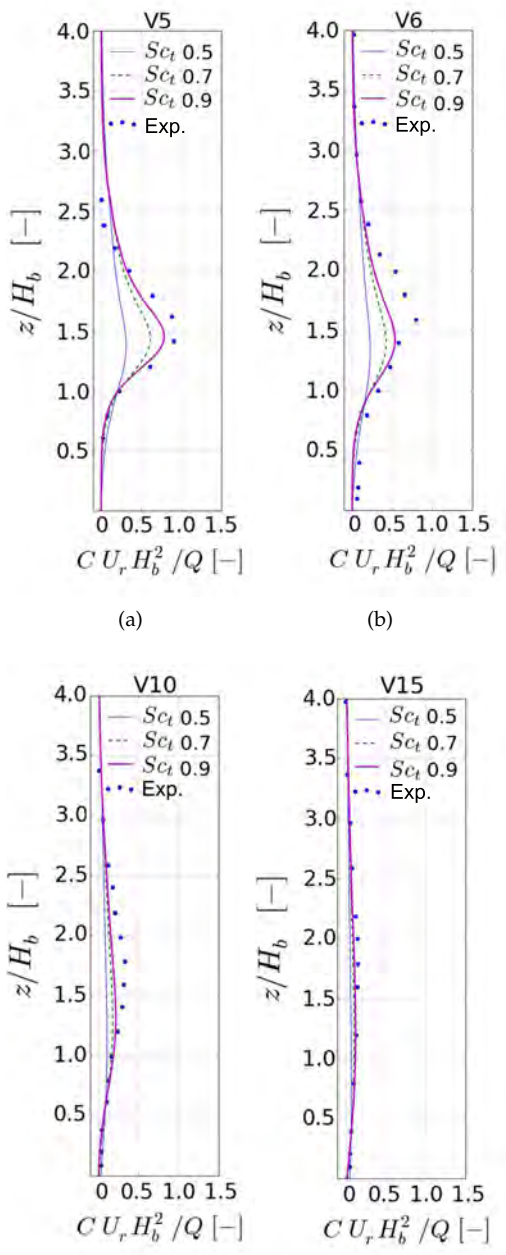

Figure 7.11: Time-averaged pollutant concentrations along lines (a) V5, (b) V6, (c) V10 and (d) V15: comparison between RANS with different turbulent Schmidt numbers and experimental data.

Figure 7.12 shows the time-averaged pollutant concentration along the horizontal lines. Also here the large effect of the turbulent Schmidt number is observed. It represents a considerable limitation for the applicability of RANS to pollutant dispersion problems [24, 47, 155, 208]. Results obtained by means of LES simulations, which can be less affected by such shortcomings, are presented in the next section.

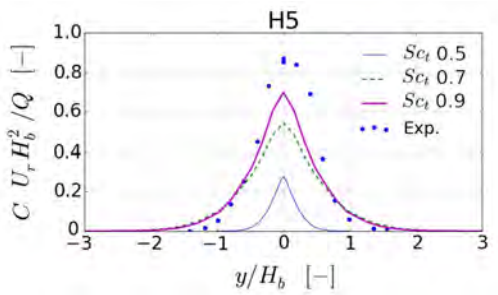

(a)

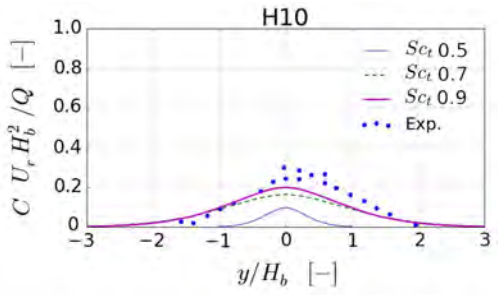

(b)

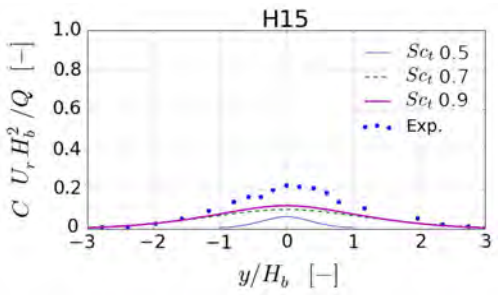

(c)

Figure 7.12: Time-averaged pollutant concentrations along lines (a) H5, (b) H10 and (c) H15: comparison between RANS with different turbulent Schmidt numbers and experimental data.

7.5.2 *LES results*

Fig. 7.13 (a) shows the time history of the pollutant concentration in point $(5H_b, 0, 1.5H_b)$, while Fig. 7.13 (b) shows the corresponding moving residual calculated on its time-averaged value for the grid sizing M2 and the KET subgrid-scale model, according to the procedure described in Section 7.4.2.1. After 350t* the residual is lower than 1.2%, therefore a satisfactory convergence of the time-averaged pollutant concentration is considered to be achieved.

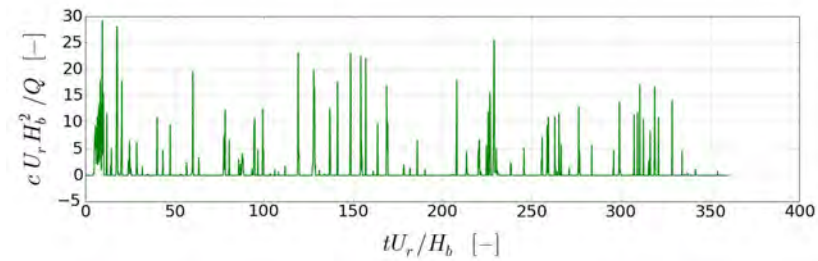

(a)

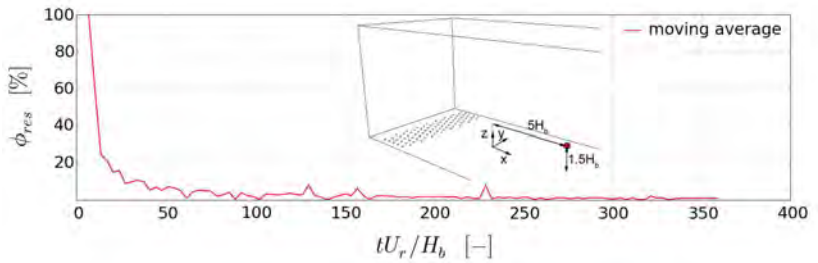

(b)

Figure 7.13: Convergence of pollutant concentrations at $(5H_b, 0, 1.5H_b)$: (a) time history of the concentration and (b) percentage residuals of its time-averaged value for the grid M2 and the KET subgrid-scale model.

The time-averaged pollutant concentrations obtained from LES along vertical lines V5 and V6 (see Fig. 7.5) are plotted in Fig. 7.14. In particular, Fig. 7.14 (a) and (b) compare the results obtained with the grids M1, M2 and M3 for the lines V5 and V6, respectively. These figures show that a clear monotonic grid convergence is not reached. In particular, at V5 the absolute relative difference between numerical and experimental data in terms of maximum concentration is equal to 16.9% and 3.4% for the grids M2 and M3, respectively. Conversely, when the line V6 is analysed, results obtained with M2 are more accurate, being the

absolute relative differences equal to 3.8% and 20.0% for M2 and M3, respectively. Since the accuracy of the results in terms of maximum concentration obtained with the two grids is comparable in the lines considered, grid M2 is adopted in the following due to its reduced computational cost compared to grid M3.

Fig. 7.14 (c) and (d) compare the results obtained with the KET and the dynamic KET subgrid-scale models for the lines V5 and V6, respectively. Considering the maximum value of the time-averaged pollutant concentration, results obtained with the KET subgrid-scale model appear to be more accurate than those obtained with the dynamic KET subgrid-scale model, being the absolute relative differences with respect to experimental data equal to 15.5% and 3.75% for V5 and V6, respectively. Due to this consideration, in the following only results obtained with the KET subgrid-scale model are further discussed.

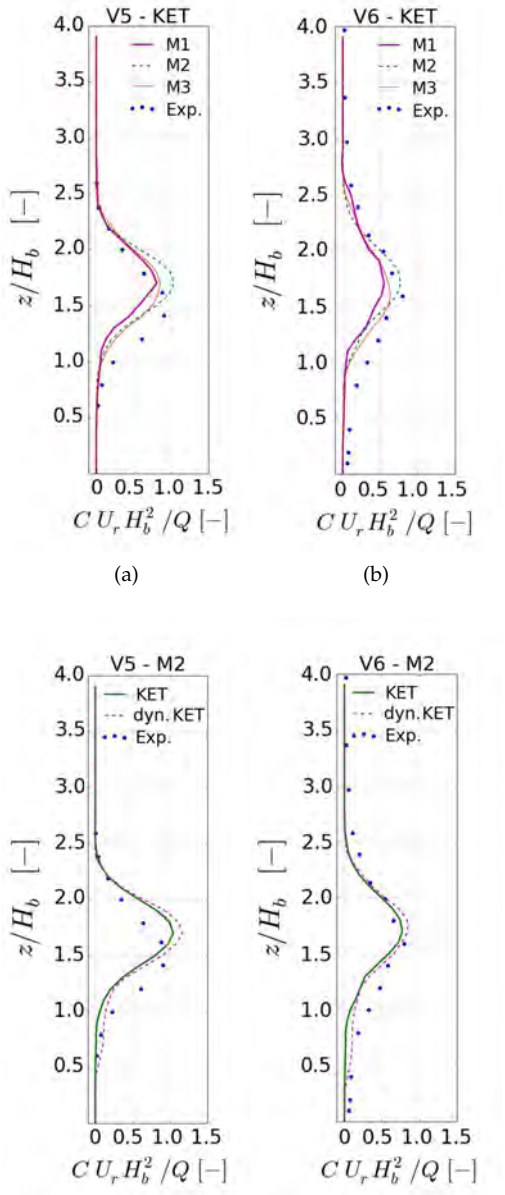

Figure 7.14: Time-averaged pollutant concentrations obtained from LES: comparisons between different grids and subgrid-scale models in correspondence of lines V5 and V6.

In particular, Figures 7.15 (a), (b), (c) and (d) show the time-averaged pollutant concentrations along vertical lines V5, V6, V10 and V15, respectively. Focussing on the height of the plume centerline, the effective height calculated using Eq. (7.14) leads to $h_e/H_b = 1.69$ and is plotted in Fig. 7.15 as a horizontal black line. Due to the absence of buoyancy effects, h_e reaches a constant value. It is observed that in all the considered locations the numerical prediction of h_e is in good agreement with its empirical estimate, while experiments show a lower height of the plume centerline, in particular at V5. It should be noted that as the height of the plume centerline is mainly determined by the time-averaged flow field, this might indicate some discrepancies between the time-averaged velocity field in experiments and in the numerical simulations. Nevertheless, proceeding further downwind, the agreement between experimental data and numerical and empirical predictions of h_e improves, being these values almost overlapped in correspondence of the lines V10 and V15.

Considering now the maximum value of the time-averaged pollutant concentration along each vertical line, numerical simulations show a satisfactory accuracy, being the maximum absolute relative difference with respect to experimental data equal to 15.0%, 3.8%, 6.1% and 6.6% for V5, V6, V10 and V15, respectively.

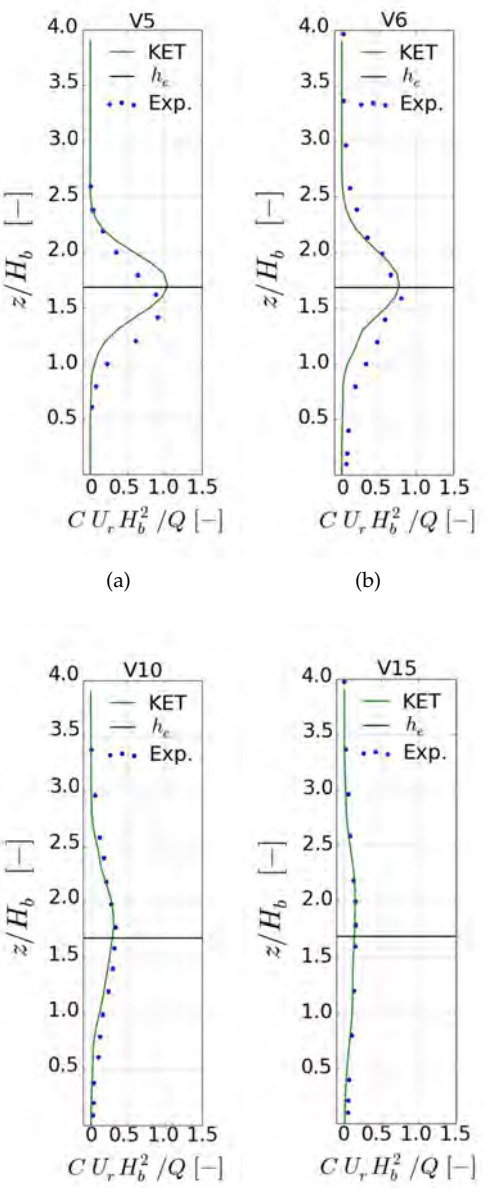

Figure 7.15: Time-averaged pollutant concentrations along lines (a) V5, (b) V6, (c) V10 and (d) V15: comparison between KET subgrid-scale model and experimental data.

With reference to the horizontal lines, Fig. 7.16 (a), (b) and (c) show the time-averaged pollutant concentration along lines H5, H10 and H15, respectively. In this case, the maximum absolute relative difference between numerical and experimental data in terms of maximum time-averaged concentration is equal to 9.3%, 4.6% and 31.8% for H5, H10 and H15, respectively.

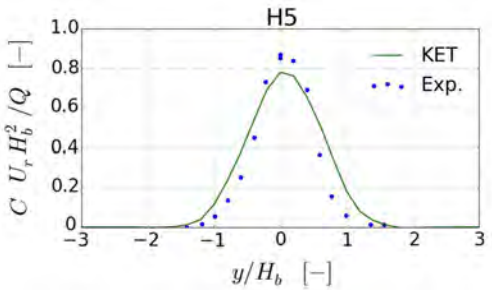

(a)

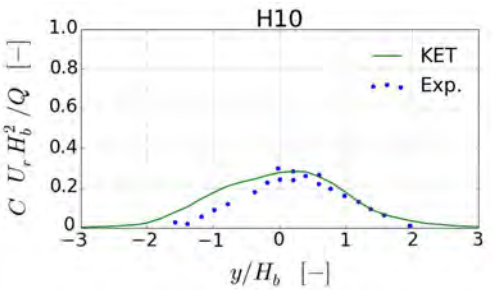

(b)

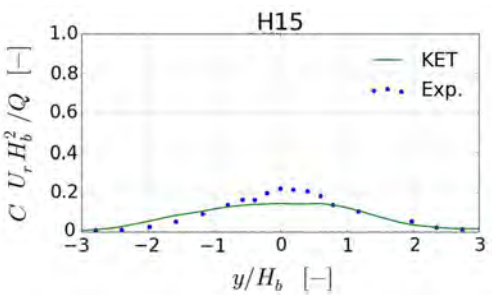

(c)

Figure 7.16: Time-averaged pollutant concentrations along lines (a) H5, (b) H10 and (c) H15: comparison between KET subgrid-scale model and experimental data.

A comparison between the along-wind evolution of σ_z and σ_y is provided in Fig. 7.17 (a) and (b) respectively where they are compared to estimates obtained by means of the theoretical, empirical and semi-empirical approaches previously described in Section 7.2.

In particular, Fig. 7.17 (a) shows that that numerical simulations slightly underestimate the value of σ_z, being the average relative difference between experimental and numerical data equal to 28%. It is interesting to note that in this case the numerical data are very close to the stability class D, which according to the Briggs' classification [190] represents the neutral atmospheric boundary layer, while experimental data are close to the class C, which corresponds to the slightly unstable one. Analysing the $\sigma_\theta - \sigma_e$ Model, it appears to systematically underestimate the value of σ_z, leading to and underestimation of 44% in relative terms with respect to experimental data at $x/H_b = 15$. With respect to the results obtained by means of the stochastic model, it should be noted that its parameters have been calibrated based on the spectra measured in the numerical simulations.

Different from what previously observed for σ_z, when the dispersion parameter σ_y is analysed, Fig. 7.17 (b) shows that numerical simulations tend to overestimate its value. In this case, the Briggs' classification [190] shows that while experimental data are close to the neutral category D, numerical results are slightly shifted towards the slightly unstable condition C. Nevertheless, notwithstanding these considerations, it is interesting to note that numerical simulations are satisfactorily accurate, being the average relative difference between experimental data and numerical predictions of σ_y equal to 26%. As previously observed for σ_z, also in this case the stochastic model shows good performances, being the average relative difference with respect to numerical simulations equal to 13%.

Fig. 7.18 reports the isosurfaces of instantaneous concentration at $cU_r H_b^2/Q = 0.1$. It is observed that the incoming turbulence moves the instantaneous plume in both the vertical (see Fig. 7.18 (a)) and horizontal directions (see Fig. 7.18 (b)), leading to a complex turbulent plume that widens proceeding downwind of the pollutant source.

The widening of the plume dimensions is apparent when the isosurfaces of time-averaged concentration reported in Fig. 7.19 (a) and (b) are observed. The vertical and horizontal sections of the same figures are shown in Fig. 7.19 (c) and (d) respectively. Fig. 7.19 (c) shows that concentrations higher than $CU_r H_b^2/Q = 0.5$ are recorded also quite far downwind of the source, until approximately $x/H_b = 9$. Furthermore, by comparing the plume width in the vertical and in the horizontal directions (see Fig. 7.19 (c) and (d) respectively)), it is observed that

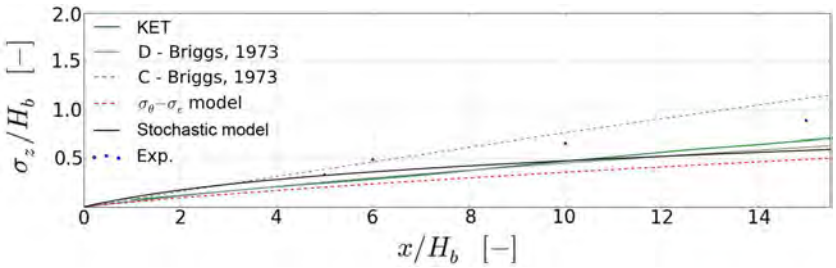

(a)

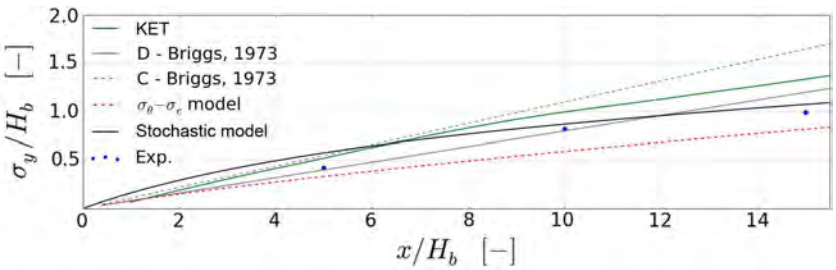

(b)

Figure 7.17: Dispersion parameters evolution with respect to the along-wind distance from the source: (a) vertical variance σ_z and (b) horizontal variance σ_y.

numerical simulations predict different plume dimensions, providing a visual evidence of the anisotropy of the turbulent velocity field previously observed in terms of σ_z and σ_y in Fig. 7.17 (a) and (b).

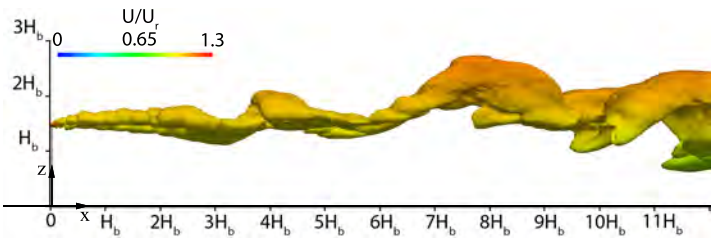

(a)

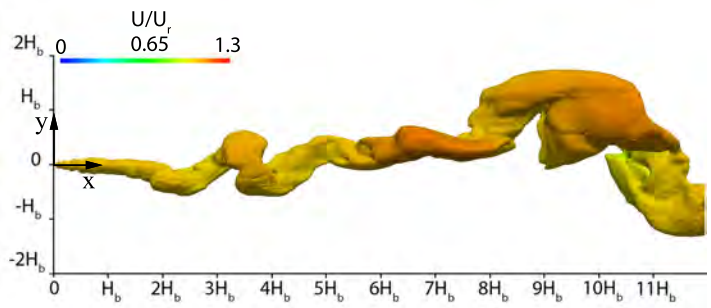

(b)

Figure 7.18: Isosurfaces of instantaneous concentration at $cU_rH_b^2/Q = 0.1$ referred to (a) the xz plane through $(0, 0, 0)$ and to (b) the xy plane through $(0, 0, 1.5H_b)$. Isosurfaces are coloured with the time-averaged wind velocity magnitude.

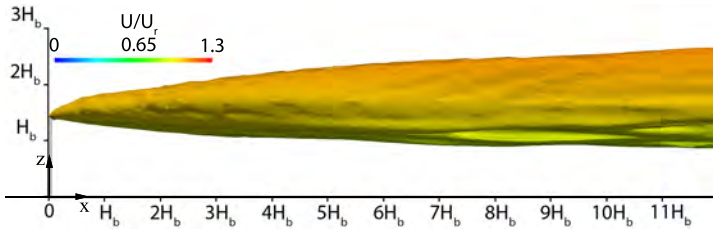

(a)

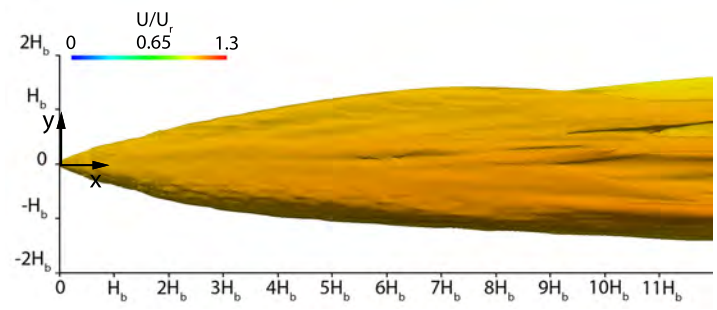

(b)

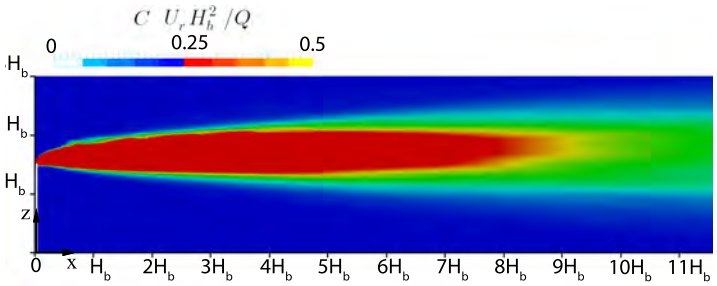

(c)

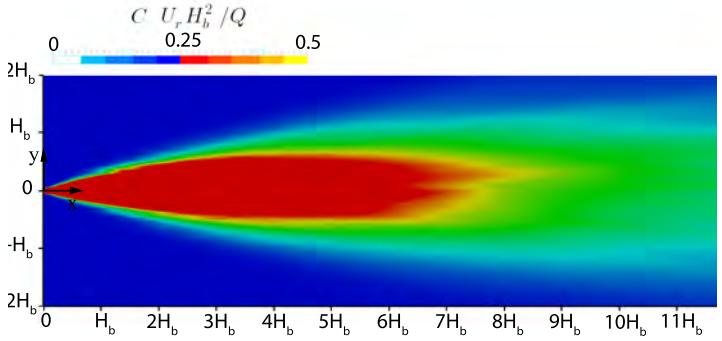

(d)

Figure 7.19: (a),(b) Isosurfaces of time-averaged concentration at $CU_rH_b^2/Q = 0.1$ and (c),(d) isocontours of time-averaged concentration. Views (a) and (c) are referred to the xz plane through $(0,0,0)$ while views (b) and (d) are referred to the xy plane through $(0,0,1.5H_b)$. Isosurfaces are coloured with the time-averaged velocity magnitude.

7.5.3 *Height of the plume centerline: comparison between RANS and LES*

An interesting difference between RANS and LES results is represented by the height of the plume centerline of the time-averaged concentration field. As previously observed, the height of the plume centerline is controlled by the time-averaged velocity field. In this context, the time-averaged flow field obtained from RANS and LES is investigated and Fig. 7.20 shows the time-averaged streamlines coloured with the vertical time-averaged velocity component W in the proximity of the pollutant source. Close to the top of the stack in RANS simulation the loss of momentum in the vertical direction is higher than in LES simulation. Furthermore, looking at Fig. 7.21, which shows the isocontours of the invariant λ_2 for RANS and LES simulations, it is observed that LES simulation predicts the presence of a vortex structure that is not reproduced by RANS.

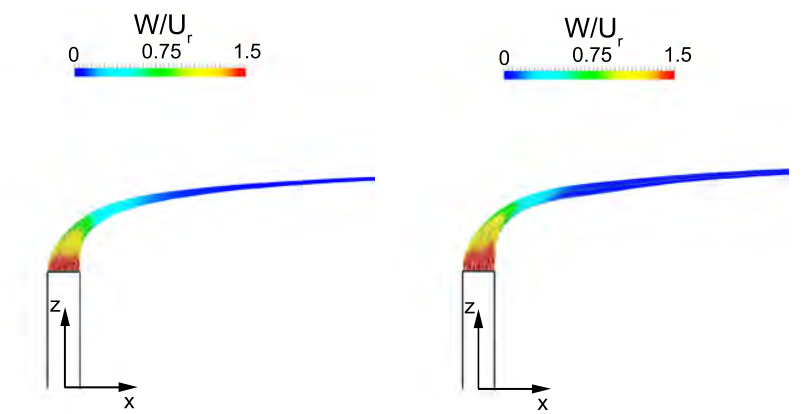

(a) RANS (b) LES

Figure 7.20: Comparison between the time-averaged flow field obtained with RANS and LES: view of the xz plane through $(0,0,0)$ of the time-averaged streamlines coming from the stack coloured with the vertical time-averaged velocity component W.

The higher loss of vertical momentum observed in RANS with respect to LES as well as the different flow organization in the proximity of the stack might contribute to the systematic underestimation of the height of the plume centerline observed for RANS (see Fig. 7.11).

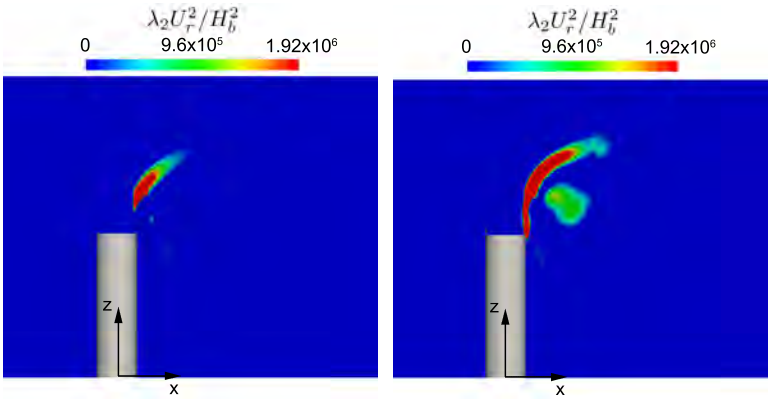

(a) RANS (b) LES

Figure 7.21: Comparison between the λ_2 isocontours obtained with RANS and LES close to the pollutant source: view of the xz plane through $(0, 0, 0)$.

7.6 POLLUTANT DISPERSION FROM A STACK PLACED DOWNWIND OF A BUILDING

The numerical methodology adopted in the previous section is used to analyse the flow field when the building is introduced and placed upwind of the stack. In this case the convergence of the time-averaged pollutant concentrations is declared after $400t^*$, when the moving residual obtained are lower than 1.1%.

Fig. 7.22 (a) and (b) show the isosurfaces of instantaneous concentration at $cU_rH_b^2/Q = 0.1$ for the vertical and the horizontal planes, respectively, while Fig. 7.23 shows the time-averaged streamlines on the xz plane through $(0, 0, 0)$. It is observed that a recirculation region is present downwind of the building, causing the time-averaged flow to be deviated downwards.

The recirculation bubble observed in Fig. 7.23 is the main responsible for the time-averaged pollutant convective transport from the top of the stack towards the ground. This is also depicted in Fig. 7.24, which shows the isosurfaces and the isocontours of the time-averaged concentration field in the vertical plane passing through the origin and in the horizontal plane passing through $(0, 0, 1.5H_b)$. In particular, it is interesting to compare the isocontours of the time-averaged concentration field taken in the vertical plane and reported in 7.24 (c) to the corresponding ones obtained from the isolated stack case and reported in Fig. 7.19 (c). The plume is clearly inclined downwards when the build-

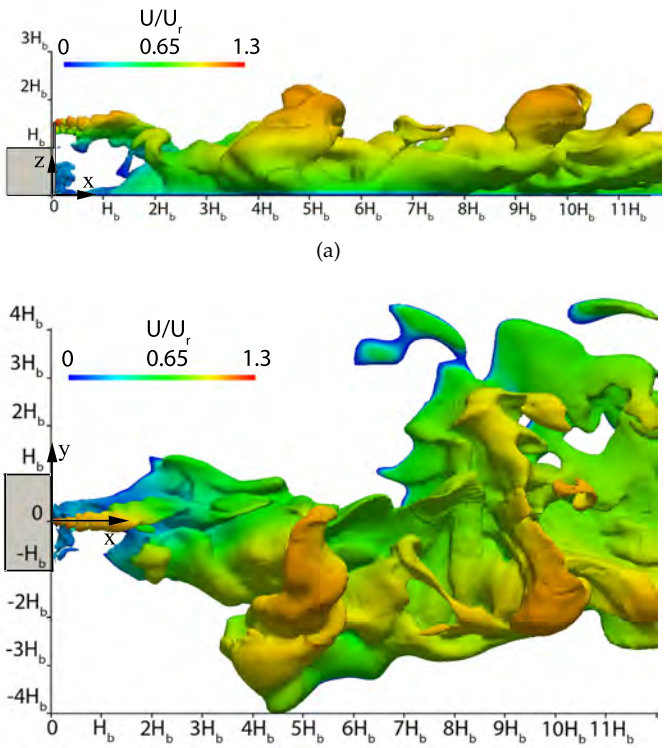

Figure 7.22: Isosurfaces of instantaneous concentration at $cU_rH_b^2/Q = 0.1$ for (a) the xz plane through $(0,0,0)$ and for (b) the xy plane through $(0,0,1.5H_b)$. Isosurfaces are coloured with the time-averaged velocity magnitude.

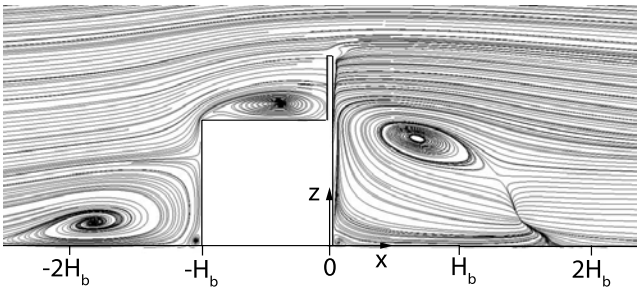

Figure 7.23: View at the xz plane through $(0,0,0)$ of time-averaged streamlines.

ing is introduced, increasing the time-averaged pollutant concentrations near the ground and consequently at the pedestrian level, which is an undesirable effect. Although the increase of the pollutant concen-

tration near the ground is a negative effect, it should be observed that, compared to the configuration with the isolated stack, the decay of the time-averaged pollutant concentration is sharper: an along-wind distance from the source equal to approximately $9H_b$ is needed in the case of the isolated stack in order to obtain concentrations lower than $CU_rH_b^2/Q = 0.5$ while, when the building is introduced, the same threshold is reached at approximately $5.5H_b$. This effect is mainly caused by the building aerodynamics, since the turbulent structures in the wake of the building enhance the turbulent pollutant mixing, leading to a rapid spreading of the pollutant in the wake.

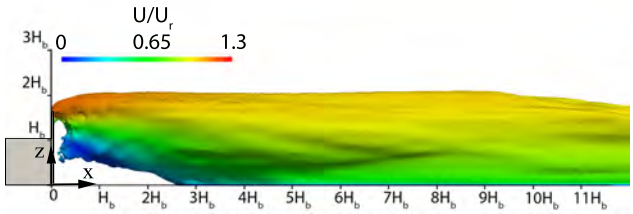

(a)

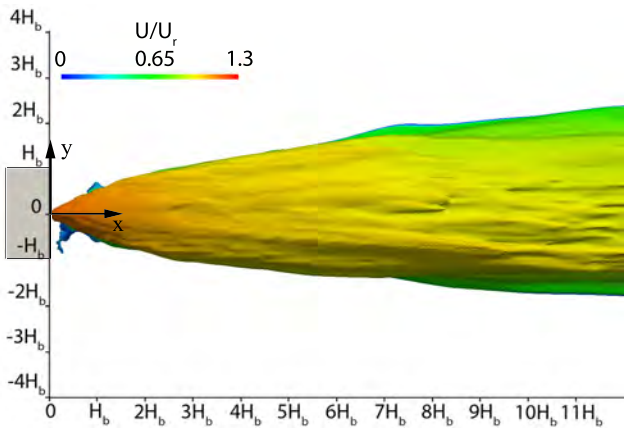

(b)

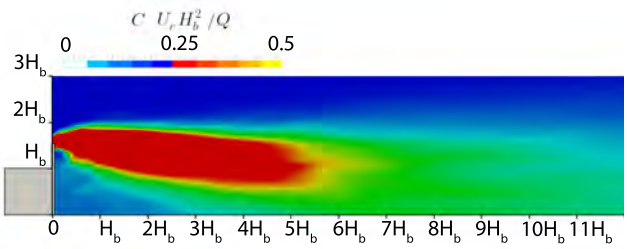

(c)

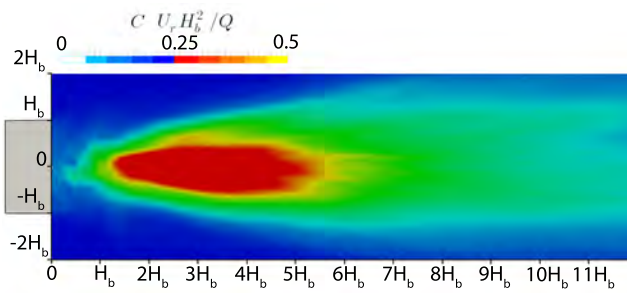

(d)

Figure 7.24: (a),(b) isosurfaces of time-averaged concentration at $CU_rH_b^2/Q = 0.1$ and (c),(d) isocontours of time-averaged concentration. Views (a) and (c) are referred to the xz plane through $(0,0,0)$ while views (b) and (d) are referred to the xy plane through $(0,0,1.5H_b)$. Isosurfaces are coloured with the time-averaged velocity magnitude.

The mixing caused by the turbulent wake of building can be better appreciated in terms of time-averaged pollutant concentrations distributions in Fig. 7.25 and 7.26. In particular, Fig. 7.25 shows the time-averaged pollutant concentrations along vertical lines V5, V10 and V15 together with the experimental data. It is shown that LES simulations are quite accurate for all the considered lines, being the maximum absolute relative difference with respect to experimental data in terms of maximum concentration over all the vertical lines considered equal to 26.7%. In particular, it is interesting to note that a good accuracy of numerical simulations is achieved also far downwind of the pollutant source, that is in correspondence of the alignment V15, where the maximum absolute relative difference between simulations and experiments equals 27.2%.

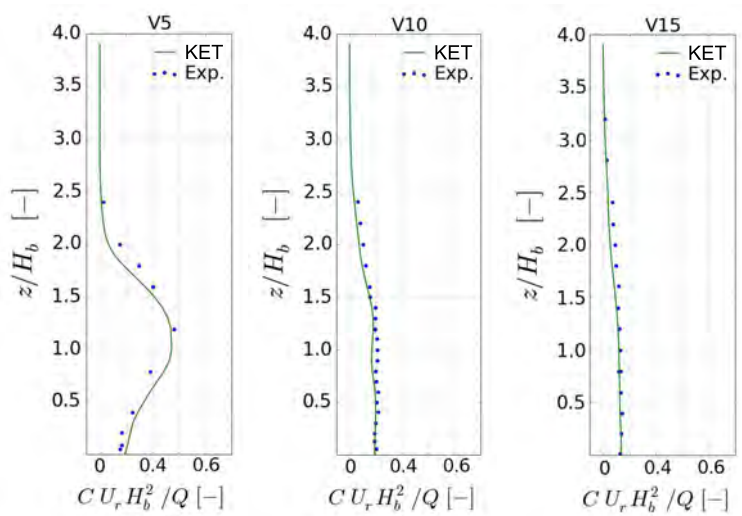

Figure 7.25: Time-averaged pollutant concentrations along lines (a) V5, (b) V10 and V15: comparison between KET subgrid-scale model and experimental data.

Analogously to Fig. 7.25, but focussing on horizontal lines, Fig. 7.26 shows the time-averaged pollutant concentration along lines H5, H10, H10g and H15g together with the experimental data. As observed for vertical lines, LES results are in good agreement with experimental data for all the horizontal lines considered. In particular, the maximum time-averaged concentrations at the ground level, reported in Fig. 7.26 (c) and (d) are accurately predicted by LES, being the maximum abso-

lute relative difference between simulations and experiments equal to 5.5%.

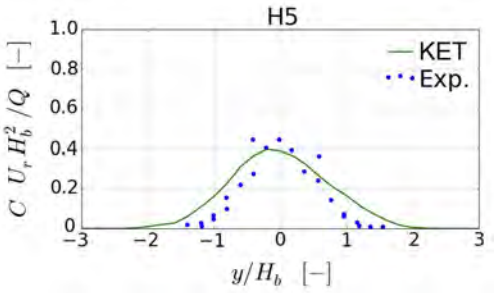

(a)

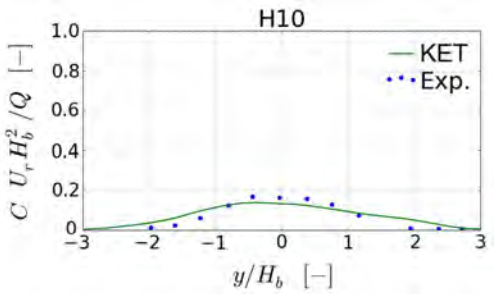

(b)

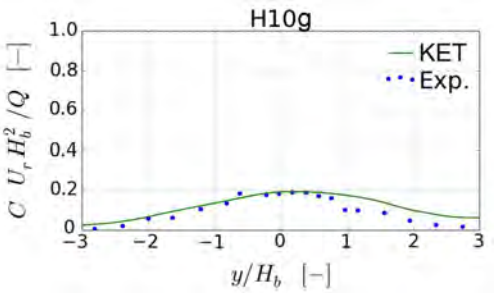

(c)

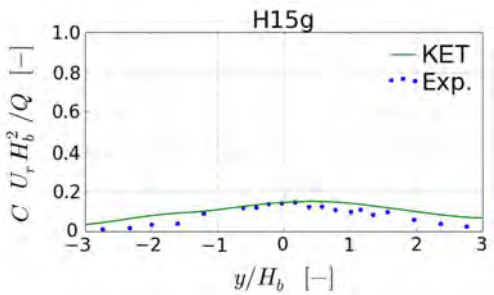

(d)

Figure 7.26: Time-averaged pollutant concentrations along lines (a) H5, (b) H10, (c) H10g and (d) H15g: comparison between KET subgrid-scale model and experimental data.

In order to compare numerical results and experimental data taking into consideration all the available lines, Fig. 7.27 (a) and (b) show the correlation plots in terms of time-averaged pollutant concentrations for the two analysed cases, with and without the building, respectively. Data are coloured with the along-wind distance from the pollutant source and the correlation graphs are characterised by means of the Mean Normalized Bias (MNB) index, which is defined as the average relative error between numerical predictions and experimental data:

$$MNB = \frac{1}{N}\sum_{i=1}^{N}\left(\frac{Q_{i,num} - Q_{i,exp}}{Q_{i,exp}}\right), \tag{7.28}$$

where N is the number of data, while $Q_{i,num}$ and $Q_{i,exp}$ are the considered quantities obtained from numerical simulations and from the experiments, respectively.

When the configuration with the isolated stack is analysed, Fig. 7.27 (a) shows that the percentage of data with a relative difference compared to experiments lower than 30% is of about 70%, while the absolute MNB is equal to 29.6%. Conversely, when the configuration with the building and the stack is considered, Fig. 7.27 (b) shows that the percentage of data within the 30% range increases up to 91.0% and the absolute MNB is reduced to 17.6%, indicating that numerical simulations are more accurate in this case.

7.7 CONCLUSIONS

In the present paper, the capabilities of LES to predict the pollutant dispersion in a turbulent atmospheric boundary layer are investigated. In particular, two different configurations are analysed: the pollutant dispersion from an isolated stack and from a stack placed downwind of a building. The numerical results obtained are analysed in terms of time-averaged pollutant concentrations and systematically compared to experimental data as well as to theoretical, empirical and semi-empirical approaches.

Firstly, the pollutant dispersion from an isolated stack is simulated using both RANS and LES approaches. As expected, RANS results are significantly affected by the turbulent Schmidt number adopted. The need for an *a posteriori* calibration of the turbulent Schmidt number represents a strong limit for RANS applications and led to the application of LES in the present research work. Indeed, in the framework of LES the large-scale turbulent fluctuations are directly reproduced within the computational domain leading to a direct prediction of the

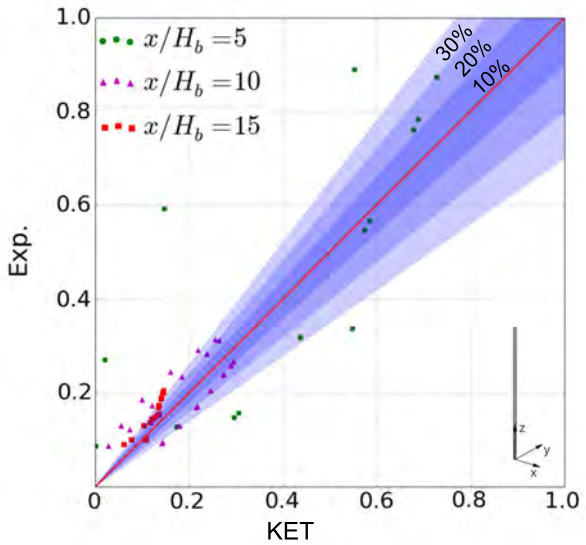

(a)

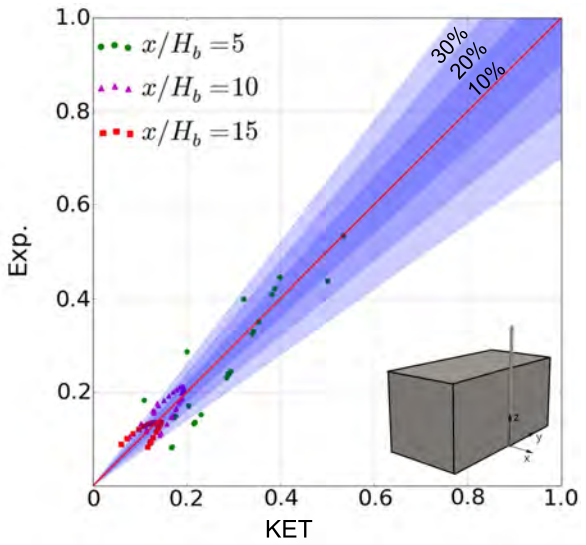

(b)

Figure 7.27: Correlation plots for the time-averaged concentration: (a) case of the isolated stack and (b) case with the stack and the building.

large-scale turbulent transport mechanisms. In the case of the isolated stack, this also leads to a strong dependence of the results obtained on the adopted inflow conditions, which in this case were not completely

characterised in the experimental report. In particular, only the time-averaged wind velocity profile and the along-wind turbulence intensity were reported, so that the turbulence intensities along the other directions as well as the turbulence spectra have been assumed according to the existing literature. Despite such difficulties, the average relative difference between LES simulations and experiments is equal to 28% and 26% in terms of variances of the time-averaged pollutant concentration distribution in the vertical and horizontal directions, respectively. The presence of local aerodynamic mechanisms in the proximity of the stack also contributes to different results obtained using RANS and LES approaches.

Then, a rectangular building is placed upwind of the considered stack. In this case, LES results are found to be quite accurate also far downwind of the pollutant source, being the maximum relative difference with respect to experimental data over all the vertical lines considered equal to 26.7%. Furthermore, when the building is considered, LES simulations provide an overall better agreement with experimental data if compared to the isolated stack configuration, being the absolute MNB reduced from 29.6% to 17.6%. The improvement of the LES results can be attributed to the fact that, downwind of the building, the pollutant concentration field is mainly controlled by the turbulent wake generated by the building itself rather than by the turbulence of the simulated atmospheric boundary layer, so rendering the simulation less sensitive to inflow parameters which are usually difficult to be evaluated *a priori*.

Summarising, a significant dependence of LES results on the characteristics of the incoming turbulence is observed, in particular when the configuration with the isolated stack is analysed. Nevertheless, different from RANS approaches, the LES results are not significantly affected by the turbulent Schmidt number and they show good performances when surrounding obstacles are taken into account. The combination of these two characteristics renders LES particularly attractive for assessing pollutant dispersion in the urban environment.

ACKNOWLEDGEMENTS

The authors are thankful to CINECA for providing the HPC facilities needed to accomplish the present research work. Twan van Hooff is currently a postdoctoral fellow of the Research Foundation – Flanders (FWO) and acknowledges its financial support (project FWO 12R9718N).

CONCLUSIONS

8 CONCLUSIONS

This thesis is composed by three parts: Part I focuses on LES applications to bluff body aerodynamics, with a particular emphasis on the aerodynamics of a rectangular cylinder 5:1, Part II focuses on LES applications for wind loads assessment on a low-rise and a high-rise building and Part III focuses on LES applications to pollutant dispersion problems in the urban environment. In this chapter, for each part the main findings are summarised and briefly commented.

8.1 LES APPLICATIONS TO BLUFF BODY AERODYNAMICS

Part I is composed by Chapters 3 and 4 and focuses on LES applications to bluff body aerodynamics. In particular, the flow field around a rectangular cylinder with an aspect ratio of 5:1 is analysed.

In Chapter 3, LES are performed to study the unsteady flow field around a rectangular cylinder with aspect ratio 5:1 at a 4° angle of attack when a small level of incoming turbulence is taken into account. Two different subgrid-scale (SGS) models are considered, namely the classical Smagorinsky-Lilly model and the Kinetic Energy Transport model. Simulations are performed for both laminar inflow conditions as well as by adopting an inflow turbulence intensity of 0.7%. The results are analysed in terms of first and second-order statistics of the pressure distributions on the cylinder. It is observed that when the Smagorinsky-Lilly model is adopted, even in the presence of only small values of the incoming flow turbulence intensity are present, the modelling of a realistic unsteady turbulent inflow is important in order to obtain accurate results. Conversely, the Kinetic Energy Transport model proved to be less sensitive to the low inflow turbulence, showing comparable results for both the analysed inflow conditions that are qualitatively intermediate between the results by the Smagorinsky-Lilly model with perfectly smooth and with low level of incoming turbulence. This can be explained by considering that, differently from the Smagorinsky-Lilly model, the Kinetic Energy Transport model can modify the turbulent viscosity depending on the subgrid kinetic energy transport equation and thus it is able to allow the shear layer in-

stabilities to develop even without directly triggering them with incoming disturbances. Overall, when incoming turbulence is taken into account, a good agreement between numerical and experimental results is achieved for both investigated SGS models, in particular in terms of time-averaged pressure distributions. Furthermore, the differences between the two considered SGS models decrease when turbulent inflow conditions are considered.

In Chapter 4, LES simulations are performed in order to study the effects of different levels of inflow turbulence on the aerodynamic characteristics of a rectangular cylinder with aspect ratio 5:1. Two different inflow conditions, corresponding to mild and strong inflow turbulence levels are analysed, with the twofold objective of analysing the main flow features modifications and assess LES capabilities to reproduce such cases. It is found that LES can satisfactorily reproduce the changes in the flow topology due to the presence of incoming turbulence and is able to correctly predict the upwind shifting of the shear layer instabilities when the higher level of inflow turbulence is analysed. In this case, the ratio between the inflow turbulence length scale and the spanwise domain dimension plays an important role, showing that the accuracy of the obtained results significantly improves as this ratio decreases. Overall, the numerical results are in good agreement with the experimental data and show that the numerical model adopted can satisfactorily reproduce the flow topology changes caused by different inflow turbulence characteristics.

8.2 LES APPLICATIONS FOR WIND LOADS ASSESSMENT ON BUILDINGS

Part II is composed by Chapters 5 and 6 and focuses on LES applications for the assessment of wind loads on buildings.

In Chapter 5, LES simulations of the turbulent flow around a low-rise building are performed in order to assess the accuracy of LES, which might be adopted as complementary design tool alongside wind tunnel tests. Different wind angles of attack are taken into account and results show that the mean pressure coefficient field is predicted by LES simulations with a satisfactory accuracy, while predictions of its standard deviation are less accurate. Nevertheless, at 90% of the monitored points the difference between experimental data and numerical predictions of the standard deviation of the pressure coefficient is smaller than 30%. Starting from both experimental and numerical predictions of the pressure field, linear dynamic structural analyses are

performed and results are analysed in terms of internal forces on the structural members. Average internal forces show to be in good accordance with respect to predictions obtained starting from experimental results. Conversely, when the standard deviations of the internal forces are analysed, numerical results are less accurate. In particular, the accuracy shown by LES in terms of standard deviations of the pressure fields is not maintained when standard deviations of internal forces are considered. Nevertheless, if the maximum standard deviations of internal forces obtained over all the analysed wind angles of attack are considered, the LES results improve. This fact might be due to difficulties in accurately simulating secondary flow mechanisms when a single angle of attack is considered. Summarising, it can be stated that in order to assess LES capabilities as design tool, it is not sufficient to perform a validation in terms of statistics of the pressure field, since many parameters can deeply influence the structural response to the wind action, such as the spectra of the incoming flow turbulence as well as its spatial and temporal correlations. Furthermore, it is found that considering a single wind angle of attack might be excessively restrictive and the use of envelopes of results obtained from different wind directions, as usually required in the design practice, leads to an improvement of the numerical results.

In Chapter 6, LES simulations are adopted to investigate the turbulent flow around an isolated high-rise building, with the aim to compare the internal forces on the structural members obtained starting from numerical and experimental predictions of the pressure field. Also in this case, when the mean pressure field is analysed, a good agreement between simulations and experiments is achieved for all the considered angles of attack, being the maximum mean relative error over the considered angles of attack equal to 9.47%. The LES results showed to be slightly less accurate for the fluctuating part of the pressure field; the maximum mean relative error between simulations and experiments over the considered angles of attack is equal to 19.0%. It appears that the accuracy of LES in reproducing the standard deviations of pressure field is not maintained when the standard deviations of the internal forces are considered, i.e. the maximum mean relative error in terms of axial forces over the considered angles of attack is equal to 33.5%. It is also observed that LES simulations tend to systematically underestimate the internal forces and an accurate analysis of the pressure correlation fields shows that some discrepancies between the flow dynamics from simulations and experiments are present. However, when the peak axial forces, defined as the mean values plus (and minus) 3.5 times the standard deviations, and the envelope of all the

considered angles of attack is considered, the mean relative error is reduced to 8.28%, indicating that a satisfactory level of accuracy could be considered to be achieved. Summarising, it can be stated that in the view of using LES as a design tool, the use of peak axial forces as design parameters can lead to a satisfactory accuracy especially when the envelope of several angles of attack is considered.

In the awareness that the experimental practice based on wind tunnel tests has always been considered to be the most reliable approach to assess wind loads on structures, the results obtained in this part can be considered encouraging for adopting LES as a complementary design tool in the near future, even if some research work is still needed in order to assess their accuracy and reliability.

8.3 LES APPLICATIONS TO POLLUTANT DISPERSION PROBLEMS

Part III is composed by Chapter 7 and focuses on LES applications to pollutant dispersion problems.

In Chapter 7 the capabilities of LES to predict pollutant dispersion in a turbulent atmospheric boundary layer are investigated in two different configurations: pollutant dispersion from (I) an isolated stack and (II) from a stack placed downstream of a building. The results are analysed in terms of time-averaged pollutant concentrations and systematically compared to available experimental data, as well as to results from empirical and theoretical models.

For the isolated stack, both Reynolds-averaged Navier-Stokes (RANS) and LES simulations are performed. The RANS results are significantly affected by the adopted turbulent Schmidt number, which is *a priori* unknown and whose value is case dependent. The need for *a priori* calibration of the turbulent Schmidt number represents a strong limit for RANS applications to engineering problems and therefore, suggests the adoption of LES instead. Indeed, in the framework of LES the large-scale turbulent fluctuations of velocities and concentrations are directly reproduced within the computational domain leading to a direct prediction of large-scale turbulent mass transport. This amounts to the fact that, differently from the RANS model adopted, LES can take into account turbulence anisotropy and can thus more accurately predict large-scales turbulent fluxes.

Differently from RANS, LES simulations require that a turbulent inflow fluctuation field is generated and introduced at the inlet in the computational domain. In order to generate this field, some turbu-

lence characteristics have been assumed since they are not reported in the experimental report, i.e. the turbulence intensity in the vertical and across-wind directions as well as the turbulence length scales. Notwithstanding these assumptions, LES results show a very good agreement with the empirical formulae for the effective plume height. Compared to the experiments, the LES simulations predict a lower effective plume height in general, and in particular downwind close to the stack, while the agreement improves proceeding further downwind.

When the dispersion parameters obtained from LES simulations are analysed, it is observed that an accurate prediction of the pollutant concentration field requires that the turbulence characteristics of the simulated atmospheric boundary layer have to be reproduced everywhere in the computational domain rather than only in the approaching flow. This agreement might be challenging to be achieved, since the atmospheric boundary layer characteristics might evolve in the computational domain as well as in experiments. Notwithstanding these considerations, a satisfactory agreement between LES simulations and experiments in terms of dispersion parameters is achieved, being the average relative difference between the two approaches equal to 28% and 26% for the dispersion parameters in the vertical and horizontal directions, respectively.

In order to assess LES capabilities in reproducing the time-averaged pollutant concentration field when a configuration of practical interest for Civil Engineering applications is considered, a rectangular building is introduced upstream of the considered stack and an LES simulation is performed. In this case, LES results are found to provide a better agreement with experimental results than in the isolated stack configuration. The improvement of the LES results can be due to the fact that downwind of the building the pollutant dispersion is mainly controlled by the turbulent wake generated by the building itself rather than by the turbulence of the simulated atmospheric boundary layer. Conversely, in the isolated stack configuration the pollutant dispersion is mainly controlled by the turbulence of the simulated atmospheric boundary layer, whose characteristics at the inlet of the computational domain have been partially assumed due to the lack of experimental measurements.

Summarising, as expected, a significant dependence of LES results on the turbulence characteristics of the simulated atmospheric boundary layer is observed. Nevertheless, differently from RANS approaches, the LES results are not significantly affected by any case-specific model parameter and they show good performance when surrounding obstacles are taken into account. The combination of these two characteris-

tics renders LES particularly attractive for assessing pollutant dispersion in the urban environment.

REFERENCES

[1] Blocken B. "Computational Fluid Dynamics for Urban Physics: Importance, scales, possibilities, limitations and ten tips and tricks towards accurate and reliable simulations." In: *Building and Environment* 91 (2015), pp. 219–245.

[2] Blocken B. and Carmeliet J. "Pedestrian Wind Environment around Buildings: Literature Review and Practical Examples." In: *Journal of Building Physics* 28 (2004), pp. 107–159.

[3] Dagnew A.K. and Bitsuamlak G.T. "LES evaluation of wind pressures on a standard tall building with and without a neighboring building." In: *Fifth Int. Symosium Comput. Wind Eng. Chapel Hill, North Carolina, USA* 2007 (2010).

[4] A.L. Braun and A.M. Awruch. "Aerodynamic and aeroelastic analyses on the CAARC standard tall building model using numerical simulation." In: *Computers and Structures* 87.9-10 (2009), pp. 564–581.

[5] Y. Zhang, W.G. Habashi, and R.A. Khurram. "Predicting wind-induced vibrations of high-rise buildings using unsteady CFD and modal analysis." In: *Journal of Wind Engineering and Industrial Aerodynamics* 136 (2015), pp. 165–179.

[6] van Hooff T. and Blocken B. "Coupled urban wind flow and indoor natural ventilation modelling on a high-resolution grid: A case study for the Amsterdam ArenA stadium." In: *Environmental Modelling & Software* 25 (2010), pp. 51–65.

[7] Tokyo Polytechnic University. *TPU Aerodynamic Database*. 2003.

[8] "Geometrical model of the Burj Khalifa in the wind tunnel." In: *Http://people.bath.ac.uk/abscjkw/LectureNotes/Structures4/* ().

[9] B. Blocken. "50 years of Computational Wind Engineering: Past, present and future." In: *Journal of Wind Engineering and Industrial Aerodynamics* 129 (2014), pp. 69–102.

[10] L. Bruno, D. Fransos, N. Coste, and A. Bosco. "3D flow around a rectangular cylinder: A computational study." In: *Journal of Wind Engineering and Industrial Aerodynamics* 98 (2010), pp. 263–276.

[11] L. Bruno, N. Coste, and D. Fransos. "Simulated flow around a rectangular 5:1 cylinder: Spanwise discretisation effects and emerging flow features." In: *Journal of Wind Engineering and Industrial Aerodynamics* 104-106 (2012), pp. 203–215.

[12] L. Patruno, M. Ricci, S. de Mir anda, and F. Ubertini. "Numerical simulation of a 5:1 rectangular cylinder at non-null angles of attack." In: *Journal of Wind Engineering and Industrial Aerodynamics* 151 (2016), pp. 146–157.

[13] D.C. Wilcox. *Turbulence modeling for CFD*. Vol. 93. 1993.

[14] H.K. Versteeg and W. Malalasekera. *An Introduction to Computational Fluid Dynamics - The Finite Volume Method*. Ed. by McGraw-Hill. 1995, p. 267.

[15] Ahmed Elsaher, Haitam Aboshosha, Girma Bitsuamlak, and Ashraf El Damatty. "LES evaluation of wind-induced responses for an isolated and a surrounded tall building." In: *Engineering Structures* 115 (2016), pp. 179–195.

[16] K. Nozawa and T. Tamura. "Large eddy simulation of the flow around a low-rise building immersed in a rough-wall turbulent boundary layer." In: *Journal of Wind Engineering and Industrial Aerodynamics* 90 (2002), pp. 1151–1162.

[17] Shenghong Huang, Q.S. Li, and Shengli Xu. "Numerical evaluation of wind effects on a tall steel building by CFD." In: *Journal of Constructional Steel Research* 63.5 (2007), pp. 612–627.

[18] T. Tamura, K. Nozawa, and K. Kondo. "AIJ guide for numerical prediction of wind loads on buildings." In: *Journal of Wind Engineering and Industrial Aerodynamics* 96.10-11 (2008), pp. 1974–1984.

[19] A.K. Dagnew and G.T. Bitsuamlak. "Computational evaluation of wind loads on a standard tall building using LES." In: *Wind and Structures* 18.5 (2014), pp. 567–598.

[20] Yoshihide Tominaga and Ted Stathopoulos. "Numerical simulation of dispersion around an isolated cubic building: Comparison of various types of k-ϵ models." In: *Atmospheric Environment* 43.20 (2009), pp. 3200–3210.

[21] Y. Tominaga and T. Stathopoulos. "Numerical simulation of dispersion around an isolated cubic building: Model evaluation of RANS and LES." In: *Building and Environment* 45.10 (2010), pp. 2231–2239.

[22] Yoshihide Tominaga and Ted Stathopoulos. "CFD modeling of pollution dispersion in a street canyon: Comparison between LES and RANS." In: *Journal of Wind Engineering and Industrial Aerodynamics* 99.4 (2011), pp. 340–348.

[23] Y. Tominaga and T. Stathopoulos. "CFD simulation of near-field pollutant dispersion in the urban environment: A review of current modeling techniques." In: *Atmospheric Environment* 79 (2013), pp. 716–730.

[24] P. Gousseau, B. Blocken, van Heijst, and G. J F. "CFD simulation of pollutant dispersion around isolated buildings: On the role of convective and turbulent mass fluxes in the prediction accuracy." In: *Journal of Hazardous Materials* 194 (2011), pp. 422–434.

[25] Gousseau P., Blocken B., Stathopoulos T., and van Heijst G.J.F. "Near-field pollutant dispersion in an actual urban area: Analysis of the mass transport mechanism by high-resolution Large Eddy Simulations." In: *Computers & Fluids* 114 (2015), pp. 151–162.

[26] B. Blocken, T. Stathopoulos, and J. Carmeliet. "CFD simulation of the atmospheric boundary layer: wall function problems." In: *Atmospheric Environment* 41.2 (2007), pp. 238–252.

[27] M. Ricci, L. Patruno, and S. de Mir anda. "Wind loads and structural response: Benchmarking LES on a low-rise building." In: *Engineering Structures* 144 (2017), pp. 26–42.

[28] Y. Kim, I.P. Castro, and Z.T. Xie. "Divergence-free turbulence inflow conditions for large-eddy simulations with incompressible flow solvers." In: *Computers and Fluids* 84 (2013), pp. 56–68.

[29] R. Smirnov, S. Shi, and I. Celik. "Random flow generation technique for large eddy simulations and particle-dynamics modeling." In: *Journal of Fluids Engineering* 123 (2001), pp. 359–371.

[30] S. H. Huang, Q. S. Li, and J. R. Wu. "A general inflow turbulence generator for large eddy simulation." In: *Journal of Wind Engineering and Industrial Aerodynamics* 98.10-11 (2010), pp. 600–617.

[31] Zheng-Tong Xie and Ian p. Castro. "Efficient Generation of Inflow Conditions for Large Eddy Simulation of Street-Scale Flows." In: *Flow, Turbulence and Combustion* 81.3 (2008), pp. 449–470.

[32] L. Patruno and M. Ricci. "On the generation of synthetic divergence-free homogeneous anisotropic turbulence." In: *Computer Methods in Applied Mechanics and Engineering* 315 (2017), pp. 396–417.

[33] Stephen B. Pope. *Turbulent Flows*. 2000.

[34] B.E. Launder. *An Introduction to the Modeling of Turbulence*. VKI Lecture Series, 1991.

[35] J.H. Ferzinger and M. Perić. *Computational methods for fluid dynamics*. 1999.

[36] J. Boussinesq. "Essai sur la théorie des eaux courantes." In: *Mémoires présentés par divers savants à l'Académie des Sciences* 23.1 (1877), pp. 1–680.

[37] M. Ricci, L. Patruno, S. de Mir anda, and F. Ubertini. "Effects of Low Incoming Turbulence on the Flow around a 5 : 1 Rectangular Cylinder at Non-Null-Attack Angle." In: *Mathematical Problems in Engineering* 2016 (2016).

[38] F.R. Menter. "Two-equation eddy-viscosity turbulence models for engineering applications." In: *AIAA Journal* 32.8 (1994), pp. 1598–1605.

[39] R.H. Nichols. *Turbulence models and their application to complex flows*. University of Alabama at Birmingham, 2010.

[40] M. Germano, U. Piomelli, P. Moin, and W.H. Cabot. "A dynamic subgrid-scale eddy viscosity model." In: *Physics of Fluids A: Fluid Dynamics* 3.7 (1991), pp. 1760–1765.

[41] D.K. Lilly. "A proposed modification of the Germano subgrid-scale closure method." In: *Physics of Fluids* 4 (1991), pp. 633–635.

[42] Nicoud F. and Ducros F. "Subgrid-Scale Stress Modelling Based on the Square of the Velocity Gradient Tensor." In: *Flow, Turbulence and Combustion* 62 (1999), pp. 183–200.

[43] Nelson C.C. "Simulations of Spatially Resolved Compressible Turbulence Using a Local Dynamic Subgrid Model." In: (1997). Ed. by Ph.D. thesis.

[44] J.S. Smagorinsky. "General Circulation Experiments with the Primitive Equations I: The Basic Experiment." In: *Monthly Whather Review* 91 (1963), pp. 99–164.

[45] Sayadi T. and Moin P. "Predicting natural transition using large eddy simulation." In: *Center for Turbulence Research Annual Research Briefs* (2011).

[46] Rossi R. and Iaccarino G. "Numerical simulation of scalar dispersion downstream of a square obstacle using gradient-transport type models." In: *Atmospheric Environment* 43 (2009), pp. 2518–2531.

[47] B. Blocken, T. Stathopoulos, P. Saathoff, and X. Wang. "Numerical evaluation of pollutant dispersion in the built environment: Comparisons between models and experiments." In: *Journal of Wind Engineering and Industrial Aerodynamics* 96.10-11 (2008), pp. 1817–1831.

[48] S. Di Sabatino, R. Buccolieri, B. Pulvirenti, and R.E. Britter. "Flow and pollutant dispersion in street canyons using FLUENT and ADMS-Urban." In: *Environmental Modeling and Assessment* 13(3) (2008), pp. 369–381.

[49] K. Suga. "Improvement of second moment closure for turbulent obstacle flow and heat transfer." In: *International Journal of Heat and Fluid Flow* 25(5) (2004), pp. 776–784.

[50] J. Nakamura and Y. Ohya. "The effects of turbulence on the mean flow past two-dimensional rectangular cylinders." In: *Journal of Fluid Mechanics* 149 (1984), pp. 255–273.

[51] R. Mills, J. Sheridan, and K. Hourigan. "Response of base suction and vortex shedding from rectangular prisms to transverse forcing." In: *Journal of Fluid Mechanics* 461 (2002), pp. 25–49.

[52] R. Mills, J. Sheridan, and K. Hourigan. "Particle image velocimetry and visualization of natural and forced flow around rectangular cylinders." In: *Journal of Fluid Mechanics* 478 (2003), pp. 299–323.

[53] H. Noda and A Nakayama. "Free-stream turbulence effects on the instantaneous pressure and forces on cylinders of rectangular cross section." In: *Experiments in Fluids* 34.3 (2003), pp. 332–344.

[54] R. Hillier and N.J. Cherry. "The effects of stream turbulence on separation bubbles." In: *Journal of Wind Engineering and Industrial Aerodynamics* 8 (1981), pp. 49–58.

[55] M. Kiya and K. Sasaki. "Free-stream turbulence effects on a separation bubble." In: *Journal of Wind Engineering and Industrial Aerodynamics* 14 (1983), pp. 375–386.

[56] D. Yu and A. Kareem. "Parametric study of flow around rectangular prisms using LES." In: *Journal of Wind Engineering and Industrial Aerodynamics* 77 (1998), pp. 653–662.

[57] A. Sohankar, Norberg C., and L. Davidson. "Numerical simulation of unsteady low-Reynolds number flow around rectangular cylinders at incidence." In: *Journal of Wind Engineering and Industrial Aerodynamics* 69 (1997), pp. 189–201.

[58] K. Shimada and T. Ishihara. "Application of a modified $k-\varepsilon$ model to the prediction of aerodynamic characteristics of rectangular cross-section cylinders." In: *Journal of Fluids and Structures* 16 (2002), pp. 465–485.

[59] S. de Miranda, L. Patruno, F. Ubertini, and G. Vairo. "On the identification of flutter derivatives of bridge decks via RANS-based numerical models: benchmarking on rectangular prisms." In: *Engineering Structures* 76 (2014), pp. 359–370.

[60] T. Tamura and Y. Ono. "LES analysis on aeroelastic instability of prisms in turbulent flow." In: *Journal of Wind Engineering and Industrial Aerodynamics* 91 (2003), pp. 1827–46.

[61] S.J. Daniels, I.P. Castro, and Z.T. Xie. "Numerical analysis of freestream turbulence effects on the vortex-induced vibrations of a rectangular cylinder." In: *Journal of Wind Engineering and Industrial Aerodynamics* 153 (2016), pp. 13–25.

[62] S. de Miranda, L. Patruno, M. Ricci, and F. Ubertini. "Numerical study of a twin box bridge deck with increasing gap ratio by using RANS and LES approaches." In: *Engineering Structures* 99 (2015), pp. 546–558.

[63] G. Bartoli, L. Bruno, G. Buresti, F. Ricciardelli, M.V. Salvetti, and A. Zasso. "BARC overview document." In: *<http://www.aniv-iawe.org/barc>.* (2008).

[64] L. Bruno, M.V. Salvetti, and F. Ricciardelli. "Benchmark on the aerodynamics of a rectangular 5:1 cylinder: An overview after the first four years of activity." In: *Journal of Wind Engineering and Industrial Aerodynamics* 126 (2014), pp. 87–106.

[65] J. A. S. Witteveen, P. S. Omrani, A. Mariotti, and M. V. Salvetti. "Uncertainty quantification of a Rectangular 5:1 Cylinder." In: *American Insitute of Aeronautics and Astronautics* 663 (2015).

[66] Vreman A.W. "An eddy-viscosity subgrid-scale model for turbulent shear flow: algebraic theory and applications." In: *Physics of Fluids* 16 (2007), pp. 3670–3681.

[67] A. Yoshizawa and K. Horiuti. "A Statiscally-Derived Subgrid-Scale Kinetic Energy Model for the Large-Eddy Simulations of Turbulent Flows." In: *Journal of the Physical Society of Japan* 54 (1985), pp. 2834–2839.

[68] L. Patruno, M. Ricci, de Mir anda, and F. S. Ubertini. "Numerical simulation of a 5:1 rectangular cylinder at non-null angles of attack." In: *Journal of Wind Engineering and Industrial Aerodynamics* 151 (2015), pp. 146–157.

[69] C. Mannini, A. M. Marra, L. Pigolotti, and G. Bartoli. "The effects of free-stream turbulence and angle of attack on the aerodynamics of a cylinder with rectangular 5:1 cross section." In: *Journal of Wind Engineering and Industrial Aerodynamics* 161 (2017), pp. 42–58.

[70] C. Mannini, A.M. Marra, L. Pigolotti, and G. Bartoli. "Unsteady pressure and wake characteristics of a benchmark rectangular section in smooth and turbulent flow." In: *Proceedings of the 14th International Conference on Wind Engineering,21-26 June 2015, Porto Alegre, Brazil.* (2015).

[71] H.G. Castro and R.R. Paz. "A time and space correlated turbulence synthesis method for Large Eddy Simulations." In: *Journal of Computational Physics* 235 (2013), pp. 742–763.

[72] L. Bruno, N. Coste, and D. Fransos. "Effect of the spanwise feature of the computational domainf on the simulated flow around a 5:1 cylinder." In: *Proceedings of the 13th International Conference on Wind Engineering, Amsterdam, The Netherl ands.* (2011).

[73] Grozescu A.N., Bruno L., Franzos D., and Salvetti M.V. "Three-dimensional numerical simulation of flow around a 1:5 rectangular cylinder." In: *Proceedings of the XX Italian Conference on Theoretical and Applied Mechanics, Bologna, Italy.* (2011).

[74] Mannini C. "Numerical investigation on the three-dimensional unsteady flow past a 5:1 rectangular cylinder." In: *Journal of Wind Engineering and Industrial Aerodynamics* 99 (2011), pp. 469–482.

[75] H. Weller. "Controlling the Computational Modes of the Arbitrarily Structured C Grid." In: *Monthly Weather Review* 140 (2014), pp. 3220–3234.

[76] J. Jeong and F. Hussain. "On the identification of a vortex." In: *Journal of Fluid Mechanics* 285.1 (1995), p. 69.

[77] M. Kiya and K. Sasaki. "NFree-stream turbulence effects on a separation bubble." In: *Journal of Wind Engineering and Industrial Aerodynamics* 14.1-3 (1983), pp. 375–386.

[78] L. Patruno. "Accuracy of numerically evaluated flutter derivatives of bridge deck sections using RANS: effects on the flutter onset velocity." In: *Engineering Structures* 89 (2015), pp. 49–65.

[79] F. Brusiani, S. de Mir anda, L. Patruno, F. Ubertini, and P. Vaona. "On the evaluation of bridge deck flutter derivatives using RANS turbulence models." In: *Journal of Wind Engineering and Industrial Aerodynamics* 119 (2013), pp. 39–47.

[80] L. Huang, L. Haili, W. Bin, and L. Yongle. "Numerical simulation for aerodynamic derivatives of bridge deck." In: *Simulation Modelling Practice and Theory* 17 (2009), pp. 719–29.

[81] A. Larsen. "Advances in aeroelastic analyses of suspension and cable-stayed bridges." In: *Journal of Wind Engineering and Industrial Aerodynamics* 74 (1998), pp. 73–90.

[82] S. de Miranda, L. Patruno, F. Ubertini, and G. Vairo. "Indicial functions and flutter derivatives: a generalized approach to the motion-related wind loads." In: *Journal of Fluids and Structures* 42 (2013), pp. 466–487.

[83] D. Sun, J.S. Owen, N.G. Wright, and K. Liaw. "Fluid-structure interaction of prismatic line-like structures using LES and block-iterative coupling." In: *Journal of Wind Engineering and Industrial Aerodynamics* 96 (2008), pp. 840–858.

[84] D. Sun, J.S. Owen, and N.G. Wright. "Application of the $k-\omega$ turbulence model for a wind-induced vibration study of 2D bluff bodies." In: *Journal of Wind Engineering and Industrial Aerodynamics* 97 (2009), pp. 77–87.

[85] G. Vairo. "A numerical model for wind loads simulation on long-span bridges." In: *Simulation Modelling Practice and Theory* 11 (2003), pp. 315–351.

[86] D. Fransos and L. Bruno. "Edge degree-of-sharpness and free-stream turbulence scale effects on the aerodynamics of a bridge deck." In: *Journal of Wind Engineering and Industrial Aerodynamics* 98 (2010), pp. 661–671.

[87] Q.S. Li. and W.J. Melbourne. "The effect of large-scale turbulence on pressure fluctuations in separated and reattaching flows." In: *Journal of Wind Engineering and Industrial Aerodynamics* 83 (1999), pp. 159–169.

[88] A. Mariotti, M.V. Salvetti, P. Shoeibi Omrani, and J.A.S. Witteveen. "Stochastic analysis of the impact of freestream conditions on the aerodynamics of a rectangular 5:1 cylinder." In: *Computers & Fluids* 136 (2016), pp. 170–192.

[89] G.R. Tabor and M.H. Baba-Ahmedi. "Inlet conditions for large eddy simulation: a review." In: *Computers & Fluids* 39 (2010), pp. 553–567.

[90] K.L. Liu and R.H. Pletcher. "Inflow conditions for the large eddy simulation of turbulent boundary layers: a dynamic recycling procedure." In: *Computational Physics* 219 (2006), pp. 1–6.

[91] M. Hoshija. "Simulation of multi-correlated r andom processes and application to structural vibration problems." In: *Proceedings of JSCE* 204 (1972), pp. 121–128.

[92] K. Kondo and A. Murakami. "Generation of velocity fluctuations for inflow boundary condition of LES." In: *Journal of Wind Engineering and Industrial Aerodynamics* 67 (1997), pp. 51–64.

[93] F. Athey, D. Cokljat, J.P. Bertoglio, and E. Sergent. "Assessment of the vortex method for large eddy simulation inlet conditions." In: *Progress in Computational Fluid Dynamics* 6 (2006), pp. 1–3.

[94] R. Poletto, T. Craft, and A. Revell. "A New Divergence Free Synthetic Eddy Method for the Reproduction of Inlet Flow Conditions for LES." In: *International Journal of Heat and Fluid Flow* 91 (2013), pp. 519–539.

[95] R.H. Kraichnan. "Diffusion by a r andom velocity field." In: *Physics of Fluids* 13 (1970), pp. 22–31.

[96] J.L. Lumley and H.A. Panofsky. "The Structure of Atmospheric Turbulence." In: *Wiley-Interscience, New York.* (1964, pages = 239).

[97] Q.S. Li, Y.Q. Xiao, J.Y. Fu, and Z.N. Li. "Full scale measurements of wind effects on the Jin Mao Building." In: *Journal of Wind Engineering and Industrial Aerodynamics* 95 (2007), pp. 445–466.

[98] R.I. Issa. "Solution of the implicity discretized fluid flow equations by operator-splitting." In: *Journal of Computational Physics* 62 (1985), pp. 40–65.

[99] T. Tamura, T. Miyagi, and T. Kitagishi. "Numerical prediction of unsteady pressures on a square cylinder with various corner shapes." In: *Journal of Wind Engineering and Industrial Aerodynamics* 74 (1998), pp. 531–542.

[100] A. Mariotti, L. Sincolfi, and M. V. Salvetti. "Stochastic sensitivity analysis of large-eddy simulation predictions of the flow around a 5:1 rectangular cylinder." In: *European Journal of Mechanics - B/Fluids* 62 (2017), pp. 149–165.

[101] H. Shirato, Y. Sato, O. Sasaki, and D. Van Bao. "Coherent structure of surface pressures on 2-D rectangular cylinders." In: *The Fifth Symposium on Computational Wind Engineering, Chapel Hill, North Carolina, USA, May 23-27.* (2010).

[102] B. Bienkiewicz, Y. Tamura, H. Ham, H. Ueda, and H. Hibi. "Proper orthogonal decomposition and reconstruction of multi-channel roof pressure." In: *Journal of Wind Engineering and Industrial Aerodynamics* 54-55 (1995), pp. 369–381.

[103] L. Carassale and M. Marré Brunenghi. "Statistical analysis of wind-induced pressure fields: A methodological perspective." In: *Journal of Wind Engineering and Industrial Aerodynamics* 99 (2011), pp. 700–710.

[104] S. Murakami. "Current status and future trends in computational wind engineering." In: *Journal of Wind Engineering and Industrial Aerodynamics* 67-68 (1997), pp. 3–34.

[105] T. Stathopoulos. "Computational wind engineering: Past achievements and future challenges." In: *Journal of Wind Engineering and Industrial Aerodynamics* 67-68 (1997), pp. 509–532.

[106] L. Cochran and R. Derickson. "A physical modeler's view of Computational Wind Engineering." In: *Journal of Wind Engineering and Industrial Aerodynamics* 99.4 (2011), pp. 139–153.

[107] A. Mattana, S. Salvadori, T. Morbiato, and C. Borri. "On the ground-vehicle induced flows and obstacle interaction for energy harvesting purposes." In: *Journal of Wind Engineering and Industrial Aerodynamics* 124 (2014), pp. 121–131.

[108] W. Rodi. "Large-eddy simulations of the flow past bluff bodies : State-of-the art." In: *JSME Int. J. B-Fluid. T.* 41.2 (1998), pp. 361–374.

[109] K.B. Shah and J.H. Ferziger. "A fluid mechanicians view of wind engineering: Large eddy simulation of flow past a cubic obstacle." In: *Journal of Wind Engineering and Industrial Aerodynamics* 67-68 (1997), pp. 211–224.

[110] T.G. Lim H.C. andThomas and I.P. Castro. "Flow around a cube in a turbulent boundary layer: LES and experiment." In: *Journal of Wind Engineering and Industrial Aerodynamics* 97.2 (2009), pp. 96–109.

[111] M. Saeedi, P.P. LePoudre, and B. Wang. "Direct numerical simulation of turbulent wake behind a surface-mounted square cylinder." In: *Journal of Fluids and Structures* 51 (2014), pp. 20–39.

[112] L. Bruno, D. Fransos, N. Coste, and A. Bosco. "3D flow around a rectangular cylinder: A computational study." In: *Journal of Wind Engineering and Industrial Aerodynamics* 98.6-7 (2010), pp. 263–276.

[113] H. W. Tieleman, M.R. Hajj, and T.A. Reinhold. "Wind tunnel simulation requirements to assess wind loads on low-rise buildings." In: *Journal of Wind Engineering and Industrial Aerodynamics* 74-76 (1998), pp. 675–685.

[114] H.W. Tieleman. "Wind tunnel simulation of wind loading on low-rise structures: A review." In: *Journal of Wind Engineering and Industrial Aerodynamics* 91.12-15 (2003), pp. 1627–1649.

[115] H. Irtaza, R.G. Beale, M.H.R. Godley, and A. Jameel. "Comparison of wind pressure measurements on Silsoe experimental building from full-scale observation, wind-tunnel experiments and various CFD techniques." In: *International Journal of Engineering, Science and Technology* 5.1 (2013), pp. 28–41.

[116] P.J. Richards and R.P. Hoxey. "Computational and wind tunnel modelling of mean wind loads on the Silsoe structures building." In: *Journal of Wind Engineering and Industrial Aerodynamics* 43.1-3 (1992), pp. 1641–1652.

[117] P.J. Richards and B.S. Wanigaratne. "A comparison of computer and wind-tunnel models of turbulence around the Silsoe Structures Building." In: *Journal of Wind Engineering and Industrial Aerodynamics* 46-47 (1993), pp. 439–447.

[118] Y. Ozmen, E. Baydar, van Beeck, and J.P.A.J. "Wind flow over the low-rise building models with gabled roofs having different pitch angles." In: *Building and Environment* 95 (2016), pp. 63–74.

[119] Architectural Institute of Japan. "AIJ Recommendations for Loads on Buildings." In: (2004).

[120] H. Lettau. "Note on Aerodynamic Roughness-Parameter Estimation on the Basis of Roughness-Element Description.pdf." In: *J. Appl. Meteor.* 8 (1969), pp. 828–832.

[121] EN 1991-1-4. "Eurocode 1: Actions on structures -Part 1-4: General actions -Wind actions." In: *European Committee for St andardization* 4.2005 (2005), pp. 1–148.

[122] Y. Tominaga, A. Mochida, R. Yoshie, H. Kataoka, T. Nozu, M. Yoshikawa, and T. Shirasawa. "AIJ guidelines for practical applications of CFD to pedestrian wind environment around buildings." In: *Journal of Wind Engineering and Industrial Aerodynamics* 96.10-11 (2008), pp. 1749–1761.

[123] D.K. Lilly. "A Proposed Modification of the Germano-Subgrid-Scale Closure Method." In: *Physics of Fluids a-Fluid Dynamics* 4.3 (1992), pp. 633–635.

[124] H. Weller. "Controlling the Computational Modes of the Arbitrarily Structured C Grid." In: *Monthly Weather Review* 140 (2012), pp. 3220–3234.

[125] Y.C. Kim and Y. Tamura. "Effects of Incident Flows on Wind Loads and Their Combinations on a Low-Rise Building Immersed in a Long Upstream Fetch." In: *Journal of Structural Engineering* 140 (2014).

[126] C. Dyrbye and S.O. Hansen. *Wind Loads on Structures*. Chichester, West Sussex, Engl and: Wiley, 1999.

[127] L. Patruno, M. Ricci, S. de Mir anda, and F. Ubertini. "An efficient approach to the evaluation of wind effects on structures based on recorded pressure fields." In: *Engineering Structures* 124 (2016), pp. 207–220.

[128] P.A. Irwin. "Wind engineering challenges of the new generation of super-tall buildings." In: *Journal of Wind Engineering and Industrial Aerodynamics* 97.7-8 (2009), pp. 328–334.

[129] T. Tschanz and A.G. Davenport. "The base balance technique for the determination of dynamic wind loads." In: *Journal of Wind Engineering and Industrial Aerodynamics* 13.1-3 (1983), pp. 429–439.

[130] A.G. Davenport. "The application of statistical concepts to the wind loading of structures." In: *ICE Proceedings*. 6480. 1961.

[131] A. Kareem. "Model for predicting the acrosswind response of buildings." In: *Engineering Structures* 6.2 (1984), pp. 136–141.

[132] A. Kareem and Y. Zhou. "Gust loading factor - past, present and future." In: *Journal of Wind Engineering and Industrial Aerodynamics* 91.12-15 (2003), pp. 1301–1328.

[133] X. Chen and A. Kareem. "Coupled Dynamic Analysis and Equivalent Static Wind Loads on Buildings with Three-Dimensional Modes." In: *Journal of Structural Engineering* 131.7 (2005), pp. 1071–1082.

[134] J. Xie and P.A. Irwin. "Application of the force balance technique to a building complex." In: *Journal of Wind Engineering and Industrial Aerodynamics* 77-78 (1998), pp. 579–590.

[135] P. A. Irwin and W. W. Kochanski. "Measurements of structural wind loads using the high frequency pressure integration method." In: *Proceedings of the 13th Structures Congress* (1995), pp. 1631–1634.

[136] J. Franke, A. Hellsten, H. Schlünzen, and B. Carissimo. *Best practice guideline for the CFD simulation of flows in the urban environment*. Vol. 44. May. 2007, pp. 1–52.

[137] W.P. Elliott. "The growth of the atmospheric internal boundary layer." In: *Eos, Transactions American Geophysical Union* 39.6 (1958), pp. 1048–1054.

[138] In: ().

[139] B. Cabral and L.C. Leedom. "Imaging vector fields using line integral convolution." In: *Proc. SIGGRAPH* (1993), pp. 263–270.

[140] H. Noda and A. Nakayama. "Reproducibility of flow past two-dimensional rectangular cylinders in a homogeneous turbulent flow by LES." In: *Journal of Wind Engineering and Industrial Aerodynamics* 91.1-2 (2003), pp. 265–278.

[141] B.S. Taranath. *Structural analysis and design of tall buildings*. McGraw-Hill, 1988.

[142] L. Patruno, M. Ricci, S. de Mir anda, and F. Ubertini. "An efficient approach to the evaluation of wind effects on structures based on recorded pressure fields." In: *Engineering Structures* 124 (2016), pp. 207–220.

[143] B. Brunekreef and S.T. Holgate. *Air pollution and health*. 2002.

[144] W.W. Li and R.N. Meroney. "Gas dispersion near a cubical model building. Part I. Mean concentration measurements." In: *Journal of Wind Engineering and Industrial Aerodynamics* 12.1 (1983), pp. 15–33.

[145] W.W. Li, Meroney, and R.N. "Gas dispersion near a cubical model building. Part II. Concentration fluctuation measurements." In: *Journal of Wind Engineering and Industrial Aerodynamics* 12.1 (1983), pp. 35–47.

[146] A.H. Huber and W.H. Snyder. "Wind tunnel investigation of the effects of a rectangular-shaped building on dispersion of effluents from short adjacent stacks." In: *Atmospheric Environment* 16 (1982), pp. 2837–2848.

[147] P. Saathoff, T. Stathopoulos, and H. Wu. "The influence of freestream turbulence on nearfield dilution of exhaust from building vents." In: *Journal of Wind Engineering and Industrial Aerodynamics* 77-78 (1998), pp. 741–752.

[148] B.M. Leitl, P. Kastner-Klein, M. Rau, and R.N. Meroney. "Concentration and flow distributions in the vicinity of U-shaped buildings: Wind-tunnel and computational data." In: *Journal of Wind Engineering and Industrial Aerodynamics* 67-68 (1997), pp. 745–755.

[149] T. Stathopoulos, L. Lazure, P. Saathoff, and X. Wei. "Dilution of exhaust from a rooftop stack on a cubical building in an urban environment." In: *Atmospheric Environment* 36.29 (2002), pp. 4577–4591.

[150] T. Stathopoulos, L. Lazure, P. Saathoff, and A. Gupta. "The Effect of Stack Height, Stack Location and Rooftop Structures on Air Intake Contamination: A Laboratory and Full-scale Study." PhD thesis. 2004.

[151] D. J. Wilson and B. K. Lamb. "Dispersion of exhaust gases from roof-level stacks and vents on a laboratory building: Author's reply." In: *Atmospheric Environment* 31.7 (1997), pp. 1091–1093.

[152] M. L. Barad. "Project Prairie Grass: a field program in diffusion vol II." In: *Geophysical Research Paper* Vol II.59 (1958), pp. 1–218.

[153] L. Lazure, P. Saathoff, and T. Stathopoulos. "Air intake contamination by building exhausts: Tracer gas investigation of atmospheric dispersion models in the urban environment." In: *Journal of the Air and Waste Management Association* 52.2 (2002), pp. 160–166.

[154] R. N. Meroney. "Ten questions concerning hybrid computational/physical model simulation of wind flow in the built environment." In: *Building and Environment* 96 (2016), pp. 12–21.

[155] Y. Tominaga and T. Stathopoulos. "Ten questions concerning modeling of near-field pollutant dispersion in the built environment." In: *Building and Environment* 105 (2016), pp. 390–402.

[156] B. Blocken, Y. Tominaga, and T. Stathopoulos. "Editorial to virtual special issue: CFD simulation of micro-scale pollutant dispersion in the built environment. Building and Environment." In: *Building and Environment* 64 (2013), pp. 225–230.

[157] Baker C.J. "Wind engineering – Past, present and future." In: *Journal of Wind Engineering and Industrial Aerodynamics* 95.9-11 (2007), pp. 843–870.

[158] B. Blocken, Stathopoulos T., J. Carmeliet, and J.L.M. Hensen. "Application of CFD in building performance simulation for the outdoor environment: an overview." In: *Journal of Building Performance Simulation* 4.2 (2011), pp. 157–184.

[159] R.N Meroney. "Wind tunnel and numerical simulation of pollution dispersion: a hybrid approach." In: *Paper for Invited Lecture at the Croucher Advanced Study Institute, Hong Kong University of Science and Technology*. 6-10 December 2004.

[160] R. N. Meroney. "Virtual Reality in Wind Engineering: The windy world within the computer." In: *Researchgate*. 14 October 2014. URL: https://www.researchgate.net/profile/Robert_Meroney/publication/266854651_Virtual_Reality_in_Wind_Engineering_The_Windy_World_within_the_Computer/links/\newline/543d8b6f0cf2d6934ebcf735.pdf.

[161] S. Murakami. "Overview of turbulence models applied in CWE-1997." In: *Journal of Wind Engineering and Industrial Aerodynamics* 74-76 (1998), pp. 1–24.

[162] M. Lateb, R.N. Meroney, M. Yataghene, H. Fellouah, F. Saleh, and M.C. Boufadel. "On the use of numerical modelling for near-field pollutant dispersion in urban environments - A review." In: *Environmental Pollution* 208 (2016), pp. 271–283.

[163] Y. Li and T. Stathopoulos. "Numerical evaluation of wind-induced dispersion of pollutants around a building." In: *Journal of Wind Engineering and Industrial Aerodynamics* 67-68 (1997), pp. 757–766.

[164] Robert N. Meroney, Bernd M. Leitl, Stillianos Rafailidis, and Michael Schatzmann. "Wind-tunnel and numerical modeling of flow and dispersion about several building shapes." In: *Journal of Wind Engineering and Industrial Aerodynamics* 81.1-3 (1999), pp. 333–345.

[165] Jane Meri Santos, Neyval Costa Reis, Elisa Valentim Goulart, and Ilias Mavroidis. "Numerical simulation of flow and dispersion around an isolated cubical building: The effect of the atmospheric stratification." In: *Atmospheric Environment* 43.34 (2009), pp. 5484–5492.

[166] T. L. Chan, G. Dong, C. W. Leung, C. S. Cheung, and W. T. Hung. "Validation of a two-dimensional pollutant dispersion model in an isolated street canyon." In: *Atmospheric Environment* 36.5 (2002), pp. 861–872.

[167] Christof Gromke, Riccardo Buccolieri, Silvana Di Sabatino, and Bodo Ruck. "Dispersion study in a street canyon with tree planting by means of wind tunnel and numerical investigations - Evaluation of CFD data with experimental data." In: *Atmospheric Environment* 42.37 (2008), pp. 8640–8650.

[168] Riccardo Buccolieri, Mats Sandberg, and Silvana Di Sabatino. "City breathability and its link to pollutant concentration distribution within urban-like geometries." In: *Atmospheric Environment* 44.15 (2010), pp. 1894–1903.

[169] A. Dejoan, J. L. Santiago, A. Martilli, F. Martin, and A. Pinelli. "Comparison between large-eddy sand Reynolds-Averaged Navier-Stokes computations for the MUST field experiment. Part II: Effects of incident wind angle deviation on the mean flow and plume dispersion." In: *Boundary-Layer Meteorology* 135.1 (2010), pp. 133–150.

[170] Bing Chen Wang, Eugene Yee, and Fue Sang Lien. "Numerical study of dispersing pollutant clouds in a built-up environment." In: *International Journal of Heat and Fluid Flow* 30.1 (2009), pp. 3–19.

[171] R. F. Shi, G. X. Cui, Z. S. Wang, C. X. Xu, and Z. S. Zhang. "Large eddy simulation of wind field and plume dispersion in building array." In: *Atmospheric Environment* 42.5 (2008), pp. 1083–1097.

[172] Jae Jin Kim and Jong Jin Baik. "A numerical study of the effects of ambient wind direction on flow and dispersion in urban street canyons using the RNG k-ϵ turbulence model." In: *Atmospheric Environment* 38.19 (2004), pp. 3039–3048.

[173] M. Pontiggia, M. Derudi, M. Alba, M. Scaioni, and R. Rota. "Hazardous gas releases in urban areas: Assessment of consequences through CFD modelling." In: *Journal of Hazardous Materials* 176.1-3 (2010), pp. 589–596.

[174] Jong-Jin Baik, Seung-Bu Park, and Jae-Jin Kim. "Urban Flow and Dispersion Simulation Using a CFD Model Coupled to a Mesoscale Model." In: *Journal of Applied Meteorology and Climatology* 48.8 (2009), pp. 1667–1681.

[175] Steven R. Hanna, Michael J. Brown, Fernando E. Camelli, Stevens T. Chan, William J. Coirier, Olav R. Hansen, Alan H. Huber, Sura Kim, and R. Michael Reynolds. "Detailed simulations of atmospheric flow and dispersion in downtown Manhattan: An applications of five computational fluid dynamics models." In: *Bulletin of the American Meteorological Society* 87.12 (2006), pp. 1713–1726.

[176] Gopal Patnaik, Jay P. Boris, Theodore R. Young, and Fernando F. Grinstein. "Large Scale Urban Contaminant Transport Simulations With Miles." In: *Journal of Fluids Engineering* 129.August (2007), p. 1524.

[177] S. R. Hanna, G. A. Briggs, and R. P. Hosker. *H andbook of Atmospheric Diffusion*. Technical Information Center U.S. Department of Energy, 1982.

[178] C.M. Grinstead and J.L. Snell. "Markov Chains." In: *Introduction to Probability* (2010), pp. 1–66.

[179] G. I. Taylor. "Diffusion by continuous movements." In: *Proceedings of the London Mathematical Society* s2-20.1 (1922), pp. 196–212.

[180] Norbert Wiener. "Generalized Harmonic Analysis." In: *Acta Mathematica* 55 (1930), pp. 117–258.

[181] Andrei Kolmogorov. "Über die analytischen Methoden in der Wahrscheinlichkeitsrechnung." In: *Analytical Methods in the Theory of Probabilitya* 104.1 (1931), pp. 415–458.

[182] S. K. Kao. "Theories of Atmospheric Transport and Diffusion." In: *Atmospheric Science and Power Production*. Ed. by U.S. Dept. Commerce. Springfield, VA, 1984. Chap. 6, pp. 189–239.

[183] O. G. Sutton. "A Theory of Eddy Diffusion in the Atmosphere." In: *Proceedings of the Royal Society A*. 1932, pp. 143–165.

[184] F. Pasquill. "The estimation of the dispersion of windborne material." In: *The Meteorological Magazine* 90 (1961), pp. 33–49.

[185] F. A. Gifford. "An Outline of Theories of Diffusion in the Lower Layers of the Atmosphere." In: *Meteorology and Applied Atomic Energy* 1968 (1968), pp. 66–116.

[186] P. Skelsey, A.A.M. Holtslag, and W. van der Werf. "Development and validation of a quasi-Gaussian plume model for the transport of botanical spores." In: *Agricultural and Forest Meteorology* 148.8-9 (2008), pp. 1383–1394.

[187] F. Toja-Silva, Chen J., Hachinger S., and F. Hase. "CFD simulation of CO2 dispersion from urban thermal power plant: Analysis of turbulent Schmidt number and comparison with Gaussian plume model and measurements." In: *Journal of Wind Engineering and Industrial Aerodynamics* 169 (2017), pp. 177–193.

[188] S.R. Hanna, J.C. Chang, and D.G. Strimaitis. "Hazardous gas model evaluation with field observations." In: *Atmospheric Environment. Part A. General Topics* 27.15 (1993), pp. 2265–2285.

[189] G. A. Briggs. *Plume Rise*. U.S. Atomic Energy Commission, 1969.

[190] G. A. Briggs. *Diffusion Estimation for Small Emissions*. Tech. rep. Atmospheric Turbulence and Diffusion Laboratory, 1973.

[191] M. E. Smith. *Recommendend Guide for the Prediction of the Dispersion of Airborne Effluents*. Ed. by American Society for Mechanical Engineers. New York, 1968.

[192] F. Pasquill. *Atmospheric Dispersion Parameters in Gaussian Plume Modeling: Part II. Possible Requirements for Change in the Turner Workbook Values*. Tech. rep. U.S. Enviromental Protection Agency, 1976.

[193] J. C. Doran, T. W. Horst, and P. W. Nickola. "Variations in Measured Values of Lateral Diffusion Parameters." In: *Journal of Applied Meteorology* 17(6) (1978), pp. 825–831.

[194] R. R. Draxler. "Determination of atmospheric diffusion parameters." In: *Atmospheric Environment (1967)* 10.2 (1976), pp. 99–105.

[195] J.S. Irwin. "Estimating Plume Dispersion-A Comparison of Several Sigma Schemes." In: *Journal of Climate and Applied Meteorology* 22.1 (1983), pp. 92–114.

[196] A.H. Huber, W.H. Snyder, and R.E. Lawson. *The effects of a squat building on short stack effluents - a wind tunnel study*. Tech. rep. North Carolina, USA: U.S. Environmental Protection Agency, 1980.

[197] A.G. Davenport. "The relationship of wind structures to wind loading." In: *Proceedings of the Conference of Wind Effects on Buildings*. London, 1963, pp. 54–102.

[198] W.H. Snyder. *Guideline for fluid modelin of atmospheric diffusion*. Tech. rep. U.S. Environmental Protection Agency, 1981.

[199] R.I. Harris. "Measurements of wind structure at heights up to 598 feet above ground level." In: *Symposium on Wind Effects on Building and Structures*. Loughbotough University of Technology, UK, 1968.

[200] J.T. Lin, H.T. Liu, Y.H. Pao, D.K. Lilly, L. Israeli, and S.A. Orzag. *Laboratory and Numerical Simulation Of Plume Dispersion In Stably Stratified Flow Over Complex Terrain*. Tech. rep. U.S. Environmental Protection Agency, 1974.

[201] I.R. Cowan, I.P. Castro, and Robins A.G. "Numerical considerations for simulations of flow and dispersion around buildings." In: *Journal of Wind Engineering and Industrial Aerodynamics* 67-68 (1997), pp. 535–545.

[202] A. Scaperdas and S. Gilham. "Best practice advice for civil construction and HVAC." In: *The QNET-CFD Network Newsletter* 2.4 (2004), pp. 28–33.

[203] J.G. Bartzis, D. Vlachogiannis, and A. Sfetsos. "Best practice advice for environmental flows." In: *The QNET-CFD Network Newsletter* 2.4 (2004), pp. 34–39.

[204] B. E. Launder and D. B. Spalding. "The numerical computation of turbulent flows." In: *Computer Methods in Applied Mechanics and Engineering* 2.3 (1974), pp. 269–289.

[205] H. Jasak, H. G. Weller, and A. D. Gosman. "High resolution NVD differencing scheme for arbitrarily unstructured meshes." In: *International Journal for Numerical Methods in Fluids* 31.2 (1999), pp. 431–449.

[206] F. Menter. "Zonal Two Equation k-w Turbulence Models For Aerodynamic Flows." In: *23rd Fluid Dynamics, Plasmadynamics, and Lasers Conference*. 1993.

[207] F.R. Menter, M.L. Kuntz, and R. Langtry. "Ten Years of Industrial Experience with the SST Turbulence Model." In: *Turbulence Heat and Mass Transfer 4* 4 (2003), pp. 625–632.

[208] C. Gromke and B. Blocken. "Influence of avenue-trees on air quality at the urban neighborhood scale. Part I: Quality assurance studies and turbulent Schmidt number analysis for RANS CFD simulations." In: *Environmental Pollution* 196.1 (2015), pp. 214–223.

[209] "OpenFOAM+ v. 1612." In: *http://www.openfoam.com/releases/openfoam-v1612+/* (2016).

[210] Y. Tominaga and T. Stathopoulos. "Turbulent Schmidt numbers for CFD analysis with various types of flowfield." In: *Atmospheric Environment* 41.37 (2007), pp. 8091–8099.

Curriculum Vitae

Mattia Ricci was born on 13 April 1988 in Forlimpopoli, Italy. He graduated cum Laude in Civil Engineering (Structural Engineering) at the University of Bologna in Italy in 2013. From 2014, he started the first Ph.D. project in the framework of a double-degree agreement between the University of Bologna and the Eindhoven University of Technology, of which the results are presented in this dissertation. In addition, Mattia was involved in education, being teaching assistant of several courses for bachelor and master tracks in Civil Engineering at the University of Bologna, where he has also been co-supervisor of two bachelor and one master thesis.

Mattia has published 11 papers in international (ISI) journals and 12 conference papers and he is member of several scientific associations, among these the International Association for Wind Engineering (IAWE), the Italian Association for Wind Engineering (ANIV) and the Italian Association of Applied and Theoretical Mechanics (AIMETA). Mattia is also reviewer for the Journal of Wind Engineering and Industrial Aerodynamics, the Journal of Earthquake Engineering and Applied Mathematical Modelling.

PUBLICATIONS

INTERNATIONAL PEER-REVIEWED JOURNALS

- M. Ricci, L. Patruno, I. Kalkman, S. de Miranda, B. Blocken, *Towards LES as a design tool: wind loads assessment on a high-rise building*, Journal of Wind Engineering and Industrial Aerodynamics, under review.
- L. Patruno, M. Ricci, S. de Miranda, *Equivalent Static Wind Loads: Recent developments and analysis of a suspended roof*, Engineering Structures, 2017; 148:1-10.
- L. Patruno, M. Ricci, *On the generation of synthetic divergence-free homogeneous anisotropic turbulence*, Computer methods in applied mechanics and engineering, 2017; 315:396-417.
- M. Ricci, L. Patruno, S. de Miranda, *Wind loads and structural response: benchmarking LES on a low-rise building*, Engineering Structures, 2017; 144:26-42.
- M. Ricci, L.Patruno, S. de Miranda and F. Ubertini, *Flow field around a 5:1 rectangular cylinder using LES: Influence of inflow turbulence conditions, spanwise domain size and their interaction*, Computers & Fluids, 2017; 149:181-193.
- L. Patruno, M. Ricci, S. de Miranda and F. Ubertini, *An efficient approach to the determination of Equivalent Static Wind Loads*, Fluid & Structures, 2017; 68:1-14.
- M. Ricci, L. Patruno, S. de Miranda and F. Ubertini, *Effects of low incoming turbulence on the flow around a 5:1 rectangular cylinder at non-null attack angle*, Mathematical Problems in Engineering, 2016; Vol. 2016.
- L. Patruno, M. Ricci, S. de Miranda and F. Ubertini, *Numerical Simulation of a 5:1 rectangular cylinder at non-null angles of attack*, Journal of Wind Engineering and Industrial Aerodynamics, 2016; 151:146-157.
- L. Patruno, M. Ricci, S. de Miranda and F. Ubertini, *An efficient approach to the evaluation of wind effects on structures based on recorded pressure fields.*, Engineering Structures, 2016; 124:207-220.
- M. Ricci , L. Patruno, S. de Miranda, R. Saponelli and F. Ubertini, *Prediction and correction of mould shape dimensions for ceramic sanitary wares*, Journal of Materials Processing Technology, 2015; 215(1):309-319.
- S. de Miranda, L. Patruno, M. Ricci and F. Ubertini, *Numerical study of a twin box bridge deck with increasing gap ratio by using RANS and LES approaches*, Engineering Structures, 2015; 99:546-558.

- S. de Miranda, L. Patruno, M. Ricci, R. Saponelli, F. Ubertini, *Ceramic sanitary wares: prediction of the deformed shape after the production process*, Journal of Materials Processing Technology, 2015: 215:309-319.

CONFERENCES

- M. Ricci, L. Patruno, I. Kalkman, B. Blocken, S. de Miranda, *An LES approach for wind loads assessment on low-rise and high-rise buildings*, AIMETA Conference, 4-7 September 2017, Salerno, Italy.
- L. Patruno, M. Ricci, S. de Miranda, *Recent advancement in the extraction of Equivalent Static Wind Loads*, European-African Conference on Wind Engineering, 4-7 July 2017, Liége, Belgium.
- M. Ricci, L. Patruno, I. Kalkman, B. Blocken, S. de Miranda, *An LES approach to wind loads assessment*, Burgers Symposium, 30-31 May 2017, Lunteren, the Netherlands.
- M. Ricci, L. Patruno, I. Kalkman, B. Blocken, S. de Miranda, *Large Eddy Simulation for wind loads assessment: benchmarking on a high-rise building*, European-African Conference on Wind Engineering, 4-7 July 2017, Liége, Belgium.
- L. Patruno, M. Ricci, S. de Miranda, *Reduced structural models for the analysis of wind loading*, In-Vento Conference, 25-28 September 2016, Terni, Italy.
- L. Patruno, M. Ricci, B. Blocken, S. de Miranda, *Large Eddy Simulation for wind loads assessment on a low-rise building*, In-Vento Conference, 25-28 September 2016, Terni, Italy.
- L. Patruno, M. Ricci, S. de Miranda, F. Ubertini, *An efficient approach for linear buffeting analysis*, GIMC-GMA, 27-29 June 2016, Lucca, Italy.
- S. de Miranda, L. Patruno, M. Ricci , F. Ubertini, N. Cosentino, M. Majowiecki, *Wind loading: a work-flow for systematic comparison between CFD and experimental data*, VII International Conference on Textile Composites and Inflatable Structures, 19-21 October 2015, Barcelona, Spain.
- S. de Miranda, L. Patruno, M. Ricci and F. Ubertini, *Numerical study of the flow around rectangular cylinder 5:1 by using LES and RANS approaches*, AIMETA 2015, Genova, Italy.
- L. Patruno, M. Ricci, A. Cimarelli, S. de Miranda, A. Talamelli and F. Ubertini, *Large Eddy Simulation of turbulent flows: benchmarking on a rectangular prism*, iTi 2014, Bertinoro, Italy.
- S. de Miranda, L. Patruno, M. Ricci, R. Saponelli, F. Ubertini, *Ceramic sanitary wares: reverse engineering strategy for mould prototyping*, GIMC-GMA 2014, Cassino, Italy.

- S. de Miranda, L. Patruno, M. Ricci, R. Saponelli, F. Ubertini,*Ceramic sanitary wares: from the forming mould to the final product*, AIAS 2014, Rimini, Italy.

Bouwstenen is een publikatiereeks van de Faculteit Bouwkunde, Technische Universiteit Eindhoven. Zij presenteert resultaten van onderzoek en andere aktiviteiten op het vakgebied der Bouwkunde, uitgevoerd in het kader van deze Faculteit.

Bouwstenen zijn telefonisch te bestellen op nummer
040 - 2472383

Kernredaktie
MTOZ

Reeds verschenen in de serie
Bouwstenen

nr 1
Elan: A Computer Model for Building Energy Design: Theory and Validation
Martin H. de Wit
H.H. Driessen
R.M.M. van der Velden

nr 2
Kwaliteit, Keuzevrijheid en Kosten: Evaluatie van Experiment Klarendal, Arnhem
J. Smeets
C. le Nobel
M. Broos
J. Frenken
A. v.d. Sanden

nr 3
Crooswijk: Van 'Bijzonder' naar 'Gewoon'
Vincent Smit
Kees Noort

nr 4
Staal in de Woningbouw
Edwin J.F. Delsing

nr 5
Mathematical Theory of Stressed Skin Action in Profiled Sheeting with Various Edge Conditions
Andre W.A.M.J. van den Bogaard

nr 6
Hoe Berekenbaar en Betrouwbaar is de Coëfficiënt k in x-ksigma en x-ks?
K.B. Lub
A.J. Bosch

nr 7
Het Typologisch Gereedschap: Een Verkennende Studie Omtrent Typologie en Omtrent de Aanpak van Typologisch Onderzoek
J.H. Luiten

nr 8
Informatievoorziening en Beheerprocessen
A. Nauta
Jos Smeets (red.)
Helga Fassbinder (projectleider)
Adrie Proveniers
J. v.d. Moosdijk

nr 9
Strukturering en Verwerking van Tijdgegevens voor de Uitvoering van Bouwwerken
ir. W.F. Schaefer
P.A. Erkelens

nr 10
Stedebouw en de Vorming van een Speciale Wetenschap
K. Doevendans

nr 11
Informatica en Ondersteuning van Ruimtelijke Besluitvorming
G.G. van der Meulen

nr 12
Staal in de Woningbouw, Korrosie-Bescherming van de Begane Grondvloer
Edwin J.F. Delsing

nr 13
Een Thermisch Model voor de Berekening van Staalplaatbetonvloeren onder Brandomstandigheden
A.F. Hamerlinck

nr 14
De Wijkgedachte in Nederland: Gemeenschapsstreven in een Stedebouwkundige Context
K. Doevendans
R. Stolzenburg

nr 15
Diaphragm Effect of Trapezoidally Profiled Steel Sheets: Experimental Research into the Influence of Force Application
Andre W.A.M.J. van den Bogaard

nr 16
Versterken met Spuit-Ferrocement: Het Mechanische Gedrag van met Spuit-Ferrocement Versterkte Gewapend Betonbalken
K.B. Lubir
M.C.G. van Wanroy

nr 17
De Tractaten van Jean Nicolas Louis Durand
G. van Zeyl

nr 18
Wonen onder een Plat Dak: Drie Opstellen over Enkele Vooronderstellingen van de Stedebouw
K. Doevendans

nr 19
Supporting Decision Making Processes: A Graphical and Interactive Analysis of Multivariate Data
W. Adams

nr 20
Self-Help Building Productivity: A Method for Improving House Building by Low-Income Groups Applied to Kenya 1990-2000
P. A. Erkelens

nr 21
De Verdeling van Woningen: Een Kwestie van Onderhandelen
Vincent Smit

nr 22
Flexibiliteit en Kosten in het Ontwerpproces: Een Besluitvormingondersteunend Model
M. Prins

nr 23
Spontane Nederzettingen Begeleid: Voorwaarden en Criteria in Sri Lanka
Po Hin Thung

nr 24
Fundamentals of the Design of Bamboo Structures
Oscar Arce-Villalobos

nr 25
Concepten van de Bouwkunde
M.F.Th. Bax (red.)
H.M.G.J. Trum (red.)

nr 26
Meaning of the Site
Xiaodong Li

nr 27
Het Woonmilieu op Begrip Gebracht: Een Speurtocht naar de Betekenis van het Begrip 'Woonmilieu'
Jaap Ketelaar

nr 28
Urban Environment in Developing Countries
editors: Peter A. Erkelens
George G. van der Meulen (red.)

nr 29
Stategische Plannen voor de Stad: Onderzoek en Planning in Drie Steden
prof.dr. H. Fassbinder (red.)
H. Rikhof (red.)

nr 30
Stedebouwkunde en Stadsbestuur
Piet Beekman

nr 31
De Architectuur van Djenné: Een Onderzoek naar de Historische Stad
P.C.M. Maas

nr 32
Conjoint Experiments and Retail Planning
Harmen Oppewal

nr 33
Strukturformen Indonesischer Bautechnik: Entwicklung Methodischer Grundlagen für eine 'Konstruktive Pattern Language' in Indonesien
Heinz Frick arch. SIA

nr 34
Styles of Architectural Designing: Empirical Research on Working Styles and Personality Dispositions
Anton P.M. van Bakel

nr 35
Conjoint Choice Models for Urban Tourism Planning and Marketing
Benedict Dellaert

nr 36
Stedelijke Planvorming als Co-Produktie
Helga Fassbinder (red.)

nr 37
Design Research in the Netherlands
editors: R.M. Oxman
M.F.Th. Bax
H.H. Achten

nr 38
Communication in the Building Industry
Bauke de Vries

nr 39
Optimaal Dimensioneren van Gelaste Plaatliggers
J.B.W. Stark
F. van Pelt
L.F.M. van Gorp
B.W.E.M. van Hove

nr 40
Huisvesting en Overwinning van Armoede
P.H. Thung
P. Beekman (red.)

nr 41
Urban Habitat: The Environment of Tomorrow
George G. van der Meulen
Peter A. Erkelens

nr 42
A Typology of Joints
John C.M. Olie

nr 43
Modeling Constraints-Based Choices for Leisure Mobility Planning
Marcus P. Stemerding

nr 44
Activity-Based Travel Demand Modeling
Dick Ettema

nr 45
Wind-Induced Pressure Fluctuations on Building Facades
Chris Geurts

nr 46
Generic Representations
Henri Achten

nr 47
Johann Santini Aichel: Architectuur en Ambiguiteit
Dirk De Meyer

nr 48
Concrete Behaviour in Multiaxial Compression
Erik van Geel

nr 49
Modelling Site Selection
Frank Witlox

nr 50
Ecolemma Model
Ferdinand Beetstra

nr 51
Conjoint Approaches to Developing Activity-Based Models
Donggen Wang

nr 52
On the Effectiveness of Ventilation
Ad Roos

nr 53
Conjoint Modeling Approaches for Residential Group preferences
Eric Molin

nr 54
Modelling Architectural Design Information by Features
Jos van Leeuwen

nr 55
A Spatial Decision Support System for the Planning of Retail and Service Facilities
Theo Arentze

nr 56
Integrated Lighting System Assistant
Ellie de Groot

nr 57
Ontwerpend Leren, Leren Ontwerpen
J.T. Boekholt

nr 58
Temporal Aspects of Theme Park Choice Behavior
Astrid Kemperman

nr 59
Ontwerp van een Geïndustrialiseerde Funderingswijze
Faas Moonen

nr 60
Merlin: A Decision Support System for Outdoor Leisure Planning
Manon van Middelkoop

nr 61
The Aura of Modernity
Jos Bosman

nr 62
Urban Form and Activity-Travel Patterns
Daniëlle Snellen

nr 63
Design Research in the Netherlands 2000
Henri Achten

nr 64
Computer Aided Dimensional Control in Building Construction
Rui Wu

nr 65
Beyond Sustainable Building
editors: Peter A. Erkelens
Sander de Jonge
August A.M. van Vliet
co-editor: Ruth J.G. Verhagen

nr 66
Das Globalrecyclingfähige Haus
Hans Löfflad

nr 67
Cool Schools for Hot Suburbs
René J. Dierkx

nr 68
A Bamboo Building Design Decision Support Tool
Fitri Mardjono

nr 69
Driving Rain on Building Envelopes
Fabien van Mook

nr 70
Heating Monumental Churches
Henk Schellen

nr 71
Van Woningverhuurder naar Aanbieder van Woongenot
Patrick Dogge

nr 72
Moisture Transfer Properties of Coated Gypsum
Emile Goossens

nr 73
Plybamboo Wall-Panels for Housing
Guillermo E. González-Beltrán

nr 74
The Future Site-Proceedings
Ger Maas
Frans van Gassel

nr 75
Radon transport in Autoclaved Aerated Concrete
Michel van der Pal

nr 76
The Reliability and Validity of Interactive Virtual Reality Computer Experiments
Amy Tan

nr 77
Measuring Housing Preferences Using Virtual Reality and Belief Networks
Maciej A. Orzechowski

nr 78
Computational Representations of Words and Associations in Architectural Design
Nicole Segers

nr 79
Measuring and Predicting Adaptation in Multidimensional Activity-Travel Patterns
Chang-Hyeon Joh

nr 80
Strategic Briefing
Fayez Al Hassan

nr 81
Well Being in Hospitals
Simona Di Cicco

nr 82
Solares Bauen: Implementierungs- und Umsetzungs-Aspekte in der Hochschulausbildung in Österreich
Gerhard Schuster

nr 83
Supporting Strategic Design of Workplace Environments with Case-Based Reasoning
Shauna Mallory-Hill

nr 84
ACCEL: A Tool for Supporting Concept Generation in the Early Design Phase
Maxim Ivashkov

nr 85
Brick-Mortar Interaction in Masonry under Compression
Ad Vermeltfoort

nr 86
Zelfredzaam Wonen
Guus van Vliet

nr 87
Een Ensemble met Grootstedelijke Allure
Jos Bosman
Hans Schippers

nr 88
On the Computation of Well-Structured Graphic Representations in Architectural Design
Henri Achten

nr 89
De Evolutie van een West-Afrikaanse Vernaculaire Architectuur
Wolf Schijns

nr 90
ROMBO Tactiek
Christoph Maria Ravesloot

nr 91
External Coupling between Building Energy Simulation and Computational Fluid Dynamics
Ery Djunaedy

nr 92
Design Research in the Netherlands 2005
editors: Henri Achten
Kees Dorst
Pieter Jan Stappers
Bauke de Vries

nr 93
Ein Modell zur Baulichen Transformation
Jalil H. Saber Zaimian

nr 94
Human Lighting Demands: Healthy Lighting in an Office Environment
Myriam Aries

nr 95
A Spatial Decision Support System for the Provision and Monitoring of Urban Greenspace
Claudia Pelizaro

nr 96
Leren Creëren
Adri Proveniers

nr 97
Simlandscape
Rob de Waard

nr 98
Design Team Communication
Ad den Otter

nr 99
Humaan-Ecologisch Georiënteerde Woningbouw
Juri Czabanowski

nr 100
Hambase
Martin de Wit

nr 101
Sound Transmission through Pipe Systems and into Building Structures
Susanne Bron-van der Jagt

nr 102
Het Bouwkundig Contrapunt
Jan Francis Boelen

nr 103
A Framework for a Multi-Agent Planning Support System
Dick Saarloos

nr 104
Bracing Steel Frames with Calcium Silicate Element Walls
Bright Mweene Ng'andu

nr 105
Naar een Nieuwe Houtskeletbouw
F.N.G. De Medts

nr 106 and 107
Niet gepubliceerd

nr 108
Geborgenheid
T.E.L. van Pinxteren

nr 109
Modelling Strategic Behaviour in Anticipation of Congestion
Qi Han

nr 110
Reflecties op het Woondomein
Fred Sanders

nr 111
On Assessment of Wind Comfort by Sand Erosion
Gábor Dezsö

nr 112
Bench Heating in Monumental Churches
Dionne Limpens-Neilen

nr 113
RE. Architecture
Ana Pereira Roders

nr 114
Toward Applicable Green Architecture
Usama El Fiky

nr 115
Knowledge Representation under Inherent Uncertainty in a Multi-Agent System for Land Use Planning
Liying Ma

nr 116
Integrated Heat Air and Moisture Modeling and Simulation
Jos van Schijndel

nr 117
Concrete Behaviour in Multiaxial Compression
J.P.W. Bongers

nr 118
The Image of the Urban Landscape
Ana Moya Pellitero

nr 119
The Self-Organizing City in Vietnam
Stephanie Geertman

nr 120
A Multi-Agent Planning Support System for Assessing Externalities of Urban Form Scenarios
Rachel Katoshevski-Cavari

nr 121
Den Schulbau Neu Denken, Fühlen und Wollen
Urs Christian Maurer-Dietrich

nr 122
Peter Eisenman Theories and Practices
Bernhard Kormoss

nr 123
User Simulation of Space Utilisation
Vincent Tabak

nr 125
In Search of a Complex System Model
Oswald Devisch

nr 126
Lighting at Work: Environmental Study of Direct Effects of Lighting Level and Spectrum on Psycho-Physiological Variables
Grazyna Górnicka

nr 127
Flanking Sound Transmission through Lightweight Framed Double Leaf Walls
Stefan Schoenwald

nr 128
Bounded Rationality and Spatio-Temporal Pedestrian Shopping Behavior
Wei Zhu

nr 129
Travel Information: Impact on Activity Travel Pattern
Zhongwei Sun

nr 130
Co-Simulation for Performance Prediction of Innovative Integrated Mechanical Energy Systems in Buildings
Marija Trčka

nr 131
Niet gepubliceerd

nr 132
Architectural Cue Model in Evacuation Simulation for Underground Space Design
Chengyu Sun

nr 133
Uncertainty and Sensitivity Analysis in Building Performance Simulation for Decision Support and Design Optimization
Christina Hopfe

nr 134
Facilitating Distributed Collaboration in the AEC/FM Sector Using Semantic Web Technologies
Jacob Beetz

nr 135
Circumferentially Adhesive Bonded Glass Panes for Bracing Steel Frame in Façades
Edwin Huveners

nr 136
Influence of Temperature on Concrete Beams Strengthened in Flexure with CFRP
Ernst-Lucas Klamer

nr 137
Sturen op Klantwaarde
Jos Smeets

nr 139
Lateral Behavior of Steel Frames with Discretely Connected Precast Concrete Infill Panels
Paul Teewen

nr 140
Integral Design Method in the Context of Sustainable Building Design
Perica Savanović

nr 141
Household Activity-Travel Behavior: Implementation of Within-Household Interactions
Renni Anggraini

nr 142
Design Research in the Netherlands 2010
Henri Achten

nr 143
Modelling Life Trajectories and Transport Mode Choice Using Bayesian Belief Networks
Marloes Verhoeven

nr 144
Assessing Construction Project Performance in Ghana
William Gyadu-Asiedu

nr 145
Empowering Seniors through Domotic Homes
Masi Mohammadi

nr 146
An Integral Design Concept for Ecological Self-Compacting Concrete
Martin Hunger

nr 147
Governing Multi-Actor Decision Processes in Dutch Industrial Area Redevelopment
Erik Blokhuis

nr 148
A Multifunctional Design Approach for Sustainable Concrete
Götz Hüsken

nr 149
Quality Monitoring in Infrastructural Design-Build Projects
Ruben Favié

nr 150
Assessment Matrix for Conservation of Valuable Timber Structures
Michael Abels

nr 151
Co-simulation of Building Energy Simulation and Computational Fluid Dynamics for Whole-Building Heat, Air and Moisture Engineering
Mohammad Mirsadeghi

nr 152
External Coupling of Building Energy Simulation and Building Element Heat, Air and Moisture Simulation
Daniel Cóstola

nr 153
Adaptive Decision Making In Multi-Stakeholder Retail Planning
Ingrid Janssen

nr 154
Landscape Generator
Kymo Slager

nr 155
Constraint Specification in Architecture
Remco Niemeijer

nr 156
A Need-Based Approach to Dynamic Activity Generation
Linda Nijland

nr 157
Modeling Office Firm Dynamics in an Agent-Based Micro Simulation Framework
Gustavo Garcia Manzato

nr 158
Lightweight Floor System for Vibration Comfort
Sander Zegers

nr 159
Aanpasbaarheid van de Draagstructuur
Roel Gijsbers

nr 160
'Village in the City' in Guangzhou, China
Yanliu Lin

nr 161
Climate Risk Assessment in Museums
Marco Martens

nr 162
Social Activity-Travel Patterns
Pauline van den Berg

nr 163
Sound Concentration Caused by Curved Surfaces
Martijn Vercammen

nr 164
Design of Environmentally Friendly Calcium Sulfate-Based Building Materials: Towards an Improved Indoor Air Quality
Qingliang Yu

nr 165
Beyond Uniform Thermal Comfort on the Effects of Non-Uniformity and Individual Physiology
Lisje Schellen

nr 166
Sustainable Residential Districts
Gaby Abdalla

nr 167
Towards a Performance Assessment Methodology using Computational Simulation for Air Distribution System Designs in Operating Rooms
Mônica do Amaral Melhado

nr 168
Strategic Decision Modeling in Brownfield Redevelopment
Brano Glumac

nr 169
Pamela: A Parking Analysis Model for Predicting Effects in Local Areas
Peter van der Waerden

nr 170
A Vision Driven Wayfinding Simulation-System Based on the Architectural Features Perceived in the Office Environment
Qunli Chen

nr 171
Measuring Mental Representations Underlying Activity-Travel Choices
Oliver Horeni

nr 172
Modelling the Effects of Social Networks on Activity and Travel Behaviour
Nicole Ronald

nr 173
Uncertainty Propagation and Sensitivity Analysis Techniques in Building Performance Simulation to Support Conceptual Building and System Design
Christian Struck

nr 174
Numerical Modeling of Micro-Scale Wind-Induced Pollutant Dispersion in the Built Environment
Pierre Gousseau

nr 175
Modeling Recreation Choices over the Family Lifecycle
Anna Beatriz Grigolon

nr 176
Experimental and Numerical Analysis of Mixing Ventilation at Laminar, Transitional and Turbulent Slot Reynolds Numbers
Twan van Hooff

nr 177
Collaborative Design Support: Workshops to Stimulate Interaction and Knowledge Exchange Between Practitioners
Emile M.C.J. Quanjel

nr 178
Future-Proof Platforms for Aging-in-Place
Michiel Brink

nr 179
Motivate: A Context-Aware Mobile Application for Physical Activity Promotion
Yuzhong Lin

nr 180
Experience the City: Analysis of Space-Time Behaviour and Spatial Learning
Anastasia Moiseeva

nr 181
Unbonded Post-Tensioned Shear Walls of Calcium Silicate Element Masonry
Lex van der Meer

nr 182
Construction and Demolition Waste Recycling into Innovative Building Materials for Sustainable Construction in Tanzania
Mwita M. Sabai

nr 183
Durability of Concrete with Emphasis on Chloride Migration
Przemysław Spiesz

nr 184
Computational Modeling of Urban Wind Flow and Natural Ventilation Potential of Buildings
Rubina Ramponi

nr 185
A Distributed Dynamic Simulation Mechanism for Buildings Automation and Control Systems
Azzedine Yahiaoui

nr 186
Modeling Cognitive Learning of Urban Networks in Daily Activity-Travel Behavior
Şehnaz Cenani Durmazoğlu

nr 187
Functionality and Adaptability of Design Solutions for Public Apartment Buildings in Ghana
Stephen Agyefi-Mensah

nr 188
A Construction Waste Generation Model for Developing Countries
Lilliana Abarca-Guerrero

nr 189
Synchronizing Networks: The Modeling of Supernetworks for Activity-Travel Behavior
Feixiong Liao

nr 190
Time and Money Allocation Decisions in Out-of-Home Leisure Activity Choices
Gamze Zeynep Dane

nr 191
How to Measure Added Value of CRE and Building Design
Rianne Appel-Meulenbroek

nr 192
Secondary Materials in Cement-Based Products: Treatment, Modeling and Environmental Interaction
Miruna Florea

nr 193
Concepts for the Robustness Improvement of Self-Compacting Concrete: Effects of Admixtures and Mixture Components on the Rheology and Early Hydration at Varying Temperatures
Wolfram Schmidt

nr 194
Modelling and Simulation of Virtual Natural Lighting Solutions in Buildings
Rizki A. Mangkuto

nr 195
Nano-Silica Production at Low Temperatures from the Dissolution of Olivine - Synthesis, Tailoring and Modelling
Alberto Lazaro Garcia

nr 196
Building Energy Simulation Based Assessment of Industrial Halls for Design Support
Bruno Lee

nr 197
Computational Performance Prediction of the Potential of Hybrid Adaptable Thermal Storage Concepts for Lightweight Low-Energy Houses
Pieter-Jan Hoes

nr 198
Application of Nano-Silica in Concrete
George Quercia Bianchi

nr 199
Dynamics of Social Networks and Activity Travel Behaviour
Fariya Sharmeen

nr 200
Building Structural Design Generation and Optimisation including Spatial Modification
Juan Manuel Davila Delgado

nr 201
Hydration and Thermal Decomposition of Cement/Calcium-Sulphate Based Materials
Ariën de Korte

nr 202
Republiek van Beelden:
De Politieke Werkingen van het Ontwerp in Regionale Planvorming
Bart de Zwart

nr 203
Effects of Energy Price Increases on Individual Activity-Travel Repertoires and Energy Consumption
Dujuan Yang

nr 204
Geometry and Ventilation:
Evaluation of the Leeward Sawtooth Roof Potential in the Natural Ventilation of Buildings
Jorge Isaac Perén Montero

nr 205
Computational Modelling of Evaporative Cooling as a Climate Change Adaptation Measure at the Spatial Scale of Buildings and Streets
Hamid Montazeri

nr 206
Local Buckling of Aluminium Beams in Fire Conditions
Ronald van der Meulen

nr 207
Historic Urban Landscapes:
Framing the Integration of Urban and Heritage Planning in Multilevel Governance
Loes Veldpaus

nr 208
Sustainable Transformation of the Cities:
Urban Design Pragmatics to Achieve a Sustainable City
Ernesto Antonio Zumelzu Scheel

nr 209
Development of Sustainable Protective Ultra-High Performance Fibre Reinforced Concrete (UHPFRC):
Design, Assessment and Modeling
Rui Yu

nr 210
Uncertainty in Modeling Activity-Travel Demand in Complex Uban Systems
Soora Rasouli

nr 211
Simulation-based Performance Assessment of Climate Adaptive Greenhouse Shells
Chul-sung Lee

nr 212
Green Cities:
Modelling the Spatial Transformation of the Urban Environment using Renewable Energy Technologies
Saleh Mohammadi

nr 213
A Bounded Rationality Model of Short and Long-Term Dynamics of Activity-Travel Behavior
Ifigeneia Psarra

nr 214
Effects of Pricing Strategies on Dynamic Repertoires of Activity-Travel Behaviour
Elaheh Khademi

nr 215
Handstorm Principles for Creative and Collaborative Working
Frans van Gassel

nr 216
Light Conditions in Nursing Homes: Visual Comfort and Visual Functioning of Residents
Marianne M. Sinoo

nr 217
Woonsporen: De Sociale en Ruimtelijke Biografie van een Stedelijk Bouwblok in de Amsterdamse Transvaalbuurt
Hüseyin Hüsnü Yegenoglu

nr 218
Studies on User Control in Ambient Intelligent Systems
Berent Willem Meerbeek

nr 219
Daily Livings in a Smart Home: Users' Living Preference Modeling of Smart Homes
Erfaneh Allameh

nr 220
Smart Home Design: Spatial Preference Modeling of Smart Homes
Mohammadali Heidari Jozam

nr 221
Wonen: Discoursen, Praktijken, Perspectieven
Jos Smeets

nr 222
Personal Control over Indoor Climate in Offices: Impact on Comfort, Health and Productivity
Atze Christiaan Boerstra

nr 223
Personalized Route Finding in Multimodal Transportation Networks
Jianwe Zhang

nr 224
The Design of an Adaptive Healing Room for Stroke Patients
Elke Daemen

nr 225
Experimental and Numerical Analysis of Climate Change Induced Risks to Historic Buildings and Collections
Zara Huijbregts

nr 226
Wind Flow Modeling in Urban Areas Through Experimental and Numerical Techniques
Alessio Ricci

nr 227
Clever Climate Control for Culture: Energy Efficient Indoor Climate Control Strategies for Museums Respecting Collection Preservation and Thermal Comfort of Visitors
Rick Kramer

nr 228
nog niet bekend / gepubliceerd

nr 229
nog niet bekend / gepubliceerd

nr 230
Environmental assessment of Building Integrated Photovoltaics: Numerical and Experimental Carrying Capacity Based Approach
Michiel Ritzen

nr 231
Design and Performance of Plasticizing Admixture and Secondary Minerals in Alkali Activated Concrete: Sustaining a Concrete Future
Arno Keulen

nr 232
nog niet bekend / gepubliceerd

nr 233
Stage Acoustics and Sound Exposure in Performance and Rehearsal Spaces for Orchestras:
Methods for Physical Measurements
Remy Wenmaekers

nr 234
titel nog niet bekend / gepubliceerd

nr 235
Large Eddy Simulations Applied to Wind Loading and Pollutant Dispersion
Mattia Ricci